Toward an improved understanding of the Southern Ocean's biological pump: Phytoplankton group-specific contributions to nitrogen and carbon cycling across the Subantarctic Indian Ocean

Heather Forrer

Dissertation presented for the Degree of Master of Science
in the Department of Oceanography
University of Cape Town

August 2020

Supervisor: Dr Sarah Fawcett
Co-supervisor: Dr Angela Knapp

Plagiarism Declaration

I know the meaning of plagiarism and declare that all of the work in this dissertation, save for that which is properly acknowledged, is my own.

Signed by candidate

_____

Heather Forrer

_____

Date

Abstract

Iron (and silicate) (co-)limitation of phytoplankton is considered a primary cause of the Southern Ocean's inefficient biological pump. However, the role of phytoplankton community structure and response to nutrient cycling remains poorly understood. In a mass balance sense, phytoplankton consumption of new nitrogen (N; e.g., allochthonous nitrate) is proportional to net carbon (C) export, while growth fueled by recycled N (e.g., ammonium) yields no net C flux. The N isotope ratio ($\delta^{15}N$) of surface biomass has long been used as an integrative tracer of new versus regenerated uptake. This approach is rendered more accurate by coupling either fluorescence-activated cell sorting (FACS; of nano- and picophytoplankton; 0.4-20 μm) or microscopy (for microphytoplankton; >20 um) with group-specific $\delta^{15}N$ measurements. Samples were collected for the analysis of nutrients and nitrate-, FACS-, and microscopy-$\delta^{15}N$ on a mid-summer transect of the Subantarctic Indian basin during the 2016/17 Antarctic Circumnavigation Expedition (ACE) cruise. The data show that all phytoplankton populations preferentially utilize nitrate (≥55%) across the Indian Sector of the Subantarctic, potentially driving higher C export potential than previously estimated. Indeed, near the Subantarctic islands, 72% of micro- and >80% of nano- and picophytoplankton growth is supported by nitrate. This is likely due to the partial alleviation of phytoplankton iron and silicate stress, largely as a result of bathymetric upwelling, which constitutes a manifestation of the island mass effect. C export potential is lower in the open ocean region away from the islands where iron stress has been shown to be higher; here, nitrate supports >55% of micro- and picophytoplankton and 7 to 79% of nanophytoplankton growth. In terms of relative abundance (RA), the open Subantarctic is dominated by picoeukaryotes (64%), although there exists a large disconnect between relative abundance and potential contribution to C export. The three largest surface-ocean phytoplankton populations included in this study – microphytoplankton, cryptophytes, and nanoeukaryotes – each contribute ~30% to the total C export potential across the Subantarctic Indian sector while picophytoplankton contribute ~5%. Thus, as has been concluded previously, the larger phytoplankton size classes are disproportionately important drivers of the Subantarctic biological pump. Other interesting ecological findings include diatom-dominated microphytoplankton populations apparently fueled by a significant fraction of regenerated N, even in areas of iron supply, and *Synechococcus* relying near-exclusively on new N, in contrast to subtropical observations. Additionally, the abundance of *Synechococcus* appears to be controlled by the availability of iron across the Subantarctic, with silicate and temperature playing a supporting role.

Acknowledgements

Firstly, I would like to thank my supervisor Sarah Fawcett. Sarah, thank you for all the amazing opportunities you have afforded me – going to sea, attending workshops and presenting my work at conferences. This thesis has been a long but exciting journey, so thank you for your constant support, patience and encouragement to dream big. Working with you for my Honours and Masters degrees (and now having you on my PhD committee) has been a privilege. Thank you for sharing your passion for phytoplankton and N isotopes with me and proving that "phytoplankton are cooler than whales". None of this work would have been possible without you.

My sincere thanks also goes to my co-supervisor Angela Knapp. Thank you for opening up your lab to me to run samples, for helping me with the writing process (even when I hit every writer's block possible) and reminding me every day that this work is so exciting and important. These stimulating conversations have been so encouraging and I look forward to working on a PhD with you!

Support for this study was provided by the Swiss Polar Institute's Antarctic Circumnavigation Expedition (ACE), the National Research Foundation (NRF), the South African National Antarctic Program (SANAP), the University of Cape Town's (UCT) Sir Robert Kotze Travel Bursary and Florida State University's Winchester Funds, without which this research would not have been possible.

I would like to recognize the Swiss Polar Institute, chief scientist David Walton and the Captain and crew of the *R/V Akademik Treshnikov* for organizing and making sample collection possible. I would also like to thank the members of ACE Project 12, especially Samantha Waterworth, Tommy Bornman and Hazel Little (ACE Project 1) for keeping spirits up and always being willing to help me on Leg 1. Furthermore, thank you to Tahlia Henry for disentangling the CTD data and general all-round support throughout this process!

In addition to helping on the cruise, a massive thank you to Tommy Bornman (Nelson Mandela University) for the microscopy counts. Thank you for prioritizing my samples - I know it took months of your time!

Thank you to Raymond Roman (UCT Oceanography) for helping with the nutrient analysis, Keren Cooper (UCT Microbiology) and Emma Rocke (UCT Biology) for light microscopy assistance and Miranda Waldron (UCT Electron Microscope Unit) for scanning electron microscopy assistance.

I am grateful to Ronnie Dreyer (UCT Department of Immunology and Infectious Diseases) for helping me with the flow cytometry sorting of my samples. Thank you for teaching me how the Becton Dickinson FACS Aria FCM works and for always being happy to help adjust specs for my runs. I looked forward to our Monday sorting time when we discussed the weekend's rugby games (and other important scientific findings). Furthermore, thank you to Ruan Parrott (UCT Oceanography) for helping me with FlowJo and always being available to bounce ideas off.

I would like to thank the Knapp Lab including Rachel Thomas, Jeremy Whitehead and Stephanie Helefinger for helping me with the N isotope analyses. Additionally, thank you to the Fawcett Lab for the simulating conversations over years.

My sincere thanks to the UCT Oceanography Dive Unit including Pieter Truter, Hazel Little, Steven Horsley and Snippy for your continuous support, endless cups of tea and the odd dive to two to keep me sane. Thank you for also supporting my crazy new ideas and being willing to build incubators for further experiments, it is so appreciated!

I would like to acknowledge Cashifa Karriem (UCT Oceanography) for helping with lab and cruise equipment orders, send samples to the Knapp Lab and UC Davis as well as general administration. I would not know where to begin without you.

I would like to thank Samantha Knobel, Kirsten Bohle and Rachel Thomas for your support and encouragement over the years, for waving me off for cruises and dropping me/ picking me up at the airport whenever this MSc took me elsewhere.

Lastly, I would like to thank my family, Jef, Nina and Frances Forrer. Your endless support throughout this whole journey is so appreciated. Thank you for helping me label 5000+ sample bottles, load the *R/V Akademik Treshnikov*, move the -80°C freezer (that turned into more of an adventure than anticipated), adjust figures in Photoshop, and for getting the office ready for my "writing holidays". Thank you for always being excited to hear about my new findings and ideas, for jumping on airplanes to meet me around the world and for always being so proud to tell your friends I study "whale food that is stopping climate change". I could not have done this without your constant support and for that I am forever grateful.

Table of Contents:

Table of acronyms

Acronym	Full description
AABW	Antarctic Bottom Water
AAIW	Antarctic Intermediate Water
AASW	Antarctic Surface Water
ACC	Antarctic Circumpolar Current
ASF	Antarctic Slope Front
CCM	CO_2 concentrating mechanisms
Chl-a	Chlorophyll-*a*
CR	Crozet archipelago
CROZEX	CROZet natural iron bloom and EXport experiment
CRYPTO	Cryptophytes
f-ratio	Flux ratio
FACS	Fluorescence-activated cell sorting
FCM	Flow cytometer
FSC	Forward scatter
FTN	Ferritin
HAT-NRTs	High-affinity nitrate transporters
HEOBI	Heard Earth-Ocean-Biosphere Interactions
HNLC	High Nutrient-Low Chlorophyll
HR	Heard and McDonald Islands
IME	Island Mass Effect
KEOPS	KErguelen Ocean and Plateau Study
KG	Kerguelen Island
LCDW	Lower Circumpolar Deep Water
LGM	Last Glacial Maximum
LM	Light microscope
MICRO	Microphytoplankton (>20 μm)
ML	Mixed-layer
MLD	Mixed-layer depth
NEUKS	Nanoeukaryotes
OAZ	Open Antarctic Zone
OO PFZ Sector	Open Ocean Polar Frontal Zone Sector
OO SAZ Sector	Open Ocean Subantarctic Zone Sector
PE	Phycoerythrin
PEI	Prince Edward Islands
PEUKS	Picoeukaryotes
PF	Polar Front
PF Sector	Polar Frontal Sector
PFZ	Polar Frontal Zone

PON	Particulate organic nitrogen
RA	Relative abundance
RCC	Relative Carbon Contribution
SAF	Subantarctic Front
SAMW	Subantarctic Mode Water
SASW	Subantarctic Surface Water
SAZ	Subantarctic Zone
SEM	Scanning electron microscope
SSC	Side scatter
SST	Sea surface temperature
STF	Subtropical Front
SYN	*Synechococcus*
Tmin	Temperature minimum layer
UCDW	Upper Circumpolar Deep Water

1. Literature Review

1.1 The ocean's role in the global carbon cycle and climate

Ubiquitous single-celled marine photoautotrophs, phytoplankton, form the basal tropic level of the marine food web and play a crucial role in the regulation of the Earth's climate (Boyce et al., 2010; Deppler & Davidson, 2017; Dutkiewitcz et al., 2019). Phytoplankton inhabit the euphotic zone (sunlit upper layer of the ocean) where they convert dissolved atmospheric carbon dioxide (CO_2) into organic carbon (C) through the process of photosynthesis (Figure 1.1), accounting for ~50% of global primary productivity (Field et al., 1998; Boyce et al., 2010). The majority of the organic matter produced from primary production is either grazed upon by zooplankton that then fuel upper trophic levels including fish and whales, or is remineralized by bacteria in what is termed the "microbial loop" (Azam et al., 1983; Lochte et al., 1997; Christaki et al., 2014; Deppeler & Davidson, 2017). Organic C that escapes recycling within the upper ocean sinks to depth in the form of dead cells, marine snow or fecal pellets, thereby transferring C to the ocean's stratified interior where it is stored on the timescale of a season to ~1000 years (Figure 1.1) (Falkowski et al., 1988; DeVries et al., 2012). The sequestration of C (i.e., long-term storage in the deep ocean, isolated from exchange with the atmosphere on centennial timescales) lowers atmospheric CO_2 (Broecker, 1982a & b; Sigman & Boyle, 2000). Moreover, this mechanism of vertical export and sequestration of biological C that originated as atmospheric CO_2, termed the "biological pump" (Figure 1.1) (Volk & Hoffert, 1985; Berger et al., 1988; Sigman & Boyle, 2000; Ducklow et al., 2001; Karl et al., 2001), has led to the oceans becoming one of the largest active natural and anthropogenic C reservoirs (Takahashi et al., 2002; Turner, 2015; Nayak & Twardowski, 2020). Global atmospheric CO_2 concentrations having increased by 45% since the start of the industrial era (Bush, 2020), such that the oceanic C sink is becoming progressively more important to mitigate the effects of climate change (Khatiwala et al., 2013; Landschützer et al., 2014 & 2016).

Various factors affect the strength (i.e., the rate of organic C export) and efficiency (i.e., the degree to which primary productivity contributes to export from the available nutrients) of the global ocean's biological pump, including the availability of macronutrients such as nitrogen (N), phosphorous (P), and silicate (Si), as well as micronutrients such as iron (Fe) (Broecker, 1982a & b; Codispoti, 1989; Ridgwell, 2002; Salter et al., 2012 & 2014; Assmy et al., 2013). It is important to quantify the strength and efficiency of the modern-day biological pump in order to understand the potential response of the global ocean to a changing climate (Bopp et al., 2001; Kwon et al., 2009). This is difficult, however, because the rate of primary productivity in a particular system is not a good indicator of either the energy available to higher trophic levels or the contribution to C export given the potential for C recycling

within the euphotic zone (Dugdale & Goering, 1967). Originally conceptualized by Dugdale & Goering (1967), the "new production paradigm" is a tool, widely utilized over the past five decades, that links surface N assimilation to C export in a mass balance framework, ultimately allowing the biological pump's strength and efficiency to be quantified (Figure 1.2).

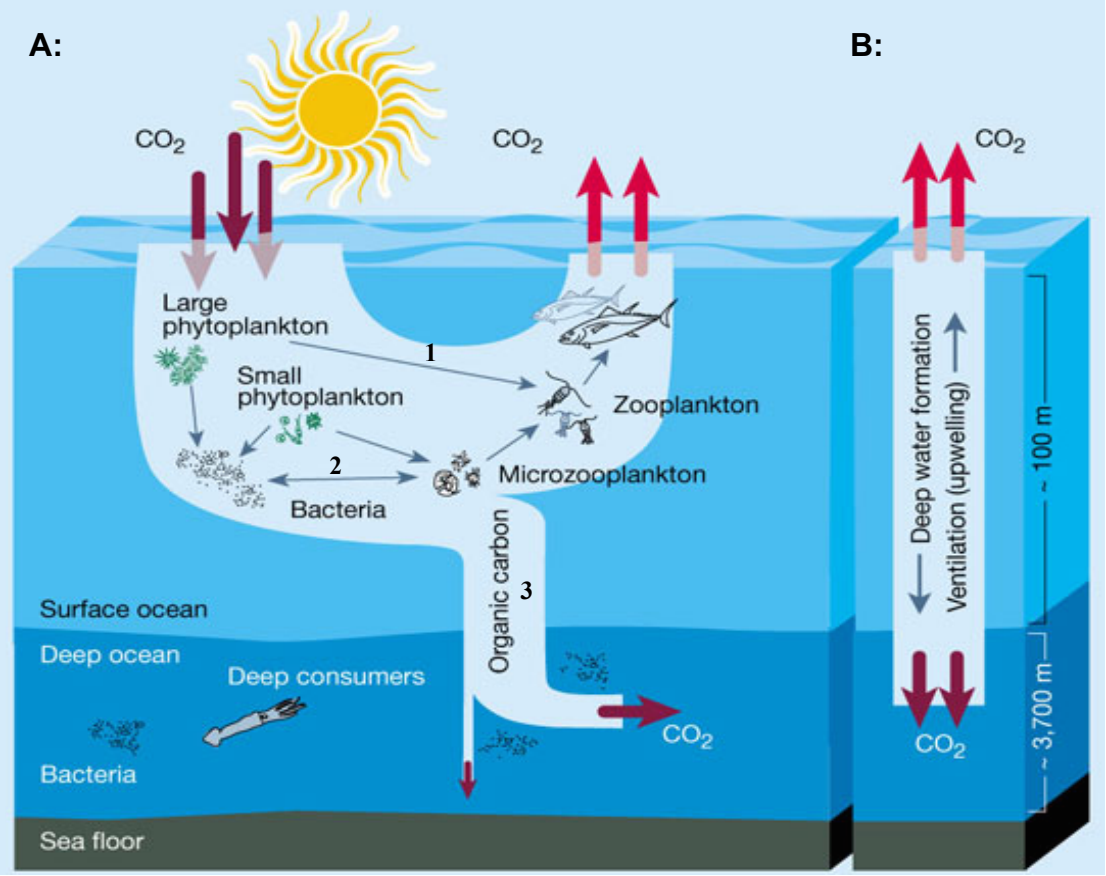

Figure 1.1: The ocean's A: biological pump drives the sequestration of carbon (C) to the deep ocean following the uptake of atmospheric CO_2 by phytoplankton during photosynthesis. This CO_2 is fixed as organic C that ultimately has three (not unrelated) fates; (1) consumption by higher tropic levels (zooplankton, that are then consumed by larger organisms) following which C is either released as CO_2 through respiration or concentrated in fecal pellets (destined for sequestration), (2) remineralization to CO_2 by heterotrophic bacteria within the euphotic zone (the "microbial loop"), or (3) sequestration in the deep ocean for ~1000 years. The growth of phytoplankton (in terms of both the species that proliferate and their abundance) and thus the corresponding uptake of CO_2 is controlled by the availability of macro- and micronutrients, which influence both the strength and efficiency of the biological pump. Additionally, the B: solubility pump augments the biological pump. Approximately 30-40% of global oceanic (and ~30% of global anthropogenic; Turner, 2015; Nayak & Twardowski, 2020) CO_2 fixation occurs in the Southern Ocean (Landschützer et al., 2014; Gruber et al., 2019; Li et al., 2019), with sequestration as the fate for ~10% of this C. (Figure adapted from Chisholm, 2000).

1.1.1 Quantifying the biological pump: new and regenerated production

Biologically available N, including nitrite (NO_2^-), ammonium (NH_4^+), dissolved and particulate organic nitrogen (DON and PON, respectively) and the most common form, nitrate (NO_3^-), can be characterized as either "new" or "regenerated" (Dugdale & Goering, 1967). While the balance between biological N sources (mainly N_2 fixation, the reduction of atmospheric $N_{2(g)}$ to ammonia, NH_3, by diazotrophs such as *Trichodesmium*) and sinks (denitrification and anammox, the conversion of fixed N to $N_{2(g)}$) determine the availability of N in the global ocean (Zehr & Ward, 2002; Gruber, 2008), the form, speciation and distribution of N is directly linked to the internal processes of assimilation (uptake by phytoplankton), ammonification (remineralization of organic N to NH_4^+), nitrification (NH_4^+ oxidation to NO_2^- and then to NO_3^-) and organic N export (Gruber, 2008; Casciotti, 2016). "New production" is phytoplankton growth fueled by new N (mainly allochthonous NO_3^- mixed up from the deep ocean reservoir, augmented in the low latitude ocean by N fixation) whereas "regenerated production" refers to phytoplankton growth supported by N recycled in the surface ocean (largely NH_4^+, as well as forms of DON, and NO_2^- and NO_3^- produced in the euphotic zone) (Dugdale & Goering, 1967). Since new production must be balanced by the export of euphotic zone organic matter on an annual timescale ("export production"), the utilization of new N for primary production is quantitatively linked to C export (Figure 1.2). By contrast, regenerated production yields no net export in a mass balance sense (Dugdale & Goering, 1967). Assuming parallel cycling of N and C (i.e., constrained by the Redfield ratio of C:N:P being 106:16:1; Redfield et al., 1934 &1958), the strength of the biological pump can be inferred from the degree to which new N is utilized relative to total N. In this framework, high rates of new production are indicative of a strong biological pump that yields significant C export and vice versa (Dugdale & Goering, 1967; Eppley & Peterson, 1979).

Phytoplankton assimilation of new versus regenerated N, largely allochthonous NO_3^- and recycled NH_4^+, respectively, underpins the new production paradigm (Dugdale & Goering, 1967). While some studies suggest that a co-provision of NO_3^- and NH_4^+ promotes co-occurring growth on both N substrates (Weissman, 1964; Britto & Kronzucker, 2002), others suggest that NH_4^+ will be preferentially taken up due to the lower energy requirements associated with its assimilation (McCarthy, 1981; Probyn & Painting 1985; Dortch, 1990; Raven et al., 1992; Sambrotto & Mace, 2000; Mosseri et al., 2008). In order for phytoplankton to assimilate NO_3^-, this nutrient needs to be reduced to NH_4^+ (equivalent to an eight electron reduction from its current oxidation state), while direct NH_4^+ assimilation requires no reduction (e.g., Dortch, 1990; Mosseri et al., 2008, Glibert et al., 2016). This already-reduced N substrate has also been shown to support higher growth rates than NO_3^- (Herndon & Cochlan, 2007; Solomon et al., 2010), likely as a result of a redistribution of cellular energy or the inhibition of NO_3^- uptake by high

NH_4^+ concentrations (Syrett & Morris, 1963; Conway et al., 1977). While the latter effect is still not yet fully understood (Wheeler & Kokkinakis, 1990; Dorch 1990; Mosseri et al., 2008) and likely depends on phytoplankton community composition, physiological (Dortch & Conway, 1984; Maguer et al., 2007) and associated nutrient status (e.g., N-rich / N-poor conditions), NO_3^- uptake inhibition can be induced by NH_4^+ concentrations of a few µM (Eppley et al., 1969; Dortch & Conway, 1984; Cochlan & Harrison, 1991; L'Helguen et al., 2008) to as low as ~0.1 – 0.3 µM, the latter seen in the Subarctic Pacific (Wheeler & Kokkinakis, 1990). While this phenomenon is highly variable and is unlikely to completely inhibit NO_3^- uptake (Cochlan & Bronk, 2003), it is important to note that the new production paradigm depends on the degree of NH_4^+ assimilation rather than NO_3^- inhibition (Glibert et al., 2016).

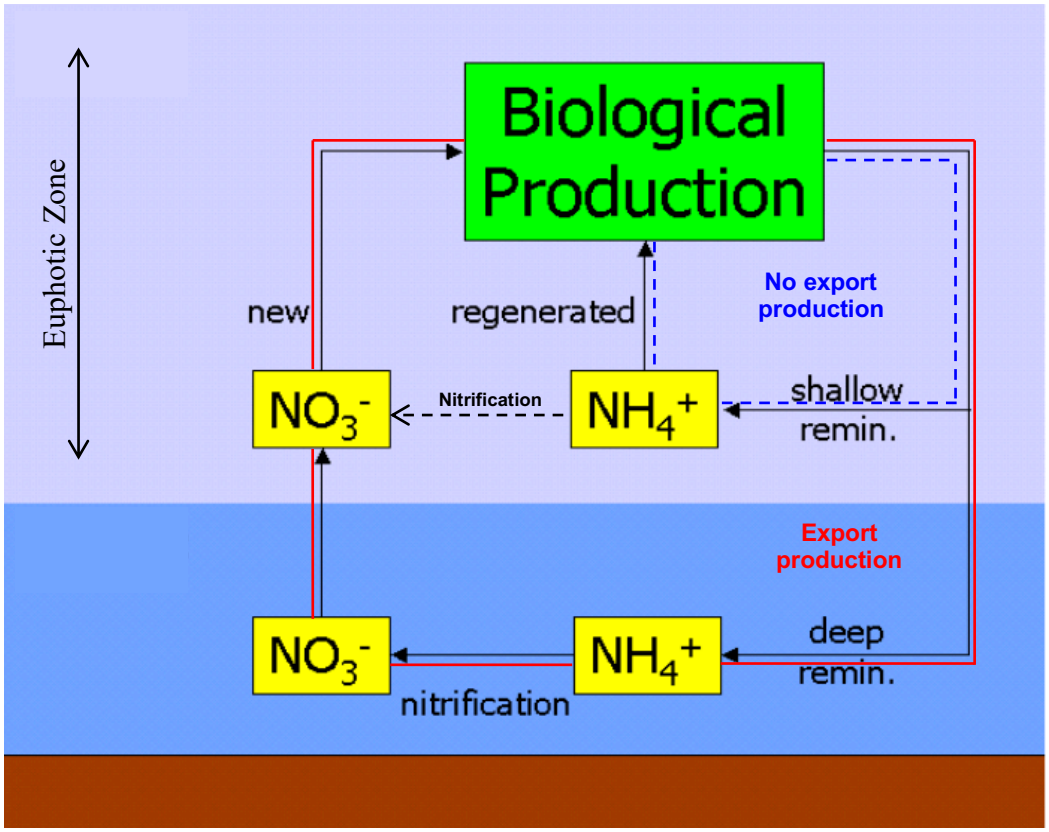

Figure 1.2: The new production paradigm, originally conceptualized by Dugdale and Goering (1967), states that over annual time scales, production fueled by "new" nutrients (e.g., allochthonous NO_3^- mixed up into the euphotic zone from depth), termed new production, is quantitatively related to export production. By contrast, production fueled by "regenerated" nutrients (e.g., NH_4^+ and NO_3^- regenerated within the euphotic zone), termed regenerated production, yields no contribution to export production. (Figure adapted from Plumbago, 2006).

Other factors such as temperature and micronutrient (i.e., Fe) availability further regulate N substrate uptake. Enzymes associated with NO_3^- and NH_4^+ assimilation are affected differently by temperature, with lower temperatures (e.g., 10 – 15°C) generally promoting NO_3^- assimilation, while NH_4^+

assimilation and temperature appear to have a positive relationship (Lomas & Glibert, 1999a & b; Fan et al., 2003; Glibert et al., 2016). This is likely a product of the coupling of NO_3^- concentrations and temperature where an inverse relationship is observed (e.g., Strickland, 1967; Traganza et al., 1980) derived from upwelling conditions (e.g., Dugdale et al., 1989; Morin et al., 1993; Switzer et al., 2003). Additionally, NH_4^+, a product of previously utilized NO_3^-, has increased assimilation rates in warmer, subtropical and tropical environments due to the slow supply of NO_3^- from depth (Menzel & Ryther, 1960; Lipschultz, 2001; Fawcett et al., 2011). Furthermore, under increased Fe fertilization, NO_3^- uptake rates increase (Timmermans et al., 1998; Cochlan et al., 2002; Cochlan & Kudela, 2006) as a result of the high Fe requirement by the nitrate and nitrite reductase enzymes (converting NO_3^- to NH_4^+; Sunda, 1989; Timmermans et al., 1994; Milligan & Harrison, 2000), while NH_4^+ uptake rates remain unaltered (Timmermans et al., 1998). However, Fe-fertilized conditions are often also associated with an increase in ambient [NH_4^+] as a result of increased primary productivity, thus increasing the potential for NO_3^- uptake inhibition (Cochlan et al., 2002; Glibert et al., 2016). These relationships are important to consider in regions such as the high nutrient-low chlorophyll (HNLC) Southern Ocean where conditions remain relatively cold year-round, with an excess of surface NO_3^- and severe Fe-limitation.

The degree of new (and thus export) production relative to total (i.e., new + regenerated) production in an ecosystem can be quantified by the *f*-ratio, shorthand for "flux ratio" (Eppley & Peterson, 1979). Regions of higher nutrient upwelling such as oceanic fronts and coastlines tend to have a higher *f*-ratio ($\geq$0.5) compared to oligotrophic gyres where regenerated production is dominant (<0.5) (Sigman & Hain, 2012). The *f*-ratio allows us to compare regions characterized by different rates of total production and evaluate the extent of nutrient recycling within the euphotic zone and potential for C export. Estimates of the *f*-ratio and C export are complicated by processes such as nitrification, which introduces a recycled source of NO_3^- to the allochthonous stock in the euphotic zone, growth on which should be classified as regenerated rather than new production (Dugdale & Goering, 1967). In addition, N fixation and atmospheric N deposition can introduce new NH_4^+, growth on which should be classified as new production (Dugdale & Goering, 1967; Bronk et al., 1994). If euphotic zone nitrification and/or N fixation/atmospheric deposition are not accounted for, export production and the *f*-ratio will either be over- or underestimated. In the HNLC Southern Ocean, euphotic zone nitrification and N fixation have been measured (DiFiore et al., 2009; González et al., 2014; Jickells et al., 2017; Mdutyana et al., 2020), but are relatively insignificant during the summer growing season due to the high surface concentrations of upwelled (i.e., new) NO_3^- that support phytoplankton growth.

1.1.2 The Southern Ocean's role in the global ocean's biological pump

The Southern Ocean, comprising ~20% of global ocean surface area, plays a disproportionate role in regulating the efficiency of the global ocean's biological pump and, by extension, the Earth's climate (Sarmiento & Toggweiler, 1984; Siegenthaler & Wenk, 1984; Knox & McElroy, 1984; Sigman & Boyle, 2000; Sigman et al., 2010; Deppeler & Davidson, 2017). For the purposes of this thesis, the Southern Ocean is defined as the waters south of the Subtropical Front where seasonal extremes in both light and temperature are mirrored by large oscillations in primary productivity (Figure 1.3A) (Arrigo et al., 2008). Of the ~30% of global anthropogenic CO_2 emissions fixed annually by phytoplankton, 40% is taken up by the Southern Ocean, and approximately 10% of this C is sequestered in the deep ocean (Raven & Falkowski, 1999; Cox et al., 2000; Takahashi et al., 2009; Siegel et al., 2014; Frölicher et al., 2015; Deppeler & Davidson, 2017). It has been estimated that without the Southern Ocean's biological pump, atmospheric CO_2 concentrations could be up to 50% higher than current levels (Cox et al., 2000; Siegel et al., 2014).

Although the modern-day biological pump of the Southern Ocean contributes significantly to global C export, its efficiency is actually limited by unconsumed upwelled euphotic zone macronutrients (i.e., NO_3^- and phosphate (PO_4^{3-})) (Weber & El-Sayed, 1987; Priddle et al., 1998) that are returned to the subsurface without supporting C fixation or export (e.g., Broecker, 1982; Sigman & Boyle, 2000). Moreover, the upwelling that drives nutrients to the surface also allows for the leakage of deep-ocean CO_2 back to the atmosphere; the reciprocal CO_2 drawdown (through photosynthesis) that occurs when CO_2-rich waters upwell in other ocean regions does not occur fully in the Southern Ocean because of the incomplete nutrient consumption (Broecker, 1982; Sigman & Boyle, 2000). The low degree of macronutrient drawdown is a consequence of combined iron (Fe), light and, in some regions, Si limitation of phytoplankton (e.g., Martin, 1990; Chisholm & Morel, 1991; Sunda & Huntsman 1997; Bracher et al., 1999; Boyd et al., 2001; Tremblay et al., 2002). Since the Southern Ocean is a "hotspot" for the formation of deep and intermediate waters, as well as continental and frontal upwelling, large volumes of water from the ocean's interior are ventilated in this region, such that fluctuations in the degree of nutrient utilization and the efficiency of the biological pump can have significant impacts on global climate (Sigman & Boyle, 2000). Furthermore, the Subantarctic (between the Subtropical and Polar Fronts) supplies nutrients to the low-latitude thermocline through Ekman divergence; thus, nutrient utilization in the Subantarctic determines the nutrient supply to the low-latitude ocean (Sigman et al., 2003; Sarmiento et al. 2004). Therefore, a better understanding of nutrient cycling in the Subantarctic is important for our greater understanding of global ocean biogeochemistry.

It has been hypothesized that an increase in Southern Ocean biological pump efficiency in the past, and thus an increase in the Southern Ocean CO_2 storage capacity, was an important driver of the glacial periods (Knox & McElroy, 1984; Sarmiento & Toggweiler, 1984; Sigman & Boyle, 2000). An atmospheric CO_2 decrease of 80 – 100 ppm during the last glacial maximum (LGM, ~ 18,000 years ago) that drove global cooling (Barnola et al., 1987; Petit et al., 1999) appears to have coincided with increased high-latitude nutrient consumption, suggesting a strong coupling between nutrient utilization by Southern Ocean phytoplankton and global climate (François et al., 1997; Sigman & Boyle, 2000; Sigman et al., 2010; Martínez-García et al., 2014). It has been hypothesized that during the glacial periods, the westerly wind belt shifted northwards, increasing dust deposition (and therefore Fe, particularly to the Subantarctic) and reducing wind-driven upwelling (particularly in the Antarctic). The synchronous input of Fe in the Subantarctic and increased mixed-layer (ML) stability (i.e., stratification) in the Antarctic, is thought to have driven more complete nutrient utilization in surface waters by both diatoms in the Subantarctic and Prymnesiophyte phytoplankton species in the Antarctic, while reducing the outgassing of deep CO_2 (Martin, 1990; François et al., 1997; Mahowald et al., 1999; Toggweiler, 1999; Stephens & Keeling, 2000; Di Tullio et al., 2000; Martínez-García et al., 2014). The combined effect of 1) a higher degree of nutrient utilization across both the Antarctic and Subantarctic (i.e., more *efficient* biological pump) and increased C export in the Subantarctic (i.e., *stronger* biological pump), and 2) reduced deep ocean CO_2 upwelling is hypothesized to have reduced atmospheric CO_2 levels and enhanced global cooling during the LGM (Sigman & Boyle, 2000; Anderson et al., 2002; Martínez-García et al., 2014).

Recent observations have shown environmental shifts in the Southern Ocean that include changes in sea ice cover, southward shifts of oceanic fronts and an increase in sea surface temperatures (SSTs) (Constable et al., 2014). It is expected that changes in salinity, wind stress, MLD, irradiance and sea ice thickness, duration, and extent are soon to follow (Boyd et al., 2016; Deppeler & Davidson, 2017), leading to further biological and chemical changes. A consequential change in Southern Ocean phytoplankton productivity, abundance, and composition is likely, which will influence ecosystem services that fuel food webs and mediate global climate (Moline et al., 2004). It is unclear whether these climate-change-induced stressors will be beneficial or detrimental to existing phytoplankton communities in the Southern Ocean (Boyd & Brown, 2015; Boyd et al., 2016), making it imperative that we better understand ecosystem functioning and feedback mechanisms under the current strong climate variability, in order to better predict how these will change as the Southern Ocean warms.

1.1.3 Hydrography and biogeochemistry of the Southern Ocean

The Subantarctic

Comprising more than 50% of the Southern Ocean area, the Subantarctic encompasses the waters between the Subtropical, Subantarctic and Polar Fronts (STF, SAF and PF, respectively), and consists of two zones: the Subantarctic Zone (SAZ), between the STF and SAF, and the Polar Frontal Zone (PFZ) between the SAF and the PF (Figure 1.3A & B) (Orsi et al., 1995). Strong westerly winds dominate the latitude band of 40° – 60°S, with the maximum surface forcing occurring in the Indian Ocean sector (Kalnay et al., 1996; Talley, 2011). This wind stress is the main driver of 1) zonal flow: the broad eastward flowing Antarctic Circumpolar Current (ACC) that connects the Atlantic, Indian and Pacific basins and drives productivity around the frontal and Subantarctic island systems (Doty & Oguri, 1956; Poulton et al., 2007; Pollard et al., 2007; Trull et al., 2015) and 2) meridional flow: extensive northward Ekman transport from the southerly Antarctic Slope Front (ASF) across the SAF and into the SAZ (Figure 1.3B) (Talley, 2011; Post et al., 2014; Deppeler & Davidson, 2017).

Northward transport of southern-sourced waters across frontal areas drives upwelling and subduction, forming and modifying water masses en route. As a result, each of the major Southern Ocean zones comprises different water masses. The PFZ contains Antarctic Surface Water (AASW), Upper and Lower Circumpolar Deep Water (UCDW and LCDW, respectively) and Antarctic Bottom Water (AABW), and is a location of Antarctic Intermediate Water (AAIW) formation (Figure 1.3A & B) (Talley, 2011 and references therein). The SAZ contains Subantarctic Surface Water (SASW), Subantarctic Mode Water (SAMW), AAIW, UCDW, LCDW and AABW. AAIW and SAMW are formed at the PF and SAF, respectively, where AASW is subducted northwards, forming the various intermediate waters (Figure 1.3A & B) (Talley, 2011 and references therein).

Despite being the largest HNLC region in the world with the highest concentrations of unconsumed surface nutrients (Martin, 1990; Boyd et al., 2007), the Subantarctic is recognized as a strong sink for atmospheric CO_2 (Metzl et al., 1999; Takahashi et al., 2009; Landschützer et al., 2014). In addition to the physical drivers of AAIW and SAMW formation that promote CO_2 drawdown via the solubility pump (Menzl et al., 1999; McNeil et al., 2001; Marinov et al., 2006), primary productivity plays an important role in C export in this region (Trull et al., 2001b & 2015; Marinov et al., 2006; Salter et al., 2007; Quéguiner, 2013; Cassar et al., 2015).

A:

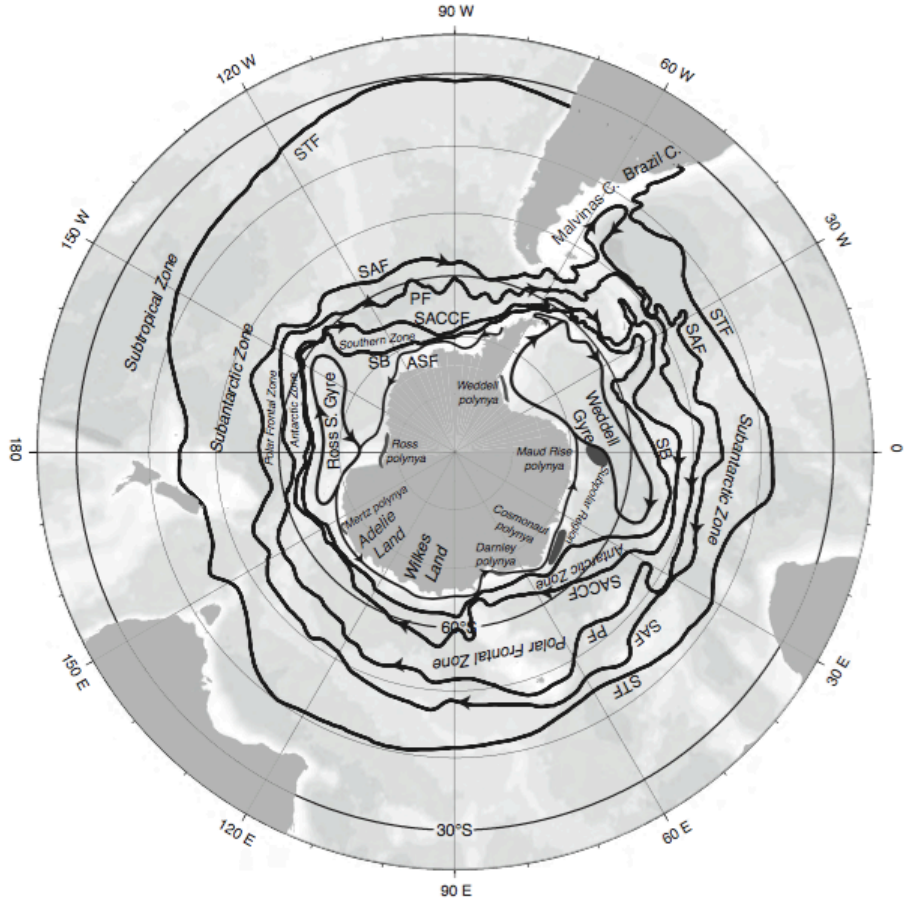
90 W
120 W
60 W
150 W
30 W
180
0
150 E
30 E
120 E
60 E
90 E
30°S
60°S
STF
SAF
PF
SACCF
Subtropical Zone
Subantarctic Zone
Polar Frontal Zone
Antarctic Zone
Southern Zone
SB
ASF
Ross S. Gyre
Weddell Gyre
Brazil C.
Malvinas C.
Weddell polynya
Ross polynya
Maud Rise polynya
Cosmonaut polynya
Darnley polynya
Mertz polynya
Adelie Land
Wilkes Land
Subpolar front
Atlantic Zone

B:

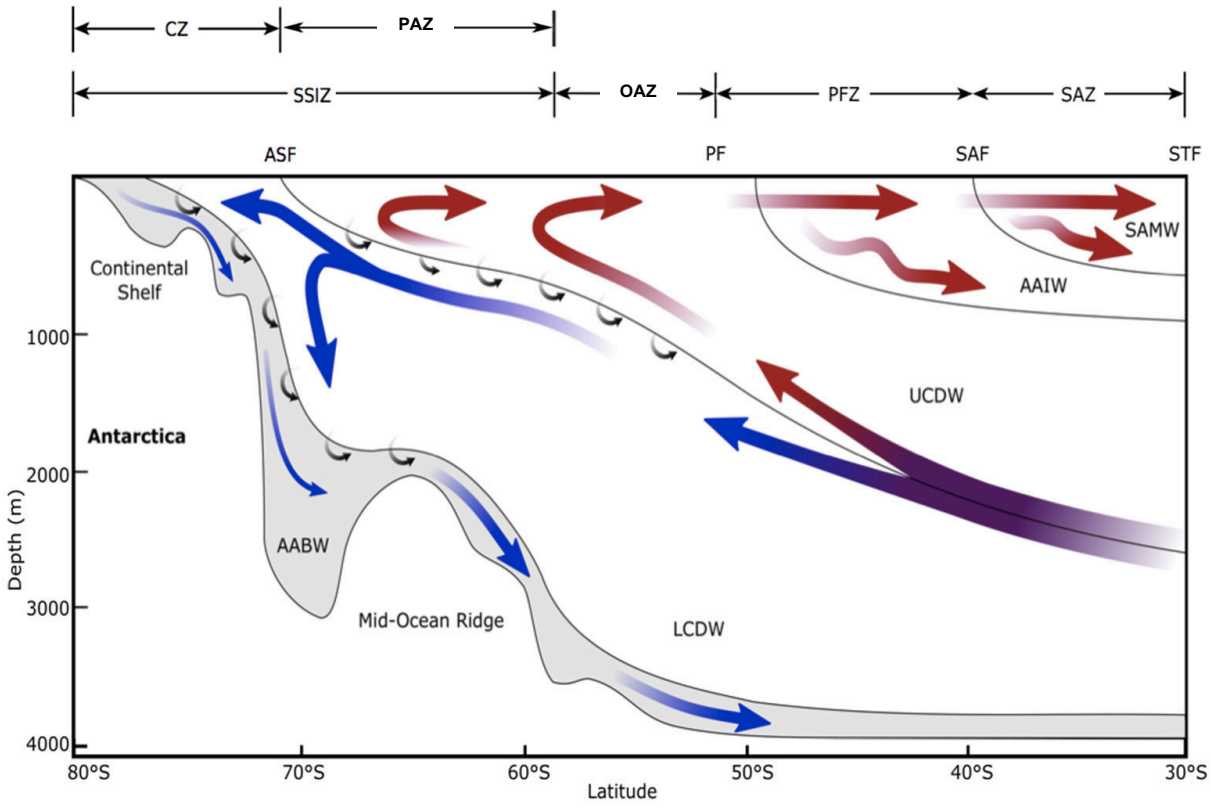
CZ
PAZ
SSIZ
OAZ
PFZ
SAZ
ASF
PF
SAF
STF
Continental Shelf
Antarctica
SAMW
AAIW
UCDW
AABW
Mid-Ocean Ridge
LCDW
Depth (m)
1000
2000
3000
4000
80°S
70°S
60°S
50°S
40°S
30°S
Latitude

Figure 1.3: Schematics of the A: Southern Ocean fronts (Orsi et al., 1995) and B: the meridional overturning circulation of the region (adapted from Post et al., 2014). The Subantarctic consists of two zones, the Subantarctic Zone (SAZ) to the north and the Polar Frontal Zone (PFZ) to the south. These zones are differentiated by the fronts; the Subtropical Front (STF) and the Subantarctic Front (SAF) border the SAZ and the SAF and the Polar Front (PF) border the PFZ. South of the PFZ and constrained by the PF and the northern limit of the winter sea ice, is the Open Antarctic Zone (OAZ). The Seasonal Sea Ice Zone (SSIZ) stretches from the OAZ to the Antarctic continent and includes the Polar Antarctic Zone (PAZ) and the Continental Zone (CZ). The PAZ lies between the OAZ and the CZ. The CZ is defined by the continent to the south and the Antarctic Shelf Front (ASF) to the north. It is at this front that upwelling of Lower and Upper Circumpolar Deep Water (LCDW and UCDW, respectively) occurs, with LCDW upwelling south of the ASF and UCDW upwelling to the north. The upwelled UDCW is advected northwards as a result of Ekman transport, and is eventually subducted to form Antarctic Intermediate Water (AAIW) in the PFZ and Subantarctic Mode Water (SAMW) in the SAZ. Deep-water formation occurs along the Antarctic continental shelf where Antarctic Bottom Water (AABW) is subducted to ~4000 m depth.

Deep-water entrainment of nutrients to the surface is the main mechanism of nutrient supply to the surface Southern Ocean, including the Subantarctic (e.g., McCartney, 1977; Sigman et al., 1999; Tréguer, 2014; Tagliabue et al., 2014; Jannsen et al., 2020). However, this mechanism supplies unequal quantities of micro- and macronutrients, thereby yielding micronutrient (e.g., Fe) limitation of phytoplankton growth (Croot et al., 2007; Ellwood et al., 2008; Bowie et al., 2009; Janssen et al., 2020). Generally in the open ocean Subantarctic (excluding fronts), an excess of macronutrients (including Si and NO_3^-) over Fe is entrained into the ML as a result of the ferricline (the maximum derivative of Fe concentration with depth) being at a depth of 100 – 300 m, which is usually below the depth of the nutricline (the maximum derivative of combined macronutrients concentration with depth) and the winter MLD, isolating Fe from vertical entrainment (Tagliabue et al., 2014; Janssen et al., 2020). As a result, Fe supply remains insufficient year-round and is a perpetually limiting nutrient across the Subantarctic (and the rest of the open Southern Ocean) (Banse, 1996; Boyd et al., 2001a, b & 2007; Hiscock et al., 2007; Doblin et al., 2011; Moore et al., 2013; Janssen et al., 2020). While there are other mechanisms of Fe supply, including aeolian deposition, resuspension of shelf sediments from the Subantarctic islands (discussed below and in section 1.3) and possible contributions from deep hydrothermal vents, these inputs remain small or localized (Blain et al., 2007; Cassar et al., 2007; Salter et al., 2007; Pollard et al., 2009; Boyd & Ellwood, 2010; Tagliabue et al., 2010; Ardyna et al., 2019). By contrast, in spring and early summer, Subantarctic surface waters are Si-replete. However, this nutrient is quickly consumed by silicifying plankton such as diatoms and silicoflagellates, resulting in Si-limiting conditions by mid-summer while NO_3^- concentrations remain high (e.g., Trull et al., 2001a; Salter et al., 2007; Pollard et al., 2002 & 2009).

The unbalanced availability of micro- and macronutrients, particularly in the spring and early summer, drives deviations in the expected macronutrient uptake ratios, with large biogeochemical consequences. For example, the expected Si:N uptake ratio of 1:1 under Fe-replete conditions (Brzezinski, 1985; Boyle, 1998; Poulton et al., 2007; Holmes et al., 2019) is skewed to >> 2:1 under Fe-limited conditions (Boyle, 1998; Smaetacek et al., 2004; de Baar et al., 2005; Poulton et al., 2007; Holmes et al., 2019) as a result of phytoplankton physiological adaptations to Fe limitation (Takeda, 1998; Timmermans et al., 2004; Moore et al., 2007b). This drives Si depletion far more rapidly than NO_3^- depletion and decouples the N and Si cycles through the preferential export of Si (Poulton et al., 2007). Additionally, a south-north Subantarctic nutrient gradient is created as a result of Ekman transport across the region (Trull et al., 2001a; Sigman et al., 2003; Difiore et al., 2006; Janssen et al., 2020), driving a meridional gradient in phytoplankton community composition (Trull et al., 2001a). Diatoms with Si frustules are abundant in the PFZ, particularly at depth, while a shift to more 'nutrient-economical' smaller phytoplankton occurs in the SAZ, including lightly-silicified diatoms, cyanobacteria and coccolithophores with carbonate shells (Trull et al., 2001b; de Salas et al., 2011). Along with the shift in community composition, greater NO_3^- utilization occurs in the SAZ, where it is estimated that the annual C export to a depth of 1000 m is higher than in the PFZ (Trull et al., 2001b), potentially challenging the idea of diatoms being efficient vectors of C export in the open ocean PFZ.

Subantarctic island archipelagoes alleviate productivity limitations by naturally fertilizing the surrounding surface waters with Fe and Si via multiple mechanisms including bathymetric-induced upwelling and island run-off (Salter et al., 2007; Pollard et al., 2009). These localized high-Fe and Si waters yield areas of relatively high primary productivity where nutrient drawdown occurs, and the associated phytoplankton blooms starkly contrast the otherwise HNLC nature of the region. This is known as the Island Mass Effect (IME) (Doty & Oguri, 1956; Heywood et al., 1990; Perissinotto et al., 1992; Gove et al., 2016). Island blooms are often dominated by heavily-silicified diatoms that increase regional C export potential as a result of their higher propensity for sinking (Salter et al., 2007 & 2012; Assmy et al., 2013; Rembauville et al., 2016a & b). The IME is discussed further in section 1.3 below.

The Open Antarctic Zone

The Open Antarctic Zone (OAZ) lies to the south of the PFZ between the PF and the northern limit of winter sea ice – the OAZ is thus permanently ice-free (Figure 1.3 A & B) (Post et al., 2014; Talley, 2011 and references therein). This region hosts similar water masses to the PFZ, although it is characterized by a shallow AASW layer and a distinctive -1.5°C to 2°C temperature minimum layer (Tmin layer) at ~

200 m (Read et al., 1995; Morrison et al., 2001; Talley, 2011 and references therein). The Tmin layer is considered the summertime residual of wind-driven deep winter mixing (Park et al., 1998; Morrison et al., 2001; Altabet & Francois, 2001; DiFiore et al., 2010). Below the Tmin lies UCDW (Park et al., 1998; Morrison et al., 2001; Talley, 2011 and references therein), which is thought to be the ultimate nutrient source to OAZ surface waters (Sigman et al., 1999; Smart et al., 2015).

There are significant differences between the Subantarctic and OAZ. The more polar extent of the OAZ leads to enhanced seasonality (Abbott et al., 2000) that influences the regional biogeochemical cycling and ecosystem functioning. Nonetheless, similar nutrient input mechanisms, including vertical deep winter mixing (e.g., Sigman et al., 1999; Abbott et al., 2000; Pollard et al., 2002; Constable et al., 2014; Taglibue et al., 2014), and persistent Fe-limitation driving a Si:N utilization ratio of 2:1 (Brzezinski et al., 2003; de Baar et al., 2005; Poulton et al., 2007) occur in both regions. Additionally, a northward meridional nutrient gradient is observed where nutrients supplied via upwelling at the ASF are consumed by phytoplankton as surface waters flow northwards via Ekman transport (Figure 1.3B) (Treguer & Jacques, 1992; Pollard et al., 2002).

In contrast to the Subantarctic, Si is replete in the OAZ (Tréguer, 2014). However, primary productivity remains low as a result of the severe Fe-limiting conditions, driving a comparatively weak biological pump (Landry et al., 2002; Quéguiner, 2013). This HNLC open ocean region is characterized by small diatom assemblages (subject to heavier grazing pressures, Semeneh et al., 1998; Mayzaud et al., 2002), as well as high abundances of nano- and picoflagellates (Mengesha et al., 1998). These flagellate populations generally contain lower chlorophyll-*a* (Chl-*a*) concentrations compared to other phytoplankton, contributing to surface Chl-*a* in the OAZ that is lower than in the Subantarctic (Becquevort et al., 2000; Moore & Abbott, 2000; Kopczyńska et al., 2001; Olguín & Alder, 2011).

While areas of Fe supply remain spatially scarce and inconsistent (e.g., iceberg movement) in the OAZ, they support large, localized diatom blooms, particularly in the spring. The northern border of the OAZ, the PF, is recognized as an important source of Fe to the region that supports diatom-dominated blooms that contribute significantly to C export (Rembauville et al., 2015a, b & 2016b; Christaki et al., 2014; Laurenceau-Cornec et al., 2015; Rigual-Hernández et al., 2015; Trull et al., 2015). Other mechanisms of natural Fe fertilization in the OAZ include melting sea ice and icebergs whereby Fe is released into surface waters south of the OAZ and redistributed northwards (Cefarelli et al., 2011; Lin et al., 2011; Vernet et al., 2011 & 2012). Over the summer season, icebergs migrate northwards and melt, sporadically fertilizing the surrounding waters with Fe, which promotes localized phytoplankton

productivity (Lin et al., 2011; Shaw et al., 2011; Vernet et al., 2011 & 2012) and upper tropic level grazing, both of which have implications for C export (Smith et al., 2011; Vernet et al., 2011).

The variable hydrography and biogeochemistry of the Subantarctic and OAZ highlights the complexities associated with assessing C export in the Southern Ocean. Physical dynamics associated with nutrient supply and water mass formation, along with the biological dynamics of nutrient utilization and the phytoplankton community (see section 1.2 below) are all interconnected and directly influence the strength and efficiency of the biological pump.

1.2 Phytoplankton communities in the Subantarctic

The phytoplankton community composition in the Subantarctic and OAZ is complex, not only due to the vastness of each region but also to the high seasonal and spatial variability experienced by their ecosystems. The generally low productivity of these regions is maintained by bottom-up limitations including Fe, Si and light, as well as top-down grazing (Banse, 1996; Boyd et al., 2001a & b; Hiscock et al., 2003; Doblin et al., 2011; Deppeler & Davidson, 2017) and a 'horizontal' control (i.e., inter-species competition). Nutrient limitation and inter-species competition are addressed in detail below. Subantarctic phytoplankton are often exposed to low light levels as a result of cloudiness and the MLD being between 70 and 100 m in the summer and sometimes deeper than 500 m during winter mixing (Bishop & Rossow, 1991; Rintoul & Trull, 2001; Deppler & Davidson, 2017). Additionally, grazing rates and abundances of microzooplankton such as copepods suggest that a significant proportion of primary productivity in the Subantarctic, particularly in the mid- to late summer, is transferred to higher tropic levels (Jones et al., 1998; Griffiths et al., 1999; Kopczyńska et al., 2001; Safi et al., 2007; Pearce et al., 2011), reducing phytoplankton abundances but potentially enhancing C export due via rapidly-sinking faecal pellets.

Si plays a profound role in shaping phytoplankton communities in the Subantarctic, when concentrations are both replete and limiting, thus affecting the strength of the biological pump (and the silica cycle) (Hildebrand, 2008; Fripiat et al., 2011). Prior incubation studies show that Si concentrations ≤1 μM do not limit NO_3^- assimilation but rather drive changes in phytoplankton community composition from diatoms to non-siliceous species (e.g., Hutchins et al., 2001; Sedwick et al., 2002). This implies that while productivity in the Subantarctic is not primarily limited by Si availability, phytoplankton community composition is shaped by the concentration of this macronutrient. Instead, the dominant control on Subantarctic primary productivity appears to be Fe (e.g., Martin, 1990; Boyd, 2002; de Baar

et al., 2005; Poulton et al., 2007; Moore et al., 2013; Holmes et al., 2019), the ambient surface concentration of which is <0.2 nM (Janssen et al. 2020). It has been suggested that Fe concentrations <0.5 nM limit primary productivity (Boyd et al., 1999; Hutchins et al., 2001; Sedwick et al., 2002; Blain et al., 2007), while Si becomes limiting to large, heavily-silicified centric (e.g. *Chaetoceros* spp.) and pennate (e.g. *Fragilariopsis kerguelensis*) diatoms at <5 μM and at ≤ 1 μM for smaller, lightly-silicified pennate diatoms (e.g. *Pseduo-Nitzchia* spp.) (Boyd et al., 1999; Franck et al., 2000; Hutchins et al., 2001; Nelson et al., 2001; Selph et al., 2001; Sedwick et al., 2002). The onset of Si limitation as the summer season progresses drives a progression in the phytoplankton community structure from a dominance of heavily-silicified diatoms (assimilating $Si>NO_3^-$) to lightly-silicified diatoms (assimilating $Si\approx NO_3^-$) and then ultimately to non-siliceous species such as *Phaeocystis* and coccolithophore spp. that are able to assimilate NO_3^- with no requirement for Si (Hutchins et al., 2001; Sedwick et al., 2002). This pattern of phytoplankton succession is not observed in the near-shore island areas due to the continuous supply of Fe and Si (Planquette et al., 2007; Poulton et al., 2007). Here, the perennial dominance of smaller pennate diatoms (e.g., *Thalassionema nitzschioides*) is thought to be the result of macrozooplankton grazing pressure, limiting the abundance of larger diatoms (Fielding et al., 2007).

In addition to the bottom-up and top-down controls discussed above, the 'horizontal' controls associated with inter-species competition influence the longevity and success of different species with regards to competition for nutrients and susceptibility to grazing (Sunda & Huntsman, 1997; Sedwick et al., 2002; Smetacek et al., 2004). These horizontal controls include the progression of biomass accumulation (i.e., bloom stage – onset, intensification, decline; Llort et al., 2015), cell size, cell shape, and cell arrangement (i.e., individual cells, chains etc.) (Sunda & Huntsman, 1997; Sedwick et al., 2002; Smetacek et al., 2004). The phytoplankton communities present in a particular region at a particular time reflect the balance of bottom-up, top down, and horizontal controls. It is important to bear this in mind when characterizing and quantifying phytoplankton communities, especially in the Subantarctic where large seasonal phytoplankton blooms are prominent, especially in the spring (Pollard et al., 2007; Trull et al., 2015), influenced by the nutrient and light supply. These blooms will in turn influence micro- and macronutrient availability, inter-species growth rates and grazer growth rates as the season progresses (e.g., Fielding et al., 2007; Queguiner, 2013; Trull et al., 2015; Liu et al., 2019).

Cell size is a central determinant of phytoplankton community structure and composition (Cullen, 1991; Moore et al., 2007b, Poulton et al., 2007) and reflects a balance between competitive nutrient requirements and defensive grazer avoidance (Thingstad et al., 2005; Poulton et al., 2007). Smaller cells have high nutrient uptake efficiencies as a result of their higher cell surface area-to-volume ratio and are

thus are less likely to experience nutrient limitation. However, they are easily targeted by rapidly-growing microzooplankton grazers (Poulton et al., 2007). As cell size increases, a negative correlation is observed between efficient nutrient acquisition and grazing pressure, where a decrease in grazing pressure due to larger cell sizes or the formation of cell chains (Assmy et al., 2013; Morel et al., 1991) is accompanied by higher nutrient requirements (Sunda & Huntsman, 1997; Timmermans et al., 2004; Poulton et al., 2007).

Pico- and nanophytoplankton assemblages dominate the HNLC waters of the Subantarctic (Weber & El-Sayed, 1987; Gervais et al., 2002) since they are more competitive for nutrients (particularly Fe) than the larger size classes (Fennel et al., 2003; Venables & Moore, 2010). Moreover, their high abundance allows them to continue to dominate under heavy grazing pressures (Sunda & Huntsman, 1997; Timmermans et al., 2004; Poulton et al., 2007). A shift to nano- and microphytoplankton dominance has been observed in the Fe-fertilized waters around the islands (Gall et al., 2001; de Baar et al., 2005; Hoffmann et al., 2006; Moore et al., 2007b). This shift to larger size classes, often with a greater contribution from siliceous species, has positive implications for C export (Cullen, 1991; Smetacek et al., 2004; de Baar et al., 2005; Poulton et al., 2007).

The two zones of the Subantarctic, the SAZ and the PFZ, are characterized by unique dominant phytoplankton populations as a result of the varied nutrient inputs. In the SAZ, a dominance of coccolithophores, cyanobacteria, and autotrophic flagellates, with low abundances of diatoms has been described while diatoms appear to be dominant in the PFZ, particularly in spring and early summer (Odate & Fukuchi, 1995; Wright et al., 1996; Popp et al., 1999; Trull et al., 2001a & b; Hanjo, 2004; Deppeler & Davidson, 2017). As the summer season progresses, nutrient limitation shifts the community towards a picophytoplankton-dominated system (Salter et al., 2007; Quéguiner, 2013; Balch et al., 2016), where smaller taxa such as coccolithophores, lightly-silicified diatoms, nanoflagellates and dinoflagellates persist (Odate & Fukuchi, 1995; Kopczyńska et al., 2001 & 2007; de Salas et al., 2011). Similar to the PFZ, the OAZ's phytoplankton community is predominantly composed of nano- and picoflagellates (Becquevort et al., 2000; Moore & Abbot, 2000; Kopczyńska et al., 2001; Olguín & Alder, 2011) and small diatoms, with large, heavily-silicified diatoms becoming more abundant under bloom conditions (Abbott et al., 2000; Becquevort et al., 2000; Timmermans et al., 2001; Stzepek et al., 2011; Christaki et al., 2014) in Fe fertilized areas such as the PF (Odate & Fukuchi, 1995; Trull et al., 2015). These diatoms contribute significantly to C and Si export (Tréguer & Van Bennekom, 1991; Trull et al., 2001b; Kemp et al., 2006; Assmy et al., 2013; Deppeler & Davidson, 2017), while in the SAZ, export production is dominated by coccolithophores (Trull et al., 2001b). Relative to the Subantarctic,

the OAZ hosts lower absolute abundances of picophytoplankton including cyanobacteria (Odate & Fukuchi, 1995), which contributes to the overall lower biomass and Chl-*a* of this region (Becquevort et al., 2000; Moore & Abbott, 2000; Kopczyńska et al., 2001; Olguín & Alder, 2011). Nonetheless, since a significant proportion of primary productivity is facilitated by smaller cells across the SAZ, PFZ, and OAZ, it has been suggested that a significant fraction of C export must be facilitated by these smaller phytoplankton size classes (Trull et al., 2001b; Cassar et al., 2015; Laurenceau-Cornec et al., 2015).

1.2.1 Picophytoplankton

As the smallest class of phytoplankton and often the most dominant contributor to biomass, picophytoplankton are ubiquitous throughout the global oceans (DuRand et al., 2001; Fawcett et al., 2011; Massana, 2011), including the Southern Ocean (Veldhuis et al., 2005). Picophytoplankton are defined as the size class <3 μm (Stockner & Anita, 1986; Stockner, 1988; Veldhuis et al., 2005; Vaulot et al., 2008), encompassing both eukaryotic and prokaryotic algae. Picoeukaryotes are typically 0.8 – 3 μm compared to the smaller prokaryotes, *Synechococcus* at ~1 – 1.6 μm and *Prochlorococcus* at ~0.6 μm (Waterbury et al., 1986; Partensky et al., 1999a & b; Johnson et al., 2006). Le Quéré et al. (2005) calculated that nearly a third of southern hemisphere phytoplankton fall in the pico- size class, and that they contribute substantially to primary productivity. This contribution is a result of a combination of high cell abundance and high surface area-to-volume ratios, which renders picophytoplankton more efficient at using nutrients and sunlight, while also having a lower requirement for these resources (Fennel et al., 2003; Venables & Moore, 2010).

While little is known of Southern Ocean picophytoplankton populations and dynamics, two broad groups have been observed across this region – *Synechococcus* and picoeukaryotes (Doolittle et al., 2008; Buitenhuis et al., 2012). *Prochlorococcus* is constrained to tropical and temperate oceans between 40°N and 40°S, likely due to temperature constraints given that this group is absent at temperatures <15°C (Moore et al., 1995; Partensky et al., 1999a & b; Johnson et al., 2006; Flombaum et al., 2013). *Synechococcus*, on the other hand, has a large geographical distribution as a result of increased physiological diversity within the group (Waterbury et al., 1986; Zwirglmaier et al., 2008; Huang et al., 2012), extending polewards to at least 50°S (Zubkov et al., 2000). The Southern Ocean also hosts eukaryotic phytoplankton populations such as diatoms and coccolithophores that sometimes occupy the pico- size class. The major phytoplankton groups are described in more detail below.

Synechococcus: prokaryote of the Southern Ocean

Synechococcus dominates the well-lit surface ocean in temperate and high-latitude waters where nutrients tend to be more abundant, and in the case of the Southern Ocean, where Fe is limited (Waterbury et al., 1986; Shapiro & Haugen, 1988; Patensky et al., 1999a; Scanlan, 2003; Treibergs et al., 2014). Although the cyanobacteria phylum evolved ~3 billion years ago when atmospheric CO_2 was high and O_2 was low (Saito et al., 2003; Tabita et al., 2007; Blankenship et al., 2007), the *Synechococcus* strain evolved more recently under higher O_2 conditions (Sanchez-Baracaldo et al., 2014; similar to diatoms, Young et al., 2012), allowing them to evolve a metabolism equipped to utilize both reduced and oxidized forms of N (Glibert et al., 2016). N assimilation by *Synechococcus* has been extensively studied; with almost all strains investigated showing the capacity for both oxidized and reduced N assimilation (Glibert et al., 1986; Paerl, 1991; Lindell et al., 1998; Collier et al., 1999; Moore et al., 2002; Bird & Wyman, 2003). However, a preference for reduced N has been reported from culture work (Glibert & Ray, 1990; Lindell & Post, 2001), as well as in the nutrient-rich Arabian Sea (Lindell & Post, 2001) and oligotrophic North Atlantic (Casey et al., 2009; Fawcett et al., 2011 & 2014; Treibergs et al., 2014). That said, other studies have reported a positive correlation of *Synechococcus* abundance with NO_3^- concentration, from which they have inferred a NO_3^--related control on *Synechococcus* growth (Glover et al., 1988; Partensky et al., 1999a; DuRand et al., 2001).

Synechococcus contains light-harvesting phycobiliprotein pigments that vary in composition with the optical properties of the water column (surface to the bottom of the euphotic zone) where they are habituated (e.g., Ong et al., 1984; Wood et al., 1985; Waterburg et al., 1986; Campbell & Vaulot, 1993; Veldhuis & Kraay, 1993; Farrant et al., 2016). *Synechococcus* appear thrive in the well-lit surface ocean, as evident in Subtropical studies (DuRand et al., 2001; Treibergs et al., 2014), while their distribution at depth (and therefore under low light conditions) is reduced as a result of their abnormally high light requirements for their photosystem I to photosystem II ratios (Sunda & Huntsman et al., 2015). In order to meet their light requirements, open ocean *Synechococcus* strains possess a large amount of the photosynthetic accessory phycobiliprotein, phycoerythrin (PE), which is uncommon for most phytoplankton species with the exception of cryptophytes (Wood et al., 1998). In HNLC regions like the Southern Ocean, the PE content of *Synechococcus* can be similar or equal to its Chl-*a* content (Glibert et al., 1986; Veldhuis et al., 2005). Additionally, *Synechococcus* contains a large amount of zeaxanthin, a photoprotective pigment that assists with survival at these high surface irradiance levels (Kana et al., 1988, Veldhuis & Kraay, 1990, Moore at al., 1995).

Owing to the ability of *Synechococcus* to use a variety of N forms, along with the fact that it contains protective zeaxanthin pigments and has a high surface area-to-volume ratio, studies suggest that open ocean *Synechococcus* populations play a significant role in marine primary productivity (Partensky et al. 1999a; Goericke & Welschmeyer, 1993; Maranon et al., 2003). Interestingly given the small size of *Synechococcus*, this genus has unusually high Fe requirements in comparison to eukaryotic phytoplankton (Raven, 1990; Brand, 1991; Wilhelm et al., 1996; Morrissey & Bowler, 2012; Lis et al., 2015). This is thought to result from a lack of C-rich moieties inside their cells (Twining & Baines, 2013) and the high ratio of Fe-rich photosystem I to Fe-poor photosystem I (Raven, 1990; Brand, 1991; Wilhelm et al., 1996; Morrissey & Bowler, 2012; Lis et al., 2015). However, since trace metal concentrations have not been measured in conjunction with species abundances, the effect Fe has on shaping the distribution and functioning of *Synechococcus* ecotypes is unclear (Sohm et al., 2016).

1.2.2 Eukaryotes

Diatoms

Diatoms (2 μm – 500 μm) are siliceous phytoplankton that contribute ~20% of total global primary productivity (Nelson et al., 1995) and control the ocean's Si cycle (Tréguer et al., 1995; Tréguer, 2014). They are the most common (by weight) but also the most nutrient-limited (by Si and Fe) phytoplankton in the Southern Ocean, itself the largest region globally where C export is dominated by diatoms (Sarthou et al., 2005; Denman, 2008; Armbrust, 2009; Rigual-Hernandez et al., 2015). Diatoms tend to be very successful in well-mixed coastal and upwelling regions (Hutchins & Bruland, 1998; Wetz & Wheeler, 2003; Fawcett & Ward, 2011), particularly evident around the Subantarctic Islands and PF (e.g., de Baar et al., 1995; Poulton et al., 2007; Trull et al., 2015). This is because of the availability of sufficient light and nutrients, including inorganic N, PO_4^{3-}, Si and trace elements (e.g., Fe), that sustain their growth (Morel & Price, 2003) along with high levels of turbulence that increase C fixation by preventing smaller diatoms cell from sinking while simultaneously enhancing the export rates of larger aggregates (Bergvist et al., 2018). As a result, diatoms dominate both productivity and biomass in these regions (e.g., Buck et al., 1992, Kudela & Dugdale, 2000; Bruland et al., 2001; Rigual-Hernandez et al., 2015; Abrantes et al., 2016; Burger et al., 2020).

Diatoms are the main vectors of C export in the Southern Ocean (Rigual-Hernandez et al., 2015; Tréguer et al., 2018). During the early spring bloom, they dominate the microphytoplankton size class due to the availability of Si and Fe, and in regions where the input of these nutrients is sustained, such as in the vicinity of island systems and fronts, they have been observed to dominate throughout the summer

season (e.g., Salter et al., 2007; Le Quéré et al., 2005; Poulton et al., 2007; Laurenceau-Cornec et al., 2015; Trull et al., 2015). Centric diatoms such as *Chaetoceros* spp. are associated with higher Fe-supply areas whereas pennate diatoms such as *Fragilariopsis kerguelensis* are more abundant in the open ocean HNLC waters (Salter et al., 2007; Laurenceau-Cornec et al., 2015; Trull et al., 2015). In the Southern Ocean, diatoms have been observed to preferentially utilize NO_3^- even when NH_4^+ is available (Maestrini et al., 1982; Probyn & Painting, 1985; Lomas & Glibert, 1999a & b), thereby strengthening the biological pump in a mass balance sense (Dugdale & Goering, 1967). While most phytoplankton groups have CO_2 concentrating mechanisms (CCMs) (Raven & Beardall, 2003; Armbrust et al., 2004; Granum et al., 2005; Wilhelm et al., 2006; Roberts et al., 2007a & b; Raven et al., 2008; Hopkinson et al., 2011), larger diatoms have a greater capacity for CCMs to aid in overcoming their smaller surface area-to-volume ratio (Wu et al., 2014a & b). Diatoms CCM-associated enzyme activity changes with exposure to different N substrates, with increased activity with oxidized forms of N (Guo et al., 2007). Therefore, the affinity for CO_2 uptake increases when diatoms utilize NO_3^-, resulting in higher C assimilation per unit N than if diatoms were to utilize NH_4^+ (Raven, 1991; Raven et al., 2008), thereby increasing the strength of the biological pump. Additionally, as a result of their size and weight, diatoms contribute more efficiently to C export than other phytoplankton through direct sinking (via ballasting effects from their dense silica frustules, Legendre & Lefévre, 1995; Tréguer et al., 2018), augmented by chain-forming physiological strategies and/or mass sedimentation post-bloom when nutrients such as Si are depleted (Nelson et al., 1995; Armstrong et al., 2001; Le Quéré et al., 2005; Tréguer et al., 2018).

Fe limitation of diatoms has large-scale biogeochemical consequences for the Southern Ocean. In comparison to other phytoplankton (pico- and nano-), diatoms require more Fe and PO_4^{3-} (Sarthou et al., 2005; Le Quéré et al., 2005), with the response of this group to Fe availability contingent upon the availability of Si, and vice versa (Boyd et al., 1999; Moore et al., 2004). For example, under conditions of Fe limitation, diatoms have been observed to consume NO_3^- and PO_4^{3-} in a ratio of (N:P) ~12:1 (Price, 2005; Green & Sambrotto, 2006) and Si and NO_3^- in a ratio >2:1 (Boyle, 1998; Franck et al., 2000; Smaetacek et al., 2004; de Baar et al., 2005). This results in nutrient N:P ratios south of the PF where diatoms dominate that are significantly higher than the canonical Redfield ratio of 16:1 (Weber & Deutsch, 2010). In addition, the preferential depletion of Si over NO_3^- in AZ surface waters means that Si is almost zero north of the PF due to northward meridional Ekman transport (Sarmiento et al., 2004). Mode and intermediate waters formed in the PFZ and SAZ that flow into the low-latitude thermocline are also characterized by low Si:N ratios, which will affect the types of phytoplankton that can proliferate when these waters upwell in the (sub)tropics (Sarmiento et al., 2004).

In order to mitigate some of the stresses associated with Fe and Si co-limitation, diatoms have adapted a number of their physical and biological characteristics. Some large North Pacific open-ocean species have the ability to move between well-lit surface waters and nutrient-rich waters at depth (~100 m) by controlling their buoyancy (Villareal et al., 1999). However, this has yet to be observed in the Southern Ocean but would allow for photosynthesis at the surface while cell division occurs at depth. In addition, diatom species that inhabit the Fe-limited open ocean have reduced their Fe requirements permanently (Sunda & Huntsman, 1995; Strzepek, 2004; Marchetti et al., 2006) with adaptations such as increased photosystem efficiency, achieved by increasing their Chl-*a* to photosystem II ratio and therefore reducing their overall Fe requirements (Strzepek et al., 2019), as well as replacing the Fe-containing electron carrier with plastocyanin, a copper-containing protein (Peers & Price, 2006). Furthermore, it has been suggested that some Southern Ocean raphid pennate diatoms such as *Pseudo-nitzschia* and *Fragilariopsis* produce ferritin (*FTN*), a compound that protects Fe from oxidation as well as acting as long-term Fe storage mechanism such that the diatoms require less Fe over time (Kustka et al., 2007; Marchetti et al., 2009; Lampe et al., 2018). Interestingly, centric diatoms appear to lack *FTN* (Malviya et al., 2016; Cohen et al., 2018) and resort to an intracellular vacuole Fe storage mechanism (Strzepek et al., 2012; Lampe et al., 2018).

Cryptophytes

Cryptophytes are relatively small (6 – 20 μm) eukaryotic phytoplankton that are abundant in both freshwater and seawater (Clay et al., 1999; Bergmann, 2004; Yih et al., 2004). They are mostly autotrophic biflagellated algae (Davis & Sieburth, 1984; Hill & Rowan, 1989) that are strong swimmers able to migrate across density gradients (Jones, 1988). Evolving from cyanobacterial red algae, cryptophytes have retained the phycobiliproteins characteristic of the former group (McFadden, 2001). Over time, the quantity of these proteins has reduced and PE is now stored in the thylakoid membrane. Cryptophytes are unique with regards to pigment composition, which allows them to thrive under limited irradiance (i.e., deep in the water column) (Ilmavirta, 1988; Doust et al., 2006), as well as withstand high irradiances (Mendes et al., 2017; Trimborn et al., 2019). Cryptophytes contain Chl-*a* and *c* and alloxanthin (*a* carotenoid) in addition to phycobiliproteins (Gould et al., 2008). They do not have photo-protective xanthophyll pigments, instead relying on chlorophyll to dissipate excess light if required (Funk et al., 2011; Kana et al., 2012).

In the coastal waters near Antarctica, cryptophytes, along with diatoms and prymnesiophytes, are the most abundant phytoplankton present in large blooms, thus contributing significantly to the C biomass (Garibotti et al., 2005; Trimborn et al., 2015). Cryptophyte blooms are often inversely correlated

temporally or spatially with diatom blooms (Moline & Prézelin, 1996), with cryptophytes proliferating at the decline of the diatom-dominated spring bloom (Ducklow et al., 2007) as surface stratification driven by ice melt increases (Moline et al., 2004). Although very little is known about Southern Ocean cryptophyte nutrient requirements, previous studies have suggested a strong affinity for reduced N (Berg et al., 2003; Glibert et al., 2016). A recent study on the effects of trace metal limitation on the physiology of cryptophytes observed an 80% decrease in their growth rate when Fe was severely limited (Koch & Trimborn, 2019). Nonetheless, cryptophytes have a lower Fe requirement than diatoms (Mendes et al., 2013), such that a potential driver of the sequential bloom relationship in the Southern Ocean is Fe availability. Further to this, cryptophytes have been observed to adapt to low-Fe environments by reducing their cell volume in order to increase their surface area-to-volume ratio – a typical phytoplankton adaption to a low-Fe environment (Raven & Kubler, 2002; Strzepek et al., 2012, Sunda, 2012). Therefore, the expectation is that under Fe-limiting conditions, cryptophytes will be smaller and relatively slower growing than those not experiencing Fe stress.

The majority of these observations mentioned above are from global cryptophyte studies. There is a lack of ecophysical studies on Southern Ocean cryptophytes (Trimborn et al., 2019), particularly in the Subantarctic where there is next-to-no understanding of cryptophyte functioning and nutrient requirements.

1.2.3 Prymnesiophytes

Coccolithophores

Accounting for a major fraction of global marine calcium carbonate ($CaCO_3$) production and export, Southern Ocean coccolithophores (Rigual-Hernández et al., 2020) are a major component of the Subantarctic phytoplankton community (Gravalosa et al., 2008; Saavedra-Pellitero et al., 2014; Malinverno et al., 2015; Charalampopoulou et al., 2016). Coccolithophores are abundant in the SAZ where they play a significant role in the biological pump (Salter et al., 2014). Through the production of their dense calcite scales (coccoliths), an increase in surface acidity associated with reduced atmospheric CO_2 dissolution occurs (i.e., the 'carbonate counter-pump') (Heinze et al., 1991; Frankingnoulle et al., 1994; Salter et al., 2014; Rigual-Hernández et al., 2020). However, this is mitigated by the subsequent enhanced export of organic C due to the ballasting effect (driving increased sinking rates) of the dense coccoliths (Buitenhuis et al., 2001; Boyd & Trull, 2007; Ziveri et al., 2007). The counter-balancing factors associated with coccolithophore growth, abundance and distribution underscores their importance for nutrient cycling and C export in the Subantarctic (Deppler & Davidson, 2017).

One of the most distinctive community shifts in the Subantarctic is from heavily-silicified diatoms in the south (near the PF) to coccolithophores in the north (SAZ). This community shift coincides with the 'Great Calcite Belt', which is an area of the Southern Ocean that exhibits increased surface reflectance resulting from calcite-shelled coccolithophores outcompeting diatoms due to Si- and Fe- depletion (Boyd et al., 2010; Lannuzel et al., 2011; Balch et al., 2014). The contribution of the Great Calcite Belt to the biological pump in the Indian Sector of the SAZ is demonstrated by sediment trap data showing a >50% contribution of calcium carbonate to export (Trull et al., 2001b). By contrast, in the PFZ, a >50% contribution of biogenic Si, indicative of diatom dominance of export, has been observed (Trull et al., 2001b). While nutrient availability (e.g., Si) might influence the diatom-coccolithophore relationship, the decrease in coccolithophore abundance southwards is largely due to temperature (Buitenhuis et al., 2008; Charalampopoulou et al., 2016; Trull et al., 2018). The optimal growth temperature for coccolithophores is ~8°C (Findlay & Giraudeau, 2000), which coincides with the positioning of the Great Calcite Belt and finding coccolithophores at temperatures below 2°C is rare (coinciding with the PF) (Buitenhuis et al., 2008).

Once Fe and Si become limiting for Southern Ocean diatoms, coccolithophores grow in abundance (Nissen et al., 2018). However, coccolithophores such as *Emiliania huxleyi*, the dominant species in the Southern Ocean (e.g., Cubillos et al., 2007; Müller et al., 2015; Rigual-Hernández et al., 2020), have been observed to react similarly to other phytoplankton species under Fe-stress in culture studies (e.g., Muggli & Harrison, 1996; Lampe et al., 2020), including decreasing their growth rates and cell sizes. Additionally, higher coccolithophore abundances are observed near the STF, SAF (Mohan et al., 2008), and landmasses, suggesting they grow better closer to Fe entrainment areas (Balch et al., 2016). N substrate utilization studies of cultured *E. huxleyi* have shown that when both forms of N are available, initial growth occurs on reduced N before oxidized forms of N are consumed (Waser et al., 1998). It has further been suggested that *E. huxleyi* is susceptible to NO_3^- uptake inhibition if NH_4^+ is present in concentrations >0.24 μM (Varela & Harrison, 1999), providing a hypothesis for the initial reduced N utilization observed by Waser et al. (1998). Under Fe-replete conditions, cultured *E. huxleyi* growth has been observed to be similar on both NO_3^- and NH_4^+; however, under Fe-stressed conditions, *E. huxleyi* have been observed to grow on NO_3^- (Muggli & Harrison, 1996) and maintain Chl-*a*:C ratios (Muggli & Harrison, 1997).

Phaeocystis

Part of the haptophyte group, the *Phaeocystis* genus has a global distribution, present as individual cells (3 – 9 μm) or in gelatinous mucous colonies (several mm to 3 cm; Chen et al., 2002) (Schoemann et al., 2005), the latter of which has large impacts on oceanic biogeochemical cycles, food-webs and climate (Lancelot et al., 1994) as they facilitate the transfer of C and sulphur between the ocean and the atmosphere (Stefels et al., 1995; DiTullio et al., 2000; Schoemann et al., 2005). Phaeocystis synthesize dimethylsulfoniopropiotherin (DMSP), that ultimately leads to the production of dimethylsulfide (DMS), which has atmospheric and climate consequences (most significantly, a cooling effect; Bates et al., 1987; Charlson et al., 1987; Sunda et al., 2002). Phaeocystis contains an array of pigments including Chl c_2, c_3 and 19′-hexanoyloxyfucoxanthin, with the latter sometimes used as a proxy for Phaeocystis abundance (Wright & Jeffrey, 1987; DiTullio & Smith, 1995; van Leeuwe et al., 2014).

Recurrent blooms of the Antarctic species, *Phaeocystis Antarctica*, occur between late November and January (Schoemann et al., 2005). This species is adapted to the cold temperatures of the Antarctic, ceasing to grow in waters above ~10°C (Buma et al., 1991; Schoemann et al., 2005). While very little is known about the N and P metabolism of *P. antarctica*, *Phaeocystis* colonies have been observed to accumulate Fe in their mucous (Davidson & Marchant, 1987; Lubbers et al., 1990; Schoemann et al., 2001 & 2005), giving the colony a competitive advantage, especially in the Southern Ocean where Fe is limiting (Schoemann et al., 2005). While it is understood that *Phaeocystis* colonies are grazed upon by herbivorous copepods, krill and other microzooplankton, these colonies are able to resist severe grazing impacts (Weisse et al., 1994) by either a size mismatch between *Phaeocystis* life forms and grazers or by mechanical hinderance attributed to the mucosal layer (Schoemann et al., 2005). Additionally, *Phaeocystis* contribution to export remains unconstrained (Wassmann, 1994; Schoemann et al., 2005). Sinking fluxes of single cells, colonies and derived aggregates range from 1 m day^{-1}, 14 m day^{-1} and 200 m day^{-1} respectively (Becquevort & Smith, 2001; Schoemann et al., 2005) suggesting that healthy cells and colonies do not contribute significantly to the export flux, but rather the sedimentation of their mucous flocs drives C export (Schoemann et al., 2005).

1.2.4 Dinoflagellates

Dinoflagellates are deemed ‘bizarre products of evolution’ due to their large array of plastids, many of which were acquired by secondary and even tertiary symbiotic relationships (Meldin & Fensome, 2013). Dinoflagellates, which often constitute harmful algal blooms, are associated with an increase in reduced N concentrations (e.g., Berg et al., 2003; Glibert et al., 2006; Heil et al., 2007; Rothenberger et al., 2009),

suggesting a preference for reduced N. When abundant, dinoflagellates drive lower community *f*-ratios (Semeneh et al., 1998). In the Southern Ocean, a seasonal increase in regenerated N concentrations has been associated with an increase in dinoflagellate abundance (Cochlan, 2008).

Along with cyanobacteria, coccolithophores and small, lightly-silicified diatoms, dinoflagellates dominate the phytoplankton community in the SAZ (Odate & Fukuchi, 1995; Kopczyńska et al., 2001 & 2007; de Salas et al., 2011). They generally start to appear when surface stratification increases and the available Fe has been exhausted (Waters et al., 2000; Kang et al., 2001; Davidson et al., 2010), often during the decline of diatoms (Cochlan, 2008) and sometimes coinciding with the appearance of cryptophytes (Moline et al., 2004; Montes-Hugo et al., 2009). Dinoflagellates have low Chl-*a* concentrations (Becquevort et al., 2000; Moore & Abbott, 2000; Kopczyńska et al., 2001) but contain ~40% more P than diatoms (Twining et al., 2004), increasing PO_4^{3-} drawdown when they are abundant. Since dinoflagellates are often dominant in Fe-deplete Southern Ocean waters, they can resort to phagotrophic mechanisms to acquire scarce nutrients (Twining et al., 2004). While dinoflagellates do not require Si, they have been observed to contain Si as a result of diatom or silicoflagellate ingestion, which they undertake in order to acquire the Fe from those cells (e.g., Tortell et al., 1996; Maldonado & Price, 1999; Schmidt & Hutchins, 1999; Twining et al., 2004).

1.3 The island mass effect (IME)

The island mass effect (IME), described as an island-localized increase in phytoplankton biomass (Doty & Oguri, 1956; Heywood et al., 1990; Perissinotto et al., 1992; Gove et al., 2016), is largely a result of modifications of the physical mechanisms driving 1) nutrient availability and 2) circulation and retention of surface waters around the islands (Figure 1.4). These mechanisms include ocean current-benthic interactions wherein the shoaling bathymetry upstream of the islands drives the upward vertical transport of deep, nutrient-rich water to the surface, while on the downstream side of the island, eddies often form (Venables & Moore, 2010; Gove et al., 2016), creating a retention zone (McCartney, 1976; Gordon et al., 1978). Interactions of internal waves (from tidal currents) with the bathymetry around the islands can also drive upwelling of deep water (Leichter et al., 2003), providing nutrients that support surface-water phytoplankton growth. A gradual bathymetric slope, such as a plateau, promotes internal wave propagation and is associated with enhanced primary production (Carter et al., 2006) compared to steeper-sloped bathymetry where internal waves are often reflected off the shelf (Gove et al., 2016).

In addition to bathymetric effects, terrestrial runoff can play a role in nutrient inputs. Submarine groundwater discharge, riverine outputs, and glacial runoff (Hawking et al., 2014; Pérez-Tribouillier et al., 2020) are known to accumulate and transport high concentrations of nutrients downstream, discharging into the local waters surrounding the islands (Figure 1.4) (Doty & Oguri, 1956; Gove et al., 2016; Tréguer, 2014). This discharge of freshwater (either meltwater from glaciers or rainwater) has a twofold influence – nutrient addition and the creation of a stable ML (Perissinotto et al., 1992) – both of which contribute to a favourable environment for phytoplankton growth. Leeward eddies also introduce a retention zone, without which, in the case of the Subantarctic islands, waters would be advected offshore in less than a day by the ACC (Perissinotto et al., 1992). Because of these retention zones, phytoplankton blooms have been observed to persist for periods of 1 – 2 weeks, and sometimes even longer (Perissinotto & Ducombe 1990a & b; Perissinotto et al., 1992).

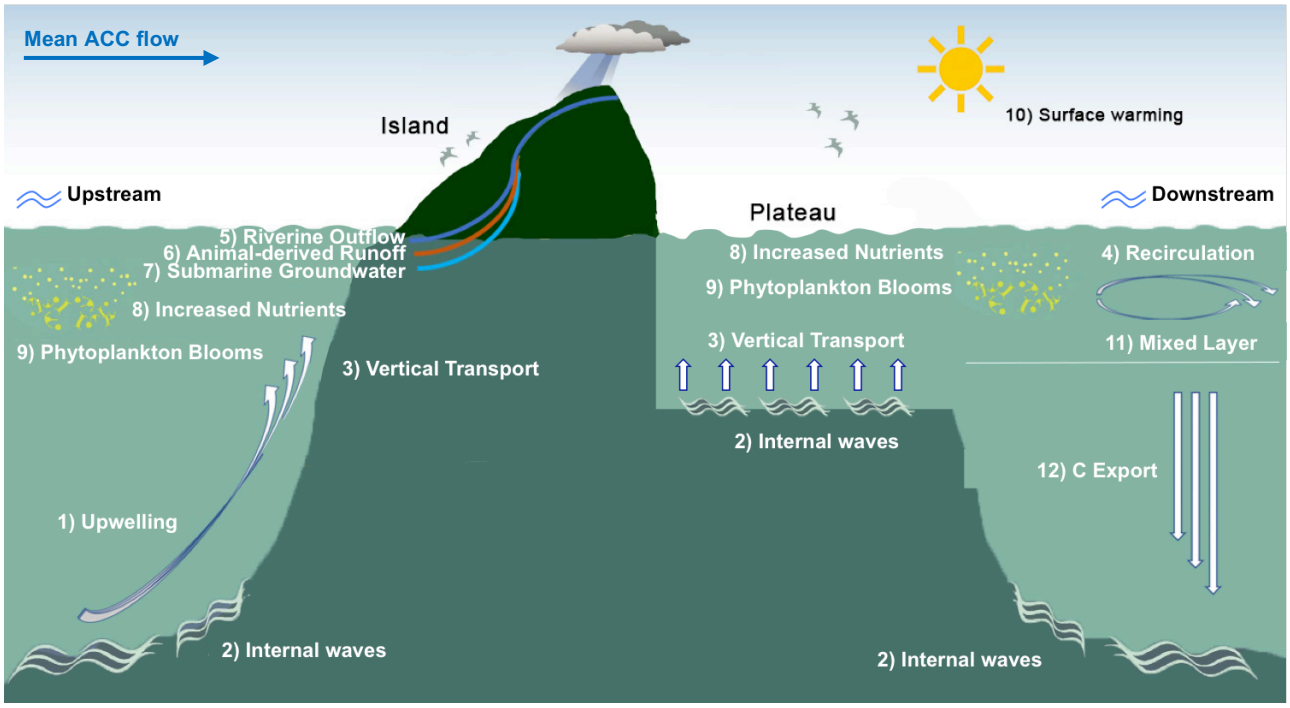

Figure 1.4: The island mass effect (IME) in the Subantarctic Southern Ocean refers to local increases in phytoplankton biomass as a result of the interplay of the ACC with local island bathymetry, as well as island-derived inputs localized to near-shore waters. The shoaling of the bathymetry around the islands leads to (1) the upwelling of upstream deep waters and (2) the formation of tidal-driven internal waves that are strengthened over the gradual slope of the plateau, both of which drive (3) vertical transport of nutrients to the surface (Fe and Si being the relevant nutrients in the case of the Subantarctic islands). Furthermore, formation of eddies on the downstream side of the island/plateau area form (4) retention or recirculation zones. Island-derived inputs include (5) riverine outflow, (6) animal-derived runoff, and (7) submarine groundwater discharge, all transporting (8) nutrient-rich material into nearshore waters. These mechanisms of nutrient supply support large localized (9) phytoplankton blooms. As the growing season progresses (spring through autumn), stratification deriving from a combination of (10) surface warming and (5, 7) freshwater inputs stabilizes the mixed-layer (11), creating an even more favourable environment for (9) continued phytoplankton growth. Elevated (12) carbon export has been

observed around the Subantarctic islands as a result of increased new nutrient utilization and the presence of large and/or siliceous phytoplankton groups that proliferate due to the alleviation of Fe and Si limitation. (Figure adapted from Gove et al., 2016)

The IME has been studied across most of the global ocean, particularly in the (sub)tropics where surface nutrients concentrations are very low, and many islands are inhabited by people (Gove et al., 2016). The IME in the Subantarctic is notably more variable, however, as a result of the strong seasonality that affects light, deep mixing, nutrient availability, frontal shifts, and animal aggregations (McQuaid, 2018). The Subantarctic IME is explored in detail below.

1.3.1 The Subantarctic IME

The Southern Ocean hosts 23 island groups (either individual islands or archipelagos), the majority of which lie in the Atlantic and Indian Subantarctic (De Broyer & Danis, 2011; McQuaid, 2018). As a result of both physical and biological dynamics that create a complex relationship between Fe, light, and Si availability, these islands support a diverse array of life, from phytoplankton and kelp to large seasonal aggregations of sea birds and seals (Perissinotto et al., 1992; McQuaid, 2018; Holmes et al., 2019). Frequent large phytoplankton blooms have been observed around the island chains, differing in composition from open ocean populations (e.g., Moore & Abbott, 2000; Ward et al., 2007; Poulton et al., 2007; Armand et al., 2008; Salter et al., 2012; Lasbleiz et al., 2016). The volcanic (basaltic) makeup of the islands renders the surrounding waters highly productive because the resuspension of shallow benthic sediments supplies Fe to surface waters. In addition, localized nutrient fertilization occurs as a result of the runoff of island sediments (containing Fe and possibly Si, although Si is dominantly supplied via bathymetry-driven upwelling) and/or guano from the bird and seal colonies (introducing reduced N) (de Baar et al., 1995; Blain et al., 2001; Moore & Abbott, 2002; Holeton et al., 2005; Tyrrell et al., 2005; Pollard et al., 2009, Salter et al., 2012). Fe- and Si-fertilized waters are associated with increases in phytoplankton diversity as well as increases in the abundance of the larger size classes, particular heavily-silicified diatoms, with implications for C export (Boyd et al., 2000; Hoffmann et al., 2006). Larger phytoplankton can escape microzooplankton grazing pressure by outgrowing them (i.e., size-escape), and large diatoms are more resistant to mechanical grazing due to their silica frustules (Sunda & Huntsman, 1997; Hamm et al., 2003; Timmermans et al., 2004; Poulton et al., 2007).

As discussed above, the biogeochemical cycles of C, N and Si are heavily influenced by Southern Ocean phytoplankton productivity (Boyle, 1998; de Baar et al., 2005). NO_3^-, while an essential nutrient for phytoplankton growth, is never assimilated to limiting levels in the open Southern Ocean because Fe

and Si limitation always occur first (Blain et al., 2007 & 2008; Mosseri et al., 2008; Dehairs et al., 2015). This decouples the N, C and Si cycles as a result of the preferential export of Si (Poulton et al., 2007). Unlike in the open ocean where the main mechanism of Fe supply is vertical mixing (Tagliabue et al., 2014), bathymetric-induced upwelling near the islands increases the Fe supply to the surface as a result of the ferricline being forced upwards, which drives increased surface entrainment (Blain et al., 2008; Schallenberg et al., 2018; Janssen et al., 2020). Even around the islands, however, the Fe supply remains insufficient to drive the consumption of all available macronutrients (Janssen et al., 2020). Nonetheless, the increased availability of Fe near the islands (relative to the open ocean) encourages an uptake ratio of Si:N that is closer to 1:1, and significant organic matter export takes place (Boyle, 1998; Smaetacek et al., 2004; de Baar et al., 2005). For the purposes of this thesis, all mention of Fe refers to total dissolved Fe (dFe). While including particulate Fe (pFe) can increase estimates of total Fe by up to 35% near the islands in the Southern Ocean (Trull et al., 2015), the bioavailability of particulate pFe is generally low (Lannuzel et al., 2011; van der Merwe et al., 2015). For example, only 1% of pFe has been estimated to be bioavailable over the Kerguelen Plateau (van der Merwe et al., 2015).

As previously described, pico- and nanophytoplankton assemblages dominate the HNLC waters of the Subantarctic (Weber & El-Sayed, 1987; Gervais et al., 2002) due to their competitive diffusive nutrient uptake rates and high abundances (allowing them to withstand heavy grazing pressures) (Sunda & Huntsman, 1997; Timmermans et al., 2004; Poulton et al., 2007), a shift to nano- and microphytoplankton dominance has been observed in the Fe-fertilized waters around the islands (Gall et al., 2001; de Baar et al., 2005; Hoffmann et al., 2006; Moore et al., 2007b). This shift to larger size classes, often with a greater contribution from siliceous species, has positive implications for C export (Cullen, 1991; Smetacek et al., 2004; de Baar et al., 2005; Poulton et al., 2007). The biomass in the near-island nano- and microphytoplankton blooms can be ~10-fold higher than in the surrounding HNLC waters (de Baar et al., 1995; Trull et al., 2015) and C export has been estimated to be 2-3 fold higher around the islands than in the open ocean (Pollard et al., 2007; Blain et al., 2008; Savoye et al., 2008).

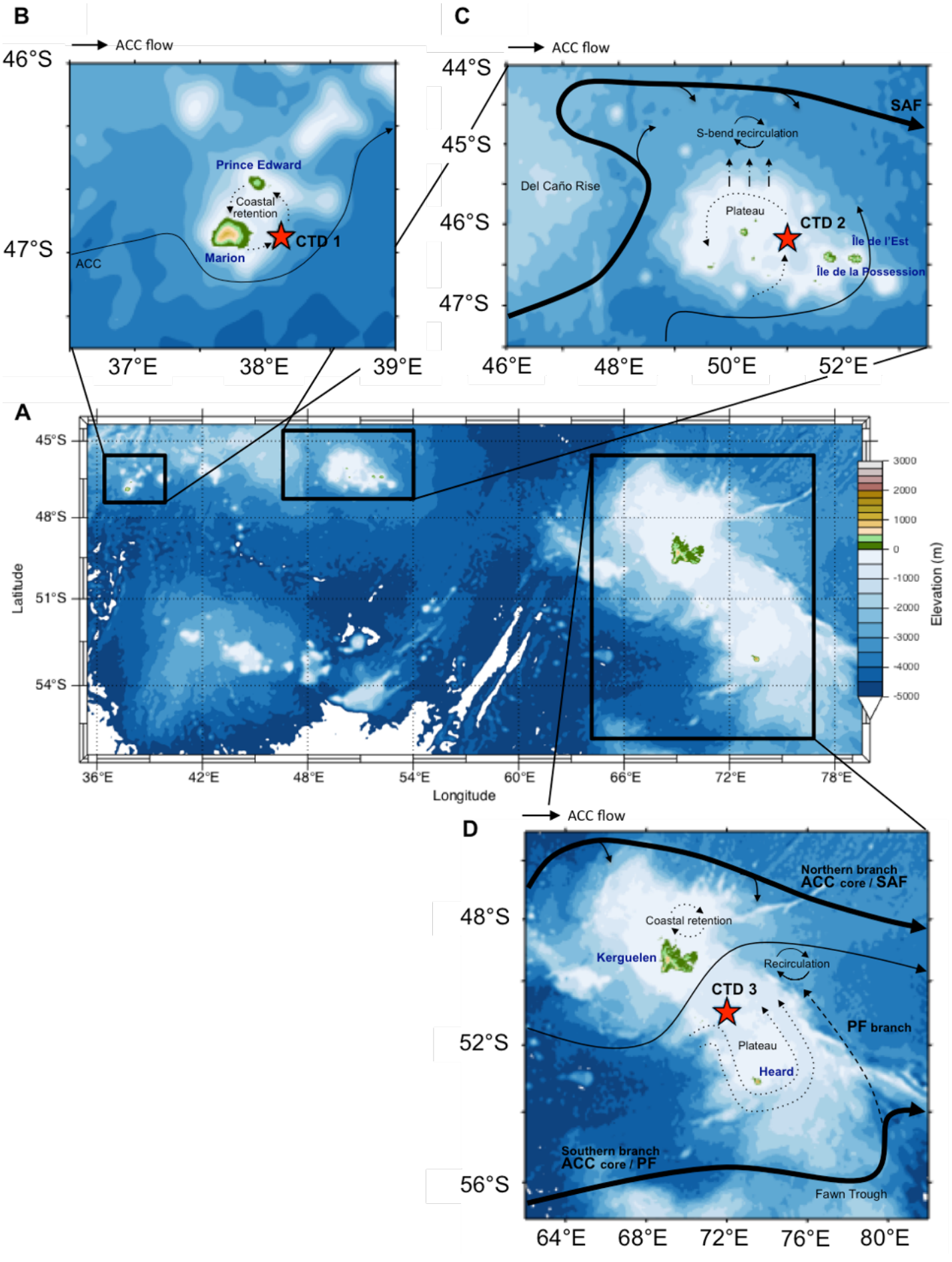
B
ACC flow
46°S
47°S
Prince Edward
Coastal retention
CTD 1
Marion
ACC
37°E
38°E
39°E
C
ACC flow
44°S
45°S
46°S
47°S
SAF
S-bend recirculation
Del Caño Rise
Plateau
CTD 2
Île de l'Est
Île de la Possession
46°E
48°E
50°E
52°E
A
45°S
48°S
51°S
54°S
Latitude
36°E
42°E
48°E
54°E
60°E
66°E
72°E
78°E
Longitude
3000
2000
1000
0
-1000
-2000
-3000
-4000
-5000
Elevation (m)
D
ACC flow
48°S
52°S
56°S
Northern branch
ACC core / SAF
Coastal retention
Kerguelen
Recirculation
CTD 3
PF branch
Plateau
Heard
Southern branch
ACC core / PF
Fawn Trough
64°E
68°E
72°E
76°E
80°E

Figure 1.5: Bathymetric schematic of A: the Subantarctic islands of the Indian sector of the Southern Ocean, including B: the Prince Edward Islands (PEIs), C: Crozet archipelago (CR), and D: Kerguelen archipelago (including Kerguelen Island, KG and Heard Island and MacDonald islands, HR). The negative elevation (depth) for the ocean is depicted by the shade of blue while the positive elevation for land is depicted by an array of green and red colours (the bathymetric data were taken from the ETOPO1 Global Relief Model using the grid version ETOPO1 Ice Surface). The circulation around the various archipelagos is represented by solid black lines and arrows and the plateau/coastal retention is depicted by dashed lines. The positions of the CTD stations sampled during the present study are indicated with red stars. The general circulation around the **PEIs** (B) is dependent on the position of the SAF. During this study, the SAF was far away from the islands, likely allowing for coastal retention on the shelf between Marion and Prince Edward Island (where CTD 1 is located) and potentially supporting a phytoplankton bloom. To the north of the **CR** (C), the SAF creates a S-bend retention zone as a result of the regional bathymetry. The Crozet plateau, including the relatively large islands of Île de la Possession and Île de l'Est to the east, gives rise to a retention area, where phytoplankton blooms regularly occur. The nutrient-rich plateau waters are ultimately advected northwards towards the S-bend recirculation zone, preconditioning the recirculation feature for a spring bloom. Around **KG** and **HR** (D), the ACC is bathymetrically forced to the north and south (Fawn Trough, channeling the Polar Front; PF) of the plateau. KG is situated on the northern side and HR is situated on the southern side of the plateau, a ~500 m-deep bathymetric feature inducing a slow flow that supports nutrient entrainment to the surface and phytoplankton blooms. Once the ACC/PF has passed through the Fawn Trough, part of the flow is bathymetrically-forced northwards to rejoin the northern branch of the ACC, forming a recirculation zone that supports an offshore phytoplankton bloom before the ACC heads eastwards. Additionally, coastal retention of nutrients around the islands, particularly around KG, promotes continuous phytoplankton blooms over the summer season. (Original circulation adapted from Pollard et al., 2007; Trull et al., 2015; Holmes et al., 2019).

Although many of the IME mechanisms occur at most of the islands, the IME is not the same at all the island archipelagos (e.g., in terms of its influence on phytoplankton production and C export). Bathymetric features such as continental shelf gradients, as well as chemical, biological, and physical activities that occur on land (e.g., tundra/glacial conditions, animal aggregations) vary from island to island, resulting in variability in the manner in which the IME manifests in the waters surrounding the islands. The study area for this thesis (Figure 1.5A), the Indian sector of the Southern Ocean, includes the Prince Edward Islands (PEI; Figure 1.5B), Crozet Islands (CR; Figure 1.5C), Kerguelen Islands (KG; Figure 1.5D) (all with mainly tundra conditions – treeless plains and low-growing vegetation including mosses, lichens and shrubs, with a permanently frozen subsoil known as permafrost) and Heard Island (HR; Figure 1.5D) (with mainly glacial conditions – extended mass of ice formed from the accumulation and compaction of snow over the years). Extensive studies have been conducted around the Crozet and Kerguelen archipelagos, including the CROZet natural iron bloom and EXport experiment (CROZEX) in the austral summer of 2004-2005 (e.g., Poulton et al., 2007; Pollard et al., 2007a & b; Planquette et al., 2007), the KErguelen Ocean and Plateau Study 1 in January/February 2005 and 2 in October/ November 2011 (KEOPS 1&2; e.g., Fripiat et al., 2011; Dehairs et al., 2015; Trull et al., 2015) and the

Heard Earth-Ocean-Biosphere Interactions (HEOBI) expedition in January/February 2016 (e.g. Holmes et al., 2019).

1.3.2 Prince Edward Islands

The Prince Edward Islands (PEI) are the western-most island group in the Indian sector of the Southern Ocean and consist of the larger Marion Island and the smaller Prince Edward Island, the latter situated 19 km northeast of Marion (Figure 1.5B). The islands are connected by a small inter-island plateau that rises from depth to ~200 m deep, with the shallowest point at 40 m (Pakhomov et al., 2000; Treasure et al., 2019).

The PEIs generally lie between the SAF and the PF in the path of the ACC (Deacon, 1983; Lutjeharms, 1985; Pakhomov et al., 2000); however, these fronts, especially the SAF, can shift (Pakhomov & Chown, 2003; Ansorge et al., 2009). The position of the SAF in relation to the islands has implications for the advective forces affecting the flow of the ACC around the plateau region and is thus essentially the major driver of primary production in this area (Pakhomov & Froneman, 1999; Ansorge et al., 1999). Strong advection off the plateau occurs when the SAF is close to the islands (Perissinotto & Duncombe Rae, 1990; Pakhomov et al., 2000), resulting in the retention of very little nutrient-rich water – either from winter water upwelling or island runoff – over the plateau. Under these conditions, nutrient concentrations over the plateau are comparable to those in the open ocean (Balarin, 2000) and the IME is dampened. Under conditions of strong advection, detectable concentrations of ammonia and urea have been observed downstream of the PEIs (Pakhomov & Froneman, 1999; Perissinotto et al., 1990). Since reduced N mainly derives from the large seal and bird colonies on the islands (Treasure et al., 2015) and would generally be consumed quickly by phytoplankton, high concentrations downstream (up to ~80 km) may be a strong indicator of rapid offshore advection (Pakhomov & Froneman, 1999; Perissinotto et al., 1990). When the SAF is distant from the PEIs (e.g., south or north), advection is weak and the environment over the plateau becomes extremely dynamic (Duncombe Rae, 1989). Anticyclonic eddies create a retention zone that accumulates nutrients on the lee side of Marion Island (Figure 1.5B) (Perissinotto & Duncombe Rae, 1990), exchanging little with offshore waters (Pakhomov et al., 2000). This retention zone also experiences freshwater inputs from the islands, which further stabilize the water column over the plateau (Allanson et al., 1985; Duncombe Rae, 1989). Combined, all these factors create a favourable environment for phytoplankton growth that is sustained over the summer growing season and mainly supports larger phytoplankton size classes (Allanson et al., 1981 & 1985; Boden, 1988; Perissinotto & Duncombe Rae, 1990).

To-date, very little work has been done in the vicinity of the PEIs on the interactions among phytoplankton, the IME, and C export potential. However, from studies around the Crozet and Kerguelen archipelagos (e.g., Poulton et al., 2007; Trull et al., 2015; Holmes et al., 2019) it can be inferred that an increase in new nutrient utilization (and by extension, C export potential) should occur near the PEIs, provided the SAF is not located near the islands.

1.3.3 Crozet Island archipelago

The Crozet islands (CR) and plateau region comprise two major islands, Île de la Possession and Île de l'Est, which lie to the east while the plateau lies to the west, with three smaller islands on the central plateau (Figure 1.5C) (Pollard et al., 2007b; Poulton et al., 2007; Planquette et al., 2007). Benthic forcing from the plateau permanently guides the northern boundary of the ACC (i.e., the SAF) northwards between the Crozet Plateau (<1000 m) and the Del Caño Rise (~2000 m) to the west, then forces the current eastwards in a S-bend (Figure 1.5C) (Pollard & Read, 2001; Pollard et al., 2007b; Poulton et al., 2007). Spring phytoplankton blooms are supported over the plateau as well as in the S-bend of the SAF where western and northern retention zone boundaries are created (Pollard et al., 2002 & 2007b). The phytoplankton bloom over the plateau is sustained as a result of the long residence time of shallow waters (~1-2 months), a shallow ML (due to stratification), and Fe fertilization from deep winter mixing and internal waves over the plateau (Pollard et al., 2002, 2007a & b; Venables et al., 2007, Poulton et al., 2007). The northern retention zone, with a residence time of ~2 months, is fed by waters rich in Fe (and other nutrients including Si, NO_3^- and P) advected northwards from the plateau, creating favourable conditions for a spring phytoplankton bloom (Pollard et al., 2002 & 2007b). The spring bloom peaks in October/November, with a second bloom in December/January. The second bloom is more constrained to the waters nearest the islands as it relies on direct Fe inputs (i.e., from island-induced upwelling) due to oceanic Fe concentrations being limiting at this time (Pollard et al., 2007a & b). Nonetheless, this second bloom appears to yield the highest rates of primary and new production in the Crozet region (Lucas et al., 2007; Seeyave et al., 2007).

Although all nutrients decline as the blooms progress due to utilization by phytoplankton, as expected, NO_3^- never reaches limiting concentrations (Pollard et al., 2007a). On the other hand, Si and Fe become near-deplete in the retention zone and plateau region, likely driving the bloom decline at the end of December (Moore et al., 2007a & b; Pollard et al., 2007a & b). Mesoscale eddies from the SAF have been observed to enter the retention zone, supplying nutrients at concentrations similar to those in the

open ocean HNLC region (since they have not passed near the islands) and creating spatial variability within the bloom (Read et al., 2007; Pollard et al., 2007a). Si concentrations around the northern part of the plateau become depleted to lower concentrations than in the surrounding HNLC waters, which evinces high diatom growth during the blooms (Franck et al., 2000; Nelson et al., 2001; Sedwick et al., 2002; Poulton et al., 2007). As the bloom progresses over the season and Si becomes depleted, siliceous phytoplankton species (that are associated with high C export potential) are succeeded by species with lower Si requirements (and lower C export potential) (Sedwick et al., 2002; Poulton et al., 2007).

1.3.4 Northern Kerguelen Plateau (Kerguelen archipelago and Heard and McDonald Islands)

One of the most studied regions of the Southern Ocean, particularly with regards to Fe dynamics, the Kerguelen Plateau is the eastern-most Subantarctic island archipelago in the Indian sector. The plateau has the most extensive shallow (<1000 m) bathymetric imprint of all the Indian sector islands, extending ~2200 km southeast from the Kerguelen Island archipelago, with the northern region of the plateau lying between Kerguelen Island (KG) to the north and Heard Island and MacDonald Islands (HR) to the south (Figure 1.5D) (Mongin et al., 2008; Holmes et al., 2019). Immediately south of KG is a trough, ~650 m deep, where previous studies have observed surface conditions corresponding to the PF (e.g., Trull et al., 2015; Holmes et al., 2019). South of this trough is the central area of the northern KG Plateau where the average depth is ~500 m. Because of the vast extent of the shallow bathymetry in this region, the ACC is forced to the north and south of the landmass (Figure 1.5D). Some of the ACC flow is diverted north of the KG archipelago (Park et al. 2008a; McCartney & Donohue 2007) where a network of eddies has been observed to originate from its meandering path (Stammer, 1997; Moore & Abbott, 2000). The remaining flow of the ACC travels through the Fawn Trough to the south of HR and corresponds with the full-depth signature of PF (e.g., surface PF characteristics align with depth characteristics such as the presence of a Tmin) (Sokolov & Rintoul et al., 2009). For the purposes of this thesis, the PF is only recognized where full depth features are observed (i.e., at the Fawn Trough).

Because the ACC splits, the flow over the plateau area is very slow, with surface velocities between 2 and 8 cm s^{-1} (Mongin et al., 2008) and a residence time of 2-3 months (Park et al., 2008b). This sluggish flow encounters intense internal tide-driven waves on the plateau (15 – 50 cm s^{-1}), which interact with the sediment and drive nutrients (especially Fe and Si) to the surface during the winter and spring until stratification occurs in the summer (Blain et al., 2007; Park et al., 2008b; Holmes et al., 2019). The upwelled supply of nutrients appears to sustain a recurring austral phytoplankton bloom over the plateau (Blain et al., 2007; Mongin et al., 2008).

Once the southern deviation of the ACC has transited through the Fawn Trough, it is bathymetrically-forced northwards, creating a recirculation zone on the eastern side of the plateau. This recirculation zone is fed equally by the northern and southern divisions of the ACC and has a residence time of 1-2 months (d'Ovidio et al., 2015; Park et al., 2014). The PF jet is also forced northwards by the regional bathymetry (Trull et al., 2015). These bathymetrically-forced currents are hypothesized to constrain the shape and magnitude of the phytoplankton bloom (Mongin et al., 2009; Maraldi et al., 2009). On the eastern edge of the recirculation zone, the ACC is no longer bathymetrically-constrained and meanders eastward (Trull et al., 2015).

Fe is the ultimate limiting nutrient in this region, both inter-annually and inter-seasonally (Janssen et al., 2020), with the exception of in the very coastal waters surrounding the island archipelago (Holmes et al., 2019), similar to the conditions at the Crozet archipelago (Planquette et al., 2007). The availability of Fe thus dictates the degree of N, P and Si utilization (Holmes et al., 2019). The supply of Fe to the region is difficult to estimate due to the variable retention times of waters over different parts of the plateau, along with the complex physical and biological dynamics at play. This is emphasized in a recent study by Pérez-Tribouillier et al. (2020) wherein export fluxes near KG are reported to be similar to those observed at other continental margins around the Southern Ocean. However, the high rate of particle dissolution in the waters surrounding KG represents a possible resupply source of nutrients to the ML (Pérez-Tribouillier et al., 2020). The highest Fe concentrations have been observed in the coastal waters close to the Kerguelen Island archipelago, which is where the first phytoplankton bloom occurs (Trull et al., 2015), followed by the plateau area, the PF, and the recirculation zone to the east, with the lowest Fe concentrations (and phytoplankton growth rates and biomass) in the open ocean HNLC region (Bowie et al., 2015; Queroue et al., 2015; van der Merwe et al., 2015; Trull et al., 2015). As the summer season progresses, the vertical supply of nutrients from the plateau is reduced as a result of stratification driven by surface warming. However, this stratification, in combination with the long residence time of waters over the plateau, supports the highest aggregation of phytoplankton biomass over the season (Trull et al., 2015).

While a high proportion of NO_3^- utilization has been reported across the plateau region because of the elevated Fe and Si supply (Mosseri et al., 2008; Trull et al., 2008 & 2015), similar to the CR plateau, the overall degree of NO_3^- drawdown is too low to limit phytoplankton productivity (Blain et al., 2007; Mosseri et al., 2008). Further to this, the plateau populations are dominated by larger phytoplankton, particularly diatoms (de Baar et al., 2005). These large diatoms have higher Si requirements compared

to the smaller phytoplankton found in the relatively consistent-upwelling regions of the coast and PF (de Baar et al., 2005; Trull et al., 2015). A greater depletion of Si over the plateau region (Blain et al., 2007; Mosseri et al., 2008) in comparison to NO_3^- by mid-summer decouples the cycles of Si and N (Boyd et al., 2004), typical of the Fe-depleted end of bloom conditions, as in the HNLC regions of the Southern Ocean.

One might assume that because of the large biomass aggregation over the plateau fueled by new N utilization, there is elevated potential for organic matter export at KG and HR. However, Trull et al. (2015) suggest that export is actually greatest in the downstream recirculation zone rather than over the plateau or inshore area. This is likely a result of low-intensity but continuous advection of nutrient-rich waters from the northeastern KG shelf by the northern deviation of the ACC (Park et al., 2014; Bowie et al., 2015; d'Ovidio et al., 2015; Trull et al., 2015). Additionally, the shorter residence time of water in the recirculation zone does not allow biomass build up, unlike over the plateau, which may have led to the apparently false assumption that more export takes place over the plateau. The increased export potential in the recirculation zone compared to the plateau area is an example of how different ecosystems are regulated by either continuous or sporadic nutrient input (Trull et al., 2015).

1.4 N Isotopes as an analytical tool

Considering that N is a fundamental component of marine biomass and the majority of marine N sources and sinks are driven by biological processes, the availability of N in its various forms exerts a disproportionate control on biogeochemical cycling in the oceans. Isotopes of N record patterns of marine N utilization and its inventory, making it a powerful tracer of physical, chemical and biological oceanic processes (Sigman et al., 1999; Sigman & Fripiat, 2019). There are two stable N isotopes, ^{14}N and ^{15}N, that exist in a naturally occurring average ratio where ^{14}N is the most abundant at 99.64% and ^{15}N occurs at 0.364%. Through various environmental processes, isotopic discrimination ('isotopic fractionation') occurs, resulting in measurable differences in the ratio of ^{15}N to ^{14}N in the various dissolved and particulate N forms relative to the average ratio found on Earth.

This ^{15}N to ^{14}N ratio is often presented in delta (δ) notation relative to the universal standard, atmospheric N_2 (Air), and units of permil (i.e., ‰ vs. Air):

$$\delta^{15}N\ (‰\ vs.\ Air) = (((^{15}N/^{14}N)_{Sample} / (^{15}N/^{14}N)_{Air} - 1) \times 1000 \quad (1.1)$$

In this notation, the $\delta^{15}N$ of atmospheric N_2 = 0‰

Isotopic fractionation that drives changes in the isotopic ratios occurs because of the preferential uptake of one of the isotopes. For most biological reactions, the "lighter", more energetically economical isotope, ^{14}N, is preferentially consumed via a kinetic, unidirectional reaction. ^{15}N, the "heavier" isotope, forms stronger bonds with other elements, and thus reacts more slowly.

For example, during NO_3^- utilization by phytoplankton, preferential consumption of ^{14}N-bearing NO_3^- means that the NO_3^- pool in the water column becomes enriched in ^{15}N (therefore yielding an increased $\delta^{15}N_{NO3}$) and the phytoplankton biomass produced will initially be enriched with the lighter isotope, ^{14}N (therefore yielding a low biomass $\delta^{15}N$). However, as NO_3^- consumption proceeds, more ^{15}N will be incorporated by the phytoplankton biomass and the biomass $\delta^{15}N$ will subsequentially rise. The differential degree to which ^{14}N and ^{15}N are converted from reactant (ambient NO_3^-) to product (biomass) is described by the kinetic isotope effect ($^{15}\varepsilon$):

$$^{15}\varepsilon\ (‰) = (1 - (^{15}k/^{14}k)) \times 1000 \qquad (1.2)$$

where ^{14}k and ^{15}k are the rate coefficients for the reactants containing ^{14}N and ^{15}N, respectively. The $^{15}\varepsilon$ can be used to predict the $\delta^{15}N$ of the biomass generated from the $\delta^{15}N$ of the reactant and the type of product produced – instantaneous or integrated (further explained in 4.1.1 below).

1.4.1 Rayleigh & steady-state model

Oceanic N isotope data are generally interpreted using the "Rayleigh" or "steady-state" models that utilize three key parameters: 1) the degree of reactant N pool consumed *(f)*, 2) the initial $\delta^{15}N$ of the reactant pool ($\delta^{15}N_{initial}$) and 3) the kinetic $^{15}\varepsilon$ (Figure 1.6).

The Rayleigh model is used to approximate isotope distributions in a closed system where a reaction proceeds with a constant $^{15}\varepsilon$ and neither replenishment nor removal of the reactant or product pools takes place (Mariotti et al., 1981; Sigman et al., 2009). An example of this is NO_3^- utilization by phytoplankton in the summer-stratified surface of the Southern Ocean. As consumption of the surface NO_3^- pool proceeds, the Rayleigh model describes the evolution of its $\delta^{15}N$ ($\delta^{15}N_{reactant}$), as well as that of the biomass (reactant) produced (equations 1.3-1.5, below). The instantaneous product ($\delta^{15}N_{instantaneous}$) is the particulate N (PN) biomass produced at any given moment from the consumption of NO_3^- and the

integrated production ($\delta^{15}N_{instegrated}$) is the accumulated biomass produced from NO_3^- uptake. The calculations are as follows:

$$\delta^{15}N_{reactant} = \delta^{15}N_{initial} - {}^{15}\varepsilon\ (\ln f) \quad (1.3)$$

$$\delta^{15}N_{instantaneous} = \delta^{15}N_{reactant} - {}^{15}\varepsilon \quad (1.4)$$

$$\delta^{15}N_{integrated} = \delta^{15}N_{initial} - {}^{15}\varepsilon\ (f/(1-f))\ln f \quad (1.5)$$

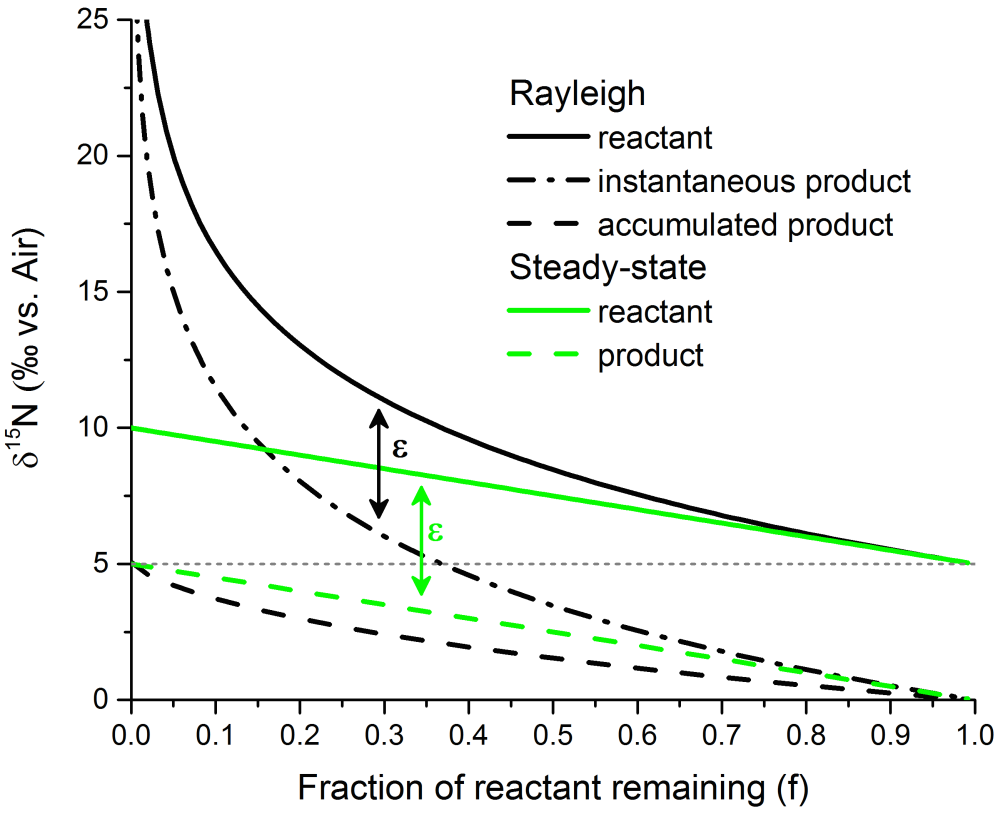

Figure 1.6: Schematic of the two simple, unidirectional models of N isotope fractionation associated with nitrate assimilation, the Rayleigh model (black lines) and the steady-state model (green lines). This schematic shows the $\delta^{15}N$ of the initial reactant (i.e., nitrate) and product (i.e., N biomass) pools as a function of the fraction of the reactant N pool left unconsumed. The same initial reactant $\delta^{15}N$ (grey dotted line) and isotope effect ($^{15}\varepsilon \sim 5‰$) are used for both models. The Rayleigh model is applicable in the case of a closed system where there is no resupply of reactant N during uptake. By contrast, the steady-state model describes an open system where the reactant pool is supplied continuously during uptake (Sigman & Fripiat, 2019).

Although the Rayleigh model is often used to describe, and is a good representation of, NO_3^- uptake during a stratified surface-layer phytoplankton bloom (Sigman et al., 1999 & 2009), this model has limitations. The most fundamental limitation of the Rayleigh model is that it describes a closed, unidirectional system. Ocean ecosystems are neither closed nor unidirectional, and often experience nutrient input in a multidirectional (vertical and lateral) fashion throughout the year. Furthermore, $\delta^{15}N_{reactant}$, $\delta^{15}N_{instantaneous}$ and $\delta^{15}N_{integrated}$ are simplified forms of more complex expressions, which can result in large errors especially when consumption is high (lower *f*) and the $^{15}\varepsilon$ is large (Sigman et al., 2009).

Regardless, visualizing NO_3^- data in "Rayleigh space", wherein $\delta^{15}N_{NO3}$ is plotted against $\ln([NO_3^-])$, can be extremely useful. The slope of the linear relationship between $\delta^{15}N_{NO3}$ and $\ln([NO_3^-])$ approximates the $^{15}\varepsilon$ of NO_3^- assimilation (Sigman et al., 1999, DiFiore et al., 2006). However, the use of the Rayleigh model is best suited to environments where there is unlikely to be stochastic resupply of nutrients and/or where *f* is relatively low.

The open system alternative to the Rayleigh model, the steady-state model, assume that the reactant pool is continuously supplied and only partially consumed, with some of the residual reactant N being exported (Figure 1.6). In this case, the rate of supply of reactant N is equivalent to the rate of product N generated plus the rate of residual N being exported. The relationship between $\delta^{15}N$ and *f* is thus linear. The parameters *f*, $^{15}\varepsilon$, $\delta^{15}N_{reactant}$ and $\delta^{15}N_{initial}$ remain the same as for the Rayleigh model, and $\delta^{15}N_{product}$ describes the product N pool (i.e., in this case there is no distinction between $\delta^{15}N_{instantaneous}$ and $\delta^{15}N_{integrated}$). The following approximate expressions are used to calculate $\delta^{15}N$ with the steady-state model:

$$\delta^{15}N_{reactant} = \delta^{15}N_{initial} + {}^{15}\varepsilon\,(1 - f) \quad (1.6)$$

$$\delta^{15}N_{product} = \delta^{15}N_{initial} - {}^{15}\varepsilon\,(f) \quad (1.7)$$

This model can be applied to processes happening in a well-mixed water column where supply and uptake are happening simultaneously.

1.4.2 Applying the Rayleigh Model to the Southern Ocean and estimating the isotope effect

Estimating the $^{15}\varepsilon$ of NO_3^- assimilation by phytoplankton in the Southern Ocean is challenging due to the complex interplay between physical and biological processes. Although the Rayleigh model ($\delta^{15}N$ vs. $\ln([NO_3^-])$) has limitations due to its closed-system assumption, the summertime Southern Ocean is considered a suitable region for application of the Rayleigh model for two reasons: 1) surface-layer stratification in summer due to surface warming, underlain by a strong pycnocline (Sigman et al., 1999; DiFiore et al., 2006 & 2009) and 2) relatively low levels of nutrient utilization, on the order of <50% over the summer season (Sigman et al., 1999). It is worth noting that the high values of *f*, the Rayleigh and steady state models yield similar results (Figure 1.6 & 1.7A) (Mariotti et al., 1981; Sigman et al., 1999, DiFiore et al., 2006).

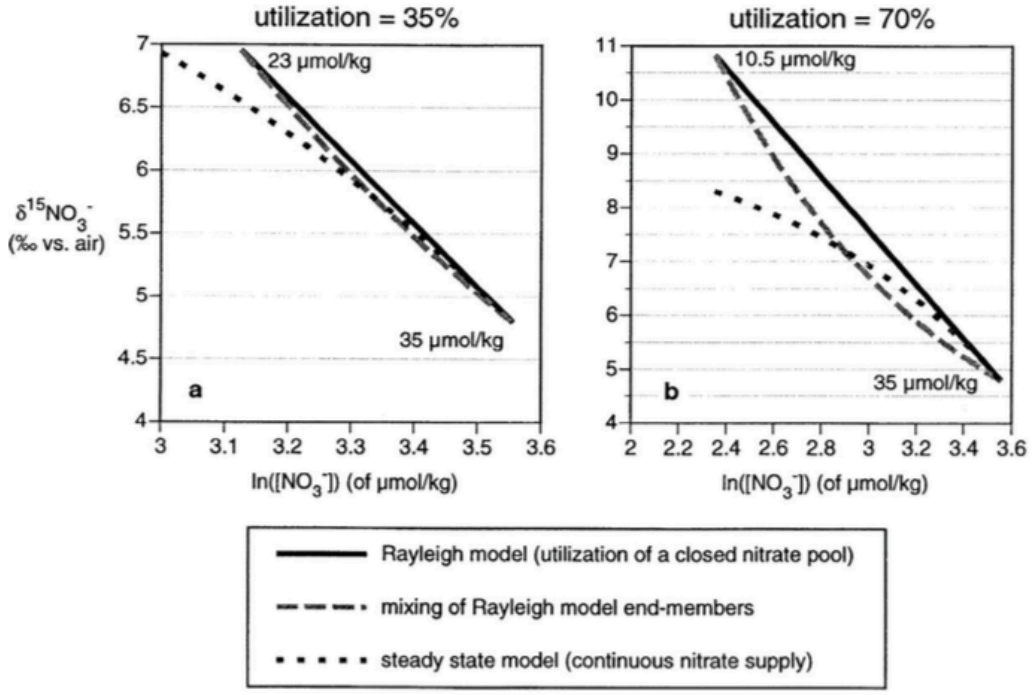

Figure 1.7: An illustration of the expected $\delta^{15}NO_3^-$ under different degrees of NO_3^- utilization, A: 35% utilization and B: 70% utilization, and applying different models for kinetic isotope fractionation, the Rayleigh model (no resupply of reactant; solid black line) and steady-state model (continuous resupply of reactant, dotted line). Also shown is the result of a mixing model (dashed line) between the initial and final NO_3^- end-members. In all cases, $\delta^{15}NO_3^-$ is plotted against the natural logarithm of $[NO_3^-]$; in Rayleigh space, the slope of the linear trend yields ε. Initial conditions for both panels, applicable to the Southern Ocean, are $[NO_3^-]$ = 35 µM, ε = 5‰ and an initial $\delta^{15}NO_3^-$ of 4.8‰. (Sigman et al., 1999a).

In order to accurately estimate the $^{15}\varepsilon$ of NO_3^- assimilation, knowledge of the NO_3^- source to surface waters is required. A large range of $^{15}\varepsilon$ has been estimated for the Subantarctic, calculated considering both lateral and vertical nutrient supplies to the summertime surface layer (Sigman et al., 1999; Difiore

et al., 2006 & 2010; Fripiat et al., 2019). The northward mixing of the OAZ waters into the PFZ and between the PFZ and SAZ influences the $\delta^{15}N_{NO3}$ and [NO_3^-] and, by extension, $^{15}\varepsilon$ (DiFiore et al., 2006 & 2010). The SAZ thermocline has an unusually low $\delta^{15}N_{NO3}$ compared to the rest of the Southern Ocean waters (Sigman et al., 2000). This, combined with a contribution of $\delta^{15}N_{NO3}$ from the PFZ surface, has led to relatively high estimates of $^{15}\varepsilon$ for the SAZ, ranging from ~6 – 9‰, with higher values to the north (Lourey et al., 2003; DiFiore et al., 2006). In the OAZ, there are a number of potential NO_3^- sources, each of which yields a different $^{15}\varepsilon$. For example, choosing the summertime Tmin as the source yields estimates of $^{15}\varepsilon$ as high as 7 – 10‰ (Karsh et al., 2003), while using UCDW as the source yields $^{15}\varepsilon$ of 4 – 6‰ (Sigman et al., 1999). In comprehensive evaluations of this issue for the Indo-Pacific (DiFiore et al., 2010) and the circumpolar AZ (Fripiat et al., 2019), it has been suggested that the Tmin (or more correctly, the winter mixed layer; Smart et al., 2015) is the most appropriate NO_3^- source to the OAZ surface, yielding for the circumpolar AZ, an $^{15}\varepsilon$ of 5.5±0.6‰ (Fripiat et al., 2019).

While not the focus of this study, the choice of the $^{15}\varepsilon$ applied to any analysis of NO_3^- and PN $\delta^{15}N$ data can have a significant effect on the interpretation (e.g., Sigman et al., 1999; Lourey et al., 2003; Fripiat et al., 2019). Here, for each of the zones of the Southern Ocean, $^{15}\varepsilon$ were conservatively estimated using the Rayleigh model applied to measurements of $\delta^{15}N_{NO3}$, previous studies, and taking into account local physical forcing (e.g., upwelling) (see methods section 3.7.3).

1.4.3 Application of the new production paradigm using N isotopes

The $\delta^{15}N$ of suspended particulate N (here, phytoplankton) is quantitatively related to the $\delta^{15}N$ of the inorganic N source that supports their growth (e.g., Wada & Hattori, 1978; Sigman et al., 2000; Knapp et al., 2005). Different forms of N have different $\delta^{15}N$ values. For example, the $\delta^{15}N$ of NO_3^- is high, with a global ocean range of 2 – 6‰ and a mean of 5‰ (Liu & Kaplan, 1989; Wu et al., 1997; Sigman et al., 2000; Knapp et al., 2005). Phytoplankton growth supported by allochthonous NO_3^- (i.e., new production) will thus yield relatively high-$\delta^{15}N$ biomass. Production supported by recycled nutrients (i.e., regenerated production) yields relatively low-$\delta^{15}N$ biomass because of the $^{15}\varepsilon$ associated with the production of recycled N (DeNiro & Epstein, 1981; Macko et al., 1986; Silfer et al., 1992; Checkley & Miller, 1989). While the $^{15}\varepsilon$ of NO_3^- assimilation must be calculated for each of the areas of study in this thesis and accounted for when calculating the $\delta^{15}N$ of the reactant and products (integrated and instantaneous), the $^{15}\varepsilon$ of NH_4^+ assimilation is of little concern. Although NH_4^+ assimilation can have a large $^{15}\varepsilon$ (Pennock et al., 1996; Waser et al., 1998), it is concentration-dependent (Waser et al., 1998; Casciotti & Buchwald, 2012) and thus not expressed in open ocean systems characterized by near-

complete NH_4^+ consumption (therefore, $^{15}\varepsilon$ ~0‰; Hoch et al., 1992; Pennock et al., 1996; Waser et al., 1998; Lourey et al., 2003). Isotopic fractionation during the processes associated with NH_4^+ production by zooplankton (e.g., controlled hydrolysis and deamination) yields the release of low-$\delta^{15}N_{NH4}$ into the water column (DeNiro & Epstein, 1981; Macko et al., 1986; Silfer et al., 1992; Checkley & Miller, 1989), with zooplankton accumulating high-δ^{15}N N within their bodies, which is ultimately released as fecal pellets (Checkley & Miller, 1989; Altabet & Small, 1990). This suggests that high-δ^{15}N phytoplankton material is preferentially exported (in a mass balance sense) from the surface ocean, while low-δ^{15}N phytoplankton continue to be part of the microbial loop in the ML (Altabet, 1988; Lourey et al., 2003).

The N isotopes can be used to estimate C export potential (Fawcett et al., 2011 & 2014; Treibergs et al., 2014; Van Oostende et al., 2017), even at low levels of N utilization. Annually, assuming an isotopic steady state, a $\delta^{15}N_{biomass}$ similar to that of the subsurface NO_3^- supply (considered the dominant source of new N even in low latitude regions, Sigman et al., 1999; Knapp et al., 2005 & 2016; Fawcett et al., 2011), is considered the link of N surface dynamics to C export to depth (Altabet, 1988; Fawcett et al., 2011; Smart et al., 2015). In the original formulation of the new production paradigm, all NO_3^- was assumed to represent a source of new N to the surface (Dugdale & Goering, 1967). For the Southern Ocean, this assumption is generally reasonable given that the primary source of NO_3^- to surface phytoplankton is deep winter entrainment (Rintoul & Trull, 2001; Sigman et al., 1999a). Moreover, it has been directly shown for the Atlantic Southern Ocean that the dominant biological process acting on the surface NO_3^- pool is assimilation in summer and nitrification in winter (Smart et al., 2015; Mdutyana et al., 2020). However, high rates of summertime surface-layer ammonification and/or nitrification have been reported near the KG archipelago (Cavagna et al., 2015), which would introduce regenerated NO_3^- to the mixed layer, potentially fueling up to 50% of total NO_3^- uptake (Dehairs et al., 2015; Fripiat et al., 2015). This regenerated NO_3^- compromises 'classical' NO_3^--based calculations of C export potential (Eppley and Peterson, 1979; Yool et al., 2007), potentially leading to overestimates of the export flux. However, measurements of natural abundance N isotopes allows for the identification of new vs. regenerated NO_3^- consumption. Phytoplankton biomass grown on regenerated NO_3^- (or other forms of regenerated N) has a low δ^{15}N, while the δ^{15}N of biomass grown on allochthonous NO_3^- is typically >2‰ higher (Sigman et al., 2009; Difiore et al., 2009; Fawcett et al., 2011; Buchwald et al., 2012; Smart et al., 2015). In other words, high-δ^{15}N phytoplankton biomass is indicative of new N assimilation and thus C export potential, while low-δ^{15}N phytoplankton biomass evinces regenerated N consumption, which, in a mass balance sense, yields no net C removal.

1.4.4 Issues associated with bulk $\delta^{15}N_{PON}$ measurements

Bulk $\delta^{15}N_{PON}$ has been used to investigate autotrophic new vs. regenerated N assimilation (e.g., Karsh et al., 2003; Trull et al., 2015). However, the bulk PON pool includes a diversity of living and detrital autotrophic and heterotrophic material (Fawcett et al. 2011). In addition, bulk $\delta^{15}N_{PON}$ integrates over longer time scales (weeks – months) than individual phytoplankton population $\delta^{15}N$ (~ days) (Rau et al., 1990; Fawcett et al., 2011), which renders PON (or some components thereof) susceptible to microbial remineralization and heterotrophic scavenging, both of which can alter its isotopic composition (Lourey & Trull, 2001; Trull et al., 2001b; Lourey et al., 2003; Hannides et al., 2013; Smart et al., 2020).

1.4.5 Coupling flow cytometry with N isotope analyses

In order to better understand how individual phytoplankton communities contribute to export production in the Southern Ocean, separation of the autotrophic component from the bulk samples needs to occur before $\delta^{15}N_{PON}$ is measured (Fawcett et al., 2011 & 2014; Treibergs et al., 2014). This can be done through an application of flow cytometry known as fluorescence-activated cell sorting (FACS). Flow cytometry has been widely used over the past few decades as a tool to initially quantify phytoplankton abundance and then to determine group-specific rates of nutrient uptake (Olson et al., 1983; Yentsch et al., 1983; Sosik & Olson, 1989; DuRand et al. 2001; Casey et al., 2009; Lomas et al., 2011). However, coupling flow cytometric sorting with N isotope analyses has only been attempted in the past decade (Casey et al., 2009; Fawcett et al., 2011 & 2014; Treibergs et al., 2014). Flow cytometry used in the marine setting is essentially the autofluorescent excitation (by lasers) of autotrophic cells at specific wavelengths and the consequent quantification of the light scattering from those excited cells. From here, individual phytoplankton populations can be enumerated from the bulk sample. Using a blue laser (488 nm), cells containing chlorophyll fluoresce in the red when excited, which is measured in the 667 nm channel, while cells containing PE will fluoresce orange, measured in the 575 nm channel. Once each of the phytoplankton populations has been identified, gated and sorted, the $\delta^{15}N$ of that population can be measured using the high sensitivity persulfate-denitrifier method (Sigman et al., 2001; Knapp et al., 2005; Fawcett et al., 2011). The result is a measurement of the $\delta^{15}N$ of 'pure' phytoplankton groups such as *Synechococcus* and picoeukaryotes, from which their contributions to new and regenerated production can be inferred (Fawcett et al., 2011).

2. Scope of Thesis

In this thesis, the first coupled flow cytometry-$\delta^{15}N$ data for the Subantarctic Ocean are presented. The Subantarctic is recognized for its disproportionate role in climate regulation, and the novel dataset described here allows the main drivers of the region's biological pump to be disentangled. Additionally, in the context of other biogeochemical and physical parameters, these data offer insight into phytoplankton population-specific C export potential and the influence of the IME on this flux.

Within the framework of the "new production paradigm" (Dugdale & Goering, 1967; Eppley & Peterson, 1979), the $\delta^{15}N$ of surface biomass can be used as an integrative tracer of NO_3^- versus NH_4^+ uptake. Previous studies have traditionally used bulk $\delta^{15}N_{PON}$ to investigate autotrophic new versus regenerated N assimilation in the Subantarctic (e.g., Karsh et al., 2003; Trull et al., 2015). However, the bulk PON pool may poorly record autotrophic N utilization because it includes an array of living and detrital autotrophic and heterotrophic material (Fawcett et al., 2011) and is susceptible to microbial remineralization and heterotrophic scavenging, which can alter its isotopic composition (Lourey & Trull, 2001; Trull et al., 2001; Lourey et al., 2003; Hannides et al., 2013; Smart et al., 2020). Thus, the flow cytometry-$\delta^{15}N$ approach is more useful (and more appropriate) because it allows for the analysis of the $\delta^{15}N$ of autotrophic phytoplankton groups in the absence of dead biomass and heterotrophs (Fawcett et al., 2011). This method also quantifies the abundance of the phytoplankton groups of interest, and thus allows for the estimation of NO_3^--based phytoplankton-specific C export potential.

The IME (Doty & Oguri, 1956) in the Subantarctic enhances C export regionally (e.g., Poulton et al., 2007; Fripiat et al., 2011; Trull et al., 2015; Holmes et al., 2019) by promoting phytoplankton growth through the supply of both micro- and macro-nutrients, including Fe and Si (e.g., Trull et al., 2015; Holmes et al., 2019; Janssen et al., 2020), which are typically limiting across this region. By using the coupled flow cytometry-$\delta^{15}N$ approach, the goal is to better constrain the N substrate utilization of Subantarctic phytoplankton groups and evaluate the influence of the IME on the extent of new versus regenerated N dependence. In this context, the main aims of this thesis include assessing: *Who* (with regards to phytoplankton populations) is there? *What* (with regards to N substrate utilization) are they doing? *Why* (with regards to the IME verses open ocean nutrient availability) are they doing it? and *What* are the implications for nutrient cycling and C potential export in this region?

This thesis begins with a description of the methodological approach, including sample collection on Leg 1 of the Antarctic Circumnavigation Expedition cruise across the Indian Sector of the Subantarctic,

as well as the subsequent sample analyses. The major results are then presented (and subsequently discussed), beginning with nutrient concentration and sea surface temperature data that provide biogeochemical and physical context, followed by the coupled flow cytometry-$\delta^{15}N$ data from both surface collections and depth profiles. Using these measurements, the reliance of each group on new versus regenerated N is assessed. Finally, the relative abundances of each phytoplankton population are described and their potential contributions to C export are estimated.

3. Methods

3.1 Sample collection

Samples were collected aboard the R/V *Akademik Treshnikov* on Leg 1 of the Antarctic Circumnavigation Expedition (ACE) cruise that took place from December 2016 to January 2017. Leg 1 crossed the Subantarctic Indian Ocean basin from Cape Town, South Africa to Hobart, Australia. Seawater samples were collected from 124 underway stations, seven conductivity-temperature-depth (CTD) hydrocast stations, and two near-island surface zodiac transects (Figure 3.1). From each of the CTD stations, calibrated temperature, conductivity and pressure probes collected data at high resolution throughout the water column. These measurements were quality controlled post-cruise to account for sensor drift. In addition, an oxygen sensor integrated with the CTD package was calibrated against Winkler titrated dissolved oxygen measurements for each cast (Carpenter, 1965; Grasshoff et al., 1983).

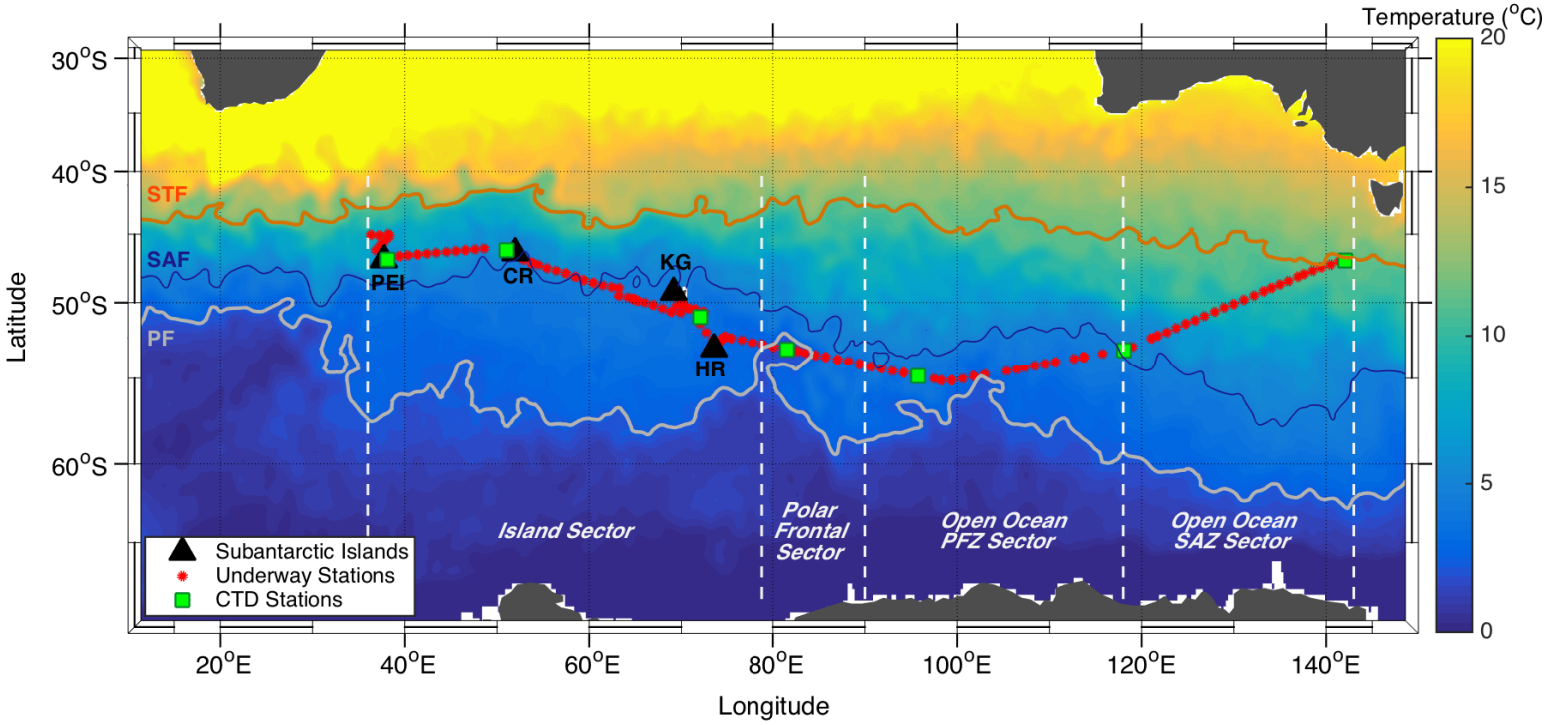

Figure 3.1: Map of the southern Indian Ocean basin showing the sampling locations of Leg 1 of the ACE voyage between Cape Town, South Africa and Hobart, Australia in December 2016 through January 2017. The 124 underway sampling stations are depicted by the red circles and the 7 CTD stations by the green squares. Six samples were also collected along two near-island surface zodiac transects offshore of Crozet and Kerguelen Islands that are not shown here. The Subantarctic Islands are indicated by the black triangles; PEI – Prince Edward Islands, CR – Crozet Islands, KG – Kerguelen Island, HR – Heard and MacDonald Island. The cruise track is plotted over a composite mean of the MODIS-AQUA sea surface temperature (SST; °C) satellite data from Level 3 browser at 4 km resolution (https://oceancolor.gsfc.nasa.gov/, methods 3.2.3). The cruise track is divided into four sectors that represent the different oceanic regimes transected (see results 4.1.2 for details). The sector boundaries are indicated by the white dashed lines, which separate the *Island Sector*, *Polar Frontal Sector* (*PF Sector*), *Open Ocean Polar Frontal Zone Sector* (*OO PFZ Sector*) and the *Open Ocean Subantarctic Zone Sector*

(*OO SAZ Sector*). The sectors were determined by a combination of nutrient data, temperature data, and frontal positions at the time of sampling. The Subtropical Front (STF) is indicated by the orange contour, the Subantarctic Front (SAF) by the dark blue contour, and the Polar Front (PF) by the grey contour.

3.1.1 Nutrient and nitrate isotope sampling

At all underway stations (water supplied to the ship via an intake at ~5 m depth, stations every 6 hours), at 10 depths on the shallow (~400 m) and 18 depths on the deep (~1000 m) CTD casts, and at all zodiac surface transect stations, the following samples were collected and immediately frozen at -20°C for later laboratory analysis: 1) nutrient samples in 50 ml Falcon tubes that were sample-rinsed three times (unless otherwise specified, all further references to "sample-rinsed" indicates rinsed with sample water three times) for later analysis of the concentrations of nitrate ($[NO_3^-]$), nitrite ($[NO_2^-]$), silicate ($[Si(OH)_4]$), and phosphate ($[PO_4^{3-}]$); 2) seawater samples for the analysis of ammonium concentrations ($[NH_4^+]$) in sample-rinsed 50 ml Falcon tubes that were "aged" with working reagent (WR; comprising 0.04 N borate buffer solution, 0.04 N sodium sulfite, and 0.002 N O-phthalaldehyde (OPA) in ethanol (Holmes et al., 1999), aged for two weeks in an opaque bottle prior to sample analysis); and 3) 0.2 µm-filtered seawater samples in 50 ml high-density polyethylene (HDPE) sample-rinsed bottles for nitrate isotope ($\delta^{15}N$ and $\delta^{18}O$) analysis.

3.1.2 Bulk particulate organic nitrogen biomass and isotope sampling

Particulate organic nitrogen (PON) samples were collected from all underway, CTD, and zodiac transect stations. Duplicate 2 L aliquots of seawater were collected in sample-rinsed opaque HDPE bottles from the surface at all stations. In addition, 2 L of seawater were sub-sampled from the Niskin bottles fired at the 8 shallowest depths (between the surface and 150 m) at the CTD stations. Each sample was filtered under gentle vacuum onto a pre-combusted (450°C for 8 hours) 25 mm 0.3 µm GF-75 glass fiber filter (GF/F) to capture the bulk particles. The filter was then folded into a pre-combusted (500°C for 5 hours) foil envelope and stored at -80°C.

3.1.3 Particle samples for fluorescence-activated cell-sorting (FACS)

At all the underway stations, surface samples were collected for fluorescence-activated cell-sorting (FACS). At the CTD stations, depths for FACS particle sampling were selected based on down-cast hydrographic and florescence profiles over the upper mixed layer (ML): surface (~5 m), ~30 m, the fluorescence maximum (F_{max}) (the maximum fluorescence measured by the CTD, taken as representative of the depth of highest biological activity, ranging between 45 m and 70 m), and 100 m. In duplicate, 4

L of seawater were collected in sample-rinsed spigot bottles and filtered under gentle vacuum filtration (20 – 40 cm Hg) through a 47 mm 0.4 µm polycarbonate (PC) filter. Vacuum filtration was stopped as soon as the last filtrate ran though the filter in order to avoid cells being pulled though the filter. The PC filters were transferred to 5 mL cryovials to which 4 mL of pre-filtered (through a 0.2 µm PC filter) low-nitrate seawater was added. The vials were shaken gently to re-suspend the cells caught on the filter. The samples were then 'fixed' with 100 µL of gluteraldehyde (final concentration of 2.5%, to protect against cell lysis; Ellwood et al., 2020) and incubated at 4°C for ~4 hours before being transferred to the -80°C freezer for storage.

3.1.4 >20 µm microphytoplankton size class sampling

Particles in the >20 µm size class (microphytoplankton, MICRO) were only sampled from the underway system due to the large volume of water required to collect sufficient material for taxonomic and isotope analysis. Duplicate aliquots of 6 – 60 L of underway water were filtered through a 20 µm nylon mesh, with the final volume dependent on the rate of gravitational filtration; filtration was stopped after three hours. Both 20 µm filters were then treated the same way as the FACS PC filters. One of the samples was incubated at 4°C for 4 hours before being stored in the -80°C freezer. The duplicate sample was stored at room temperature for later analysis of phytoplankton community composition.

3.2 Analytical hydrography

Vertical profiles of hydrographic measurements were made using a conductivity-temperature-depth profiler (SeaBird Electronics SBE 9+ CTD unit with SBE 3+ temperature sensor, SBE 4c conductivity sensor and SBE 5T pump) attached to a 24 position, 12-L Niskin bottle rosette (SBE 32 carousel). The SBE 11+ V5.2 deck unit recorded temperature, salinity and pressure. From these data, density was derived.

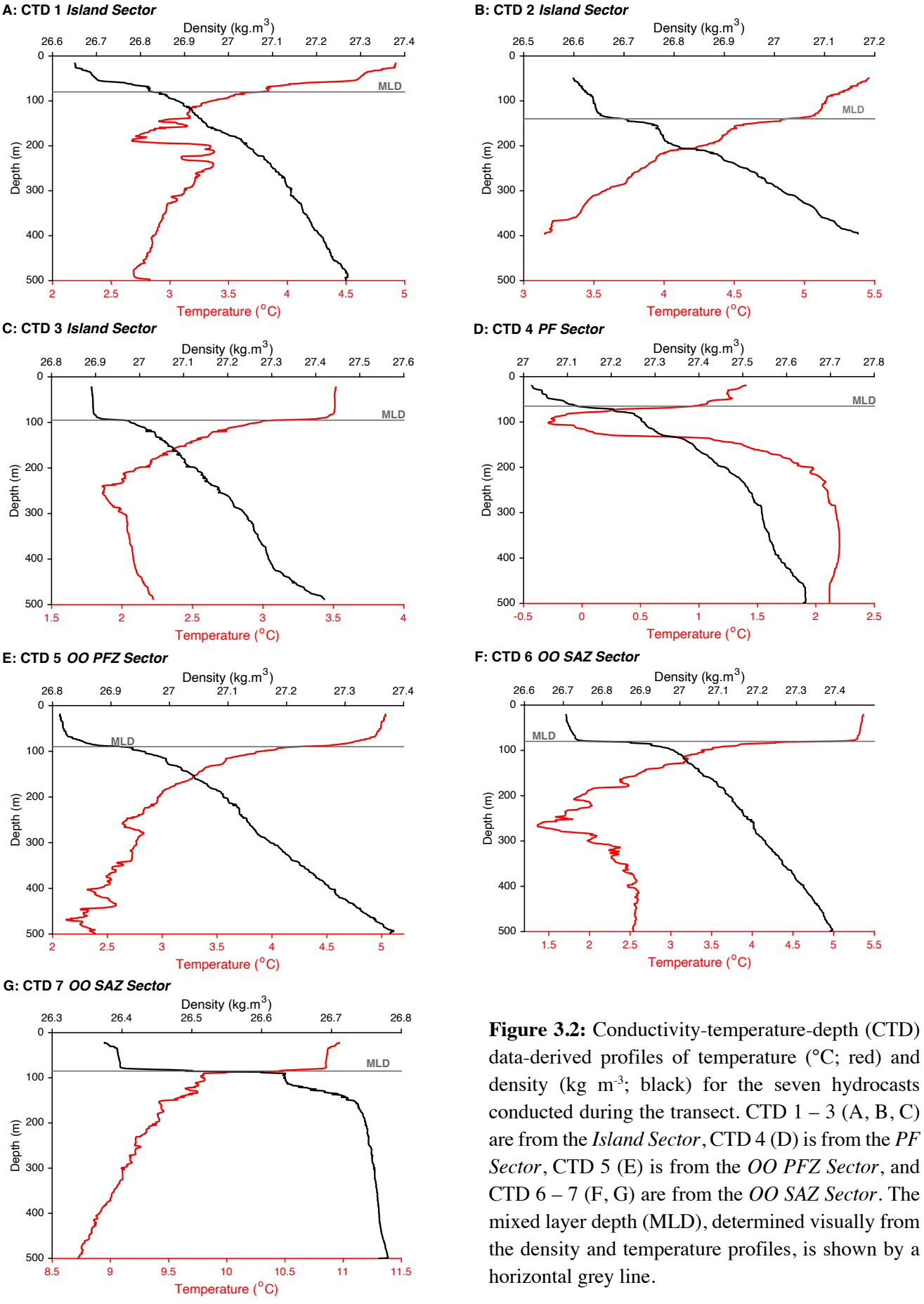

Figure 3.2: Conductivity-temperature-depth (CTD) data-derived profiles of temperature (°C; red) and density (kg m^{-3}; black) for the seven hydrocasts conducted during the transect. CTD 1 – 3 (A, B, C) are from the *Island Sector*, CTD 4 (D) is from the *PF Sector*, CTD 5 (E) is from the *OO PFZ Sector*, and CTD 6 – 7 (F, G) are from the *OO SAZ Sector*. The mixed layer depth (MLD), determined visually from the density and temperature profiles, is shown by a horizontal grey line.

3.2.1 Hydrographic variable calculations

The following variables were calculated from the CTD measurements: potential temperature (θ), absolute salinity (S_A), seawater potential density (ρ), and the seawater potential density anomaly, sigma-theta (σ_θ). θ, the temperature of a parcel of water under adiabatic movement compared to a reference pressure, and S_A, derived from a salinity calculation that incorporates the Reference-Composition Seawater scale - essentially the mass of salt in seawater - were used to compute ρ (Fofonoff, 1985). This was then used to calculate σ_θ.

$$\sigma_\theta = \rho\ (S_A, \theta, p)\ -1000\ kg\ m^{-3} \quad (3.1)$$

The Equation of State was used to compute ρ, which is a function of S_A, θ, p.

$\theta = T\ (p_0/p)^k$, where T is the temperature, p_0 is pressure at the surface and p is pressure at depth, and k is Poisson's Constant (Fofonoff, 1985). Using dry air for simplicity, k is 0.2854.

$S_A = (1.0047 \times S_p) + \delta S_A$, where S_p is derived from measurements of the conductivity of seawater (practical salinity) and δS_A is a correction for nonconductive dissolved matter.

3.2.2 MLD Calculations

Two methods were used to calculate the mixed layer depths (MLDs; Figure 3.2 and Table 3.1) for all CTD casts. The first used the Gibbs Sea-Water Oceanographic Toolbox (McDougall & Barker, 2011), which follows the de Boyer Montégut et al. (2004) MLD definition - a change in density of 0.03 kg m^{-3} or change in temperature of 0.2°C from a surface (i.e., 10 m) reference value. The second method involved visual estimation using profiles of temperature and density. This method appears to yield MLDs more suitable for the region. Hereafter, all calculations involving MLD use the estimated values listed in Table 3.1.

3.2.3 Estimates of sea surface temperature

In addition to the hydrographic data collected during the cruise, satellite data from MODIS-AQUA were used to supplement the ship-based surface measurements due to calibration issues with the underway Aqualine FerryBox. Sea surface temperature (SST) data at a Level-3 Binned browser at 4 km resolution (https://oceancolor.gsfc.nasa.gov/) were used to identify the positions of the fronts during the cruise. A composite mean of the SST was concatenated for the days of Leg 1 (Figure 3.1). This was analyzed in Matlab R2015a using the M_Map V1.4k mapping toolbox. Further to this, monthly SST data were

examined for the months preceding the cruise (September – December 2016) to better understand the regional dynamics that pre-set the conditions encountered during the expedition (Figure 3.3).

Since underway hydrographic data remain unavailable for the ACE cruise, the *Nearest Neighbor* function in Matlab R2015a was used to determine SST along the cruise track. This was done using the composite mean of the concatenated daily SST data for the duration of the cruise. While only accurate to the nearest 4 km grid point, given the distance travelled during the cruise, as well as the range of frontal zones crossed, this approach is considered sufficient.

Table 3.1: Results of MLD calculations for the CTD profiles across the Leg 1 transect. The *GSW calculated MLD* refers to that calculated using the Gibbs Sea-Water Oceanographic Toolbox (McDougall & Barker, 2011). The *Estimated MLDs* are visual estimations of the shallowest depth of the pycnocline and thermocline. The *Averaged summer MLDs* are values taken from literature for the purposes of comparison. Hereafter, for all calculations that require a MLD, the *Estimated MLD* values are used.

CTD	Sector and relative position	GSW calculated MLD[1] (m)	Estimated MLD (m)	Averaged summer MLD (m)	Reference
1	*Island* Near-shore PEI	164.6	80	80 – 100	Kara et al. 2003, DiFiore et al. 2006
2	*Island* CR Plateau	- [2]	140	80 – 100	Kara et al. 2003, DiFiore et al. 2006
3	*Island* KG Plateau	275.4	95	150 – 300	Kara et al. 2003, DiFiore et al. 2006
4	*PF*	130.8	65	50 – 100	Kara et al. 2003, DiFiore et al. 2006
5	*OO PFZ*	261.5	90	150 – 250	Kara et al. 2003, DiFiore et al. 2006
6	*OO SAZ* Near SAF	131.8	80	80 – 120	Kara et al. 2003, DiFiore et al. 2006
7	*OO SAZ* Near STF	85.3	85	50 - 100	Kara et al. 2003, DiFiore et al. 2006

[1]The Gibbs Sea-Water Oceanographic Toolbox, gsw_mlp function calculates the MLD by a change in density of 0.03 kg m^{-3} or change in temperature of 0.2°C from a surface reference value, 10 m in this case (de Boyer Montégut et al., 2004).
[2]No value could be calculated for this profile.

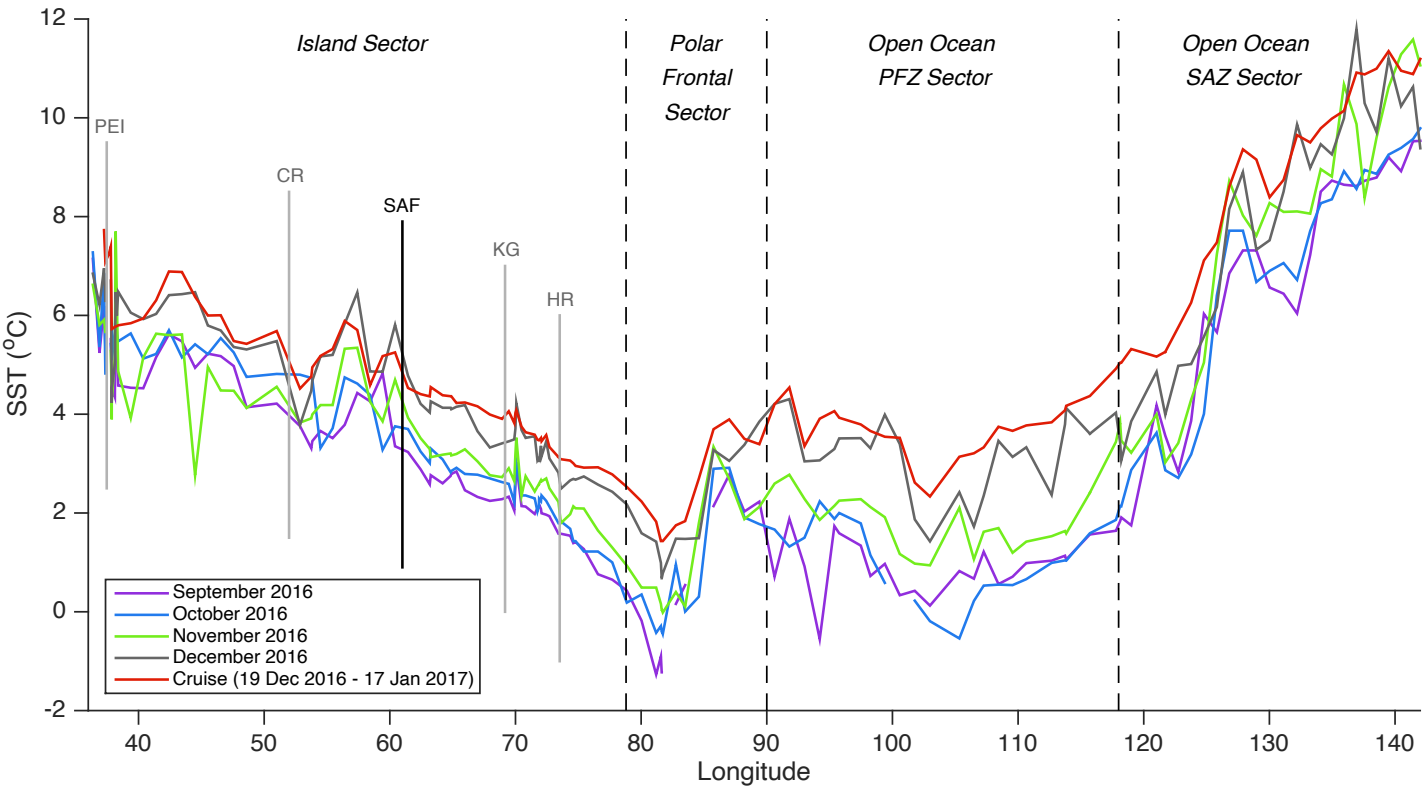

Figure 3.3: The mean sea surface temperature (SST) along the cruise track for the months preceding the cruise – September 2016 (purple), October 2016 (blue), November 2016 (green), December 2016 (grey) – and for the period of the cruise – 19 December 2016 – 17 January 2017 (red). The various sectors are labeled along the top with their boundaries indicated by the vertical dashed black lines. The positions of the Prince Edward Islands (PEI), Crozet Islands (CR), Kerguelen Island (KG), and Heard Island (HR) are indicated by the vertical grey lines and the Subantarctic Front (SAF) in the *Island Sector* is indicated by the vertical black line.

3.2.4 Bathymetric data

To better understand the dynamics occurring around the islands, bathymetric data were downloaded from NOAA's National Centers for Environmental Information page (https://www.ngdc.noaa.gov/mgg/global/). The ETOPO1 Global Relief Model was used with the grid version ETOPO1 Ice Surface. This was analyzed with Matlab R2015a using the M_Map V1.4k mapping toolbox.

3.2.5 Surface Chlorophyll-*a* data

Chlorophyll-*a* (Chl-*a*) data from near the islands, including the PEI, CR and KG, showing the advancement of the spring bloom from November 2016 to the time of the cruise, were downloaded from the MODIS-AQUA satellite product at a Level-3 Binned browser and 9 km resolution (https://oceancolor.gsfc.nasa.gov/). Monthly means were used for November 2016 and December 2016,

while a composite mean of the Chl-*a* was concatenated for the days of Leg 1 of the cruise coinciding with near-island sampling. A ~10-day 'window' period bracketed each of the island visitations as follows; PEI: 20/12/2016 – 02/01/2017, island visitation on 27/12/2016, CR: 24/12/2016 – 06/01/2017, island visitation 30/12/2016, KG & HR: 31/12/2016 – 13/01/2017, island visitations on 06/01/2017 – 08/01/2017. This window period was utilized to accommodate for cloud cover.

3.3 Laboratory nutrient analyses

All nutrient concentration measurements were conducted in the Marine Biogeochemistry Laboratory at the University of Cape Town under the supervision of Dr. Raymond Roman.

3.3.1 Nitrate and silicate concentration measurements

$[NO_3^-]$ and $[Si(OH)_4]$ were measured by flow injection and colorimetric analysis using a Lachat QuickChem Flow Analyzer in a configuration with a detection limit of <0.2 µM for both nutrients. Each sample was analyzed once on the Lachat following previously described protocols (Diamond, 1994; Grasshoff et al., 1999; Wendt, 2000).

For $[NO_3^-]$, standards of 40 µM, 20 µM, 8 µM, 4 µM, 2 µM, and 1 µM were prepared from a gravimetric stock (10 mM) and analyzed daily, yielding a standard curve covering the concentrations expected for each batch run of 100 samples. Standards of 20 µM and 8 µM were also analyzed after every 10 samples to monitor instrument performance and allow for drift correction.

During $[NO_3^-]$ analysis, a sample is passed through a copperized cadmium column, which reduces the sample NO_3^- to NO_2^-. This reduction reaction is aided by the addition of EDTA (ethylenediaminetetraacetic acid), which dampens any interference of high metal concentrations that can yield false low concentrations (Wendt, 2000). The resulting $[NO_2^-]$ is then determined by diazotizing the compound with 0.1 mL of 0.2 N sulphanilamide colour reagent after which 0.004 N N-(1-naphthyl)-ethylenediamine dihydrochloride (N-NED) is added (Strickland & Parsons, 1972). Both reagents are added in-line and produce a magenta colour, the absorbance of which at 520 nm is recorded spectrophotometrically (Wendt, 2000). Because sample NO_3^- is reduced to NO_2^-, the final concentration measurement is actually of $NO_3^-+NO_2^-$. The $[NO_2^-]$ must be measured separately and subtracted from $[NO_3^-+NO_2^-]$ to yield $[NO_3^-]$-only.

Using a separate channel on the Lachat QuickChem Flow Analyzer, [$Si(OH)_4$] was measured via colorimetric analysis (Grasshoff et al., 1999). Standards of 100 µM, 75 µM, 50 µM, 20 µM, 10 µM, 5 µM, and 2.5 µM were prepared from a gravimetric stock (10 mM) and analyzed daily, yielding a standard curve covering the concentrations expected for each batch run of 100 samples. Standards of 20 µM and 10 µM were also analyzed after every 10 samples to monitor instrument performance and allow instrument drift to be corrected.

Under acidic conditions, the $Si(OH)_4$ in the sample is reacted with 0.2 mL of 0.2 N ammonium molybdate to form β-silicomolybdic acid, which appears yellow in color. The acid is then reduced through the addition of 0.2 mL of 0.2 N ascorbic acid, forming an intense blue compound (Koroleff, 1972). Prior to colorimetric analysis, 0.2 mL of 1 N oxalic acid is added to dampen ambient phosphate interference and prevent the reduction of excess molybdate, which would detract from the "true" blue colour (Grasshoff et al., 1999). The sample and standard absorbance at 810 nm is then recorded spectrophotometrically.

3.3.2 Nitrite concentration measurements

[NO_2^-] was analyzed using the colourmetric method outlined by Bendschneider and Robinson (1952). A daily standard curve was prepared from a gravimetric stock (10 mM) at the following concentrations: 5 µM, 2.5 µM, 1.25 µM, 0.65 µM, 0.3 µM, and 0.1 µM. Sulfanilamide reagent (0.1 mL of 0.05 N) was added to 5 mL of sample/standard and vortexed to ensure homogenization. The reagent N-(1-naphthyl)-ethylenediamine dihydrochloride (0.1 mL of 0.004 N) was then added within 2 to 6 minutes of the sulfanilimide addition and the solution was vortexed again. Within 2 hours of reagent addition, sample absorbance was read using a Thermo Scientific Geneysis 30 Visible spectrophotometer at 543 nm. The detection limit was <0.05 µM.

The presence of NO_2^- has in some cases been shown to be problematic when evaluating NO_3^- isotope dynamics (Granger & Sigman 2009; Fawcett et al., 2015). [NO_2^-] in the Subantarctic summer ML is very low in comparison to that of the underutilized NO_3^- (here, [NO_2^-] = 0.3 – 3.5% of the combined [NO_3^-+NO_2^-] pool), and is thus expected to have a minor effect on the isotopic composition of NO_3^- +NO_2^- (Smart et al., 2015). Hereafter, unless stated otherwise, all NO_3^- values (concentrations and isotopic composition) are presented for NO_3^-+NO_2^-, similar to previous work conducted in the Southern Ocean (Sigman et al., 1999; DiFiore et al., 2009; Smart et al., 2015; Fripiat et al., 2019).

3.3.3 Phosphate concentration measurements

[PO_4^{3-}] was analyzed using the colourmetric method outlined by Strickland and Parsons (1972). A daily standard curve was prepared using the following standards made up from a gravimetric stock (10 mM): 5 µM, 2.5 µM, 1.25 µM, 0.65 µM, 0.3 µM, and 0.1 µM. A ratio of sample/standard to mixed reagent volume of 5:0.5 mL was combined and vortexed in a borosilicate test tube. The mixed reagent consists of 0.15 N ammonium paramolybdate, 8 N sulphuric acid, 0.002 N potassium antimonyl-tartrate, and 0.3 N ascorbic acid. Within 2 hours of reagent addition, sample absorbance was measured at 880 nm using a Thermo Scientific Geneysis 30 Visible spectrophotometer. The detection limit was <0.05 µM.

3.3.4 Ammonium concentration measurements

NH_4^+ concentrations were determined using a modified version of the Holmes et al. (1999) method. A standard curve was prepared for each batch run using the following standards made in Type-1 ultrapure Milli-Q water from a gravimetric NH_4^+ stock (1 mM): 3 µM, 1.5 µM, 1 µM, 0.5 µM, 0.25 µM, and 0.1 µM. In duplicate, 10 mL of sample/standard were pipetted into working reagent (WR)-aged Falcon tubes to which 2.5 mL of WR was added and then incubated for 3 – 4 hours in the dark. Sample and standard fluorescence was read using a Turner Trilogy Fluorometer equipped with a CDOM/NH_4^+ module and with the UV option selected (excitation at 365 nm and emission at 430 nm). The detection limit was ~0.02 µM. The matrix effect (ME) resulting from the calibration of seawater samples to Milli-Q standards was calculated according to the standard addition method (Saxberg & Kowalski, 1979). All samples were corrected for the ME (Holmes et al., 1999), which was always <10% and typically <5%.

3.3.5 PON concentrations and isotopic composition

The concentration and $\delta^{15}N$ of underway PON samples were measured in the Stable Light Isotope Laboratory (SLIL) at the University of Cape Town, and samples collected from the CTD casts were measured at the University of California, Davis Campus (UC Davis). Both the underway and CTD samples were prepared similarly for analysis.

The frozen GF/F samples were oven-dried at 40°C for 24 hours, after which they were ‘fumed’ in an acidic (HCl) environment in a desiccator for a further 24 hours to remove inorganic carbon. Once acidified, samples were oven-dried for a further 3 hours. Each GF/F was then trimmed to remove the blank outer edges (i.e., area containing no sample material), folded into a tin-capsule, and placed into a clean welled tray. Filter blanks (i.e., GF/Fs without sample material) were treated in the same manner as the samples.

At SLIL, samples were analysed using a Flash 2000 elemental analyzer interfaced with a Delta V Plus isotope ratio mass spectrometer (IRMS) via a Conflo IV gas control unit (Thermo Scientific, Germany). Samples were combusted in a reactor containing either chromium (III) oxide (at 980°C) or copper oxide (at 875°C), after which the resulting sample gas (N_2 and CO_2) was passed through a reduction reactor (column of copper filings at 650°C) and then through a drying filter containing magnesium perchlorate. The gases were separated by a chromatographic column before entering the IRMS. At UC Davis, samples were analyzed using an Elementar Vario EL Cuben elemental analyzer (Elementar Analysensysteme GmbH, Germany) interfaced with a PDZ Europa 20-20 IRMS (Sercon Ltd., UK). The samples were combusted in a reactor containing copper oxide and tungsten (VI) oxide (at 1080°C). The resultant oxides were reduced by passing the sample gas through a reduction reactor followed by a drying trap containing magnesium perchlorate. Before entering the IRMS, N_2 and CO_2 were separated using a molecular sieve adsorption trap.

Laboratory working standards, calibrated against National Institute of Standards and Technology (NIST) and International Atomic Energy Agency (IAEA) Standard Reference Materials, that are compositionally-similar to the PON samples were analyzed repeatedly with each batch of samples for post-analysis data correction (including Bovine Liver, $\delta^{15}N$ = 7.72‰ and Glutamic Acid, $\delta^{15}N$ = -6.80‰). PON $\delta^{15}N$ is expressed relative to the international standard, N_2 in air, with a standard deviation of 0.3‰.

The PON concentration ([PON]) was calculated from the measured amount of N (µg), accurate to 0.01 µg, as follows:

[PON] (µM) = N amount detected (µg) / (Molar mass (µg/µmol) x volume (L) (3.2)

3.4 Fluorescence-activated cell sorting (FACS) and oxidization of phytoplankton samples

All flow cytometric sorting was conducted in the Flow Cytometry and Sorting Core Facility of the Department of Immunology and Infectious Diseases at the University of Cape Town under the guidance of facility manager, Rodney Dreyer.

3.4.1 Sample preparation for flow cytometric sorting and analysis

The cryovials containing the FACS sample filters remained in the dark and frozen until just before analysis with the flow cytometer (FCM). Samples were then thawed at room temperature, gently agitated

(to facilitate the removal of as many fixed cells from the PC filters as possible) and pre-filtered through a 40 μm mesh sieve to remove (rare) large particles or chains that could potentially block the FCM sorting tip. The 'used' filters were returned to the -80°C freezer for later analysis of Chl-*a*, an indicator of the quantity of phytoplankton cells remaining on the filter (see section 3.4.6 below). This was found to be negligible.

3.4.2 Sort conditions

The resuspended samples were sorted using a Becton Dickinson FACS Aria FCM (Becton Dickinson Biosciences Inc., USA). The FCM has a three-laser system consisting of a blue laser (488 nm), a red laser (633 nm), and a violet laser (405 nm), although for this study, only the blue laser was used. The FCM was fitted with a 70 μm nozzle with 70 psi pressure (equal to that of the sheath pressure) that was used to allow for optimum speed while maintaining a droplet formation frequency of 90 KHz. Event rates were maintained between 700 and 900 s^{-1}. Sheath fluid was made frequently in 20 L batches and comprised 160 g NaCl, 4 g KCl, 28.8 g Na_2HPO_4–$2H_2O$, 4.8 g KH_2PO_4, which resulted in a solution with a pH of 7.4 and salinity of 9‰. Before each sample run, the FCM was calibrated and standardized using tracking beads that are referenced to a more intensive baseline calibration every two months.

The cell populations were identified and gated in forward scatter (FSC) vs. side scatter (SSC) space on a log-amplified cytogram (FCM "dot plot") in acquisition mode. FSC is classified as scatter at 180° and SSC as scatter at 90° to the laser beam. The autofluorescence of the cells, used to aid in population identification, was measured using the 575 nm channel (the approximate wavelength at which PE fluoresces orange when excited by blue light) and 667 nm channel (the approximate wavelength at which Chl-*a* fluoresces red when excited by blue light). Cytograms showing the fluorescent channels were used to enumerate various populations and sub-populations through the combination of autofluorescent markers and cell density (cells L^{-1}). In addition, beads with a known size range of 1.8 – 6.4 μm were used to assist with relative size classification (Figure 3.5). The following populations were gated for and sorted into individual falcon tubes: *Synechococcus* (SYN), picoeukaryotes (PEUKS), nanoeukaryotes (NEUKS), and cryptophytes (CRYPTO) (Figure 3.4). All non-fluorescing cells were classified as 'sample debris' and were thus not sorted. A 200 (relative) log scale threshold was placed on the FCM assay FSC channel in order to remove the bulk of this 'noise', as well as laser noise.

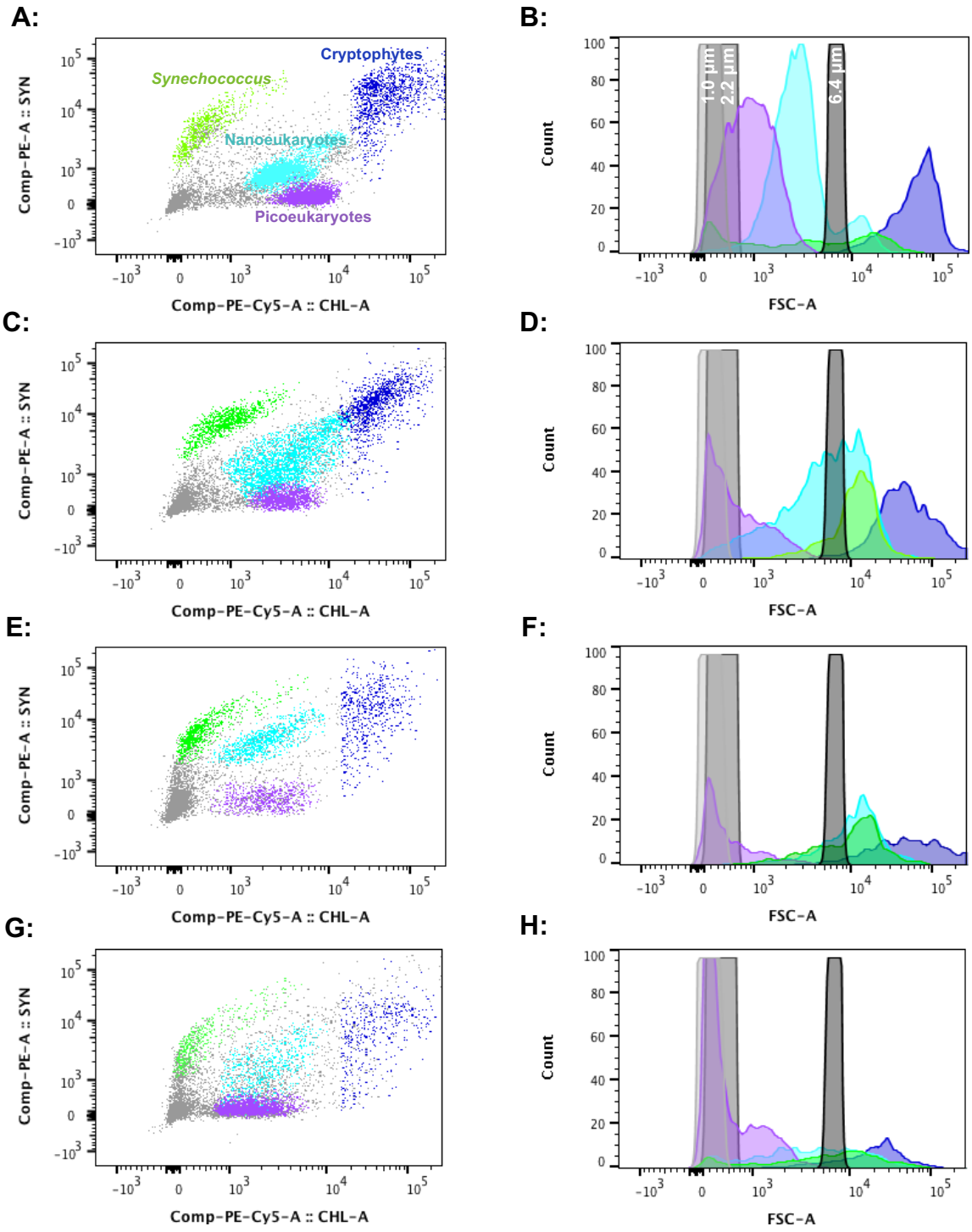

Figure 3.4: Example flow cytometry cytograms (y-axis is orange fluorescence; i.e., phycoerythrin (PE) and x-axis is red fluorescence, i.e., chlorophyll-*a* (Chl-*a*)) showing the populations that were sorted from the four sectors of the Indian Subantarctic Ocean – A: *Island Sector*, C: *PF Sector*, E: *OO PFZ Sector*, and G: *OO SAZ Sector*. The cytograms are accompanied by histograms indicating the relative cell sizes of the populations of interest compared to calibration beads of 1.0 µm, 2.0 µm, and 6.4 µm diameter – B: *Island Sector*, D: *PF Sector*, F: *OO PFZ Sector*, H: *OO SAZ Sector*. The sorted populations are distinguished as follows: *Synechococcus* (SYN) in green, Picoeukaryotes (PEUKS) in purple, Nanoeukaryotes (NEUKS) in light blue, and Cryptophytes (CRYPTO) in dark blue. The 'debris' (grey) was not sorted, and likely includes organic detrital material in addition to laser noise. While absolute cell size cannot be accurately determined from the forward scatter area (FSC-A), relative sizes can be estimated with the help of beads (see Figure 3.5) and reference to the literature (see Table 3.2).

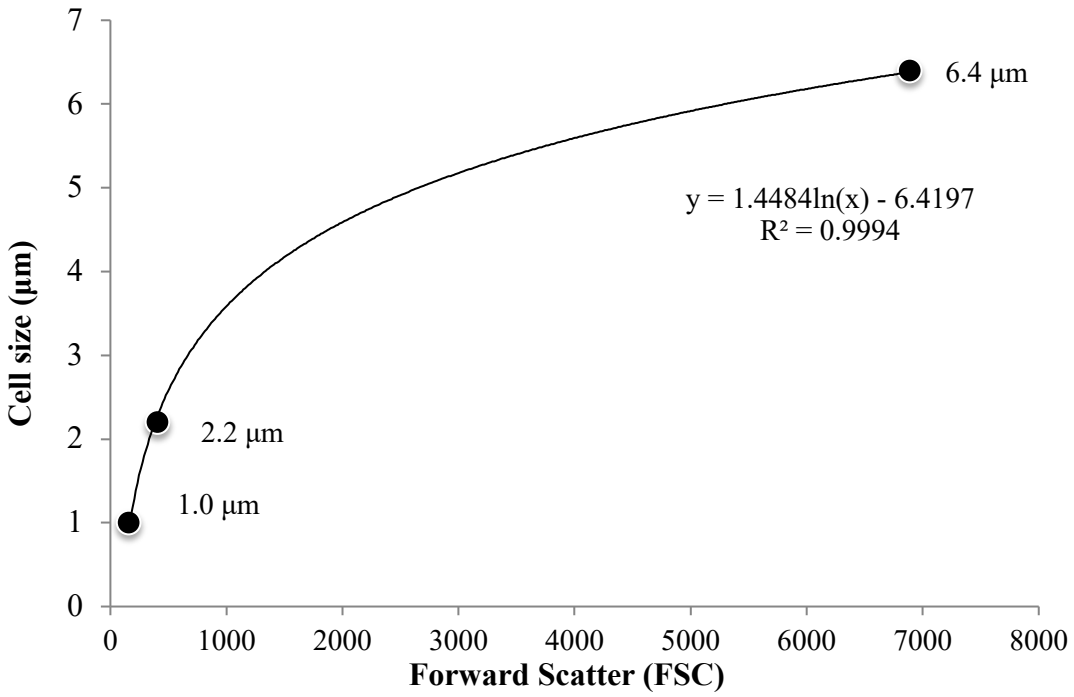

Figure 3.5: Cell size curve determined using tracking beads of known diameter (1.0 µm, 2.2 µm, and 6.4 µm) plotted against their forward scatter.

Each of the four phytoplankton populations that were gated have distinct sizes and autofluorescence characteristics (Table 3.2, Figure 3.4) as per Marie et al. (1999 & 2005), Fawcett et al. (2011) (following Casey et al. 2009), and Paulsen et al. (2015). CRYPTO exhibit high PE and Chl-*a* fluorescence in comparison to the other sorted populations and tend to be the largest group with respect to size, with an average diameter of ~9 µm (Tarran et al., 2006; Paulsen et al., 2015). PEUKS and NEUKS exhibit low PE fluorescence, intermediate Chl-*a* fluorescence in comparison to the other populations and were identified from their cell size implied by SSC, where PEUKS are ~2 µm in size (Tarran et al., 2006; Fawcett et al., 2011; Buitenhuis et al., 2012; Paulsen et al., 2015) and NEUKS are ~5 µm (Tarran et al., 2006; Buitenhuis et al., 2012; Paulsen et al., 2015). *Synechococcus* (SYN) exhibit high PE fluorescence, relatively low Chl-*a* fluorescence (Wood et al., 1998; Glibert et al., 1986; Veldhuis et al., 2005; Fourquez et al., 2020), and have a diameter of ~1.3 µm (Partensky et al., 1999a & b; Waterbury et al., 1986; Johnson et al., 2006; Buitenhuis et al., 2012; Paulsen et al., 2015; Sohm et al., 2016). When the SYN populations identified from a PE vs. Chl-*a* cytogram are plotted as event count vs. FSC-A (forward scatter using cell area) (e.g., Figure 3.4B), the FSC-A implies an unrealistically-large mean size for SYN of 6.8 µm. This appears to be an artefact of the high ratio of photosystem I to photosystem II in SYN compared to eukaryotes (Sunda & Huntsman et al., 2015), which increases the electron chain activity,

thereby lowering the excitation and increasing the emission spectrum of the SYN population (Kaprelyants & Kell, 1993).

Table 3.2: Average cell diameter, cell volume, and carbon conversion factors (CCF; the expected amount of cellular C per μm^3 of cell biovolume) for each of the sorted populations: cryptophytes (CRYPTO), nanoeukaryotes (NEUKS), picoeukaryotes (PEUKS) and *Synechococcus* (SYN). The average cell diameter for CRYPTO, NEUKS and PEUKS was determined from their population-specific FSC-A using Figure 3.5 and further augmented and confirmed using literature values (see references in Table). SYN average cell diameter was estimated solely from literature values given the large spread in FSC-A that suggests unrealistically large cell sizes (see text for details). Cell volume was computed assuming that all the cells are spherical. All CCFs are taken from the literature.

Population	Tracking beads approx. cell diameter (µm)	Average cell diameter (µm)	Reference	Cell volume (μm^3) [1]	CCF (fg C μm^{-3})	Reference
CRYPTO	9.5	9.0	Tarran et al. (2006); Paulsen et al. (2015), this study	343.5	220	Mullin et al. (1966), Booth (1988), Paulsen et al. (2015)
NEUKS	7.4	5.0	Tarran et al. (2006); Buitenhuis et al. (2012); Paulsen et al. (2015); this study	58.9	220	Mullin et al. (1966), Booth (1988), Paulsen et al. (2015)
PEUKS	1.7	2.0	Tarran et al. (2006); Buitenhuis et al. (2012); Paulsen et al. (2015); this study	3.7	220	Mullin et al. (1966), Booth (1988), Paulsen et al. (2015)
SYN	6.8[2]	1.3	Buitenhuis et al. (2012); Sohm et al. (2015); Paulsen et al. (2015)	1.0	250	Kana & Glibert (1987), Paulsen et al. (2015)

[1] Cell volume is determined assuming a spherical shape for all cells. In order to account for irregularly-shaped cells and minimize overestimations, only 90% of the total cell volume is used to calculate cellular carbon.

[2] Approximate SYN size estimated using calibration beads is hindered by the apparent lower excitation and increased emission spectrum associated with this population compared to the eukaryotes (see 3.4.2 for details; Figure 3.4B, D, F, H)

Post-sorting purity analysis was undertaken for all populations, and average purity was as follows: CRYPTO = 97.5%, NEUKS = 97.8%, PEUKS = 99.3%, and SYN = 94.9%. Although the purity for all populations was high, cell counts were nonetheless corrected for the difference of the measured purity from 100% during post-acquisition data analysis (i.e., corrected population cell count = cell count x (0.01) x purity (%)). Sort data were analyzed using BD FacsDiva Software V6.1.3, and FlowJo™ was used for data visualization and size-curve generation.

3.4.3 Determining the contribution of diatoms to the pico- and nanoeukaryote populations using scanning electron microscopy (SEM)

To quantify the diatom contribution to the smaller size classes (i.e., to the pico- and nanoeukaryotes;

diatoms cannot be separated from these broad groups via FACS), various microscopy techniques were used. A number of the sorted FACS samples representative of the various sectors across the transect were sub-sampled and analyzed under a light microscope (LM) in the department of Molecular and Cell Biology at the University of Cape Town. However, the available magnification was insufficient, so the samples were prepared for SEM analysis at the Centre for Imaging and Analysis, Chemical Engineering, University of Cape Town. Subsamples of the sorted phytoplankton groups were dehydrated in an ethanol/water dilution series of 30%, 50%, 70%, 90%, 95% and 100%. To do this, each sample was placed in an Eppendorf microcentrifuge tube with 1 mL of a 30:70 alcohol:Milli-Q water mixture and left to stand for 10 minutes, after which it was centrifuged and the 1 mL of liquid was removed. This process was repeated until the alcohol constituted 100% of the liquid addition. Because of the small volumes of sorted cells, the resultant sample-in-alcohol solution was pipetted directly onto the membrane filter (0.2 μm) mounted on an aluminum stub with carbon glue. A drop of hexamethyldisilazane (HMDS) was then added to the sample as a drying agent. Once dry, the stubs were sputter coated with a gold palladium alloy and placed under the SEM.

Although soft-bodied phytoplankton groups were not the focus of the SEM investigations, it is important to note that they do not preserve well using the dehydration method outlined above; as such, no soft-bodied taxa were identified. In addition, very few small diatoms were evident in the sorted samples viewed using SEM, implying a dominance of soft-bodied species in the pico- and nano-size classes.

3.4.4 Conversion of organic N to nitrate via persulfate oxidation

Under a gentle vacuum, the sorted populations of SYN, PEUKS, NEUKS, and CRYPTO were filtered onto pre-combusted 25 mm 0.3 μm GF-75 filters. The day before filtration, all glassware was acid washed (in 10% by volume HCl) and combusted (500°C for 5 hours) to minimize contamination. During filtration, the sample FACS tubes and glassware were rinsed three times with 9‰ purified saline solution (same salinity as that of sheath fluid used during flow-sorting) and then three times with ultra-high-purity Milli-Q water to ensure that no cells remained in the Falcon tubes or on the filtration glassware. After all the water in a sample passed through the filter, the vacuum was immediately removed to avoid cells being pulled through the filter. The GF-75 filter was then transferred using ethanol-cleaned forceps into an ethanol-cleaned, dry petri-dish and dried in a clean desiccating oven at 28°C for 4 hours or until the filter was dry. Once dry, the filter was trimmed to remove the unused outer portion and placed in a newly-combusted 4 mL Wheaton vial that was immediately sealed with an ethanol-cleaned teflon-lined cap. The MICRO phytoplankton samples (see section 3.1.4 above) were filtered onto GF-75s in a similar

manner. Forceps were used to hold the 20 µm-mesh filter so that it could be washed repeatedly with 9‰ purified saline solution to ensure that as much organic material as possible was transferred to the GF-75 filter. As for the FACS samples, the "used" mesh was then stored in the dark at -80°C for later analysis of Chl-*a* (see section 3.4.6 below); this was found to be negligible.

The organic N on the GF-75s was oxidized to NO_3^- using a potassium persulfate oxidizing reagent (POR) as per the method of Knapp et al. (2005), adapted for particle samples by Fawcett et al. (2011 & 2014) and Van Oostende et al (2017). This method involves recrystallizing potassium persulfate four times to reduce the N contaminants in the salt (Knapp et al., 2005). The final recrystallization was followed by a methanol (MS SupraSolv® for gas chromatography) rinse, which has been shown to remove remaining N contaminants and increase the rate of crystal drying (Higgins et al., 2009). To make the POR, 2.5 g of the purified persulfate crystals and 2.5 g of low-N NaOH were dissolved in 100 mL of ultra-high purity Milli-Q water (produced via a system equipped with a UV lamp and additional purification cartridges to remove all organic compounds; total organic carbon is always <10 ppb). As soon as the potassium persulfate and NaOH had completely dissolved, 1.5 mL of the POR was added in a clean fume hood to each FACS sample and the Wheaton vial was capped immediately. The vials were subsequently autoclaved at 121°C for 55 minutes on a slow-vent setting. In addition, the following blanks and standards were included in each POR batch run: three POR blanks (so that the N blank associated with the POR could be quantified), five POR + GF/F blanks (so that the N blank associated with the POR + GF-75 could be quantified; this was always <10% of the sample), five USGS41a standards ($\delta^{15}N$ = 47.57 ± 0.11 ‰ vs. N_2 in air; Qi et al. (2003)), five USGS40 standards ($\delta^{15}N$ = -4.52 ±0.06 ‰ vs. N_2 in air; Qi et al. (2003)) and five USGS40 standards + blank combusted GF-75s. Standard concentrations were 10, 20, 30, 40, and 50 µM. The MICRO size class samples were treated in the same manner as the FACS samples; however, due to the higher organic N content of these samples, 3 mL of POR were added to ensure complete oxidation of the biomass N. For the POR analyses that included the MICRO size class samples, a further five POR blanks and POR + GF-75 blanks consisting of 3 mL of POR were included.

After oxidation in the autoclave, the samples and standards containing GF-75s were centrifuged (in the Wheaton vials) at 8000 rpm for 10 minutes in order to separate the disintegrated filter from the aqueous sample. Using a Milli-Q-rinsed pipette tip, the supernatant was then transferred into a new, combusted 4 mL Wheaton vial. 12N ACS grade HCl was added to all standard and sample vials to lower the pH to a range favourable to the denitrifying bacteria (6-8; section 3.5); the pH of every sample and standard was checked using Macherey-Nagel pH paper (range of 0 to 14).

3.4.5 Analysis of the nitrate concentrations of oxidized phytoplankton groups

The resulting NO_3^- concentration of each oxidized sample, standard, and blank was measured in the Knapp Lab at Florida State University; this information is required for the denitrifier method described below (section 3.5). Sample NO_3^- was measured chemiluminescently (Garside, 1982; Braman & Hendrix, 1989) using a Thermo 42i NO_x analyzer. Using a Hamilton gas tight syringe, 100 µL of sample was injected into a 90°C acidic vanadium (V(III)) solution that reduced NO_3^-+NO_2^- quantitatively to nitric oxide gas ($NO_{(g)}$). The $NO_{(g)}$ then reacts with ozone inside the analyzer to produce light, the intensity of which is quantitatively related to the amount of $NO_{(g)}$ in the sample and thus the original NO_3^-+NO_2^- concentration. The range of detection of the instrument was adjusted according to the expected concentrations of the samples. Sample [NO_3^-] was calibrated using a standard curve that bracketed the range of samples.

3.4.6 Quantifying the phytoplankton material remaining on the filters through Chl-*a* analysis

The preserved PC filters from the FACS analysis as well as the 20 µm mesh from the MICRO size class samples were unfolded using ethanol-cleaned forceps and placed into borosilicate test tubes. 8 mL of 90% acetone was aliquoted into each of the test tubes, after which they were covered with foil and extracted in the dark at -20°C for 24 hours. Samples were then allowed to come to room temperature (still in the dark) and fluorescence was read using a Trilogy Fluorometer equipped with the non-acidified Chl-*a* module (Welschmeyer, 1994) at an excitation of 485 nm and emission of 685/10 nm, with a minimum detection limit of 0.025 µg/L. A recently-derived calibration curve was used to convert fluorescence to Chl-*a* concentration; in all cases, Chl-*a* was negligible, indicating that removal of cells from the filters was (near) complete.

3.5 Analysis of nitrogen (N) isotopes: $\delta^{15}N_{NO3}$, $\delta^{15}N_{FACS}$, and $\delta^{15}N_{MICRO}$

The central aims of this project – to quantify the contribution of different phytoplankton groups to organic C export potential and to understand how different N sources shape the microbial community – require knowledge of the $\delta^{15}N$ of ambient NO_3^- in seawater ($\delta^{15}N_{NO3}$), as well as the $\delta^{15}N$ of the various sorted phytoplankton groups ($\delta^{15}N_{FACS}$) and the MICRO size class ($\delta^{15}N_{MICRO}$) collected from the ship's underway system and the CTD casts. These measurements were made via isotope ratio mass spectrometry (IRMS) in the Knapp Laboratory at Florida State University using the "denitrifier method" (Sigman et al., 2001; Casciotti et al., 2002; McIlvin & Casciotti, 2011).

3.5.1 Denitrifier method rationale

The denitrifier method uses a naturally occurring denitrifying bacterial strain that lacks an active nitrous oxide (N_2O) reductase enzyme. These bacteria quantitatively convert NO_3^-+NO_2^- to $N_2O_{(g)}$ by the following denitrification pathway:

$$2NO_3^-{}_{(aq)} \rightarrow 2NO_2^-{}_{(aq)} \rightarrow 2NO_{(g)} \rightarrow N_2O_{(g)} \quad (3.3)$$

Provided that this reaction (3.3) proceeds to completion (i.e., that the NO_3^-+NO_2^- is fully reduced to $N_2O_{(g)}$), the N isotope ratio of the $N_2O_{(g)}$ will be the same as the starting NO_3^-+NO_2^- (and thus, in the case of the phytoplankton samples, of the organic N). In other words, the $\delta^{15}N_{product}$ will be equal to the initial $\delta^{15}N_{reactant}$ (Mariotti et al., 1981; Barford et al., 1999; Sigman et al., 2001).

3.5.2 Growth of denitrifying bacteria in liquid medium

The Casciotti et al. (2002) method was followed closely, using *Pseudomonas aureofaciens* cultures. The bacteria were grown in a growth media containing the following: tryptic soy broth (TSB), potassium nitrate (KNO_3), ammonium chloride (NH_4Cl), and dipotassium phosphate (K_2HPO_4). 500 mL crimp-sealed serum bottles of media were autoclaved for 50 minutes prior to inoculation. The media was then inoculated with a single colony of the bacterial strain and the bottles were placed on an orbital shaker set to a low speed at constant room temperature for 4-7 days, which allows sufficient time for the NO_3^- in the media to be completely consumed (Sigman et al., 2001). Prior to harvesting the bacteria, the media was tested to confirm complete removal of NO_3^-, a necessary condition to proceed with sample analysis.

3.5.3 Bacterial harvest and sample/standard addition

To harvest the bacteria, the media was divided equally into 2 x 500 mL centrifuge bottles and centrifuged at 4000 rpm for 30 minutes at 20°C. After centrifugation, the supernatant (spent medium) was carefully decanted to waste, leaving a pellet of bacteria at the bottom of the bottles. The bacteria were then resuspended in 250 mL of new, NO_3^--free media (McIlvin & Casciotti, 2011). This new media was first added to one of the centrifuge bottles that was swirled to resuspend the bacterial pellet, and then transferred to the second centrifuge bottle where the process was repeated. To the media containing resuspended bacteria from both centrifuge bottles (i.e., the bacterial concentrate), several drops of Antifoam-B emulsion were added, and the solution was gently homogenized; this emulsion prevents the bacterial concentrate from foaming during degassing. 2.9 mL of bacterial concentrate were pipetted into 28 combusted borosilicate 20 mL headspace vials. Each of the vials, along with an extra empty 'flush'

vial (to which no bacterial concentrate was added), were crimp-sealed with a grey butyl septum and an aluminum top seal. A venting needle (1.5 inch, 25-gauge) was inserted into each vial and the vials were then placed upside down on a purge rack equipped with 3/8 inch, 26-gauge needles (McIlvin & Casciotti, 2011). These shorter needles bubble the medium with 3-4 psi of helium ($He_{(g)}$) or nitrogen ($N_{2(g)}$) gas for 3 hours while the longer needles allow any N_2O and O_2 to be flushed out of the vial headspace, thereby removing contaminants and ensuring the anoxic atmosphere ultimately required for the denitrification reaction (Sigman et al., 2001; Casciotti et al., 2002; McIlvin & Casciotti, 2011).

Once the vials were degassed and removed from the purging rack, samples were injected into them using a Milli-Q rinsed, Hamilton gas-tight syringe fitted with a 25-gauge needle. The volume of sample or standard added was varied in order to achieve a constant quantity of N in each vial, most commonly 20 nmoles. This 20 nmole threshold was achieved for $\delta^{15}N_{NO3}$ samples, the higher-concentration $\delta^{15}N_{FACS}$ samples, and the $\delta^{15}N_{MICRO}$ samples (indeed, most of the MICRO samples had to be 10-fold diluted with Milli-Q because of their very high N concentrations). The sorted-phytoplankton sample concentrations varied significantly, so the samples were grouped into analyses of similar N content (of 20, 10, 5, and 2.5 nmoles of N). This was done to maximize the amount of sample added to the bacterial vials (with the 1.5 mL volume per FACS sample being the limiting factor) while still allowing, for the most part, duplicate measurements of each sample. Furthermore, grouping the samples thus reduces the error introduced by any non-linear behavior of the IRMS under low N concentrations. In addition to the $\delta^{15}N_{NO3}$, $\delta^{15}N_{FACS}$ and $\delta^{15}N_{MICRO}$ samples, the oxidized organic N standards (USGS40 and 41a) were included in the IRMS analyses. International reference materials, IAEA-NO_3 (potassium nitrate with a $\delta^{15}N$ = 4.7±0.2‰ vs. N_2 in air; Gonfiantini, 1984; Hut, 1987; Böhlke et al., 1995) and USGS34 (potassium nitrate with a $\delta^{15}N$ = -1.8±0.2‰ vs. N_2 in air; Böhlke et al., 2003) were included after every 10 samples in each batch run to facilitate post-IRMS analysis calibration and the correction of any instrument drift. The 20 mL-headspace vials were inverted several times after sample addition, then incubated in the dark overnight at room temperature to allow denitrification to completely convert NO_3^- to $N_2O_{(g)}$. The reaction was terminated 12 – 18 hours after sample addition by the introduction of 0.1 mL of 6M NaOH, which both lyses the bacteria and scavenges $CO_{2\,(g)}$ from the headspace (Sigman et al., 2001). The 'flush' vial remained untreated following degassing. In addition, a 'blank' vial containing degassed bacterial concentrate, but no sample/standard was analysed with each batch run so that the N_2O blank of the bacterial method (i.e., the N_2O that did not derive from the added sample/standard) could be quantified.

3.5.4 IRMS Analysis

Once the denitrification reaction was terminated, the samples were analyzed on a continuous flow ThermoFisher Delta V Advantage IRMS interfaced with a GasbenchII and controlled by the program Isodat (Casciotti et al., 2002; McIlvin & Casciotti, 2011). Sample $N_2O_{(g)}$ is extracted from each headspace vial by the autosampler needle and incorporated into a high-purity helium carrier-gas stream that is passed through a series of 'traps' to remove impurities including water, volatile organic compounds, and CO_2. Following this, the gas is cryogenically concentrated and focused, then chromatographically separated and transferred to the IRMS (Casciotti et al., 2002; McIlvin & Casciotti, 2011). The IRMS measures the ratios of $^{45}N_2O_{(g)}/^{44}N_2O_{(g)}$ under continuous flow relative to a reference $N_2O_{(g)}$ tank. Isodat, therefore, reports $\delta^{15}N$ values relative to the reference gas (N_2O_ref) as:

$$\delta^{15}N\ (‰\ vs.\ N_2O\_ref) = (({}^{15}R_{sample}/{}^{15}R_{N2O\_ref}) - 1) \times 1000 \quad (3.4)$$

The $\delta^{15}N$ values yielded by equation 3.4 are corrected using IAEA-NO_3 and USGS34 to values relative to N_2 in air according to:

$$\delta^{15}N_{sampleCORR}\ (‰\ vs.\ N_2\ in\ air) = (\delta^{15}N_{sample})(X) + C \quad (3.5)$$

Where X is the slope of the relationship between the measured $\delta^{15}N_{standard}$ and the true $\delta^{15}N_{standard}$ value, and C is the intercept.

The isotope measurements were also corrected for the bacterial blank, which was on average 0.4 nmol across all runs. Relative to the sample N content, the blank contribution was insignificant for the higher N content analyses, at <2% for the 10 and 20 nmole runs. The blank contribution increased for the lower N content analyses, to 8% for the 5 nmole runs and 12% for the 2.5 nmole runs. Despite the increase in bacterial blank contribution with decreasing sample size, its influence on the isotopic composition of the samples was assumed to be negligible since its $\delta^{15}N$ was always close to 0‰, and thus similar to the isotopic composition of the samples, minimizing its impact.

The average standard deviations for repeated measurements in the same run (n = 3) of IAEA-NO_3 and USGS34 were low, 0.3‰ and 0.2‰, respectively. Analyses where both IAEA-NO_3 and USGS34 standard deviations were >0.35‰ and/or the blanks contributed >5% (for the higher-concentration analyses) or >15% (for the lower-concentration analyses) of the total N measured were considered "bad" and all samples were re-analyzed. The target standard deviation for duplicate samples measured in

different batch runs was <0.35‰. If the standard deviation was greater than this and sample volume allowed, samples were measured a third time and the new standard deviation calculated from all three measurements. For example, the available sample volume for the >20 µm size class was large and the sample N content was high, allowing for triplicate measurements, which yielded a pooled standard deviation for all samples of ~0.1‰.

3.6 Microphytoplankton microscopy counts

Phytoplankton counts were conducted by Dr. Thomas Bornman at the Nelson Mandela University. The fixed microscopy samples preserved in 5 mL cryovials were sonicated to agitate the cells from the 20 µm-mesh filters. A subsample of the well-mixed content was then enumerated using a Zeiss IM 35 inverted microscope at 630x magnification. For species composition and abundance, a minimum of 300 cells per slide or station was counted.

In the case where a LM or an SEM was used for sample analysis, a second subsample was pipetted into a 1.5 mL Eppendorf microcentrifuge tube. To remove the salt, the samples were rinsed with Milli-Q water at least five times, with each rinse lasting 12-hours, following which the samples were centrifuged and the supernatant removed. In preparation for the microscope slides, the isolated plankton material was treated with 10% HCl to remove calcium carbonate particles and 37% H_2O_2 to remove any organic coating around the siliceous frustules. The SEM analyses were conducted at the High-Resolution Transmission Electron Microscopy unit of the Nelson Mandela University. A few drops of cleaned material were transferred onto Whatman Nucleopore PC track-etched membranes that were dried and mounted onto aluminum stubs and coated with a gold/rhenium target for ~6 minutes. All taxa were identified to species level where possible using taxonomic keys provided in Hasle et al. (1996), Tomas and Haste (1997), Scott and Marchant (2005) and Cefarelli et al. (2010). Species names were verified using AlgaeBase (Guiry & Guiry, 2018). Example images from the SEM analyses are shown in Figure 3.6.

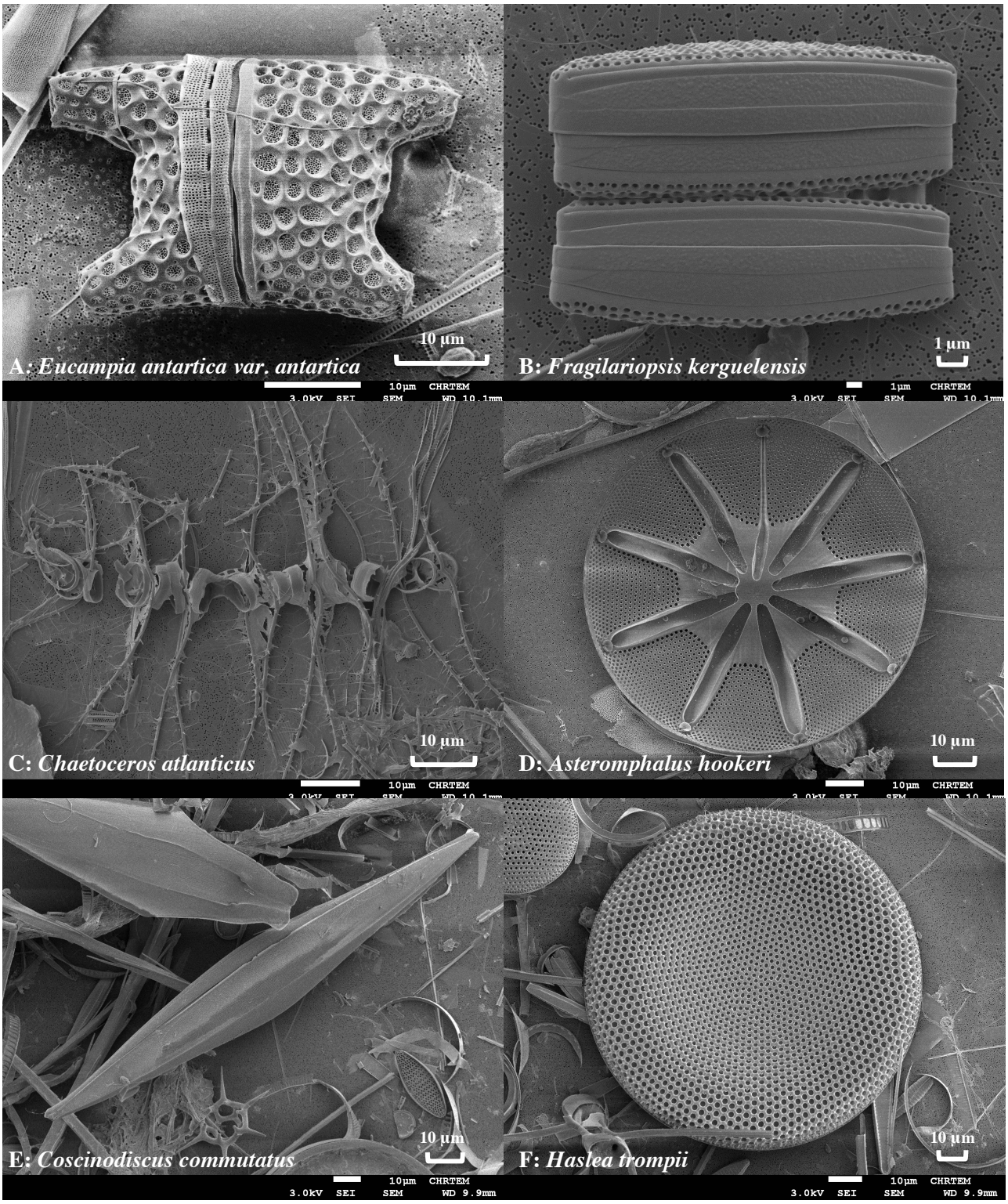

Figure 3.6: Select Scanning Electron Microscope (SEM) images of cells collected on the >20 µm filters. A: *Eucampia antarctica var. antartica,* a centric chain-forming diatom, B: *Fragilariopsis kerguelensis,* a pennate chain-forming diatom, C: *Chaetoceros atlanticus,* a centric chain-forming diatom D: *Asteromphalus hookeri,* a centric diatom, E: *Coscinodiscus commutatus,* a centric diatom F: *Haslea trompii,* a pennate diatom. Images courtesy of Dr. Thomas Bornman, Nelson Mandela University.

3.7 Derived variables:

3.7.1 Si*

Si* (μM) is an integrative tracer of water mass evolution, as well as an indicator of the nutrient status of diatoms (Sarmiento et al., 2004). In this study, Si* is used to help define the various sectors of the Indian Subantarctic crossed during the cruise. This variable is calculated as:

$$Si^* = [Si(OH)_4] - [NO_3^-] \quad (3.6)$$

The upper Subantarctic is characterized by a negative Si* concentration as a result of the preferential uptake of Si relative to NO_3^- by Fe-limited diatoms (Franck et al., 2000; Sarmiento et al., 2004). Under Fe-replete conditions, diatoms consume Si and NO_3^- in a ratio of ~1:1 (e.g., Hutchins & Bruland, 1998; Ragueneau et al., 2000; Brzezinski et al., 2002), but once Fe becomes limiting, they tend to synthesize heavily-silicified shells, taking up Si and NO_3^- in a ratio >2:1 (e.g., Franck et al., 2000; de Baar et al., 2005; Poulton et al., 2007; Holmes et al., 2019). The net effect of this is that the surface nutrient pool becomes progressively depleted in Si relative to NO_3^- towards the equator, driving Si* to negative values (-15 to -5 μM) by the SAZ (Sarmiento et al., 2004; Henley et al. 2020). At the PF, strong upwelling of nutrients, including ~0.05 nM d^{-1} of dFe (de Baar et al., 1995), partially alleviates Fe stress and stabilizes the Si:N uptake ratio in diatoms. As a result, Si* in this region is ~5 μM (de Baar et al., 1995).

3.7.2 Fe*

Fe* (μM) is used as an indicator of Fe limitation based on assumed phytoplankton uptake ratios of Fe and nutrients (Parekh et al., 2005; Holmes et al., 2019). For the purposes of this study, the Fe* tracer is calculated using ambient NO_3^- concentrations (Parekh et al., 2005; Bowie et al., 2009; Rijkenberg et al., 2014; Holmes et al., 2019) assuming an Fe/N uptake ratio of 0.039 (Anderson & Sarmiento, 1994; Parekh et al., 2005; Holmes et al., 2019).

$$Fe^*(N) = [DFe] - ((Fe/N \text{ uptake ratio} \times [NO_3^-]) \quad (3.7)$$

Here, [DFe] is the dissolved Fe concentration measured for samples collected at the same time as the NO_3^- and phytoplankton samples during the ACE cruise (Janssen et al. 2020), and $[NO_3^-]$ is the measured nitrate concentration. Positive Fe* values indicate that the Fe supply is sufficient to theoretically drive NO_3^- concentrations to depletion while a negative Fe* indicates that the Fe supply is insufficient, implying Fe limitation (Holmes et al., 2019).

3.7.3 New and recycled N isotopic end members

As per the new production paradigm (Dugdale & Goering, 1967), phytoplankton utilization of new N (predominantly NO_3^- upwelled from depth) is quantitatively related to carbon export potential. Moreover, the isotopic composition of new N is expected to be different from that of regenerated N (predominantly NH_4^+ recycled in surface waters, with occasional contributions of regenerated NO_2^- and NO_3^- from ML nitrification) (Checkley & Miller, 1989; Pennock et al., 1996; Montoya et al., 2002; DiFiore et al., 2009; Fawcett et al., 2011). Predominant assimilation of new N yields phytoplankton biomass that is relatively high in $\delta^{15}N$ and regenerated N utilization yields a relatively low-$\delta^{15}N$ biomass (Rau et al., 1990; Fawcett et al., 2011; Treibergs et al., 2014).

While it is unclear whether N biomass in surface waters is better characterized as the instantaneous or accumulated product of N assimilation, in this study, the sorted phytoplankton populations are taken to represent the instantaneous product due to their short lifetime in the ML (Fawcett et al., 2011). Bulk PON, by contrast, is a combination of diverse living autotrophs and heterotrophs, as well as detritus (Rau et al., 1990; Fawcett et al., 2011 & 2014), and is thus better described as the accumulated product of N assimilation (Van Oostende et al., 2017). It should be noted, however, that bulk PON can be altered by non-autotrophic processes, such as the excretion of NH_4^+ by heterotrophs, which would raise bulk PON $\delta^{15}N$ (Checkley & Miller, 1989; Altabet et al., 1991; Möbius, 2013; Smart et al., 2020) or the inclusion of heterotrophic bacteria, which have been shown to be low in $\delta^{15}N$ (Fawcett et al., 2011). Thus, efforts to attribute a degree of new N dependence to the bulk PON pool must be interpreted with caution.

The flow-sorted biomass $\delta^{15}N$ that is expected if phytoplankton assimilate only new N ($\delta^{15}N_{New\ N}$) can be calculated using the instantaneous product equation as:

$$\delta^{15}N_{New\ N}\ (‰\ vs.\ N_2\ in\ air) = Conc.W\ \delta^{15}N_{NO3} - {}^{15}\varepsilon \qquad (3.8)$$

Where concentration-weighted $\delta^{15}N_{NO3}$ (Conc.W $\delta^{15}N_{NO3}$) is the average $[NO_3^-]$-weighted $\delta^{15}N_{NO3}$ for each sector and $^{15}\varepsilon$ is the sector-specific NO_3^- assimilation isotope effect (Table 3.3). Both the ambient $[NO_3^-]$ and $\delta^{15}N_{NO3}$ are the measured surface values. $^{15}\varepsilon$ was calculated from the CTD profiles using a Rayleigh model linearization of the measured $\delta^{15}N_{NO3}$ and $[NO_3^-]$ from the source to surface waters in each sector. Estimates of $^{15}\varepsilon$ reported in the literature were also considered. For the *Island*, *PF* and *OO PFZ Sectors*, the $^{15}\varepsilon$ estimates of 4.6‰, 5.3‰, and 5.1‰, respectively, aligned well with literature values (Sigman et al., 1999; Fripiat et al., 2010; DiFiore et al., 2006 & 2010) and were used in all further calculations (Table 3.3). The $^{15}\varepsilon$ estimated for the *OO PFZ Sector* of 4.8‰ was calculated using CTD

casts and supplemented with literature values (Sigman et al., 1999; DiFiore et al., 2006) in order to best represent the large latitudinal variation (Figure 3.1) observed between the CTD casts and thus across the sector (Table 3.3).

The values of $^{15}\varepsilon$ estimated from the NO_3^- measurements were applied to all eukaryotic phytoplankton samples. For SYN, however, culture studies have shown that $^{15}\varepsilon$ is lower than for eukaryotic phytoplankton, averaging 3.9‰ (Granger et al., 2010). An $^{15}\varepsilon$ of 3.9‰ was thus applied to all SYN populations across the transect, regardless of sector (Table 3.3).

To calculate the expected $\delta^{15}N$ of bulk PON if all phytoplankton were to only assimilate new N ($\delta^{15}N_{New\ N\text{-}PON}$), the accumulated product equation is used:

$$\delta^{15}N_{New\ N\text{-}PON}\ (‰) = Conc.W\ \delta^{15}N_{NO3} + {}^{15}\varepsilon\ (\ln(f))\ x\ (f\ /\ 1\text{-}f) \quad (3.9)$$

where f is the fraction of the NO_3^- pool remaining in the ML following consumption relative to the NO_3^- initially supplied, defined as:

$$f = [NO_3^-]_{ML\_average} / [NO_3^-]_{source} \quad (3.10)$$

$[NO_3^-]_{ML\_average}$ is the expected average $[NO_3^-]$ of the ML at the time of sampling. This was calculated as the combined ML $[NO_3^-]$ average from the CTDs in each of the sectors. The $[NO_3^-]_{source}$ is the $[NO_3^-]$ of the underlying winter water layer. The $[NO_3^-]_{source}$ of the winter water was calculated using a combination of measured CTD $[NO_3^-]$ data as well as literature values since the source of the NO_3^- supply to the Southern Ocean surface remains uncertain (DiFiore et al., 2010, Smart et al., 2015) (Table 3.3).

If phytoplankton were to exclusively assimilate regenerated N, their $\delta^{15}N$ would be set directly by $\delta^{15}N_{Reg.\ N}$. There is no need to account for isotopic fractionation during regenerated N assimilation because the $^{15}\varepsilon$ of NH_4^+ uptake approaches zero at low $[NH_4^+]$ and NH_4^+ is always (near-)completely consumed in open ocean surface waters (Hoch et al., 1992; Pennock et al., 1996; Waser et al., 1998; Lourey et al., 2003; Liu et al., 2013). Thus, for phytoplankton assimilating only regenerated N:

$$^{15}N_{Reg.\ N}\ (‰) = \delta^{15}N_{NH4} \text{ and } \delta^{15}N_{Reg.\ N\text{-}PON}\ (‰) = \delta^{15}N_{Reg.\ N} \quad (3.11)$$

where $\delta^{15}N_{Reg.\ N}$ (‰) = -1 ± 1

$\delta^{15}N_{Reg.N}$ is generally always lower than $\delta^{15}N_{New\ N}$ due to the pathways associated with regenerated N (i.e., NH_4^+) production (Checkley & Miller, 1989; Pennock et al., 1996; Fawcett et al., 2011; Knapp et al., 2011). It is estimated here from the literature since $\delta^{15}N_{Reg.\ N}$ typically cannot be measured at the low regenerated N concentrations encountered in the open ocean.

3.7.4 New N dependence calculations

New N dependence is a measure of the more traditionally-named *f*-ratio (Eppley & Peterson, 1979), and is defined as the degree (0 – 1) of new N utilization relative to that of new + regenerated N utilization by the sorted phytoplankton groups and bulk PON, with the caveat that bulk PON can be altered by more than just autotrophic new- and regenerated N uptake (Checkley & Miller, 1989; Altabet et al., 1991; Fawcett et al., 2011; Möbius, 2013). The higher the degree of new N dependence, the higher the C export potential associated with a particular phytoplankton group (Dugdale & Goering, 1967). New N dependence is calculated by rearranging a simple isotope mixing model that assumes new N and regenerated N are the only two possible N sources to phytoplankton:

$$\text{New N dependence} = (\text{Conc. W } \delta^{15}N_{population} - \delta^{15}N_{Reg.\ N})/(\delta^{15}N_{New\ N} - \delta^{15}N_{Reg.\ N}) \quad (3.12)$$

Where Conc. W $\delta^{15}N_{population}$ is the biomass concentrated-weighted $\delta^{15}N$ of each sorted phytoplankton population.

3.7.5 Relative abundance and carbon contribution of sorted phytoplankton groups

Relative abundance (RA) and relative carbon contribution (RCC) were calculated from the purity-adjusted (PA) FACS data for the SYN, PEUKS, NEUKS, and CRYPTO populations and from the microscopy counts for the MICRO size class. RCC also uses cell volumes (calculated from cell diameter assuming spherical shapes, accounting for geometric irregularities by subtracting 10% of the calculated volume). Carbon conversion factor (CCF) values were taken from the literature (Table 3.2 and references within; Cornet Barthaux et al., 2007; Menden-Deuer & Lessard, 2000). Relative rather than absolute abundances and carbon contributions were calculated due to the conservative sorting conditions applied to the <20 µm size classes, which are necessary to yield robust (i.e., "pure") $\delta^{15}N_{population}$ data (Fawcett et al., 2011 & 2014; Treibergs et al., 2014) but will have excluded a lot of the phytoplankton cells. RA and RCC are thus calculated as the contribution by a particular sorted group relative to the sum of all

the sorted cells:

$RA_{population}$ (%) = (PA Population Count / Total Count) x 100 (3.13)

For example, where the PEUKS PA Population Count is 61 cells ml^{-1} and the Total Count = $\Sigma Count_{populations}$, where 'populations' refers to the individual phytoplankton populations identified by flow cytometry and the >20 μm size class (i.e., $Count_{SYN}$+ $Count_{PEUKS}$ + $Count_{NEUKS}$ + $Count_{CRYPTO}$ + $Count_{MICRO}$) is 129 cells ml^{-1}, the RA_{PEUKS} = (61 cells ml^{-1})/(129 cells ml^{-1}) x 100 = 47%.

$RCC_{population}$ (%) = ((Cell volume (0.9)) x CCF x PA Population Count) / Total C Contribution x 100 (3.14)

Where Total C Contribution is the amount of C contributed by all the phytoplankton groups together, i.e., Total C contribution = $\Sigma C_{populations}$. For example, assuming PEUKS have a diameter of 2.0 μm, yielding a volume of 3.7 μm^3 (when corrected for geometric irregularities, i.e., -10%), a CCF of 0.22 pg C μm^{-3} (Mullin et al., 1966; Booth, 1988; Paulsen et al., 2015), a PA population count of 61 ml^{-1}, and the total C contribution is 2934 pg C μm^{-1}; RCC_{PEUKS} = (3.7 μm^3)(0.22 pg C μm^{-3})(61 ml^{-1})/(2934 pg C μm^{-1}) = 0.2%.

3.7.6 Phytoplankton-specific *f*-ratio estimates

The *f*-ratio is defined as the fraction (0 – 1) of total primary productivity supported by new N and is an estimate of the fraction of organic C production that escapes recycling in the surface and sinks below the ML (Eppley & Peterson, 1979). A phytoplankton-specific *f*-ratio is defined here as:

phytoplankton-specific *f*-ratio = Σ(New N dependence x RCC (%))$_{population}$ (3.15)

For example, the phytoplankton-specific *f*-ratio in the *Island Sector* = SYN(0.88 x 0.00) + PEUKS(0.88 x 0.02) + NEUKS(0.95 x 0.31) + CRYPTO(0.69 x 0.43) + MICRO(0.72 x 0.25) = 0.80

3.7.7 Phytoplankton potential contribution to C export

Using the phytoplankton-specific *f*-ratio for each sorted population, the potential contribution of each group (SYN, PEUKS, NEUKS, CRYPTO and MICRO) to C export (*sensu* the new production paradigm; Dugdale & Goering, 1967) can be calculated:

Contribution to C export (%) = (New N dependence x RCC (%)) / phytoplankton-specific *f*-ratio (3.16)

For example, NEUKS potential contribution to C export in the *Island Sector* = (0.95 x 0.31%)/0.8 = 0.37%

3.8 Motivation for methods utilized

The methods used in this body of work are not only suitable for the questions asked but are also novel to this region. As previously discussed, bulk PON concentrations and isotopic ratios can be altered by microbial remineralization and heterotrophic scavenging. Coupling flow cytometric sorting of the autotrophic component from bulk (<20 μm) samples or microscopy of the larger size classes (>20 μm) with group-specific N isotopic analysis is currently the only way to constrain phytoplankton group-specific N substrate preference and potential contribution to C export. Although flow cytometric sorting is necessarily conservative to ensure 'pure' populations are separated, using a relative measure with regards to abundance and potential contribution to C export allows for qualitative and semi-quantitative understanding of phytoplankton dynamics within an area and across the Indian Sector of the Subantarctic.

Table 3.3: End-member values for each sector used to calculate the extent of dependence on new versus recycled nitrogen (N)

Variables	Units	Sectors				CTD Casts						
		Island	*PF*	*OO PFZ*	*OO SAZ*	1 *Island* (PEI)	2 *Island* (CR)	3 *Island* (KG)	4 *PF*	5 *OO PFZ*	6 *OO SAZ* (SAF)	7 *OO SAZ* (STF)
Conc. W $\delta^{15}N_{NO3}$ [1]	(‰)	6.9	6.9	7.3	8.4	7.3	6.8	6.8	6.9	7.2	6.5	6.5
$^{15}\varepsilon$ [2]	(‰)	4.6	5.3	5.1	5.0	4.6	4.6	4.6	5.3	5.1	5.0	5.0
$^{15}\varepsilon_{syn}$ [3]	(‰)	3.9	3.9	3.9	3.9	3.9	3.9	3.9	3.9	3.9	3.9	3.9
$[NO_3^-]_{ML\_average}$ [4]	[μM]	21.1	22.8	20.1	12.7	18.6	21.6	23.2	22.9	20.1	16.1	9.3
$[NO_3^-]_{source}$ [5]	[μM]	23.6	28.1	21.2	18.1	22.9	23.2	24.6	28.1	21.2	24.2	11.9
f [6]		0.9	0.8	0.9	0.7	0.8	0.9	0.9	0.8	0.9	0.7	0.8
$\delta^{15}N_{NN\text{-}Euk}$	(‰)	2.4	1.7	2.2	3.4	2.7	2.2	2.2	1.6	2.1	1.5	1.5
$\delta^{15}N_{NN\text{-}Syn}$	(‰)	3.0	3.0	3.4	4.5	3.4	2.9	2.9	3.0	3.3	2.6	2.6
$\delta^{15}N_{NN\text{-}PON}$	(‰)	2.1	1.1	2.1	2.5	2.4	1.9	2.0	1.1	2.0	0.9	0.9
$\delta^{15}N_{RN}$	(‰)	-1.0	-1.0	-1.0	-1.0	-1.0	-1.0	-1.0	-1.0	-1.0	-1.0	-1.0

[1] For the *Island* and *PF Sectors*, the concentration-weighted (Conc. W) $\delta^{15}N_{NO3}$ was calculated as the MLD average due to extreme turbidity and mixing in the region as a result of bathymetric and frontal effects. For the *OO PFZ* and *OO SAZ Sectors*, the Conc. W $\delta^{15}N_{NO3}$ was calculated as a concentration-weighted average of the surface samples. For each of the CTD casts, individual Conc. W $\delta^{15}N_{NO3}$ were calculated by averaging over the MLD.

[2] The isotope effect of nitrate assimilation for the eukaryotic phytoplankton groups for each region.

[3] The isotope effect of nitrate assimilation for the prokaryotic group, *Synechococcus* (SYN; $^{15}\varepsilon_{syn}$), is taken to be different from that calculated for the eukaryotic groups (the latter taken to be the whole community $^{15}\varepsilon$) based on values derived from culture experiments with SYN (Granger et al., 2010).

[4] Calculated as the average MLD $[NO_3^-]$ measured from the CTD casts in the region.

[5] The average $[NO_3^-]$ measured in the water mass just below the MLD in the *Island, OO PFZ* and *OO SAZ Sectors* or in the T_{min} in the *PF Sector*; the T_{min} was identified from the CTD-derived temperature data (Figure 3.3D).

[6] Degree of consumption of reactant N pool (0-10) calculated using 3.10, methods 3.7.3.

4. Results

4.1 Hydrographic Context

4.1.1 Frontal identification

Three oceanographic regions were sampled during the summertime southern Indian Ocean cruise, the Subantarctic Zone (SAZ), Polar Frontal Zone (PFZ), and a small intrusion of the Open Antarctic Zone (OAZ) (Figure 3.1). These regions encompass a wide range of biogeochemical conditions and are separated by frontal systems. The Subtropical Front (STF) occurs between 42°S and 47°S, coinciding with a sea surface temperature (SST) of ~11.5°C and a salinity of 34.6 – 35.0 at 100 m (Deacon, 1982; Orsi et al., 1995; see Appendix A for TS plots). The Subantarctic Front (SAF) is positioned between 46 and 56°S, with a SST of ~4°C and a salinity decrease to <34.2 (Figure 3.1, Appendix A; Sievers & Emery, 1978; Orsi et al., 1995; Wong, 2005). The SAF is one of the widest frontal systems of the Southern Ocean (200 – 300 km) where the surface "step-wise" temperature changes are displaced from the subsurface physical features (Lutjeharms & Valentine, 1984; Holliday & Read, 1997). As a result, the SAF in Figure 3.1 is positioned to accommodate both the surface and extrapolated subsurface features (the latter from the CTD casts; Figure 3.2, Appendix A); however, frontal effects are expected to influence areas immediately north and south of this position. The Polar Front (PF) occurs between 50°S and 63°S, coincident with a maximum rate of SST change to ~2.5°C (Figure 3.1; Lutjeharms & Valentine 1984; Sparrow et al. 1996; PF2 in Holliday & Read, 1997), indicating the start of the southern Antarctic Surface Waters (AASW) and the northernmost extent of the subsurface 'Winter Water' temperature minimum layer (Tmin) (Belkin & Gordon, 1996). Similar to the SAF, the PF has both surface and subsurface expressions (Sparrow et al., 1996; Dong et al., 2006). This is particularly relevant for efforts to identify the PF in the vicinity of the Kerguelen (KG) Plateau (Deacon, 1983; Belkin & Gordon, 1996; Sparrow et al., 1996; Holliday & Read, 1997). Here, the PF occurs as numerous filaments (Figures 3.1 & 3.3, note the temperature variability around the KG Plateau), making its position complex to constrain. Additionally, there is debate regarding the effect of topographic steering on the PF due to the significant bathymetric changes that occur in the region – it appears that this can result in the subsurface expression of the PF being routed differently from the surface expression (Deacon, 1933 & 1937; Lutjeharms & Valentine, 1984; Holliday & Read, 1997; Park et al., 2014). Many studies have identified the PF passing through the mid-depth (~650 m deep) channel between KG and Heard (HR) islands (PF1 Holliday & Read, 1997; Dong et al., 2006; Park et al., 2014), while others suggest that it is routed south of the plateau through the southern Fawn Trough (Figure 1.5) where a full-depth PF

expression has been observed (Sparrow et al., 1996; PF2 in Holliday & Read, 1997). In the present study, the PF is identified, on the basis of physical and biogeochemical data, as passing south of HR and following a similar path to that described by Sparrow et al. (1996) and of PF2 as defined in Holliday and Read (1997) (Figure 1.5, Appendix A). A study conducted in this region in early spring suggested that the PF moves south as the season progresses (Trull et al., 2015), supporting the placement of the PF to the south of the KG Plateau during mid-summer.

4.1.2 Sector classification

Each of the sectors – *Island*, *PF*, *OO PFZ* and *OO SAZ* – are classified by its physical properties (e.g., SST, Figure 3.3) and nutrient distributions (e.g., Si*, Figure 4.2).

The *Island Sector* (36 – 79°E) incorporates all the Subantarctic Islands (PEI, CR, KG, and HR) as well as two oceanic zones, the SAZ and the PFZ. Not only do the islands limit SST change from early-spring to mid-summer compared to the *Open Ocean Sectors* (Figure 3.3) as a result of topographic steering (Gordon et al., 1978; Chelton et al., 1990; Gille, 1994; Orsi et al., 1995; Holliday & Read, 1997; Moore et al., 1999; Salleé et al., 2006; Dong et al., 2006), but they also drive higher surface nutrient concentrations (Figure 4.1; e.g., Tyrrell et al., 2005; Blain et al., 2001; Planquette et al., 2007; Trull et al., 2015; Holmes et al., 2019).

The *Polar Frontal Sector* (*PF Sector,* 79 – 90°E) to the east of the *Island Sector* is classified as such because a PF filament (Holliday & Read, 1997; Dong et al., 2006) carrying OAZ nutrient and temperature properties was encountered during the transect. A sharp decrease in SST by ~2ºC from the *Island Sector* to the *PF Sector* is apparent throughout the early- to mid-summer season (Figure 3.3), suggesting a semi-permanent filament. Additionally, elevated OAZ Si and Si* concentrations are observed in the *PF Sector* (Figure 4.1B & 4.2) (Sarmiento et al., 2004), which includes an area of the PFZ to the west (Figure 3.1) where residual PF nutrient characteristics are apparent in this region (Figure 4.1B & 4.2). Consequently, these stations have been included in the *PF Sector*.

The *Open Ocean Polar Frontal Sector* (*OO PFZ Sector*, 90 – 118°E) is defined as the open ocean region south of the SAF that is largely free of the biogeochemical characteristics of the PF; specifically, the concentrations of Si and Si* are low (Figure 4.1B & 4.2). As the cruise track passes into the deep ocean basin region (Dong et al., 2006) that includes the *OO PFZ Sector*, the highest temporal SST variability prior is observed (Figure 3.3). This is a result of weak topographical steering, which allows for a wider,

more dynamic frontal region (Dong et al., 2006). From the satellite SST data, the sector appears to be PF filament-free between October and December 2016, with the last PF intrusion observed in September (at 94°E where a sharp SST decrease to -0.6°C is seen, indicative of OAZ intrusion; Figure 3.3). Therefore, any residual effect of PF filaments is assumed to be insignificant by the time of the cruise. Although the cruise track appears to pass close to the PF in Figure 3.1, the SST and nutrient data indicate no PF influence during the sampling period (Figure 41.B & 4.2).

The *Open Ocean Subantarctic Zone* (*OO SAZ Sector*, 118 –143°E) is the easternmost sector of the cruise transect, located in the open ocean region between the STF and the SAF. A uniform increase in SST from the SAF to the STF is apparent (Figure 3.3) and 'step-wise' features associated with the surface expression of the SAF are seen (Lutjeharms & Valentine, 1984; Holliday & Read, 1997). Compared to the *OO PFZ*, SST is less variable in the months preceding the cruise (Figure 3.3). Additionally, the low Si concentration observed in this sector (Figure 4.1B) and the increasing Si* (driven by a decline in $[NO_3^-]$ rather than a rise in $[Si(OH)_4]$; Figure 4.2) are characteristic of Subantarctic surface waters (Brzezinski et al., 2003; Sarmiento et al., 2004).

4.1.3 Water mass identification

A combination of CTD-derived salinity and temperature data and satellite SST data were used to identify the water masses across the three oceanic regions (SAZ, PFZ and OAZ) and four sectors (*Island Sector, PF Sector, OO PFZ Sector* and *OO SAZ Sector*). It is important to note that when identifying water masses across this transect, the majority of the CTD casts were conducted either in the vicinity of landmasses (e.g., CTD 1 near-shore PEI, CTD 2 at CR Plateau and CTD 3 at KG Plateau) or fronts (e.g., CTD 6 near the SAF and CTD 7 near the STF) (Table 3.1), such that bathymetric-induced- and/or frontal upwelling may alter water mass characteristics. The cruise largely transected the Subantarctic Indian basin, crossing the SAZ and PFZ. The surface water mass, Subantarctic Surface Water (SASW), is found to the north of the SAF in the SAZ and a transition zone from Antarctic Surface Water (AASW) to SASW is observed in the PFZ (Carter et al., 2008). Across the SAZ, SASW is identified by the SST data, ranging from ~5 – 11.5°C (Figure 3.1), from the STF in the north to the SAF in the south (Orsi et al., 1995). This is confirmed by the *Island Sector* CTDs 1 and 2 and the *OO SAZ Sector* CTDs 6 and 7 where CTD-derived surface temperatures are as follows: CTD 1 = 4.9°C, CTD 2 = 5.5°C, CTD 6 = 5.0°C, and CTD 7 = 11°C (Figure 3.2, Appendix A). While the surface salinity of CTD 7 is consistent with expected Indian SASW (>34.3, Carter et al., 2008), the salinities of CTD 1, 2 and 6 are low at 33.9 – 34.0, similar to SASW salinities observed in the southeast Pacific Southern Ocean and Drake Passage.

These lower salinities are thought to be due to vertical mixing (Morris et al., 2001), which is to be expected given the close proximity of CTDs 1, 2, and 6 to islands and fronts.

SASW overlays Subantarctic Mode Water (SAMW) that subducts in the summer as a result of surface warming, after which this well-mixed and well-ventilated water mass flows northward (Carter et al., 2008, Cerovečki et al., 2013). In the Indian Sector of the Subantarctic, there are two types of SAMW, a "lighter" (σ_θ = 26.7 kg m^{-3}) SAMW found on the western side of the basin and a "denser" (σ_θ = 26.9 kg m^{-3}) southeast Indian SAMW (SEISAMW) found to the east (Cerovečki et al., 2013). While the western SAMW sinks to a depth of 200 – 300 m, the ML in the SAZ deepens eastwards (Dong et al., 2008), leading to SEISAMW sinking to depths of 500 – 550 m (Cerovečki et al., 2013). In the *Island Sector*, SAMW is seen just below the ML in CTD 1 with a σ_θ of 26.7 kg m^{-3}, a salinity of ~34.0, and a high oxygen content that reaches a maximum at 190 m (Appendix A & B). Similar characteristics are observed for CTD 2, although there is no clear oxygen maximum. On the eastern side of the Subantarctic basin, SEISAMW is observed for CTD 6 in the *OO SAZ Sector*, with an oxygen maximum at ~260 m, coincident with a σ_θ of 26.7 kg m^{-3} and a salinity of ~34.0. That SEISAMW occurs shallower at CTD 6 than 500 – 550 m (Cerovečki et al., 2013) is likely a result of the CTD cast occurring near the SAF and thus the region of SEISAMW formation. SEISAMW is not observed in the CTD 7 profile, likely due to the water mass occurring below the 500 m depth to which the CTD was deployed.

Forming in the surface of the PFZ, Antarctic Intermediate Water (AAIW) descends to depths of 800 – 1000 m and travels northwards below SAMW (Pickard & Emery, 1990; Talley, 1996). The processes driving AAIW formation remain unclear but are theorized to involve wind-forcing and density-driven sinking of AASW (which is similar in salinity to AAIW; Molinelli, 1981; Carter et al., 2008), with the further mixing with SAMW in the SAZ adding to AAIW renewal (McCartney et al., 1977; Sloyan & Rintoul, 2001). AAIW is identified by its characteristic salinity of 34.3 – 34.5, temperature of 3 – 7°C (Carter et al., 2008), and σ_θ of 27.3 kg m^{-3} (Molinelli, 1981; Piola & Georgi, 1982). AAIW is present at the base of CTD 1 (~350 m) where salinity is 34.4, temperature is 2.8 – 3.0°C, and σ_θ is 27.3 kg m^{-3} (Appendix A). Additionally, there is evidence of AAIW at 400 m in CTD 2 (at the base of the CTD cast), where salinity is 34.4, temperature is 3.0°C, and σ_θ is ~ 27.3 kg m^{-3}. In the PFZ of the *Island Sector* (CTD 3), a water mass is apparent with a salinity of 34.3 and an σ_θ of 27.3 kg m^{-3}, but with a low temperature of 2.0°C at ~300 m. It is likely that this water mass is AAIW with the lower temperatures indicating recent subduction of AASW (temperature range of <0°C to 2.5°C, Gordon, 1975; Deacon, 1982) at the PF, which is near the CTD station. AAIW is also seen at ~300 m at CTD 5 (*OO PFZ Sector*), where a salinity of 34.3 and a σ_θ of 27.3 kg m^{-3} coincide with a temperature of 2.8°C, slightly below the

3.0°C that is characteristic of this water mass and likely due to the proximity of CTD 5 to the PF (Appendix A). AAIW is observed at ~350 m in the *OO SAZ Sector* (CTD 6), where salinity is 34.3, σ_θ is 27.3 kg m^{-3}, and temperatures are ~2.5°C. The consistently low temperatures associated with AAIW contradict reports that Indian Sector AAIW is the warmest AAIW (>5.6°C at 43°S and 600 m depth; Santoso & England, 2004). The low temperatures (and shallow depth; ~300 m) are likely due to the southern position of the CTD casts, near the area of AAIW formation, along with the local dynamics within the regions (e.g., bathymetric-induced and frontal upwelling).

An intrusion of AASW is evident at the surface of CTD 3 and CTD 5 in the PFZ, similar to surface conditions observed in the *PF Sector* at CTD 4. South of the PF, AASW is a surface layer of ~100 m thick, with a temperature of <0°C to 4°C (Gordon, 1975; Deacon, 1982; Talley, 2011), and low salinity of 33.0 to 34.5 (Talley, 2011). Low-salinity (<34.0) and low-temperature (1.5°C) surface water occurs in the ML of CTD 4, indicative of AASW that overlays the Tmin layer below (Appendix A). A distinctive Tmin occurs at 70 m, with its core at ~100 m (-0.3°C). In the PFZ, AASW sinks to form AAIW (Molinelli, 1981; Carter et al., 2008), but also remains the dominant surface water mass (Talley, 2011). At CTD 3, AASW has a temperature of 3.5°C at the surface, decreasing to 1.8°C at ~250 m, and a salinity of 34.1 – 34.2. The elevated surface temperatures are attributed to increased surface warming over the summer season (Trull et al., 2015). Similarly, elevated surface temperatures are evident within the AASW layer at CTD 5 where temperatures of 5.0°C at the surface and 2.5°C at ~250 m and a salinity of 34.2 – 34.3 is observed.

Below AASW (and therefore the Tmin) in the OAZ and AAIW in the PFZ and SAZ, characteristically high-nutrient, low-oxygen Upper Circumpolar Deep Water (UCDW) (Whitworth et al., 1998; Orsi et al., 1999; Rintoul et al., 2001; Tomczak & Liefrink, 2005) is found at a depth of 1400 – 2500 m (Carter et al., 2008) and therefore lies below most of the CTD casts. Below the Tmin in the OAZ, temperature rises to a maximum of ~2.2°C, which is characteristic of UCDW in this region (Tomczak & Liefrink, 2005) while coinciding with the expected decrease in oxygen (Appendix A & B). Interestingly, UCDW is apparent at ~250 m at CTD 4, where a decrease in oxygen content and a temperature of 2.2°C is observed. The shallow appearance of this water mass likely a result of deep, turbulent mixing driven by the bathymetry.

4.2 Biogeochemical context

4.2.1 Surface nutrient trends

In the *Island Sector*, surface [NO_3^-], [$Si(OH)_4$], [PO_4^{3-}], and [NH_4^+] show a high degree of variability, with higher concentrations typically observed near the islands and SAF. The mean concentrations measured for the *Island Sector* are 21.8±3.0 μM, 7.3±4.4 μM, 1.6±0 .2 μM, and 1.6±1.2 μM for NO_3^-, $Si(OH)_4$, PO_4^{3-} and NH_4^+, respectively.

A significant increase in [$Si(OH)_4$] is apparent at the transition from the *Island Sector* to the *PF Sector*, with an average [$Si(OH)_4$] for the *PF Sector* of 22.7±4.7 μM (Figure 4.1B). Coincidentally, [NO_3^-] increases slightly to 24.3±2.3 μM (Figure 4.1A). By contrast, the average [PO_4^{3-}] (1.6±0.1 μM) is the same as in the *Island Sector*, while [NH_4^+] decreases to 0.4±0.3 μM (Figure 4.1C & D, respectively).

Across the *OO PFZ* and *OO SAZ*, [$Si(OH)_4$] and [NH_4^+] remain consistently low (Figure 4.1B & D, respectively). For [$Si(OH)_4$], a mean of 2.6±2.3 μM and 1.0±0.4 μM are measured for the *OO PFZ* and *OO SAZ*, respectively, while for [NH_4^+], a mean of 0.6±0.3 μM and 0.5±0.5 μM are measured. Low variability in [NO_3^-] and [PO_4^{3-}] are observed across the *OO PFZ Sector*, with means of 23.1±1.3 μM and 1.6±0.1 μM, respectively (Figure 4.1A & C). [NO_3^-] and [PO_4^{3-}] decrease in the *OO PFZ Sector*, from values of 21.4 μM and 1.5 μM, respectively, near the SAF to 3.2 μM and 0.6 μM, respectively, near the northerly STF. These large decreases in [NO_3^-] and [PO_4^{3-}] result in elevated standard deviations for the *OO PFZ Sector* averages of 14.1±5.3 μM and 1.1±0.3 μM for [NO_3^-] and [PO_4^{3-}], respectively.

4.2.2 Surface PON

The surface PON concentrations – an indicator of N biomass – are highly variable in the *Island Sector*, increasing from a between-island mean of 0.8 ± 0.1 μM to concentrations ≥1.4 μM around the islands (i.e., 1.6 μM at the PEI, 1.4 μM at CR, 1.5 μM at KG, and 1.9 μM at HR). Across the *PF Sector*, *OO PFZ* and *OO SAZ Sectors*, variability is reduced, and the following means are calculated: 0.8 ± 0.2 μM, 1.0 ± 0.1 μM, and 0.9 ± 0.2 μM, respectively.

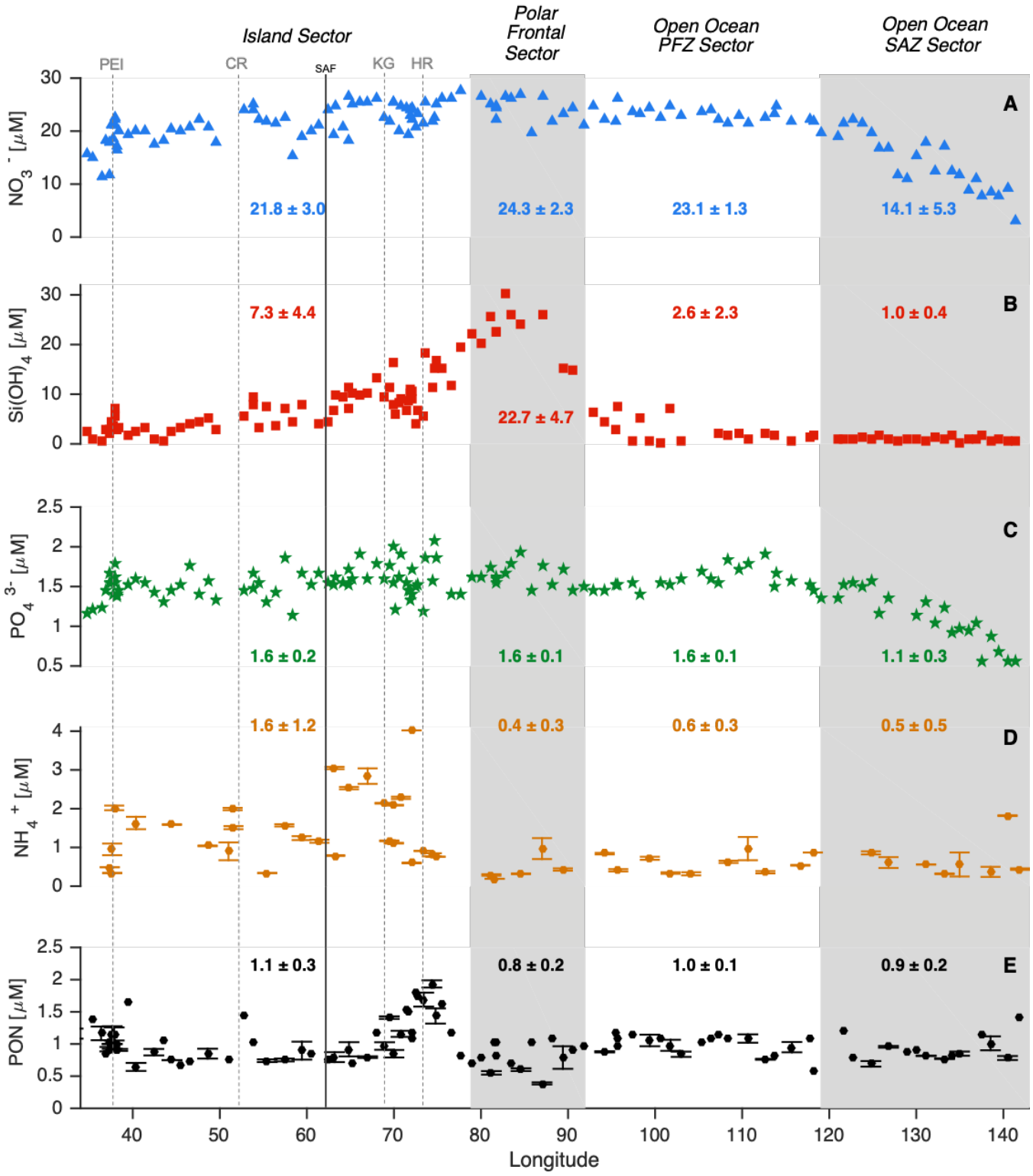

Figure 4.1: Surface concentrations with latitude of A: Nitrate [μM] (blue), B: Silicate [μM] (red), C: Phosphate [μM] (green), D: Ammonium [μM] (orange), and E: Particulate organic nitrogen (PON) [μM] (black) for the summertime transect. The sectors are shown by the alternating white and grey shaded areas, the islands – PEI, CR, KG and HR – are indicated by the dashed grey vertical lines and the SAF in the *Island Sector* is indicated by the solid vertical black line. Error bars indicate one standard deviation (± 1 S.D.), plotted where available, and the average nutrient/PON concentration for each sector (± 1 S.D.) is labelled on the panels. Underway and surface (i.e., ~10 m) CTD data are included in all panels.

4.2.3 Surface Si*

Si* was used to help define the different sectors encountered along the sampling transect. The *Island Sector* shows the greatest Si* variability, especially around PEI, CR, and KG where values are similar to those found in regions of SAMW and AAIW formation (-10 to -15 µM; Figure 4.2) (Sarmiento et al., 2004). The transition from the *Island Sector* to the *PF Sector* coincides with a decrease in SST (from ~3.5°C to 1.4°C) and an increase in Si*, from an *Island Sector* mean of -14.5±3.0 µM to a *PF Sector* mean of -2.7±4.2 µM (although reaching values as high as 4.0 µM). In the open Subantarctic, Si* decreases in the *OO PAZ Sector* to the lowest mean value measured during the cruise, -20.4 ± 1.7 µM. Si* and SST then increase in consort across the *OO SAZ Sector*, from -21.1 µM and 5.0°C at the SAF to -2.7 µM and 11.2°C at the STF.

Figure 4.2: Surface Si* concentrations [µM] (red) and SST (°C) (blue) with latitude for the summertime transect. The sectors are shown by the alternating white and grey shaded areas, the islands – PEI, CR, KG and HR – are indicated by the dashed grey vertical lines, and the SAF in the *Island Sector* is indicated by the solid vertical black line. The Si* concentrations are calculated from equation 3.5 and the average Si* concentrations (± S.D.) for each sector are labeled on the plot. The SST values are calculated from satellite measurements (see section 3.2.3).

4.2.4 Surface N isotope ratios

The $\delta^{15}N$ of surface ocean NO_3^- is influenced by the degree of NO_3^- assimilation and reflects consumption over the whole growing season whereas the $\delta^{15}N$ of PON is influenced by type of N substrate assimilated (i.e., NO_3^- vs. NH_4^+), as well as microbial regeneration, and integrates over shorter time scales (e.g., Lourey et al., 2003; Casciotti, 2012; Rafter et al., 2012 & 2019; Smart et al., 2020). Nonetheless, similar trends are apparent in the $\delta^{15}N$ of NO_3^- and PON (Figure 4.3). A general increase in $\delta^{15}N_{NO3}$ and $\delta^{15}N_{PON}$ is observed in the vicinity of the islands (except for $\delta^{15}N_{NO3}$ at CR) and the SAF. $\delta^{15}N_{NO3}$ increases from ~7‰ to 8‰ in these areas, whereas $\delta^{15}N_{PON}$ increases by ~3‰, from -0.7‰ to >2.0‰, reaching values as high as 5‰ across the KG Plateau. Here, all samples have a [PON] >1.25 µM and the average $\delta^{15}N_{PON}$ is 2.8±1.7‰, reaching a maximum of 3.4±0.3‰ downstream of HR. An *Island Sector* mean of 7.1±0.5‰ is calculated for $\delta^{15}N_{NO3}$, while $\delta^{15}N_{PON}$ has a mean of 0.3±1.4‰.

While the $\delta^{15}N_{PON}$ range from -2.4‰ to 2.4‰ across the *PF Sector* (average of -1.1±1.3‰), the $\delta^{15}N_{NO3}$ stays fairly constant at 6.7±0.5‰ (Figure 4.3). There is an overall increase in mean $\delta^{15}N_{NO3}$ in the *OO PFZ* to 7.2±0.5‰ and in $\delta^{15}N_{PON}$ to -0.8±1.0‰. Slight local increases in $\delta^{15}N_{PON}$ coincide with increases in $\delta^{15}N_{NO3}$ (e.g., at 103°E).

The *OO SAZ* shows the highest variability in both $\delta^{15}N_{NO3}$ and $\delta^{15}N_{PON}$ (average of 9.0±0.8‰ and 0.2±1.8‰, respectively) due to the large meridional range included in this sector (Figure 4.3). $\delta^{15}N_{NO3}$ increases from 8.1‰ at 124°E to 10.0‰ at 135°E, and $\delta^{15}N_{PON}$ increases from -3.5±0.2‰ to 2.5±0.1‰ over the same distance.

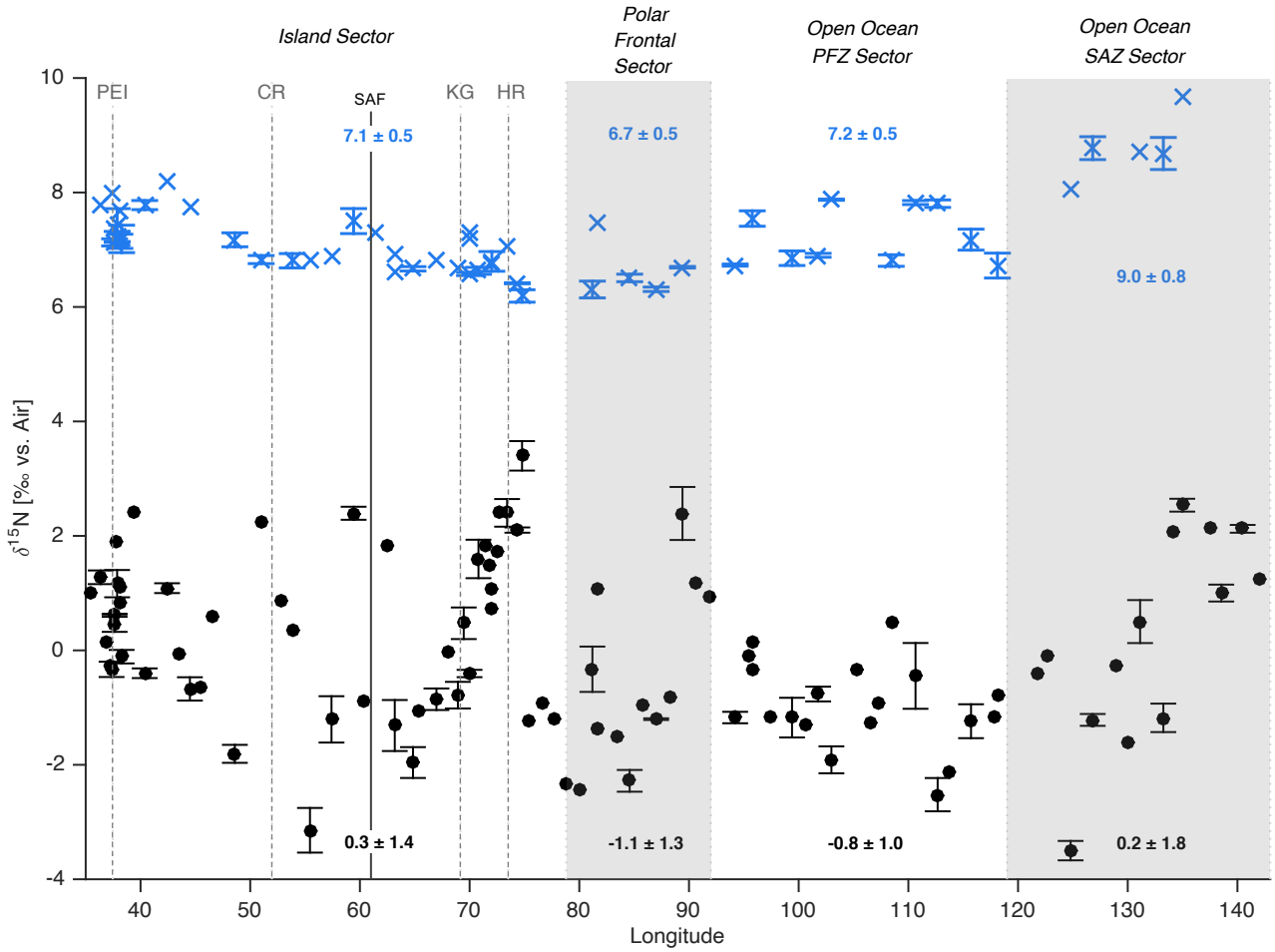

Figure 4.3: Surface $\delta^{15}N_{NO3}$ [‰ vs. Air] (blue) and $\delta^{15}N_{PON}$ (black) [‰ vs. Air] with latitude for the summertime transect. The sectors are shown by the alternating white and grey shaded areas, the islands – PEI, CR, KG and HR – are indicated by the dashed grey vertical lines and the SAF in the *Island Sector* is indicated by the solid vertical black line. Sector concentration-weighted averages (± S.D.) are labelled on the plot and where available, error bars indicate ± 1 S.D. Underway and surface (i.e., ~5 m) CTD data are included.

4.2.5 Depth profiles of nutrient concentrations

Nutrient distributions within the ML and at depth vary by sector (Figure 4.4 & 4.5). ML [NO_3^-] for the *Island*, *PF* and *OO PAZ* CTDs range from 20 to 25 µM, decreasing from deep values of >28 µM (Figures 4.4A & 4.5A). CTD 6 in the *OO SAZ Sector* shows the largest decrease into the ML, with deep values (~400 m) of 30 µM decreasing to 15 µM at the surface. Relatively low [NO_3^-] is observed for CTD 7, 14.6 µM at 500 m deep, decreasing to 9.0 µM at the surface. These low NO_3^- concentrations are consistent with the trends in [Si(OH)4] and [PO_4^{3-}] and coincide with lower oxygen content subsurface waters compared to the other CTD casts (Appendix B), suggesting enhanced respiration of organic material at depth (Janssen et al., 2020).

The [NO_3^-] decrease into the upper ML is accompanied by an increase in the $\delta^{15}N_{NO3}$ (Figures 4.4B & 4.5B). Here, $\delta^{15}N_{NO3}$ for the *Island*, *PF*, *OO PFZ* and CTD 6 of the *OO SAZ* ranges between 6.3‰ and 7.5‰ (Figure 4.5B), higher than the values measured for the deep NO_3^- supply (UCDW) of 5.3 – 5.8‰ at 400 – 500 m (i.e., at the subsurface [NO_3^-] maximum; Figure 4.4A; Sigman et al. 1999 & 2009; Rafter et al., 2013). The $\delta^{15}N_{NO3}$ supply for CTD 4 (*PF Sector*) is likely the Tmin layer (DiFiore et al., 2009 & 2010) between 90 m and 140 m, which has a $\delta^{15}N_{NO3}$ of 5.2 – 5.5‰ (Figure 4.5B). The core of UCDW is apparent deeper in the water column at ~200 m, with a $\delta^{15}N_{NO3}$ of 5.1‰ and a [NO_3^-] of 31.3 µM (Figure 4.4B & A, respectively). The highest ML mean $\delta^{15}N_{NO3}$ occurs at CTD 7 in the *OO SAZ* (9.8±0.2‰) (Figure 4.5B). A sharp decline in the $\delta^{15}N_{NO3}$ to 7.3‰ is apparent at 100 m, similar to the surface $\delta^{15}N_{NO3}$ values of the more southern CTD 6 cast as well as the $\delta^{15}N_{NO3}$ value at 100 m at CTD 5 in the *OO PFZ*. This is consistent with equatorward transport of water masses in the SAZ and indicates that the subsurface supply in the *OO PFZ* and *OO SAZ* are similar (i.e., AAIW and SAMW; e.g., Talley, 1996; Herraiz-Borreguero & Rintoul, 2011)

Similar to [NO_3^-], consistent decreases in the concentrations of $Si(OH)_4$ (Figure 4.4C & 4.5C) relative to a decrease in depth are observed in the ML for all casts. The *OO PFZ* and *OO SAZ Sector's* ML [$Si(OH)_4$] averages are low (Figure 4.5C: 4.6±0.8 µM for CTD 5, 2.2±2.3 µM for CTD 6 and 0.8±0.2 µM for CTD 7), while the *Island Sector* ML [$Si(OH)_4$] averages are fairly high (Figure 4.5C: 7.2±0.1 µM for CTD 2 and 10.3±0.3 µM for CTD 3). The highest average ML [$Si(OH)_4$] is observed in the *PF Sector* (22.6±0.3 µM for CTD 4), as is characteristic of this region (Sarmiento et al., 2004; Freeman et al., 2018). The [$Si(OH)_4$] profiles of the Subantarctic, CTDs 1 –3, 5 and 6, appear to converge on 35 to 40 µM at 400 m depth (Figure 4.4A), while in the *PF Sector* (CTD 4) and *OO SAZ Sector* (CTD 7), [$Si(OH)_4$] is 81.1 µM and 4.6 µM at 400 m, respectively.

Trends in the Si* concentrations with depth are very similar to those of [$Si(OH)_4$] (Figures 4.4D & 4.4C, respectively), suggesting that this derived variable is driven more strongly by $Si(OH)_4$ than NO_3^- across the Subantarctic (Boyd et al., 1999; Franck et al., 2000; Hutchins et al., 2001; Nelson et al., 2001; Sedwick et al., 2002; Sarmiento et al. 2004). Si* is between -13.0±0.4 and -15.7±1.9 µM in the upper ML of the *Island Sector* (Figure 4.5D; CTDs 1-3). Very similar upper ML values of -16.3±0.6 µM and -14.0±0.4 µM are observed for CTD 5 in the *OO PFZ* and for CTD 6 in the *OO SAZ*, respectively. At 400 m, the three above-mentioned sectors have similar Si* concentrations of ~12 µM (Figure 4.4D). CTD 7 (*OO SAZ*, near the STF) shows an invariant Si* concentration from the surface to 500 m, with an average for the full depth profile of -8.6±0.7 µM. This trend is a result of the equatorward advection of $Si(OH)_4$-deplete SASW (Sarmiento et al., 2007). The *PF Sector*, by contrast, is characterized by high

concentrations of Si* at depth, reaching a maximum of 50.5 µM at 400 m, while in the surface ML, Si* is on average ~0 µM (Figure 4.5D).

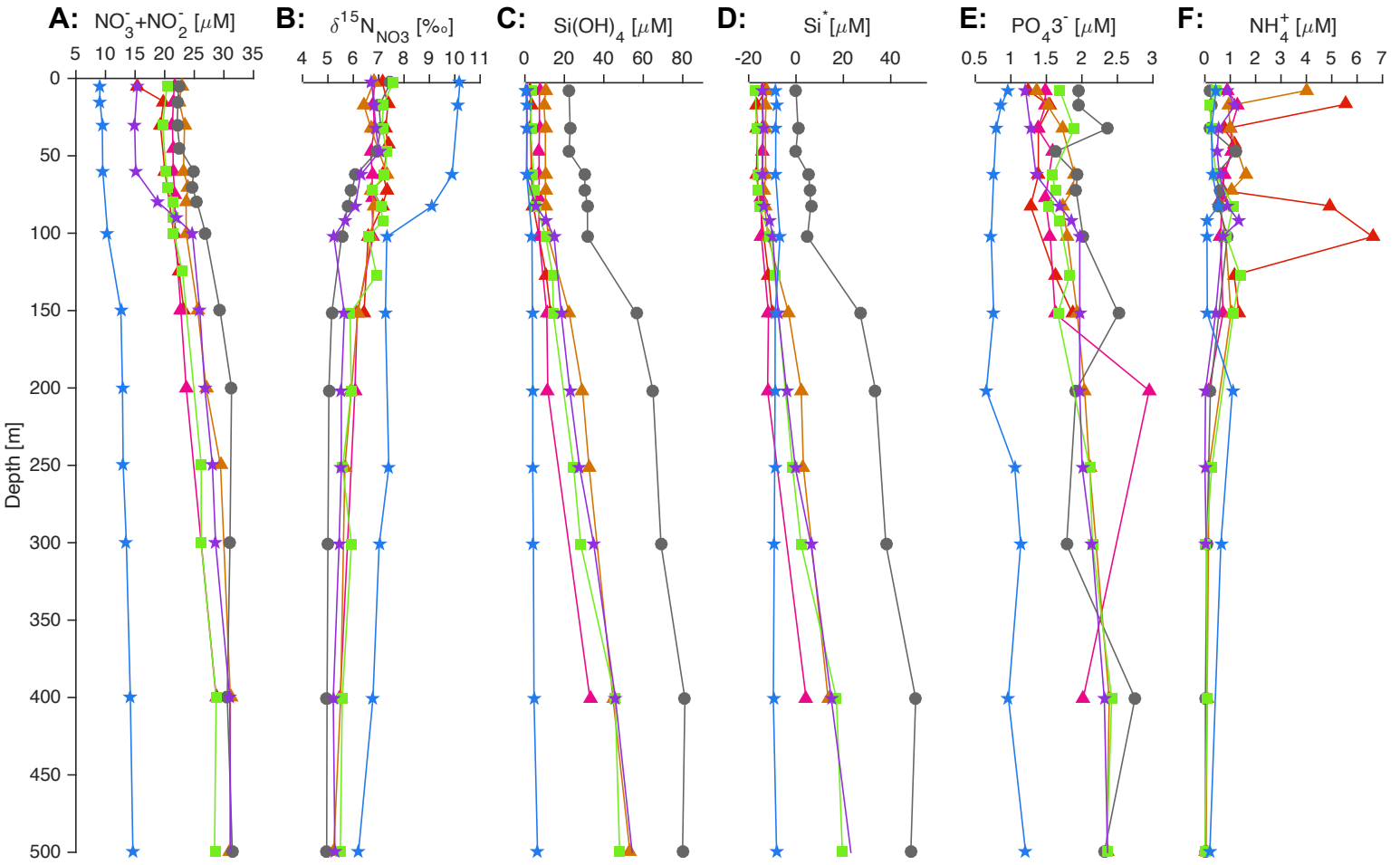

Figure 4.4: Vertical nutrient profiles (surface to 500 m) from the seven CTD casts conducted during the summertime transect. A: Nitrate [µM], B: $\delta^{15}N_{NO3}$ [‰ vs. Air], C: Silicate [µM], D: Si* [µM], E: Phosphate [µM], F: Ammonium [µM]. The sectors are indicated by the different marker shapes – triangles for the *Island Sector*, circles for the *PF Sector*, squares for the *OO PFZ Sector*, and stars for the *OO SAZ Sector*. CTD 3 was deployed to a maximum depth of 400 m and for all casts, PON samples were only collected to a maximum depth of 150 m.

$[PO_4^{3-}]$ is similar at depth for CTDs 1 – 6, converging on ~2.3 µM at 500 m, while the surface values range from 1.2 – 2.0 µM (Figure 4.4E). The lowest $[PO_4^{3-}]$ for the transect is observed for CTD 7, where the average ML concentration is 0.8±0.1 µM (Figure 4.5E) and the profile average to 500 m is 0.9±0.2 µM (Figure 4.4E).

The [NH_4^+] is highest in the surface waters of the *Island Sector* profiles (triangles and warm colours in Figure 4.4F & 4.5F), consistent with the surface trends seen in Figure 4.1D. Very high surface [NH_4^+] are observed for CTD 1 (close proximity to PEI) and CTD 3 (close proximity to KG and HR), 5.5 µM and 4.0 µM, respectively. These high surface values decrease rapidly with depth, resulting in a ML average [NH_4^+] of 0.8±0.2 µM for CTD 1 and 1.0±0.4 µM for CTD 3 (Figure 4.5F). A second maximum in [NH_4^+] is observed below the MLD at 100 m for CTD 1, approaching 7 µM. Very low [NH_4^+] is seen in the upper ML of CTD 2 in comparison to the other near-island casts (0.9 µM). These concentrations are similar to the *OO PFZ* and *OO SAZ* casts (CTDs 5 to 7) where the values range from 0.2 – 1.3 µM in the upper ML and are <0.02 µM (limit of detection) below 250 m. The *PF Sector* CTD 4 shows relatively low [NH_4^+], with a maximum of 1.2 µM at 45 m and an average for the ML of 0.5±0.4 µM (Figure 4.5F).

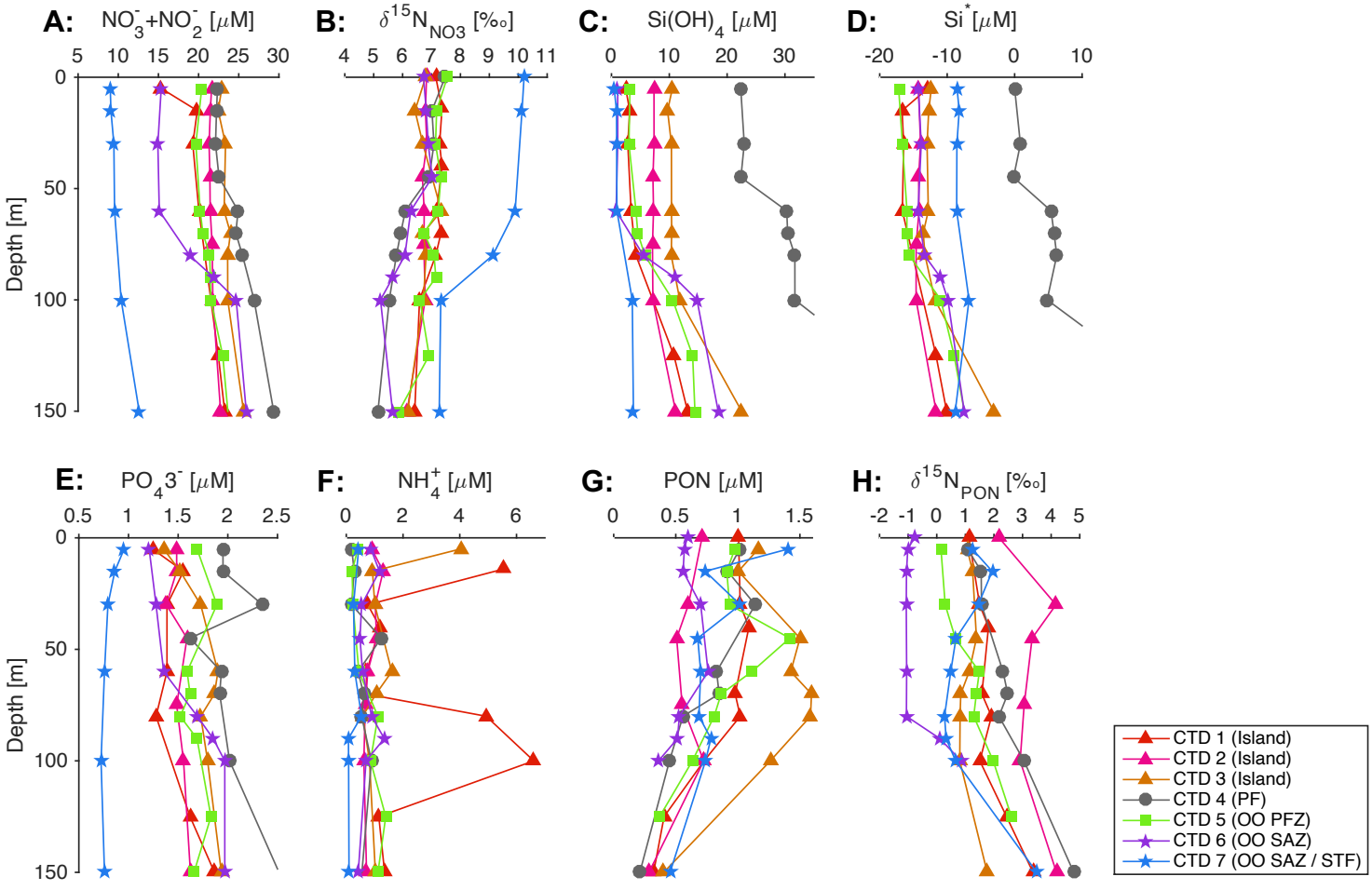

Figure 4.5: Zoomed-in upper layer (surface to 150m) CTD-derived nutrient profiles from the seven casts shown in Figure 4.4. A: Nitrate [µM], B: $\delta^{15}N_{NO3}$ [‰ vs. Air], C: Silicate [µM], D: Si* [µM], E: Phosphate [µM], F: Ammonium [µM], G: PON [µM], H: $\delta^{15}N_{PON}$ [‰ vs. Air]. Casts conducted in the different sectors are indicated by the different marker shapes – triangles for the *Island Sector*, circles for the *PF Sector*, squares for the *OO PFZ Sector*, and stars for the *OO SAZ Sector*.

4.2.6 Depth profiles of PON concentration and $\delta^{15}N_{PON}$

Bulk PON was sampled down to 150 m, below which the concentrations are very low. The surface values range from 0.5 to 1.5 μM, with the highest surface value observed for CTD 7 and the lowest for CTD 6, both in the *OO SAZ Sector* (although it is worth noting that the ML mean concentrations are similar for CTDs 6 and 7; 0.6±0.1 μM and 0.9±0.3 μM, respectively; Figure 4.5G). No distinctive trends are apparent among the various sectors; however, an increase in [PON] is evident at the F_{max} (60 – 90 m) for most of the CTD casts, except CTD 2 and CTD 7 where local [PON] maxima occur elsewhere in the depth profiles. In contrast, $\delta^{15}N_{PON}$ shows sector-specific trends (Figure 4.5H). The highest $\delta^{15}N_{PON}$ occurs at CTD 2 in the *Islands sector* (all values >2.2‰), while CTD 1 and 3 show similar, relatively high mean ML values of 1.6±0.3‰ and 1.1±0.2‰, respectively, as does CTD 4 in the *PF Sector* with a ML mean of 1.6±0.5‰. The *OO PFZ* CTD 5 has a low surface $\delta^{15}N_{PON}$ of 0.2‰, which increases gradually with depth. The lowest mean ML $\delta^{15}N_{PON}$ is observed at CTD 6 in the *OO SAZ* (ML average of -1.0±0.2‰), while a mean ML $\delta^{15}N_{PON}$ of 1.0±0.6‰ is apparent at CTD 7. For all profiles, $\delta^{15}N_{PON}$ increases at depth (i.e., ~150 m) due to isotopic fractionation associated with heterotrophic bacterial degradation of PON (Möbius, 2013, Hannides et al., 2013, Knapp et al., 2018).

4.3 Relative abundances and carbon contributions of surface phytoplankton

4.3.1 Temporal development of surface Chl-*a*

Satellite Chl-*a* can be used as a proxy for primary productivity (Behrenfeld & Falkowski, 1997). The satellite data show a decline in Chl-*a* from November 2016 until the cruise (Figure 4.6). Around the PEI, near-shore Chl-*a* concentrations of >1 mg m^{-3} are observed in November 2016 (Figure 4.6A), moving northeast offshore in December 2016 (Figure 4.6B). At the time of the cruise, very low Chl-*a* concentrations are observed around the islands, with a concentration of ~0.4 mg m^{-3} near CTD 1 (Figure 4.6C). A large Chl-*a* bloom in the northeast S-bend retention zone of the CR plateau is observed in November 2016, with concentrations >1 mg m^{-3} (Figure 4.6D). The bloom declines in size and intensity in December 2016 (Figure 4.6E) and has nearly disappeared by the time of the cruise (average Chl-*a* in the 'S'-bend is ~0.5 mg.m^{-3} and 0.4-0.5 mg.m^{-3} at CTD 2; Figure 4.6F). While a similar decline in the extent of the KG and HR bloom is observed from November/December 2016 (Figure 4.6G & H) to the time of the cruise (Figure 4.6I), elevated Chl-*a* is still apparent within the coastal retention zone northeast of KG and HR as well as over the KG Plateau, with concentrations >1 mg m^{-3}. At the CTD 5, Chl-*a* concentrations are between 0.8 and 1.0 mg m^{-3}. All three of the island-derived Chl-*a* blooms are thus in their decline stages at the time of the cruise.

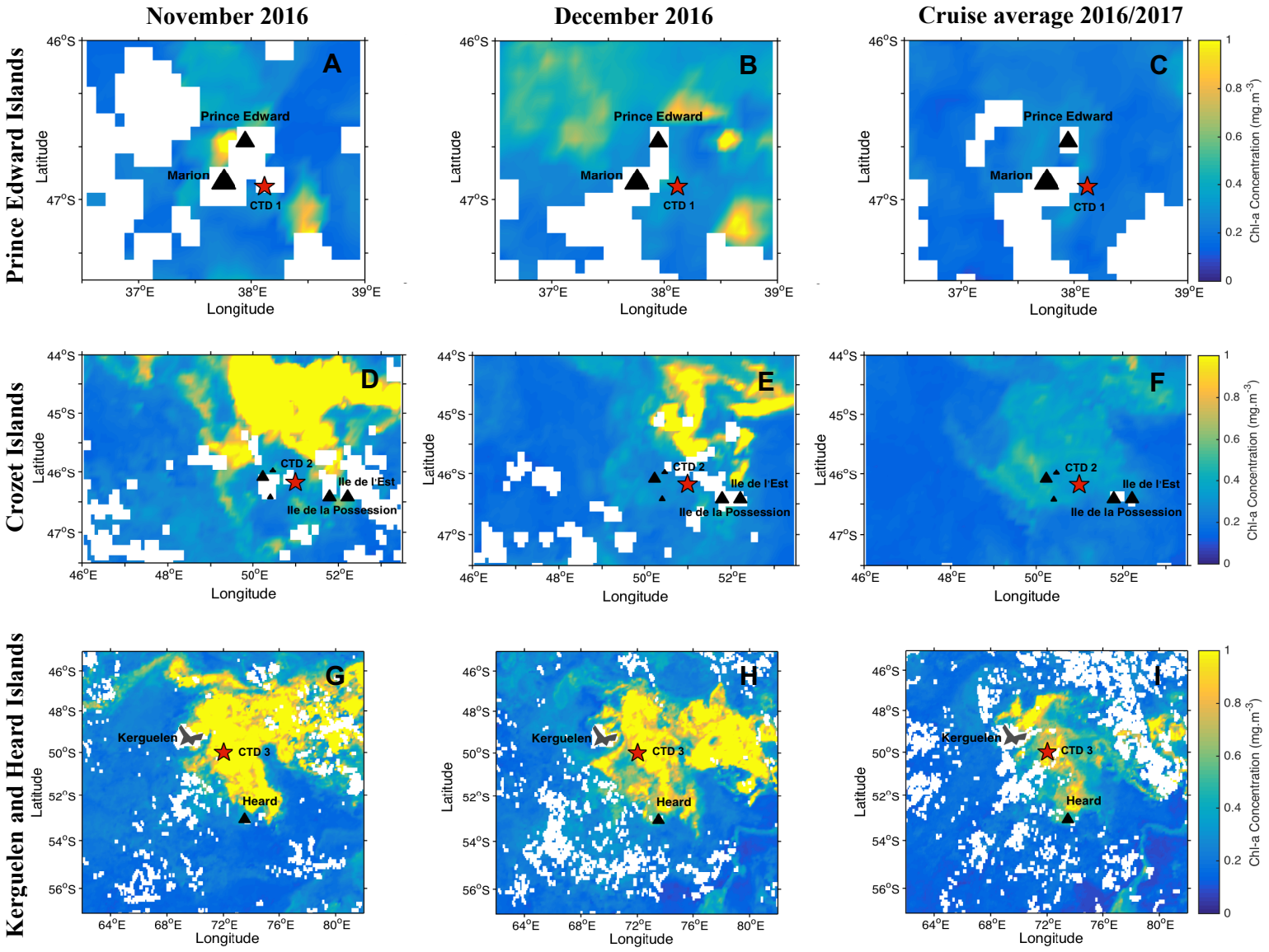

Figure 4.6: Temporal development of surface chlorophyll-*a* (Chl-*a*) concentrations (mg.m^{-3}) over the summer season around the islands of PEI (A, B, and C), CR (D, E, and F), and KG and HR (G, H, and I) from monthly averages for November 2016 (A, D, and G), December 2016 (B, E, and H), and a cruise average (dates; C (20/12/2016 – 02/01/2017), F (24/12/2016 – 06/01/2017), and I (31/12/2016 – 13/01/2017)). The Chl-*a* concentration is indicated by the colour bar, where warmer colours (yellow) indicate higher concentrations. Island locations are shown by black triangles and CTD stations (CTD 1 PEI, CTD 2 CR, and CTD 3 KG Plateau) are denoted by red stars. This satellite product is taken from MODIS-AQUA chlorophyll concentration satellite data from Level 3 browser at 9 km resolution (https://oceancolor.gsfc.nasa.gov/, methods 3.2.5.

4.3.2 Microplankton

Microplankton (>20 µm, MICRO) are the least abundant size class across the basin, with an average relative abundance (RA) of <1% (Figure 4.7A). Across the Subantarctic, the MICRO size class is

dominated by diatoms (67%), except in the *OO SAZ* where dinoflagellates dominate (70%). MICRO RA increases near the islands (particularly the PEI and CR) and fronts (SAF and PF), despite remaining low at 1 to 2%. The *Island Sector* MICRO community is dominated by chain-forming pennate diatoms such as the ubiquitous *Fragilariopsis kerguelensis*, which constitute between 70% and >95% of the MICRO size class (Figure 4.7C). The exception to this is at two stations upstream of CR where chain-forming centric diatoms (*Chaetoceros spp.;* ~97% of the bulk MICRO population) and dinoflagellates (specifically, *Protoperidium spp*. and *Creatium spp*.; each ~50% of the bulk MICRO population) dominate. A high diversity of chain-forming centric diatom species is present at low abundances near the CR and KG plateaus, as well as downstream of the KG archipelago, including *Chaetoceros* spp. with a MICRO diatom RA of 12%, *Eucampia antarctica* at 10%, *Odontella weissflogii* at 8%, *Asteromphalus roperanus* at 5%, and *Thalassiosira* spp. at 4%. An increase in the RA of chain-forming centric diatoms is observed across the *PF* and *OO PFZ Sectors*, dominated by *Chaetoceros radicans*, which reaches a maximum MICRO RA of 84%, and *Corethron inerme*, which reaches a maximum MICRO RA of 33%. The *OO SAZ Sector* is dominated by dinoflagellates, with *Ceratium lineatum* being the most common species observed.

In spite of their low RA, MICRO phytoplankton contribute the most C on average relative to the other size classes around islands and fronts (Figure 4.7B). This is a result of their larger volumes and related per-cell C content. The highest relative C contribution (RCC) from MICRO phytoplankton in the *Island Sector* occurs around the PEIs (76% relative to total phytoplankton), CR (90%) and at the SAF (55%). Low RCCs occur between the island chains and, unexpectedly, around KG, where RCC is dominated by NEUKS (~60%; see 4.3.3 below). In the *PF Sector*, the average MICRO RCC is 28%. Large increases in the MICRO RCC occur in the open ocean Subantarctic, reaching a maximum of 98% at the SAF. While diatoms, mainly chain-forming pennates and centrics, dominate the MICRO RA across the basin (Figure 4.7C), dinoflagellates contribute the most C per cell to the MICRO group, and by extension, to the total phytoplankton community, as a result of their larger size and higher C density (Figure 4.7D; Menden-Deuer & Lassard, 2000). Dinoflagellates are less abundant in the *Island Sector* compared to the eastern side of the basin, dominating the RCC at only half of the island sampling stations. Downstream of HR, the RCC of the dinoflagellates rises (barring one station) into the *Open Ocean Sectors*. Dinoflagellate RCCs of >90% (relative to bulk MICRO; Figure 4.7D) are observed at six stations - these stations are dominated by *Ceratium spp*.

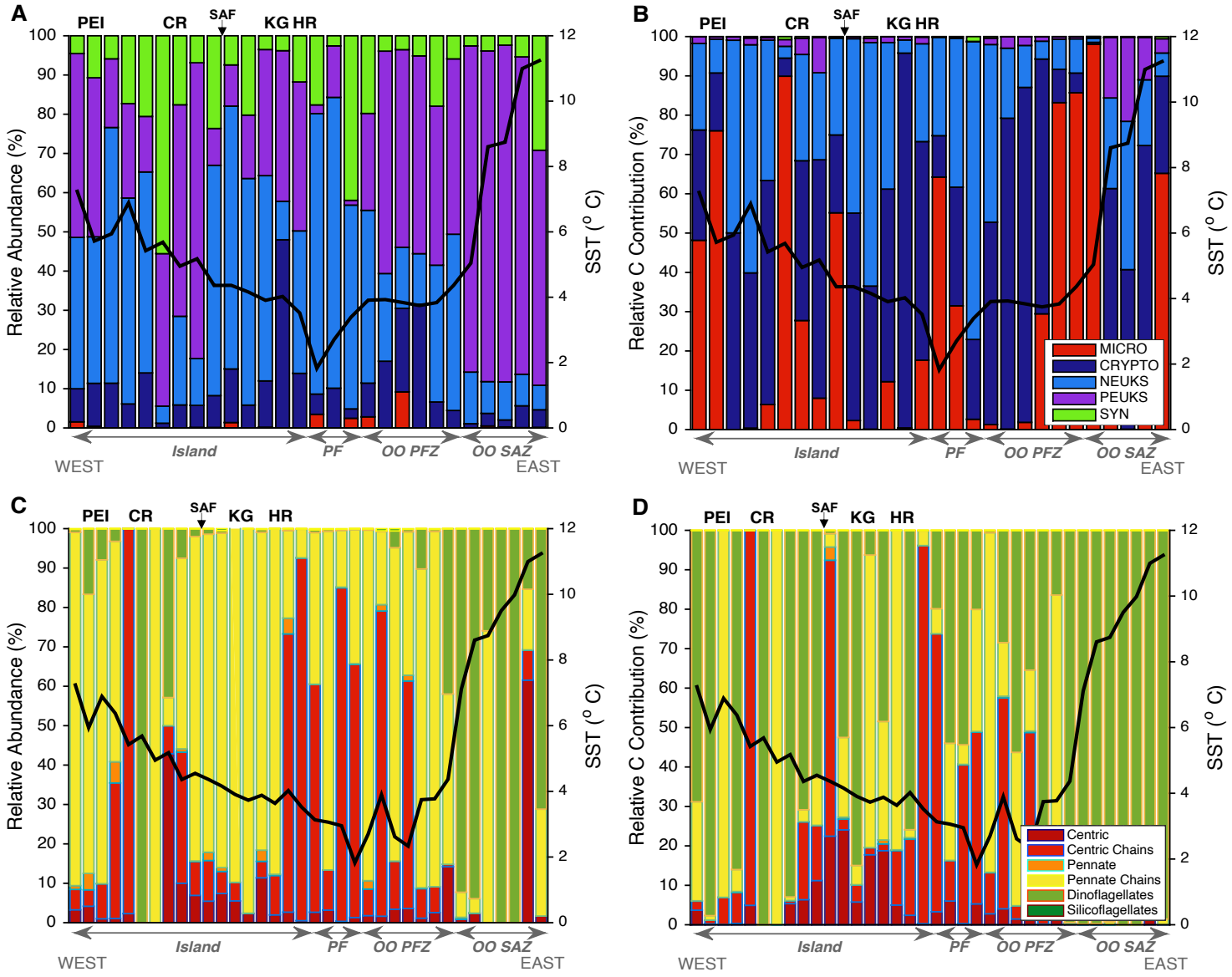

Figure 4.7: Histograms showing the relative abundance (RA; %) and relative carbon contribution (RCC; %) of phytoplankton sampled from surface waters across the transect. A: RA of micro-, nano-, and picoplankton populations; B: RCC by micro-, nano-, and picoplankton populations; C: RA of microplankton subgroups; D: RCC of microplankton subgroups. For panels A and B, the MICRO size class is depicted in red, CRYPTO in dark blue, NEUKS in light blue, PEUKS in purple, and SYN in green. For panels C and D, individual centric diatoms are shown in dark red, centric chains in light red, single pennate diatoms in orange, pennate chains in yellow, dinoflagellates in light green, and silicoflagellates in dark green. RA is calculated from the flow cytometric count data as well as the microscopy counts (section methods 3.7.5). RCC is calculated from the count data along with cell size and carbon conversion factors (section methods 3.7.5, Table 3.2). SST (right y-axis) for the transect is shown by the black line. The various sectors are indicated along the x-axis from west to east and the positions of the islands and *Island Sector* SAF are labeled along the top of the plots.

4.3.3 Nanoplankton

Cryptophytes (~9 μm, CRYPTO) typically appear in relatively low abundances across the transect in comparison to the smaller size classes (Figure 4.7A), maintaining an average surface RA of ~11%. In the vicinity of KG, CRYPTO reach a maximum average RA of 48%. Their RA in the *PF Sector* is low, at ~7%, while in the *OO PFZ Sector*, a stepwise increase in RA is apparent, reaching a maximum of 31%. This increase occurs at four consecutive stations where the SST is around 4°C. As SST rises to the north to >11°C at the last station along the transect, the CRYPTO RAs decrease, averaging 3% in the *OO SAZ Sector* (Figure 4.7A).

Nanoeukaryotes (~5 μm, NEUKS) maintain the highest RA of all the phytoplankton groups in the *Island* (excluding downstream of CR) and *PF Sectors* (41% and 63%, respectively; Figure 4.7A). Near and downstream of CR, NEUKS RA is low, averaging 13%. Maximum NEUKS abundances occur in the vicinity of the PF, where RAs of 73% are observed. A significant decrease occurs in the *Open Ocean Sectors,* with RAs in the *OO PFZ Sector* of <20%, increasing to 45% at the SAF, and then decreasing again to a mean RA of 9% across the *OO SAZ*.

On average, nanoplankton contribute the second highest relative amount of phytoplankton C after the MICRO, 35% (Figure 4.7B). Even though NEUKS outnumber CRYPTO by 4:1 in the *Island Sector* (Figure 4.7A), CRYPTO has a higher mean RCC of 47% due to its larger size, while NEUKS has a mean RCC of 30%. NEUKS dominate the RCC in the *PF Sector*, contributing 48% (relative to CRYPTO's 30%), while CRYPTO dominate in the *OO PFZ* with an RCC of 49% (relative to NEUKS's 16%) (Figure 4.7B). A significant decrease in the RCC of both CRYPTO (to ≤5%) and NEUKS (to ~5%) is observed near the SAF. In the *OO SAZ*, CRYPTO contribute 37% and NEUKS contribute 17% of the phytoplankton carbon.

4.3.4 Picoplankton

Picoeukaryotes (~2 μm, PEUKS) appear to follow an opposing trend to that of NEUKS, with their highest RAs in the *Open Ocean Sectors*, especially the *OO SAZ Sector*, while lower RAs are observed in the *Island Sector* (Figure 4.7A). An average PEUKS RA of 32% occurs in the across the *Island Sector*, increasing to 76% downstream of CR. PEUKS RA is 8% in the *PF Sector*, increasing to 45% in the *OO PFZ Sector* and 79% in the *OO SAZ Sector*.

Synechococcus (~1.3 µm, SYN), the smallest phytoplankton group in this study, appears to be more abundant near the islands and fronts, coinciding with significant changes in SST (Figure 4.7A). SYN RA in the *Island Sector* is highly variable, and although a mean RA of 15% is calculated for the sector, large increases such as the one near CR (56%) and decreases such as upstream from KG (4%) are observed. SYN RA across the *OO PFZ* and *OO SAZ* sectors is low at 4%, although RA increases around the PF, SAF, and STF to 43%, 18%, and 29% respectively.

Both picoplankton groups contribute very little C to the bulk phytoplankton, even when their RA is high (e.g., PEUKS in the *OO SAZ*) (Figure 4.7B). This is due to their small sizes and low C:vol ratios in comparison to the larger, more C-dense nano- and microphytoplankton. The highest RCC by PEUKS, 11%, occurs in the *OO SAZ Sector*, while across the Subantarctic, PEUKS RCC is 3% on average (Figure 4.7B). SYN contribute even less C than PEUKS, with a mean <1% across the entire transect. The only areas where SYN exceeds an RCC of >1% is in the vicinity of islands or fronts.

4.4 Depth profiles of pico- and nanoplankton RA and RCC

The pico- and nanoplankton RA depth profiles are generally consistent with the surface trends (Figure 4.8A). CRYPTO and SYN maintain low RAs in comparison to NEUKS and PEUKS, with PEUKS dominating overall within the ML (RA = 49% on average for pico- and nanoplankton). For the *Island Sector*, the populations near PEI (CTD 1) are similar between the surface and Fmax, while large surface-to-Fmax decreases in SYN and increases in PEUKS are observed near CR (CTD 2). SYN is dominant at the surface (56%) and decreases to a mean RA of 18% at the Fmax while PEUKS increase from 40% at the surface to a mean RA of 65% at depth. KG Plateau ML populations (CTD 3) share similar surface trends to the PEI samples; however CRYPTO and PEUKS RA increase slightly with depth – CRYPTO RA increases from 14% at the surface to 28% at the MLD while PEUKS increase in abundance by ~10% from the surface to the MLD. By contrast, NEUKS and SYN RAs decrease with depth, by 15% and 12%, respectively. CRYPTO are associated with the highest RCC across the *Island Sector* (76%), which generally increases with depth, yielding a mean RCC of >80% within the ML at all the *Island Sector* CTDs (Figure 4.8B). NEUKS show the second highest RCC across the *Island Sector* with a mean of 17%, followed by PEUKS at 7% and SYN at 1%.

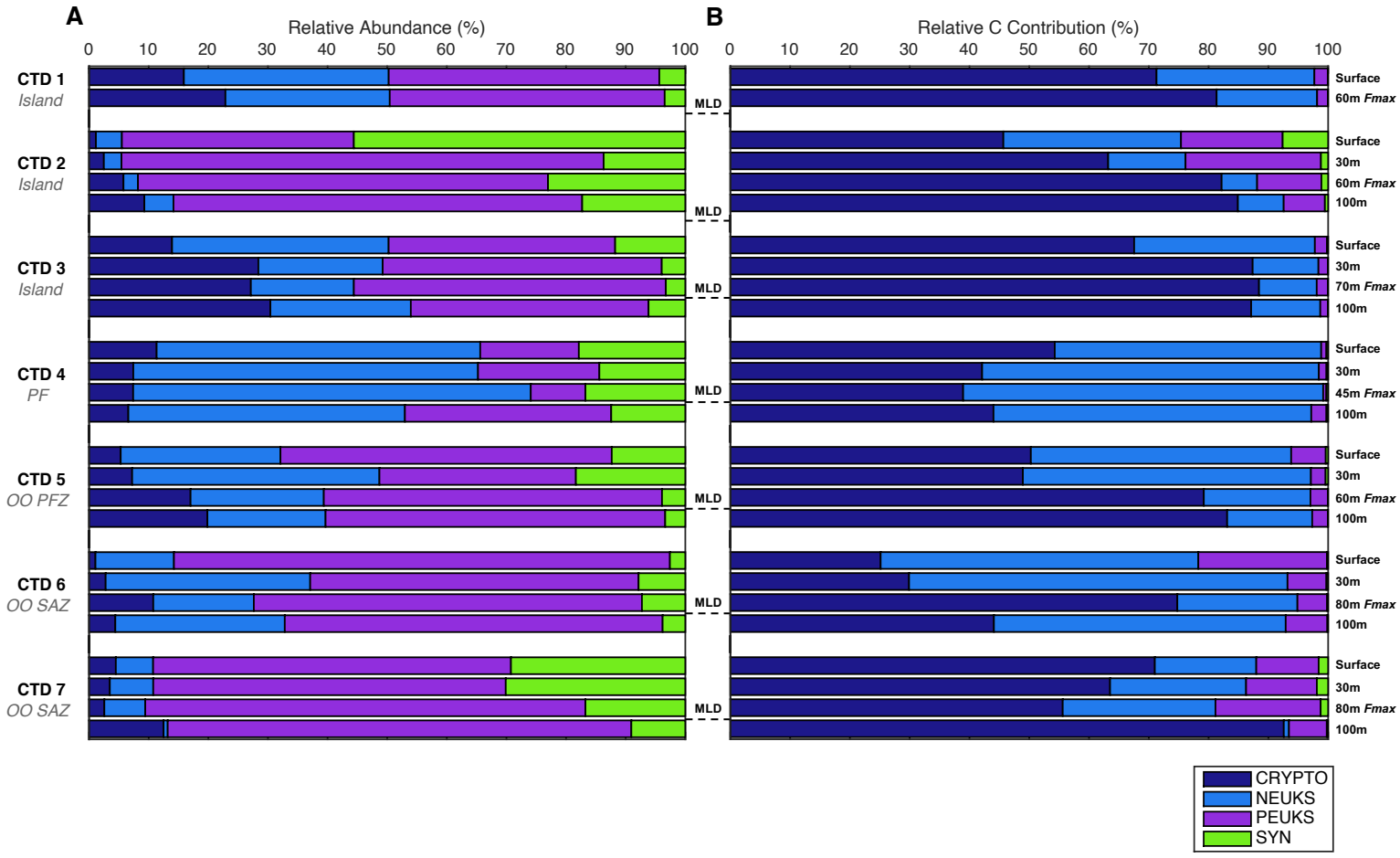

Figure 4.8: Histograms showing A: relative abundance (RA; %) and B: relative carbon contribution (RCC; %) of the sorted pico- and nanoplankton (<20 µm) in the ML. Sampling depths are indicated on the right and the various sectors are labeled below the CTD numbers on the left. The MLDs are indicated between the two panels. The CRYPTO populations are shown in dark blue, NEUKS in light blue, PEUKS in purple, and SYN in green.

The CTD 4 data from the *PF Sector* show a fairly homogenous upper ML, with roughly invariant RAs of the pico- and nanoplankton populations (Figure 4.8A). NEUKS dominate the profile with an average RA of 56% and a RCC of 54% (Figure 4.8A & B, respectively). The CRYPTO group, although significantly lower in RA at 8%, has an RCC of 45%. PEUKS and SYN have similar RAs of ~18% and RCCs of ≤1%.

PEUKS are the numerically-dominant population in the open Subantarctic ML, with an open ocean average RA of 66% (Figure 4.8A). In the *OO PFZ Sector*, PEUKS RA is 48%, much higher than that of CRYPTO and NEUKS, with RAs of 7% and 26%, respectively. Generally, CRYPTO RA increases and NEUKS RA decreases with depth in the open ocean, opposite to the trend observed in the *PF Sector*. The small size (and thus C content) of the PEUKS means that the nanoplankton (CRYPTO + NEUKS) RCC is highest despite the high RA of the PEUKS. CRYPTO contributes the majority of the C in the

OO PFZ ML with a mean RCC of 59%, followed by NEUKS at 37% (Figure 4.8B).

The *OO SAZ Sector* hosts a high abundance of PEUKS within the ML, with an average RA of 66% (Figure 4.8A). Conversely, CRYPTO are the least abundant population, with a mean RA of <5%. In general, CRYPTO and NEUKS abundances decrease towards the STF, while the RA of SYN increases, especially in the upper ML. Nevertheless, the larger size classes dominate the RCC, with CRYPTO contributing the highest proportion of total C with a ML (mean of 53%), followed by NEUKS (34%) (Figure 4.8B).

4.5 Phytoplankton biomass $\delta^{15}N$

4.5.1 Bulk PON $\delta^{15}N$

As described in section 4.2.2 above, the surface $\delta^{15}N_{PON}$ is highest in the *Island Sector*. Here, the *Island Sector* concentration-weighted $\delta^{15}N_{PON}$ average of 0.6±0.1‰ is driven by the high $\delta^{15}N_{PON}$ and [PON] near the islands (especially KG and HR) and SAF (~61°E) (Figure 4.9A). The higher the $\delta^{15}N_{PON}$, the larger the relative contribution of new N (NO_3^-) to PON production (with the solid horizontal line in Figure 4.9A indicating the $\delta^{15}N$ expected if all PON were produced from new N assimilation; see methods 3.7.3). In between the islands and fronts, lower [PON] and $\delta^{15}N_{PON}$ values are observed, many of them falling into the $\delta^{15}N$ range expected for regenerated N (i.e., NH_4^+) uptake (grey shaded region in Figure 4.9). The large range in the $\delta^{15}N_{PON}$ across the *Island Sector* qualitatively (since $\delta^{15}N_{PON}$ can be altered by non-autotrophic processes too, as discussed in section 1.4.4) indicates a high degree of variability in the relative proportions of new and regenerated N being consumed by the various phytoplankton groups. Furthermore, the fairly homogenous ML $\delta^{15}N_{PON}$ values from CTD 1 (Figure 4.10A) and CTD 3 (Figure 4.10C) near PEI and KG as described in section 4.2.6 above, falls within the new N and regenerated N utilization threshold. However, CTD 2 (Figure 4.10B), near CR, has a deeper MLD and higher $\delta^{15}N_{PON}$ over the upper 100 m averages, 3.1± 0.7‰, falling above the new N utilization threshold.

The *PF Sector* is characterized by lower [PON] and surface concentration-weighted $\delta^{15}N_{PON}$ values, with averages of 0.8±1.4 μM and -1.1±0.2‰, respectively (Figure 4.9A). The low-$\delta^{15}N_{PON}$ values consistently fall in the regenerated N threshold, except near the PF. The high ML $\delta^{15}N_{PON}$ from CTD 4 described in section 4.2.6 is consistent with expectations for near-exclusive new N utilization. However, the high-$\delta^{15}N_{PON}$ may also derive, at least in part, from non-assimilation processes (Rau et al., 1990; Lourey & Trull, 2001).

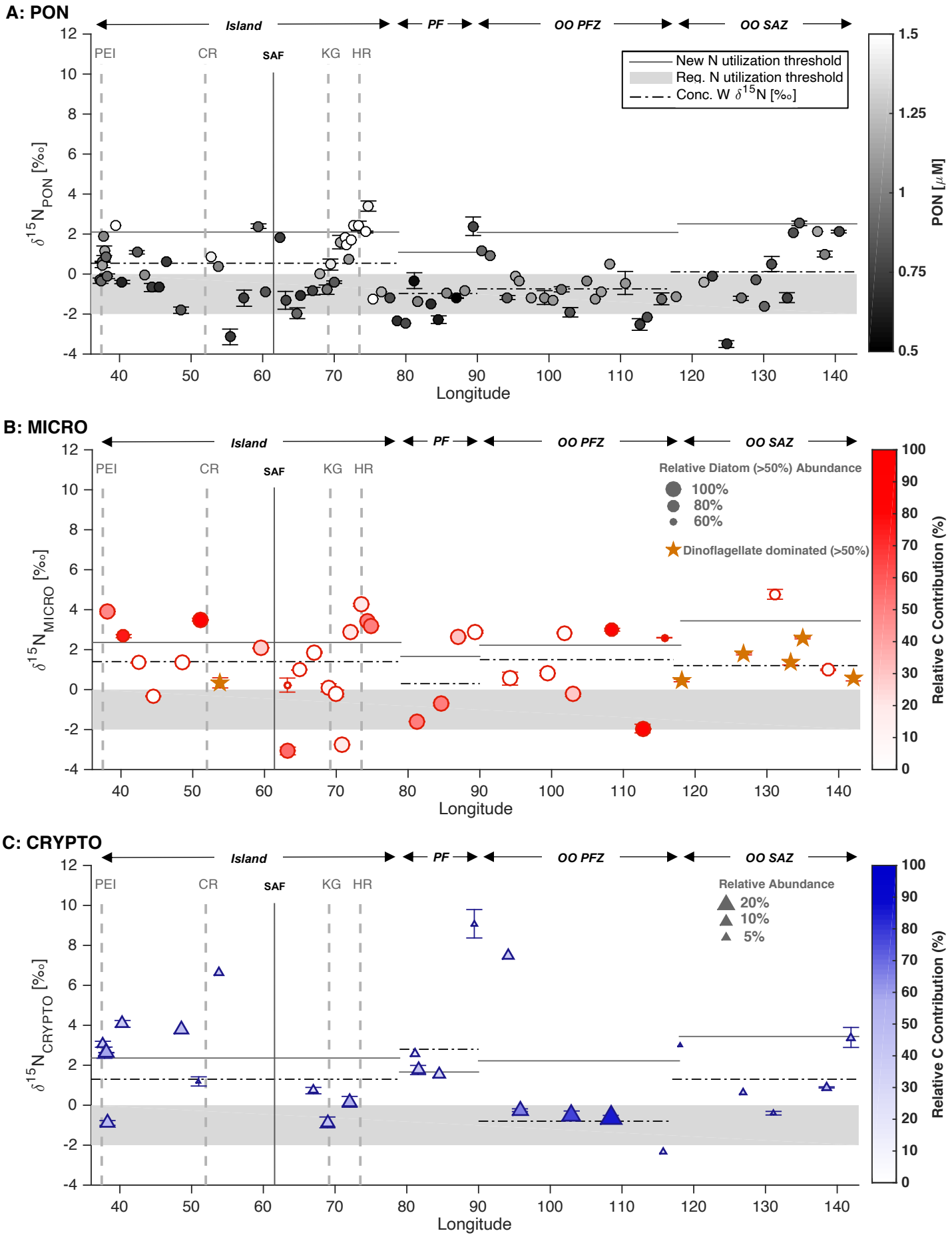
A: PON
Island
PF
OO PFZ
OO SAZ
PEI
CR
SAF
KG
HR
New N utilization threshold
Reg. N utilization threshold
Conc. W δ15N [‰]
δ15NPON [‰]
PON [μM]
Longitude
B: MICRO
Relative Diatom (>50%) Abundance
100%
80%
60%
Dinoflagellate dominated (>50%)
δ15NMICRO [‰]
Relative C Contribution (%)
C: CRYPTO
Relative Abundance
20%
10%
5%
δ15NCRYPTO [‰]

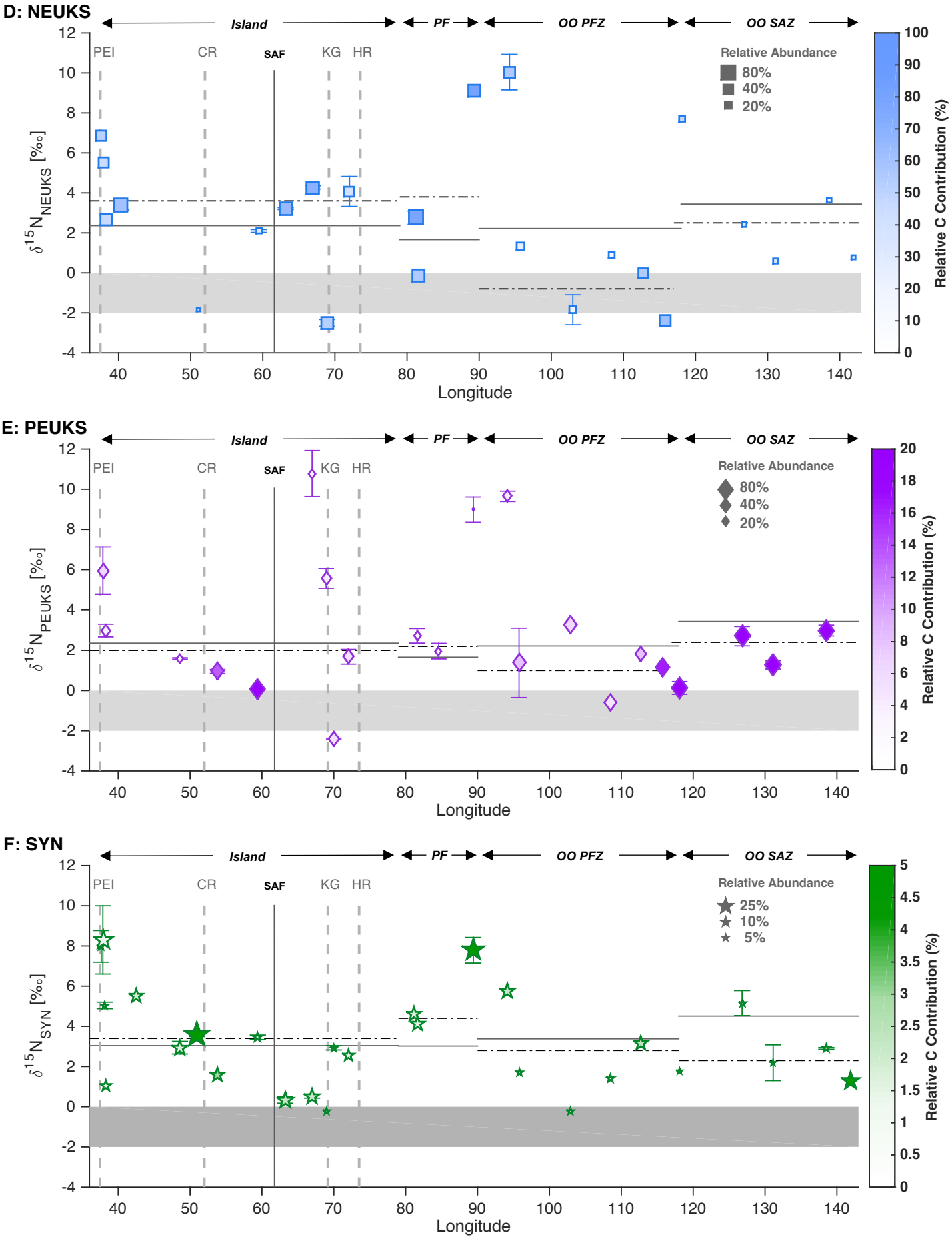
D: NEUKS
Island
PF
OO PFZ
OO SAZ
PEI
CR
SAF
KG
HR
Relative Abundance
80%
40%
20%
$\delta^{15}N_{NEUKS}$ [‰]
Relative C Contribution (%)
Longitude
E: PEUKS
Relative Abundance
80%
40%
20%
$\delta^{15}N_{PEUKS}$ [‰]
Relative C Contribution (%)
Longitude
F: SYN
Relative Abundance
25%
10%
5%
$\delta^{15}N_{SYN}$ [‰]
Relative C Contribution (%)
Longitude

Figure 4.9: $\delta^{15}N$ [‰ vs. Air] of particulate organic matter (PON) and phytoplankton populations inhabiting the surface waters across the transect. A: Bulk PON, B: Microplankton (>20 μm), C: Cryptophytes, D: Nanoeukaryotes, E: Picoeukaryotes, and F: *Synechococcus*. The intensity of the marker colour is indicative of the RCC (%, colour bar on right y-axis) while the size of the marker scales with RA (%, size scale provided on the top right of each plot; not the same for all populations). For panel B, diatom populations with abundances constituting >50% of the MICRO population are shown as circles while dinoflagellates with abundances >50% are shown as stars. The sectors are labeled along the top of the panels, the locations of the islands – PEI, CR, KG and HR – are shown by the vertical dashed grey lines, and the *Island Sector* SAF is shown by the vertical solid black line. The $\delta^{15}N$ that is expected if all biomass derives from new N assimilation (i.e., the new N utilization threshold) is represented by the solid black horizontal line and is different for each sector (see Methods 3.7.2. Note that the integrated product equation (equation 3.9, methods 3.7.3) is used to calculate the bulk PON new N threshold while the instantaneous product equation (equation 3.8, methods, 3.7.3) is used for the sorted phytoplankton population new N threshold calculations). The recycled nutrient (RN) utilization threshold is represented by the grey shaded region between -2‰ and 0‰ across the transect (e.g., Checkley & Miller, 1989; Waser et al., 1998; Lourey et al., 2003). The new N utilization threshold for SYN is different from that of the other phytoplankton groups because a lower-amplitude nitrate assimilation isotope effect is used (Table 3.3; Granger et al., 2010). The horizontal dash-dot line shows the concentration-weighted average $\delta^{15}N$ for each sector. Error bars show ± 1 standard deviation and are plotted where available. Underway and surface (i.e., ~5 m) CTD data are included.

Although the [PON] increases in the *OO PFZ Sector* to (section 4.2.2), the $\delta^{15}N_{PON}$ remains similar to that of the *PF Sector*, with a concentration-weighted average of -0.8±0.1‰, generally falling within the regenerated N threshold (Figure 4.9A). Between the surface and MLD of CTD 5, $\delta^{15}N_{PON}$ rises slightly, yielding a ML mean of 0.9±0.6‰ (Figure 4.10E).

A northward increase in concentration-weighted $\delta^{15}N_{PON}$ is observed from the *OO PFZ Sector* to the *OO SAZ Sector* (from -0.8±0.1‰ to 0.2±0.1‰, respectively) while the [PON] remains fairly constant at ~0.9 μM (Figure 4.9A). Due to the higher degree of NO_3^- assimilation in the SAZ (Figure 4.5A & B), the new N utilization threshold is elevated in $\delta^{15}N$ space compared to the other sectors (2.5‰ for the integrated product). While bulk particles near the SAF fall within the regenerated N threshold, from 135°E, they fall between the new and regenerated N thresholds (Figure 4.9A). This apparent shift in N source is reflected in the depth profiles; from a low-$\delta^{15}N_{PON}$ ML at CTD 6 near the SAF, to a high-$\delta^{15}N_{PON}$ ML at CTD 7 near the STF (Figure 4.10F & G, respectively).

4.5.2 Microplankton $\delta^{15}N$

The MICRO size class has a mean concentration-weighted $\delta^{15}N_{MICRO}$ of 1.4±0.1‰ in the *Island Sector* (Figure 4.9B). The MICRO populations surrounding the islands comprise almost 100% of diatoms with high $\delta^{15}N_{MICRO}$ values (near-island mean of 3.5±0.5‰) and they contribute >40% to the total C inventory

(Figure 4.9B). The MICRO populations from between the islands generally have lower $\delta^{15}N$ and RCC values, mainly falling between the new and regenerated N utilization thresholds. Surprisingly, a few diatom-dominated MICRO communities fall within the exclusively regenerated N utilization threshold in the *Island Sector*. These communities include those found between PEI and CR, just south of the SAF and in the vicinity of KG. At the one station downstream of CR where dinoflagellates dominate the MICRO population with a $\delta^{15}N_{MICRO}$ is 0.3±0.3‰, falling within the combined new and regenerated N utilization threshold (Figure 4.9B).

Low $\delta^{15}N_{MICRO}$ values (mean of -1.2±0.6‰) are observed in the western *PF Sector*, while higher values (mean of 2.8 ± 0.2‰) are observed to the east, with a concentration-weighted sector average of 0.3±0.1‰ (Figure 4.9B). The western MICRO samples contribute more to total phytoplankton C (~50%) and fall within the regenerated N threshold, while the eastern samples contribute ~15% of total C and fall within the new N utilization threshold.

The *OO PFZ Sector* has variable $\delta^{15}N_{MICRO}$ values (ranging from -2.0 to 3.0‰), indicating both new and regenerated N substrate dependence, with a similar concentration-weighted mean to that of the *Island Sector*, 1.5±0.2‰ (Figure 4.9B). Additionally, the MICRO RCC increases eastwards from <10% near the PF to >80% near the SAF, along with a decrease in diatom and an increase in dinoflagellate RAs.

The MICRO communities in the *OO SAZ Sector*, where dinoflagellates generally dominate, has a mean concentration-weighted $\delta^{15}N_{MICRO}$ of 1.2±0.1‰ (Figure 4.9B), suggestive of combined new and regenerated N utilization across this sector. Interestingly, these dinoflagellate populations yield low RCCs (Figure 4.7B), likely as a result of their low total abundances (Figure 4.7A). Similarly, the two diatom-dominated populations in this sector contribute only ~5% of total C. The $\delta^{15}N_{MICRO}$ of the diatom dominated population in the middle of the sector (4.8±0.3‰) is consistent with exclusive new N utilization, while the diatom dominated population closer to the STF has a $\delta^{15}N_{MICRO}$ (1.0±0.0‰) suggestive of combined new and regenerated N assimilation (Figure 4.9B).

4.5.3 Nanoplankton $\delta^{15}N$

Cryptophytes

In the vicinity of PEI and CR, CRYPTO populations generally have a high $\delta^{15}N$ suggestive of new N utilization, with a $\delta^{15}N_{CRYPTO}$ maximum for the *Island Sector* observed downstream of CR (6.6‰) and a concentration-weighted sector mean $\delta^{15}N_{CRYPTO}$ of 2.8±0.1‰ (Figure 4.9C). Although the CRYPTO

RAs are fairly uniform at all the islands (~12%), the $\delta^{15}N_{CRYPTO}$ of the PEI and CR populations describe new N utilization (PEI and CR mean of 2.4±0.8‰), whereas the $\delta^{15}N_{CRYPTO}$ of the KG Plateau populations describe a shift towards regenerated N utilization (KG Plateau mean of -0.4 ± 0.7‰) (Figure 4.9C). This is consistent with the CTD profiles, with CTD 3 (near the KG Plateau) having a mean ML $\delta^{15}N_{CRYPTO}$ of -0.7±1.3‰ (Figure 4.10C). Furthermore, CRYPTO populations near CR shift towards regenerated N utilization with depth; where CTD 2 (upstream of CR) describes a $\delta^{15}N_{CRYPTO}$ of 1.2 ± 0.2‰ at the surface that increases to 2.3‰ at 30 m before decreasing to -1.4‰ below 100 m (Figure 4.10B). At the PEI (CTD 1), exclusive new N utilization is inferred within the ML from the high mean $\delta^{15}N_{CRYPTO}$ of 4.0±1.9‰ (Figure 4.10A).

The *PF Sector* CRYPTO populations are high in $\delta^{15}N$, with a concentration-weighted sector mean $\delta^{15}N_{CRYPTO}$ of 1.7±0.0‰ that overlaps near-exclusively with the new N utilization threshold (Figure 4.9C). The highest $\delta^{15}N_{CRYPTO}$ of the transect, 9.1±0.7‰, is observed at the eastern PF crossing, followed by a $\delta^{15}N_{CRYPTO}$ of 7.5‰ in the *OO PFZ Sector*. The CTD profile for the *PF Sector* (CTD 4) implies dominant use of new N within and below the ML (ML $\delta^{15}N_{CRYPTO}$ mean of 1.7±0.2‰; Figure 4.10D).

Beyond the PF, the *OO PFZ Sector* is characterized by the highest average CRYPTO RA and RCC (15% and 49%, respectively), with low $\delta^{15}N_{CRYPTO}$ values (concentration-weighted mean $\delta^{15}N_{CRYPTO}$ of -0.8±0.1‰) (Figure 4.9C) indicative of regenerated N use. CRYPTO appear to shift towards combined new and regenerated N use with depth, indicated by a higher $\delta^{15}N_{CRYPTO}$ in the ML of CTD 5 (ML $\delta^{15}N_{CRYPTO}$ mean of 0.6±0.8‰) that tracks the ML $\delta^{15}N_{PON}$ closely (Figure 4.10E).

In contrast to the *OO PFZ Sector*, the *OO SAZ Sector* has the lowest RAs of CRYPTO across the transect (mean RA of 32%; Figure 4.7A & B) with the second lowest RCC (mean of 37%). The *OO SAZ Sector* populations show a range of $\delta^{15}N_{CRYPTO}$, with high values (e.g., 3.0‰ and 3.4±0.5‰) observed near the SAF and STF fronts and low $\delta^{15}N_{CRYPTO}$ in the middle of the sector (-0.4±0.1‰; Figure 4.9C). The CTD profiles for the *OO SAZ Sector* reflect the high-$\delta^{15}N$ trends observed near the fronts, describing continuous CRYPTO new N utilization with depth given the mean ML $\delta^{15}N_{CRYPTO}$ of 2.0±1.0‰ and 4.2±1.3‰ for CTD 6 and 7, respectively (Figure 4.10F & G), reverting back low-$\delta^{15}N$ values below the MLD (e.g., 0.1‰ and 0.8‰), describing combined new and regenerated N utilization.

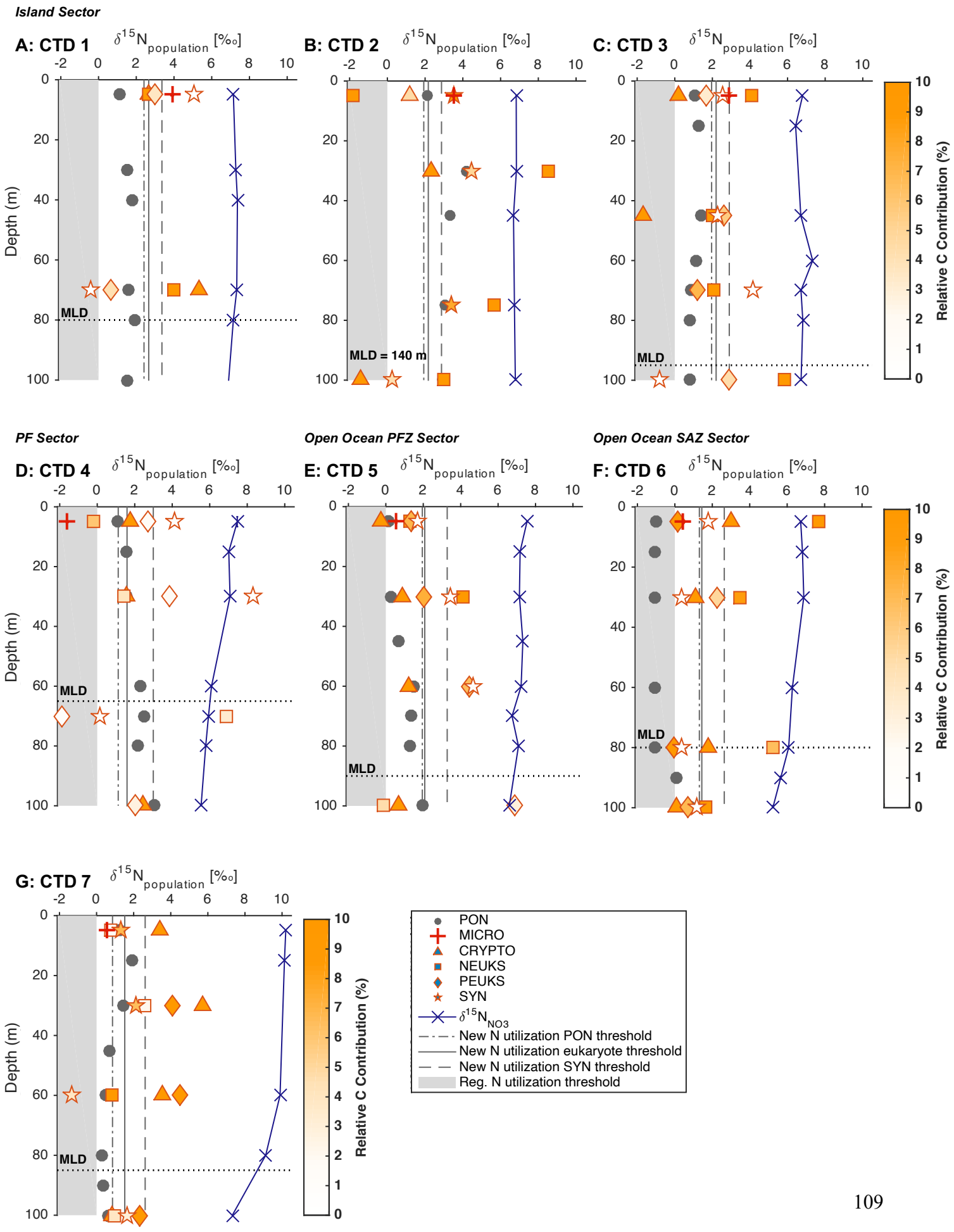
Island Sector
A: CTD 1
B: CTD 2
C: CTD 3
PF Sector
D: CTD 4
Open Ocean PFZ Sector
E: CTD 5
Open Ocean SAZ Sector
F: CTD 6
G: CTD 7
δ15N population [‰]
Depth (m)
MLD
MLD = 140 m
Relative C Contribution (%)
PON
MICRO
CRYPTO
NEUKS
PEUKS
SYN
δ15NNO3
New N utilization PON threshold
New N utilization eukaryote threshold
New N utilization SYN threshold
Reg. N utilization threshold

Figure 4.10: Vertical profiles (surface to 100 m) of the $\delta^{15}N$ [‰ vs. Air] of particulate organic matter (PON) and sorted phytoplankton populations for the seven CTD casts conducted during the transect. The different phytoplankton populations are indicated by different markers; PON by circles, CRYPTO by triangles, NEUKS by squares, PEUKS by diamonds, and SYN by stars. The intensity of the marker colour is indicative of the RCC (%), calculated relative to the total pico- and nanoplankton C contribution (i.e., excluding the MICRO, as these were only sampled at the surface; red star). Additionally, ambient $\delta^{15}N_{NO3}$ is shown by the dark blue crosses. For each cast, the MLD is indicated by the grey dotted horizontal line; where no MLD is indicated, the MLD was below the maximum depth of particle sampling. The new N utilization threshold for PON is represented by the vertical dashed-dot line (equation 3.9, methods 3.7.3), for the sorted populations of CRYPTO, NEUKS, and PEUKS by the solid black vertical line (equation 3.8, methods, 3.7.3), and for SYN by the vertical dashed line (equation 3.9, methods 3.7.3). The regenerated N utilization threshold is represented by the grey shaded region between -2‰ and 0‰ (e.g., Checkley & Miller, 1989; Waser et al., 1998; Lourey et al., 2003).

Nanoeukaryotes

The average concentration-weighted $\delta^{15}N_{NEUKS}$ across the *Island Sector* is high at 3.6±0.2‰, suggesting exclusive new N utilization (Figure 4.9D). Around PEI, HR, and upstream of KG, the NEUKS have high RAs (~60%), RCCs (~45%), and $\delta^{15}N_{NEUKS}$ (>2.4‰) (Figure 4.9D). Two stations in the *Island Sector* show low $\delta^{15}N_{NEUKS}$, including upstream of CR and in the vicinity of KG, of -1.9‰ and -2.5±0.2‰, respectively. This suggests exclusive use of regenerated N. For CTD 1 near the PEI and CTD 3 in the vicinity of the KG Plateau, the ML NEUKS are high in $\delta^{15}N$, with ML means of 3.3±1.0‰ and 2.7±1.2‰, respectively (Figure 4.10A & C). Upstream of CR at CTD 2, $\delta^{15}N_{NEUKS}$ is low in the very surface (-1.9‰), but high throughout the rest of the upper 100 m (mean $\delta^{15}N_{NEUKS}$ of 3.8±4.4‰; Figure 4.10B), suggestive of exclusive new N utilization. At 30m, the $\delta^{15}N_{NEUKS}$ is higher than the ambient $\delta^{15}N_{NO3}$ (8.5‰ and 6.8‰, respectively)

The $\delta^{15}N_{NEUKS}$ in the *PF Sector* varies, with the highest $\delta^{15}N_{NEUKS}$ near the PF crossings (up to 9.1‰) and a concentration-weighted mean $\delta^{15}N_{NEUKS}$ for the sector of 3.8±0.2‰ (Figure 4.9D). This suggests that these communities use both new and regenerated N substrates. The CTD 4 ML $\delta^{15}N_{NEUKS}$ increases with depth, from a mean of 0.6±1.1‰ in the upper 30 m (consistent with regenerated N use) to 6.9‰ just below the MLD (65m; implying exclusive new N utilization; Figure 4.10D)

The high $\delta^{15}N_{NEUKS}$ associated with the PF are also observed in the *OO PFZ Sector*, where the transect maximum $\delta^{15}N_{NEUKS}$ of 10.0±0.9‰ is observed (Figure 4.9D). Beyond the influence of the PF, a shift to lower $\delta^{15}N_{NEUKS}$ is observed with a range of 1.3‰ to -2.4‰, coinciding with lower NEUKS RAs. The concentration-weighted mean $\delta^{15}N_{NEUKS}$ for the *OO PFZ Sector* is -0.2±0.3‰, suggesting increased regenerated N assimilation compared to the previous sectors. However, this trend is not observed below

the surface where high $\delta^{15}N_{NEUKS}$ is observed (4.2‰ at 30 m) (CTD 5; Figure 4.10E). Below the ML, the $\delta^{15}N_{NEUKS}$ decreases to -0.1‰.

At the SAF crossing, the $\delta^{15}N_{NEUKS}$ is once again high (7.7‰) consistent with exclusive new N assimilation (Figure 4.9D). East of this in the *OO SAZ Sector,* the $\delta^{15}N_{NEUKS}$ decreases, as does the NEUKS RAs (<10%; Figure 4.7A). The concentration-weighted mean $\delta^{15}N_{NEUKS}$ in the *OO SAZ Sector* is 2.5±0.9‰, suggesting combined new and regenerated N utilization (Figure 4.9D). The shift from high $\delta^{15}N_{NEUKS}$ near the SAF to lower $\delta^{15}N_{NEUKS}$ northwards in the *OO SAZ Sector* is also apparent in the CTDs from the sector. CTD 6, near the SAF, shows high ML mean $\delta^{15}N_{NEUKS,}$ 5.5±2.1‰, decreasing to 1.7‰ below the MLD (80 m; Figure 4.10F). CTD 7, near the STF, shows higher $\delta^{15}N_{NEUKS}$, 2.6‰, at 30 m, with a shift to lower $\delta^{15}N_{NEUKS}$ both above (65 m) and below the MLD (85 m) (0.8‰ and 1.0‰, respectively) (Figure 4.10G).

4.5.4 Picoplankton $\delta^{15}N$

Picoeukaryotes

As for the NEUKS, the islands of PEI and upstream of KG yields $\delta^{15}N_{PEUKS}$ above the new N utilization threshold (PEI and KG mean of 6.3±3.3‰; Figure 4.9E). However, due to the higher RA of PEUKS with lower $\delta^{15}N_{PEUKS}$ near CR and HR and over the KG Plateau, the concentration-weighted mean $\delta^{15}N_{PEUKS}$ for the *Island Sector* is 2.0±0.2‰, indicative of new and regenerated N assimilation (Figure 4.9E). The high surface $\delta^{15}N_{PEUKS}$ near the PEI is not maintained at depth where lower $\delta^{15}N_{PEUKS}$ is observed (0.7‰ at 70 m; CTD1; Figure 4.10A). In contrast, the $\delta^{15}N_{PEUKS}$ over the KG Plateau is variable with depth, ranging from 1.6‰ at the surface, indicating combined new and regenerated N use, to 2.6‰ at 45 m, indicative of exclusive new N uptake, to 1.1‰ at 70 m (CTD 3; Figure 4.10C). The concentration-weighted ML mean $\delta^{15}N_{PEUKS}$ is 1.8±0.7‰ at this station. No $\delta^{15}N_{PEUKS}$ data are available for CTD 2 (Figure 4.10B).

High $\delta^{15}N_{PEUKS}$ are observed across the *PF Sector*, with a concentration-weighted mean of 2.2±0.4‰, suggesting exclusive new N utilization (Figure 4.9E). This trend holds throughout the ML, where the concentration-weighted mean $\delta^{15}N_{PEUKS}$ is 3.3±0.8‰ (CTD 4; Figure 4.10D). $\delta^{15}N_{PEUKS}$ decreases below the MLD to -1.9‰, suggesting a shift to regenerated N utilization.

The surface $\delta^{15}N_{PEUKS}$ near the PF is high, 8.9±0.6‰ and 9.7±0.3‰ in the *PF Sector* and *OO PFZ Sector,* respectively (Figure 4.9E). Downstream in the *OO PFZ Sector,* lower concentration-weighted

mean $\delta^{15}N_{PEUKS}$ is observed (1.0±0.6‰). The majority of the $\delta^{15}N_{PEUKS}$ values measured for the *OO PFZ Sector* are consistent with combined new and regenerated N use. The $\delta^{15}N_{PEUKS}$ at the surface declines towards the SAF, along with an increase in PEUKS RA and RCC. The $\delta^{15}N_{PEUKS}$ increases with depth, with a ML mean of 2.6±1.6‰ and a single value of 6.9‰ below the MLD (90 m) (CTD 5; Figure 4.10E).

Mixed N substrate utilization is sustained into the *OO SAZ Sector*, along with higher PEUKS RAs and RCCs, and the surface concentration-weighted sector mean $\delta^{15}N_{PEUKS}$ is 1.7±0.3‰ ‰ (Figure 4.9E). For CTD 6 near the SAF, $\delta^{15}N_{PEUKS}$ is 2.2‰ at 30 m, approximately equal to the new N utilization threshold, and decreases to -0.1‰ at the MLD (80 m) (Figure 4.10F). Closer to the STF, the ML PEUKS populations have high $\delta^{15}N$ values, indicating exclusive new N utilization through the ML, yielding a ML mean of $\delta^{15}N_{PEUKS}$ of 4.3±0.3‰ (CTD 7; Figure 4.10G).

Synechococcus

SYN have been assigned their own new N utilization thresholds as a result of their lower-amplitude $^{15}\varepsilon$ for NO_3^- assimilation (Granger et al., 2010). Around the PEI and upstream of CR, higher SYN RAs and $\delta^{15}N_{SYN}$ values above the new N utilization threshold of 3.0‰ are observed (Figure 4.9F; Table 3.3). Upstream and around the KG Plateau, lower $\delta^{15}N_{SYN}$ are observed, indicative of combined new and regenerated N utilization, with the station closest to KG showing exclusive regenerated N utilization (Figure 4.9F). Due to the high RAs of SYN around the PEI and CR, the surface concentration-weighted mean $\delta^{15}N_{SYN}$ for the *Island Sector* is high, 2.7±0.2‰. This trend is not observed at depth around the PEI, where a decrease in $\delta^{15}N_{SYN}$ to -0.4‰ at 70 m occurs (Figure 4.10A). By contrast, CTD 2 near CR shows high $\delta^{15}N_{SYN}$ in the ML between the surface and 75 m (ML mean of 3.8±0.6‰), shifting to lower $\delta^{15}N_{SYN}$ at 100 m (0.3‰) (Figure 4.10B). Similar $\delta^{15}N_{SYN}$ values were observed over the KG Plateau at the surface and 45 m (2.4±0.2‰), increasing to 4.1‰ at 70 m before decreasing to -0.8‰ below the MLD (Figure 4.10C).

Very high $\delta^{15}N_{SYN}$ is observed across the *PF Sector*, yielding a surface concentration-weighted mean $\delta^{15}N_{SYN}$ of 4.4±0.2‰ (Figure 4.9F). For CTD 4, ML $\delta^{15}N_{SYN}$ is also high, averaging 6.2±2.3‰, and decreasing to ~0.1‰ below the MLD (Figure 4.10D). Continuing eastwards, high $\delta^{15}N_{SYN}$ SYN RA are observed across the PF, at 7.8±0.6‰ and 43%, respectively, downstream of which both $\delta^{15}N_{SYN}$ and SYN RA decrease (Figure 4.9F).

Across the *OO PFZ Sector*, the surface concentration-weighted mean $\delta^{15}N_{SYN}$ is 1.6±0.2‰, which falls between the new and recycled N utilization thresholds (Figure 4.9F). Below the surface (30 m and 60 m), higher $\delta^{15}N_{SYN}$ is observed (3.5‰ and 4.7‰), indicating exclusive new N utilization (Figure 4.10E).

Similar to the *OO PFZ Sector*, SYN RAs are relatively low in the *OO SAZ Sector* (mean of 4%) and $\delta^{15}N_{SYN}$ is also low (surface concentration-weighted mean of 2.3±0.4‰; Figure 4.9F). On exception is a population at ~ 127°E that is high in $\delta^{15}N_{SYN}$ (5.2±0.6‰), suggesting exclusive N utilization. Unlike in the *OO PFZ Sector*, the SYN populations at depth in the *OO SAZ Sector* do not tend towards higher $\delta^{15}N_{SYN}$ but rather to lower $\delta^{15}N_{SYN}$ (mean ML of 0.8±0.8‰ and 0.7±1.8‰ for CTD 6 and 7, respectively) (Figure 10F & G).

5. Discussion

This study seeks to identify and quantify the relative abundances and C contributions of the dominant summertime phytoplankton assemblages across the Indian sector of the Subantarctic, and to determine the relative importance of NO_3^- versus NH_4^+ for supporting their growth, with implications for their contributions to C export. One prominent observation is the difference in phytoplankton community composition and apparent productivity in regions influenced by the islands compared to the open-ocean sectors. First, the implications of these observations are explored. Second, the biogeochemical and ecological consequences of NO_3^-- versus NH_4^+-supported phytoplankton growth and C export potential are addressed. Finally, a surprising ecological finding regarding the distribution and apparent nutrient utilization strategy of *Synechococcus* is discussed.

5.1 The Island Mass Effect: Shaping the chemical and biological regimes across the Indian Sector of the Subantarctic Ocean

Phytoplankton abundance and community composition are influenced by the availability of macronutrients such as NO_3^-, PO_4^{3-}, and Si, as well as by micronutrients such as Fe (e.g., Blain et al., 2001; Trull et al., 2001a & 2015; Salter et al., 2007; Planquette et al., 2007; Holmes et al., 2015). The impact of Fe availability on Southern Ocean phytoplankton communities and their ability to consume macronutrients has been well-studied, especially around the island archipelagos of Crozet (CR) and Kerguelen (KG) through research programs including CROZEX, KEOPS 1 & 2, and HEOBI (de Baar et al., 2005; Boyd et al., 2007; Pollard et al., 2007a; Poulton et al., 2007; Trull et al., 2015; Holmes et al., 2019, and others). As a result of the apparent partial alleviation of Fe limitation around these islands, up to 10-fold larger phytoplankton blooms have been observed, with near-island waters estimated to export two- to three-fold more C compared to offshore Subantarctic blooms (e.g., Blain et al., 2008; Savoye et al., 2008; Pollard et al., 2007a). Although the influence of some individual islands has been extensively studied, the combined IME of the islands in the Indian sector of the Subantarctic, and its implications for C export, is not well constrained by *in situ* measurements.

To evaluate the impact of the IME on macronutrient drawdown, phytoplankton ecology, and the biological C pump, we compare macro- and micronutrient concentrations and indicators of productivity between the *Island Sector* and the *Open Ocean Sectors* (both the *OO PFZ* and *OO SAZ Sectors*), followed by a comparison of phytoplankton community composition, relative abundance (RA), and relative C content (RCC). Comparing the *Island* and *Open Ocean Sectors* solely on the basis on of biogeochemical and ecological characteristics is justified by the fact that similar water masses are

present in these sectors since they both incorporate the SAZ and PFZ, allowing water masses to be eliminated as a contributor to the observed differences in phytoplankton abundance and composition. Physical characteristics such as SST support this conclusion, with no statistical difference between sectors (p >0.05; mean *Island Sector* SST was 4.8±1.6°C and mean *Open Ocean Sectors* was 6.3±3.0°C; evaluated here and throughout using the Kruskal-Wallis non-parametric one-way analysis of variance to test differences between means; Kruskal & Wallis, 1952). This leads to the hypothesis that the observed variability between the *Island Sector* and the *Open Ocean Sectors* is driven by a combination of localized biogeochemical processes and mesoscale physical dynamics.

5.1.1 Evidence for increased productivity in the Island Sector

Overall, primary productivity is enhanced in the *Island Sector* compared to the *Open Ocean Sectors* as a result of increased micro- and macronutrient stocks, as per this study and previous studies (discussed further in section 5.1.2; Planquette et al., 2007; Trull et al., 2015; Holmes et al., 2019; Janssen et al., 2020). Two different indicators can be used to constrain the relative rates of productivity on different time-scales: upper ocean [NH_4^+] can be used to infer productivity over short time-scales (~days) (Hoch et al., 1992; Pennock et al., 1996; Waser et al., 1998; Lourey et al., 2003), while [PON] reflects the net production of organic biomass over the growing season (Rau et al., 1990; Fawcett et al., 2011).

[NH_4^+] is an indicator of biological activity and is significantly higher in the *Island Sector* compared to the *Open Ocean Sectors* (p<<0.005) (Figure 4.1D). While there may be some contribution from island runoff (Tatur & Myrcha, 1983), this input is likely small and its impact localized (Treasure et al., 2015). Surface [NH_4^+] of >1 μM throughout the *Island Sector* (compared to <1 μM in the *Open Ocean Sectors*, Table 5.1) is attributed to higher primary productivity (and thus microbial cycling and zooplankton production) near the islands and SAF (~61°E). Indeed, zooplankton are recognized as an important driver of phytoplankton productivity in the Southern Ocean through the exertion of a top-down control (grazing, which controls 'yield') and a bottom-up control through nutrient recycling via NH_4^+ excretion (which controls 'rate'; e.g., Priddle et al., 1998; Alcaraz et al., 1998; Lehette et al., 2012; Arístegui et al., 2014). Concentrations of NH_4^+ in the ML layer of the Subantarctic are thought to be controlled by the balance between nocturnal production by zooplankton and diurnal uptake by phytoplankton (Priddle et al., 1998). Although previous studies have shown high rates of NH_4^+ assimilation in the Subantarctic, including around the islands (Mosseri et al., 2008; Cavagna et al., 2014; Mdutyana et al. 2020), the high surface concentrations in the vicinity of the islands (e.g., 4.0±0.0 μM near the KG Plateau) indicate that production far exceeds consumption. In addition to zooplankton production and phytoplankton

assimilation, [NH_4^+] is further influenced by water-mass movement, where waters retained by island-induced eddies allow for the accumulation (through regeneration) or depletion (through uptake) of nutrients, before this signal is advected offshore by the ACC (Perissinotto et al., 1992). A longer residence time for NH_4^+ is inferred at PEI (CTD 1) in comparison to CR (CTD 2) and KG (CTD 3) from the higher shallow [NH_4^+] near the PEIs (5.5±0.3 μM vs. 0.9±0.2 μM and 4.0±0.0 μM at CR and KG, respectively). In addition, a deep regeneration signature is observed between 80 m and 100 m at the PEIs, with the [NH_4^+] surpassing that at the surface (6.6±0.1 μM) (Figure 4.4C). The differences between the PEI and CR/KG observations may derive from the location of CTD 1 within a coastal retention zone while CTD 2 and 3 are potentially located upstream of the established plateau anticyclonic eddies (Figure 1.5). Regardless of water-mass residence times in the *Island Sector*, the mean elevated [NH_4^+] suggests increased biological activity, including from zooplankton, compared to the *Open Ocean Sectors.* This is a manifestation of the IME (Figure 1.4).

The concentration of PON in the ML is indicative of net biomass accumulation (with the caveat that it is susceptible to microbial remineralization and heterotrophic scavenging; Lourey & Trull, 2001; Trull et al., 2001b; Lourey et al., 2003; Hannides et al., 2013; Smart et al., 2020), which is related (at least qualitatively) to productivity. The surface [PON] shows localized increases around the islands and over the plateau regions, up to 1 μM higher in near-island waters compared to the *Open Ocean Sectors* (Figure 4.1E). [PON] is particularly high around the KG Plateau and HR (means of 1.6±0.3 μM and 3.4±0.3 μM, respectively), which can be attributed to accumulation in slow-moving waters over the plateau (Park et al., 2008b), as well as increased productivity (Trull et al., 2015; Holmes et al., 2019). This further evinces the IME, in particular its localized expression. The inter-island [PON] (~0.9 μM) is similar to the mean surface *Open Ocean Sectors* [PON] (1.0±0.2 μM), while the *Island Sector* as a whole is characterized by a mean [PON] of 1.1±0.3 μM (Table 5.1). Despite the obvious increases in [PON] near the islands, there is no significant difference (p>0.05) between mean surface or ML [PON] in the *Island* and *Open Ocean Sectors*. This result is perhaps not surprising given that the standing stock of surface PON (or indeed, biomass in any form) is not a quantitative representation of the ongoing biological activity (Rau et al., 1990; Fawcett et al., 2011). For example, more PON may be removed from surface waters in the *Island Sector* than the *Open Ocean Sector* due to: i) an enhanced (even if only slightly) and consistent export flux driven by the higher productivity of larger and/or more ballasted phytoplankton (e.g., diatoms) near the islands (Poulton et al., 2015; Trull et al., 2015) and ii) increased near-island activity by higher trophic levels such as zooplankton that remove PON through grazing (Morel et al., 1991; Poulton et al., 2015; Assmy et al., 2015).

Table 5.1: Sector averages (standard deviations) for nutrient, physical (SST), bulk particle, and phytoplankton-specific parameters.

Parameter		Units	*Island*	*PF*	*OO PFZ*	*OO SAZ*	*Subantarctic Transect*[1]
Nitrate (NO_3^-)		[µM]	21.8 (3.0)	24.3 (2.3)	23.1 (1.3)	14.1 (5.3)	20.5 (4.8)
C. W. $\delta^{15}N_{NO3}$[2]		(‰)	7.1 (0.2)	6.6 (0.1)	7.2 (0.1)	8.9 (0.2)	7.3 (0.1)
Silicate ($Si(OH)_4$)		[µM]	7.3 (4.4)	22.7 (4.7)	2.6 (2.3)	1.0 (0.4)	5.2 (4.5)
Silicate Star (Si*)		[µM]	-14.5 (3.0)	-2.7 (4.2)	-20.4 (1.7)	-12.8 (5.2)	-15.2 (4.2)
Phosphate (PO_4^{3-})		[µM]	1.6 (0.2)	1.6 (0.1)	1.6 (0.1)	1.1 (0.3)	1.5 (0.3)
Ammonium (NH_4^+)		[µM]	1.6 (1.2)	0.4 (0.3)	0.6 (0.3)	0.5 (0.5)	1.3 (1.1)
PON		[µM]	1.1 (0.3)	0.8 (0.2)	1.0 (0.1)	0.9 (0.2)	1.0 (0.3)
C. W. $\delta^{15}N_{PON}$[2]		(‰)	0.6 (0.1)	-1.1 (0.2)	-0.8 (0.1)	0.2 (0.1)	0.2 (0.1)
SST		(°C)	4.8 (1.3)	2.4 (1.0)	3.8 (0.5)	8.9 (2.0)	5.4 (2.3)
Phytoplankton populations							
MICRO	RA[3]	(%)	<1.0	1.4	<1.0	<1.0	<1.0
	RCC[4]	(%)	24.6	28.2	33.6	35.2	28.9
	C. W. $\delta^{15}N_{MICRO}$[2]	(‰)	1.4 (0.1)	0.3 (0.1)	1.5 (0.2)	1.2 (0.1)	1.4 (0.1)
CRYPTO	RA	(%)	12.2	7.3	15.3	3.2	11.3
	RCC	(%)	47.1	29.9	49.0	37.4	45.8
	C. W. $\delta^{15}N_{CRYPTO}$[2]	(‰)	2.8 (0.1)	1.7 (0.0)	-0.8 (0.1)	1.0 (0.1)	1.2 (0.2)
NEUKS	RA	(%)	40.7	63.2	29.5	9.1	33.6
	RCC	(%)	30.6	48.2	15.8	16.9	25.0
	C. W. $\delta^{15}N_{NEUKS}$[2]	(‰)	3.6 (0.2)	3.8 (0.2)	-0.2 (0.3)	2.5 (0.2)	2.8 (0.2)
PEUKS	RA	(%)	31.8	8.3	44.6	78.9	43.1
	RCC	(%)	1.8	<1.0	1.5	10.3	3.3
	C. W. $\delta^{15}N_{PEUKS}$[2]	(‰)	2.0 (0.2)	2.2 (0.4)	1.0 (0.6)	1.7 (0.3)	1.9 (0.3)
SYN	RA	(%)	15.1	20.0	9.4	8.7	12.7
	RCC	(%)	<1.0	<1.0	<1.0	<1.0	<1.0
	C. W. $\delta^{15}N_{SYN}$[2]	(‰)	2.7 (0.2)	4.4 (0.2)	1.6 (0.2)	2.3 (0.4)	2.3 (0.2)

[1]Average calculated from all the Subantarctic sectors including the *Island Sector*, the *PF Sector,* the *Open Ocean PFZ Sector* and the *Open Ocean SAZ Sector*

[2] Concentration-weighted (C. W.) $\delta^{15}N$ calculation

[3] Relative abundance (methods 3.7.5, equation 3.13)

[4] Relative carbon contribution (methods 3.7.5, equation 3.14)

5.1.2 Macro- and micronutrient supply supporting higher productivity around the islands

Various biological and physical mechanisms have been shown to naturally fertilize the otherwise Si- and Fe-deplete HNLC surface waters of the Subantarctic with micro- and macronutrients (Tyrrell et al., 2005; Blain et al., 2001; Planquette et al., 2007; Trull et al., 2015; Holmes et al., 2019). These include: i) bathymetric-induced mesoscale upwelling of deep waters with elevated [NO_3^-], [PO_4^{3-}], [$Si(OH)_4$], and sometimes [Fe] (e.g., Grindley & David, 1985; Bracher et al., 1999; Gove et al., 2016; Hoppe et al., 2017; Ardyna et al., 2019), ii) enhanced zooplankton recycling of nutrients in the upper ocean supported by elevated concentrations of phytoplankton biomass, with the main form of N excretion being NH_4^+ (e.g., Priddle et al., 1998; Alcaraz et al., 1998; Lehette et al., 2012; Arístegui et al., 2014), and iii) terrestrial runoff of ground-, rain- and/or glacial water enriched in geological minerals such Fe and Si from basaltic rock formations and/or animal-derived nutrients including NH_4^+ (Tatur & Myrcha, 1983; de Baar et al., 1995; Blain et al., 2001; Moore & Abbott, 2002; Holeton et al., 2005; Tyrrell et al., 2005; Pollard et al., 2009; Salter et al., 2012). This study considers bathymetric-induced upwelling and marine biological activity as the primary sources of nutrients related to the IME (i.e., i and ii). Terrestrial NH_4^+ sources (i.e., iii) including island-runoff and atmospheric deposition have been shown to play only a small, generally localized role (i.e., only very close to the islands in the case of runoff) in Subantarctic marine ecosystem production compared to upwelled or recycled nutrients (Planquette et al., 2007; Treasure et al., 2018).

Bathymetric-induced upwelling is a product of high-energy internal waves that drive vertical eddy diffusivity over shallower topographic features such as plateaus and continental rises (Park et al., 2008a). This deep upwelling mechanism is not only consistent with the surface nutrient distributions observed here (Figure 4.1), but also with physical dynamics such as a deepening of the MLD and colder SSTs coincident with the relatively elevated surface nutrient concentrations measured for CTDs 1, 2, and 3 near the islands (Table 3.1, Figure 3.2 & 3.3). While the *Island Sector* CTD casts do not necessarily overlap directly with upwelling sites, all casts were either positioned on bathymetric gradients where upwelling signals are evident through lateral advection and vertical eddy diffusivity (e.g., CTD 2 conducted over the CR Plateau and CTD 3 over the KG Plateau), or in potential water-mass retention zones on the leeside of islands (e.g., CTD 1 that was conducted adjacent to the PEIs; Figure 1.5 & 4.6).

The IME is evident in the differences in surface macronutrient concentrations in the *Island* versus *Open Ocean Sectors* (Figure 4.1). Higher NO_3^- and PO_4^{3-} concentrations in the *Island Sector* ($p<0.01$) are attributed to frequent deep-water sourced nutrient resupply events around the islands, which overprint (at least partly) the signal of assimilation in the surface. In the *Open Ocean Sectors*, particularly the *OO*

SAZ, NO_3^- and PO_4^{3-} concentrations decline from south to north likely due to an increased alleviation of light stress northwards, possibly encouraging a higher degree of assimilation as well as the equatorward transport of SAZ surface waters by Ekman transport (Figure 4.1; Sigman et al., 1999; Janssen et al., 2020), although they never reach limiting levels (Blain et al., 2007; Mosseri et al., 2008). In contrast, [$Si(OH)_4$] reaches near-zero concentrations across most of the *Open Ocean Sectors*, consistent with the well-recognized [$Si(OH)_4$] limitation that characterizes the Subantarctic (Table 5.1; Trull et al., 2001a & 2015; de Baar et al., 2005; Poulton et al., 2007; Holmes et al., 2019; Henley et al. 2020). Higher [$Si(OH)_4$] near the islands (7.3±4.4 µM versus 1.9±2.5 µM in the *Open Ocean Sectors*; $p<<0.005$) results from frequent deep-water sourced nutrient resupply events and suggests that [$Si(OH)_4$] is a good IME "indicator".

Depth profiles at the CTD stations show evidence of macronutrient resupply (Figure 4.4) around the islands that sustains phytoplankton blooms over the austral summer (e.g., Blain et al., 2007; Mongin et al., 2008; Planquette et al., 2007; Trull et al., 2015; Holmes et al., 2019). While the typical deep MLDs usually associated with upwelling are not apparent at the near-island CTD stations, except at CTD 2 (MLD ~140 m), there is a significant difference ($p<<0.005$) between the SST in the *Island* versus *Open Ocean Sectors,* 4.8±1.4°C and 6.3±3.0°C, respectively (Table 5.1). The colder island SST temperatures are evidence of upwelling into the surface layer. Although the [$Si(OH)_4$] profiles show a clear decrease in the ML relative to the subsurface concentrations as a result of uptake by phytoplankton, the *Island* stations nonetheless have higher ML [$Si(OH)_4$] (6.9±3.6 µM; average of CTD 1, 2 and 3) than the *Open Ocean Sector* stations (2.4±1.7 µM; average of CTD 5, 6 and 7). This, too, is consistent with recent upwelling in the vicinity of the islands.

Near the PEIs where the upper ML is shallow (85 m) relative to the other *Island Sector* stations, the mean [$Si(OH)_4$] is comparatively low at 3.2±0.7 µM. In addition, the greatest net ML Si drawdown in the *Island Sector*, calculated as the difference in [$Si(OH)_4$] between the mean ML concentration and that of UCDW at ~400 m (>30 µM), occurs around the PEIs. These observations are suggestive of a retention zone on the leeside of the island, characterized by reduced upward mixing, increased stratification, and slow advection offshore (Perissinotto & Duncombe Rae, 1990; Pakhomov et al., 2000; Ansorge & Lutjeharms, 2002). Previous studies have suggested that if the core of the SAF (and the strong currents associated with it) is displaced equatorward, as in the present study, the slower flow of the ACC in the SAZ or PFZ introduces weak advective forces that allow for the formation of eddies and retention over the plateau between the PEIs. CTDs 2 and 3 around the CR and KG plateaus were conducted upstream of recognized anticyclonic features (Pollard et al., 2007b; KG Plateau, Holmes et al., 2019). These sites

therefore have deeper MLs (140 m and 95 m, respectively) and higher mean upper ML [$Si(OH)_4$] (7.2±0.1 µM and 10.5±0.6 µM, respectively) than CTD 1, consistent with bathymetric upwelling driven by enhanced eddy diffusivity over the shoaling plateau (Figures 1.4 & 1.5). The upwelled waters are subsequently transported over the plateau region via the anticyclonic features (Pollard et al., 2007b; Holmes et al., 2019). In the case of the CR plateau, the anticyclonic flow can contribute nutrients, including Fe, to the northern S-bend retention zone that support the spring bloom (Lucas et al., 2007; Seeyave et al., 2007) and/or sustain a bloom closer to the islands in the later summer months (Pollard et al., 2002, 2007a & b; Venables et al., 2007, Poulton et al., 2007; Planquette et al., 2007). Similarly, the Kerguelen Plateau's anticyclonic circulation ultimately enters a recirculation feature to the northwest of the plateau (d'Ovidio et al., 2014; Park et al., 2014). This slow-moving flow results in a relatively long residence time (2 to 3 months) of water over the plateau (Park et al., 2008a; Holmes et al., 2019), which allows for a sustained phytoplankton bloom in this region (Blain et al., 2007; Mongin et al., 2008). With regards to other upwelled macronutrients (i.e., NO_3^- and PO_4^{3-}), similar trends to Si are evident in the *Island Sector*, with the upper ML concentrations of NO_3^- and PO_4^{3-} confirming upward mixing and a higher degree of drawdown in the retention region downstream of the PEIs.

To better understand the Fe dynamics around the islands versus in the open ocean, [DFe] data from Janssen et al. (2020) that were collected during the ACE cruise are used (Figure 5.1A), from CTD 3 over the KG Plateau to the *OO SAZ* (i.e., including KG and the open ocean). Unfortunately, no Fe data are available for CTD 1-2; here, Fe supply is inferred from the bathymetric-induced upwelling mechanisms that supply macronutrients to the ML, augmented using estimates from previous studies (e.g., Pollard et al., 2007a & b; Poulton et al., 2007; Park et al., 2008a; Mongin et al., 2008; Trull et al., 2015; Holmes et al., 2019). Low ML [DFe] (the most bioavailable form of Fe) is observed across the Subantarctic, <0.2 nM (Janssen et al., 2020), while some open ocean HNLC stations get as low as <0.1 nM (Trull et al., 2015). Although localized increases in [DFe] occur at the PF, up to ~0.26 nM (Trull et al., 2015), the concentrations broadly suggest pervasive and severe Fe-limitation across the transect (e.g., de Baar et al., 1999; Boyd et al., 1999; Hutchins et al., 2001; Sedwick et al., 2002 & 2008; Ellwood e al., 2008; Trull et al., 2015; Holmes et al., 2019; Janssen et al., 2020).

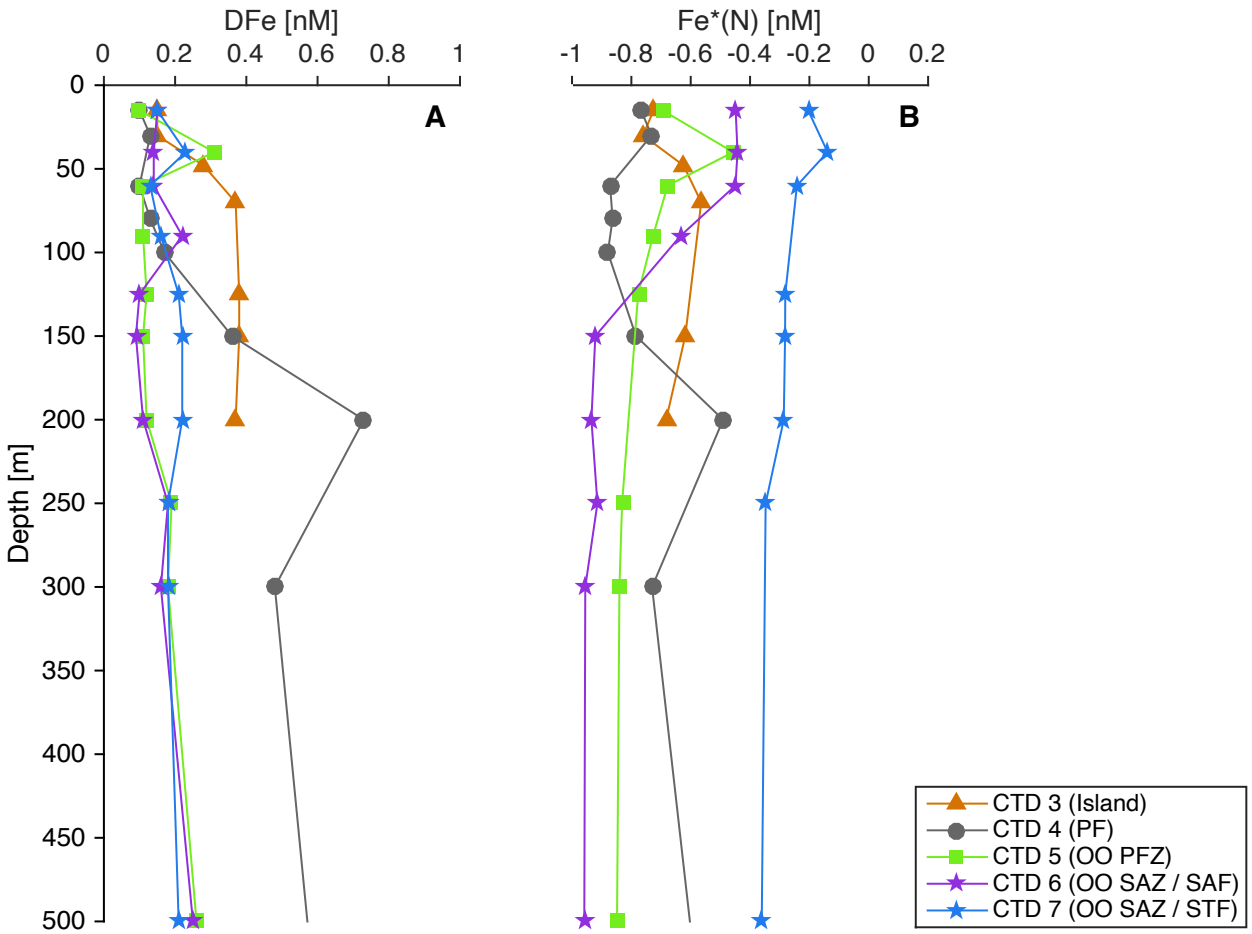

Figure 5.1: Vertical profiles (surface to 500 m) of A: dissolved iron (DFe) concentrations and B: Fe*(N) from five of the CTD casts conducted across the summertime transect, including CTD 3 – 7. Fe data are from Janssen et al., 2020, while the NO_3^- concentration data used to calculate Fe*(N) (Methods 3.7.2, equation 3.7) are from this study (Figure 4.4).

The entrainment of deep water is considered the main source of Fe (and macronutrients) to the Southern Ocean surface (Tagliabue et al., 2014). The strong decoupling between the nutricline and ferricline depths in the summer Subantarctic (including at the fronts, with the ferricline generally lying at 100 – 300 m, whereas the nutricline is generally <100 m deep; Tagliabue et al., 2014; Janssen et al., 2020) contributes to the relative excess of macronutrients compared to Fe in the ML, which limits phytoplankton growth (Croot et al., 2007; Ellwood et al., 2008; Bowie et al., 2009; Tagliabue et al., 2014; Janssen et al., 2020). The increased productivity around the islands is a consequence of the small terrestrially-derived Fe input (e.g., Martin, 1990; Ardelan et al., 2010; Gerringa et al., 2012) and a large bathymetric-induced entrainment mechanism whereby the ferricline is raised to a depth more similar to that of the nutricline (Tagliabue et al., 2014). This creates contrasting Fe environments in the *Island* versus the *Open Ocean Sectors*. The highest surface Fe concentrations are observed near-shore to the

islands, progressing to lower concentrations offshore (Holmes et al., 2019; Janssen et al., 2020). At the time of sampling, [Fe] around KG ranges from 0.4 to 0.7 nM (Figure 5.1, Janssen et al., 2020), similar to the concentrations reported by Trull et al. (2015), including a [Fe] of 0.4 nM for the recirculation feature and 0.2 nM for the plateau region. Similar mechanisms can explain the elevated [Fe] downstream of HR, observed to be >1.5 nM (Holmes et al., 2019), and CR, observed to be >1.0 nM (Planquette et al., 2007). While there are no Fe data available for PEI, increased concentrations are expected near-shore as a result of similar bathymetric-induced mechanism.

Although the elevated *Island Sector* Fe concentrations suggest an alleviation of phytoplankton Fe-stress in these regions, Holmes et al. (2019) posit that this is only the case in the waters closest to the islands, with bathymetric-induced entrainment of Fe remains largely insufficient to meet phytoplankton requirements (Twining & Baines, 2013; Bowie et al., 2015; Holmes et al., 2019; Janssen et al., 2020). This hypothesis is further investigated with the Fe* tracer (Figure 5.1B, methods 3.7.2), where a positive Fe* indicates that sufficient Fe is available to theoretically drive NO_3^- concentrations to depletion, while a negative Fe* implies that this is not the case (Holmes et al., 2019). Fe* is negative across the transect, even around KG and the fronts, indicating perennial Fe-limitation. Interestingly, the CTDs conducted near the SAF and STF (CTD 6 and 7, respectively) have the highest ML Fe* values (-0.2 nM and -0.4 nM, respectively). This likely derives from both the lower [NO_3^-] in the *OO SAZ* ML as well as frontal upwelling of Fe. Furthermore, the shallow CTD cast over the KG Plateau (CTD 3) shows the largest change in Fe* between the subsurface and the ML (Δ Fe* = 0.2 nM), indicating strong biological uptake of Fe and NO_3^-.

Regardless of the incomplete alleviation of Fe-stress, biological activity is enhanced around the islands, with implications for biogeochemical cycling (this study; Planquettte et al., 2007; Trull et al., 2015; Holmes et al., 2019). Phytoplankton responses to Fe fertilization in the Southern Ocean have been reported to include: 1) increased growth rates and contributions to new production from all phytoplankton size classes (e.g., Armstrong, 1999; Maldonado et al., 2001; Boyd, 2019), 2) preferential growth of larger phytoplankton groups as a result of the removal of a top-down community control since zooplankton grazers in HNLC regions are generally adapted to prey on small cells (Morel et al., 1991; Assmy et al., 2013), and 3) little to no increase in new production or C export because of potential increases in recycled nutrient supply and regenerated production (Mosseri et al., 2008; Coello-Camba et al., 2017). Additionally, high Fe concentrations that remain localized around the islands (e.g., Poulton et al., 2007; Planquette et al., 2007; Holmes et al., 2019) may be advection into bathymetric-induced recirculation features (e.g., north of CR and northeast of the KG plateau), which allows for the

accumulation of Fe over the winter in areas of recirculation that subsequently supports large spring blooms in October/November (Pollard et al., 2007b). Island phytoplankton blooms that occur later in the growing season usually occur closer to the Fe source – either over the plateau regions or very near-shore (Poulton et al., 2007; Planquette et al., 2007; Blain et al., 2007; Mongin et al., 2008; Holmes et a., 2019).

5.2 Phytoplankton community composition and contribution to carbon biomass: bottom-up and top-down controls

To assess phytoplankton abundance and composition, we used a combination of microscopy studies for the micro- size class and FACS for the pico- and nano- size classes (Figures. 4.7 & 4.8). The microscopy counts provide species-specific abundance information about the MICRO class, while flow cytometric sorting yields fluorescence and relative cell-size data for various populations but does not offer information at the species level. In terms of abundance, the pico- and nanoplankton groups are dominant across the transect (Figure 4.7A). SEM analysis of a representative subset of the FACS samples (including *Island* and *Open Ocean Sectors* samples) reveals few intact diatoms in the NEUKS class, particularly in the *Island Sector* samples, while a small number of broken frustules were apparent in both NEUKS and PEUKS samples from the *Open Ocean Sectors* (data not shown). This suggests that at the time of sampling, the phytoplankton dominating the decline stage of the *Island Sector* bloom (at least numerically) were lightly- and non-silicified assemblages, with the latter being poorly suited to SEM analysis (Dolgin & Adolf, 2019). The dominance of these phytoplankton groups is likely due to general shift towards Si limitation in this sector, as well as potentially heavy microzooplankton predation on silicified species in particular (Haberman et al., 2003a & b; Schultes et al., 2006). The potential contribution of diatoms to the NEUKS and PEUKS closest to the islands cannot be evaluated as none of the very few near-island samples (collected via zodiac sampling) were included in the SEM analysis due to their rarity. Nonetheless, these samples are expected to be similar to others from the *Island Sector*. The MICRO size class comprises >95% diatoms near the islands (Figure 4.7C & 4.9B), which can be explained by the alleviation of Si and Fe co-limitation. For the *Open Ocean Sectors*, the SEM results show that non-silicifying and calcifying phytoplankton species dominate in mid-summer as a result of the severely limiting ML Si concentrations (Boyd et al., 1999; Hutchins et al., 2001; Sedwick et al., 2002).

The major eukaryotic phytoplankton species contributing to the PEUKS, NEUKS, and MICRO groups can be inferred from a combination of SEM and light microscopy, as well as findings from previous

studies (e.g., Hutchins et al., 2001; Sedwick et al., 2002). Although very little is known about the community structure of PEUKS in this region (Bouman et al., 2012), this population likely includes small Chrysophyceae and Prymnesiophyceae (Kirkham et al., 2013) such as *Phaeocystis antarctica* and the widely abundant small coccolithophore, *Emiliania huxleyi*. Based on the NEUKS size distribution (~5µm; Table 3.2), this population is likely composed of larger Prymnesiophyceae, such as larger forms of *P. antarctica* and coccolithophore species such as *Calcidiscus leptoporus* and *Synacosphaera pulchra* (Bouman et al., 2012; Rigual-Hernández et al., 2020). In addition, the SEM analyses confirm the presence of the relatively small pennate diatoms, likely *Pseudo-nitzschia* spp., in both the *Island Sector* and *Open Ocean Sectors* (Hutchins et al., 2001; Sedwick et al., 2002). The MICRO group is dominated by the common HNLC chain-forming pennate diatom, *F. kerguelensis* (Figure 3.6B). Although *F. kerguelensis* is observed across the sector, centric diatoms such as *C. radicans* and *C. inerme* become more abundant in the *OO PFZ Sector*, with the dinoflagellate species *C. lineatum* increasing in the *OO SAZ* (Figure 4.7C). With regards to the SYN and CRYPTO populations, a lack of clade- and species-level studies for the Subantarctic (and elsewhere) makes it difficult to infer species information. Because of this, the SYN and CRYPTO populations are discussed at the genus level.

In general, picophytoplankton (PEUKS and SYN) and nanophytoplankton (NEUKS and CRYPTO) numerically dominate the phytoplankton assemblages across the Indian Subantarctic (Figure 4.7A; Boyd, 2002; Lasbleiz et al., 2016), with NEUKS being most abundant in the *Island Sector* (40%) and PEUKS in the *Open Ocean Sector* (60%). Due to natural Fe- and Si-fertilization from island-derived and frontal upwelling inputs, the phytoplankton community composition shifts towards larger phytoplankton species near the islands, as evidenced by the elevated contribution of the MICRO group to C biomass (Figure 4.7B). The heavily-silicified component of this biomass (large diatoms; Figure 4.7D & 4.9B) has the potential to support significant C export (see section 5.4 below; Cullen, 1991; Buesseler, 1998; Boyd & Newton, 1999; de Baar et al., 2005; Rigual-Hernandez et al., 2015), which underscores the importance of local increases in Fe and Si availability for primary productivity and C export in the HNLC Subantarctic.

Si limits larger, heavily-silicified diatom growth and productivity at concentrations <5 µM (e.g., pennate *F. kerguelensis* and centric *Chaetoceros* spp.) and ≤ 1 µM for the smaller lightly-silicified diatoms (e.g., pennate *Pseduo-Nitzchia* spp.) (Boyd et al., 1999; Frank et al., 2000; Hutchins et al., 2001; Nelson et al., 2001; Selph et al., 2001; Sedwick et al., 2002). The onset of Si limitation in the retention zones and plateau areas of the Subantarctic islands drives a progression in the phytoplankton community structure from heavily-silicified diatoms (assimilating $Si>NO_3^-$) to lightly-silicified diatoms (assimilating

Si≈NO_3^-), and then ultimately to non-siliceous species such as *Phaeocystis* and coccolithophore spp. that assimilate NO_3^- with no requirement for Si (Hutchins et al., 2001; Sedwick et al., 2002). This pattern of succession is not observed in the near-shore island areas due to the continuous supply of Fe and Si (Planquette et al., 2007; Poulton et al., 2007). Si-limiting conditions are observed in a few surface samples from the *Island Sector* (e.g., in the offshore SAZ area between the PEI and CR archipelago where [$Si(OH)_4$] is 0.5 μM and over the KG Plateau where [$Si(OH)_4$] is 4.0 μM; Figure 4.1B). In general, however, the mean [$Si(OH)_4$] of the *Island Sector* is non-limiting (>5 μM) (Boyd et al., 1999; Franck et al., 2000; Hutchins et al., 2001; Nelson et al., 2001; Selph et al., 2001; Sedwick et al., 2002) while Si-limiting conditions persist in the *Open Ocean Sectors* (mean [$Si(OH)_4$] of 1.7±1.8 μM, Figure 4.1, Table 5.1). This implies that the entire open ocean is unfavourable for large, heavily-silicified MICRO diatom growth in mid-summer. By contrast, conditions remain favourable for lightly-silicified NEUK populations such as *Pseduo-Nitzchia* spp., in the *OO PFZ* (mean [$Si(OH)_4$] of 2.6±2.3 μM) (Lasbleiz et al., 2016), but become limiting in the *OO SAZ* (mean [$Si(OH)_4$] of 1.0±0.4 μM), allowing for smaller, non-silicifying PEUKS such as *Phaeocystis* spp. and *E. huxleyi* to significantly (p <0.005) dominate the phytoplankton assemblage (Boyd et al., 1999; Hutchins et al., 2001; Sedwick et al., 2002).

Because the MICRO population is dominated by large diatoms or diatom chains across the transect (on average, diatom RA >70% of the MICRO population), one might expect a significant difference in the RA of the MICRO population between the *Island Sector* and the *Open Ocean Sectors*. This is not observed (p >0.05), however, because the composition of the MICRO population shifts from predominantly diatoms in the *Island Sector* to non-silicifying dinoflagellates in the *Open Ocean Sectors*, the latter becoming more competitive under conditions of Si limitation (Poulton et al., 2007; Trull et al., 2015). Indeed, a significant (p <0.05) increase in dinoflagellate abundance is observed in the *Open Ocean Sectors*, increasing 2.5-fold from a MICRO RA of 13% in the *Island Sector* to 34% in the *Open Ocean Sectors*. This is particularly evident in the *OO SAZ*, where dinoflagellate assemblages contribute >50% of the MICRO cell counts. Not unexpectedly, in the *Island Sector*, the largest contribution to C biomass is due to diatoms, while in the *Open Ocean Sectors*, the bulk of the C biomass is contained in large dinoflagellates (Figure 4.7D & 4.9B). Because of the ballasting effect of their dense silica frustules, diatoms are expected to export more organic C per unit of C biomass produced than dinoflagellates (Cullen, 1991; Busseler, 1998; Boyd & Newton, 1999; de Baar et al., 2005; Rigual-Hernandez et al., 2015). Moreover, the total quantity of biomass (inferred from [PON]) is highest in the *Island Sector*, which, combined with the dominance of large diatoms, suggests that C export potential should be considerably higher in this region than in the *Open Ocean Sectors*. Finally, the zonal succession of diatoms by dinoflagellates has implications for PO_4^{3-} cycling since dinoflagellates are known to contain

~40% more P than diatoms (Twining et al., 2004); their increase in abundance in the *OO SAZ* coincides with a decrease (of ~0.8 μM on average) in surface [PO_4^{3-}] (Figure 4.1C).

Fe availability not only controls productivity in the Subantarctic, it also influences the extent to which phytoplankton assimilate Si relative to NO_3^-; the nutrient status of diatoms can thus be evaluated using the Si* tracer (Sarmiento et al., 2004). Under Fe-replete conditions (>0.5 nM), diatoms have been observed to assimilate Si and NO_3^- in a ratio of ~1:1 (Brzezinski, 1985; Coale et al., 1999; Boyd et al., 1999; Hutchins et al., 2001; Sedwick et al., 2002; Blain et al., 2007; Poulton et al., 2007; Holmes et al., 2019), which yields no change in Si* and leads to a more efficient biological pump driven by high rates of diatom growth and a consequent substantial amount of C export (Poulton et al. 2007). By contrast, under Fe-deficient conditions (<0.5 nM), diatoms preferentially assimilate Si relative to NO_3^-, leading to an uptake ratio of Si:NO_3^- >2:1 (at times as high as 8:1) that depletes Si before NO_3^- (Coale et al., 1999; Boyd et al., 1999; Hutchins et al., 2001; Sedwick et al., 2002; Blain et al., 2007; Francke et al., 2000; de Baar et al., 2005; Poulton et al., 2007; Holmes et al., 2019). This drives a decrease in Si* and curtails C export as a result of the reduced growth of diatoms that are particularly effective at exporting C (Poulton et al., 2007). The preferential uptake of Si over NO_3^- is especially evident in larger, heavily-silicified diatom species such as *F. kerguelensis* and *Chaetoceros* spp. (MICRO) (Coale et al., 1999; Franck et al., 2000; Sedwick et al., 2000 & 2002) but seems less prevalent among lightly-silicified species such as *Pseudo-nitzchia* (NEUKS) (Hutchins et al., 2001; Sedwick et al. 2002). Fe-replete conditions are rarely encountered in the Indian Subantarctic (Holmes et al., 2019; Jansson et al., 2020), forcing the persistent and preferential depletion of Si relative to NO_3^- by MICRO diatoms (Holmes et al., 2019), which results in a sustained negative Si* anomaly and MICRO diatoms with a high Si:N ratio (Franck et al., 2000; Sarmiento et al., 2004). Silicification can provide a variety of functional advantages, including protection from grazing and thus, to some extent, a defense against sinking (Raven & Waite, 2004). Thinner-frustuled diatoms tend to be grazed and aggregated relatively quickly (Assmy et al., 2013), which leads to rapid sinking of the organic C contained within their shells. By contrast, heavily-silicified diatoms are protected from grazing and remain in the surface for long periods of time, which has been shown to result in the sinking of empty frustules (Assmy et al., 2013). While this maintains Si export, it decreases the organic C flux and thus the strength of the biological pump. The Si* concentration of Subantarctic surface waters is ultimately set by the conditions in the formation region of SAMW and AAIW (where Si* = -10 to -15 μM; Sarmiento et al., 2004); however, local phytoplankton-nutrient interactions will further modify this signal. The physical processes that drive Fe availability, combined with the nutrient requirements of local MICRO populations, appear to dictate the uptake ratio of Si relative to N and thus influence Si* across the Indian Subantarctic basin. This implies

that the considerably less abundant but larger and more nutrient-heavy phytoplankton are the major drivers of changes in Subantarctic biogeochemistry.

The microscopy counts show the highest abundance and diversity of MICRO diatoms in the *Island Sector*, which suggests that its biogeochemistry and C export potential, particularly closest to the islands and fronts, is driven by this larger size class. While only surface data are available for the MICRO group, they are assumed to be representative of the ML more broadly (Queguiner et al. 2011). The high sinking velocities reported for large diatoms (up to 35 m/day; Ragueneau et al., 2006; Richardson & Jackson, 2007; Miklasz & Denny, 2010; Collins & Rynerson, 2014; Turner, 2015) suggests that this assumption is reasonable. The Si* concentrations in the *Island Sector*, unsurprisingly, indicate a Fe-deficient system (mean Si* of -14.3±3.0 μM, Table 5.1), suggesting an uptake ratio of Si:NO_3^- >2:1. An increase in Si* to concentrations of -10 to -7 μM is observed closest to the islands, especially the PEI and Kerguelen archipelago, as well as at the SAF and PF. This is likely driven by: 1) a higher absolute supply of Si relative to NO_3^- associated with upwelling near the islands and fronts (i.e., supplying Si and NO_3^- in a ratio >1:1, which is characteristic of deeper Southern Ocean waters), and 2) some alleviation of Fe-limitation near the islands and fronts. Consistent with this, chain-forming pennates dominate the MICRO diatom population in the *Island Sector*, comprising 82% of the near-island diatoms and 58% of the between-island HNLC diatoms. The most ubiquitous Subantarctic pennate species, *F. kerguelensis*, comprises >70% of the near-island MICRO samples and decreases to ~50% of the between-island HNLC MICRO samples. Additionally, a high diversity of centric species occurs at low abundances near the CR and KG plateaus. Their low numbers are likely the result of sampling near the end of the seasonal centric diatom bloom (Poulton et al., 2007). In any case, abundance is not necessarily a good indicator of potential contribution to C biomass or export. For example, in the near-island samples, the RA of MICRO centric diatoms is <20% but they contribute >30% of the MICRO C biomass, while in the samples downstream of the KG Plateau, MICRO centric diatom RA is ~40%, yet they contribute > 65% of the MICRO C biomass. The disproportionately high C biomass contributions of the MICRO centric diatoms suggest that the plateau- and retention zone blooms of the spring and early-summer, which are dominated by denser centric species, will yield more C export (Poulton et al., 2007; Trull et al., 2015) than productivity in the mid-summer that is dominated by pennate diatoms. Indeed, pennate species have been reported to contain the smallest amount of C per cell, with much higher quantities of cellular C observed in a centric species (Cornet-Barthaux et al., 2007; Lasbleiz et al., 2016). A decoupling of surface abundance and contribution to C export is supported by sediment trap data from near the CR and KG archipelago that show centric diatoms *Chaetoceros* spp. and *E. antarctica* dominating export in Fe-fertilized Crozet waters while the pennate diatom, *F. kerguelensis*, dominates export in the nearby HNLC

waters, in both spring (Laurenceau-Cornec et al., 2015) and summer (Salter et al., 2007). A final consideration is the influence of cell abundance vs. cell C content on nutrient cycling, ecosystem functioning, and C export. Despite the high C export potential closer to the islands, plateaus, and retention zones associated with centric diatoms dominance, at least in the spring/early summer (Assmy et al., 2004; Armand et al., 2008; Lasbleiz et al., 2016), pennate species such as *F. kerguelensis* and the NEUK *Pseduo-Nitzchia* spp. are more abundant and persistent (Salter et al., 2007; Mosseri et al., 2008; Lasbleiz et al., 2016) across the Subantarctic as a whole. Therefore, it is possible that these groups are driving the biogeochemistry, ecosystem functioning (Cortese & Gersonde et al., 2007), and C export in this basin due to their much larger geographic extent and their ubiquitous nature compared to centric diatoms.

Although diatoms are recognized as the main vectors of C export in the Southern Ocean (Brusseler et al., 2005; Rigual-Hernandez et al., 2015), the size and abundance of the non-diatom group, CRYPTO, means that this population contributes substantially to phytoplankton C biomass. The RA of the *Island Sector* CRYPTO populations is low (~10% of total phytoplankton), but they contribute 45% of the C biomass because of their size (Figures 4.7A & B). Where environmental and biological conditions are favourable for growth, large increases in CRYPTO RA and C biomass are observed. For example, in near-shore KG waters, a CRYPTO RA of ~50% and RCC of 95% are associated with apparent post-bloom conditions where 1) Si concentrations are limiting (≤5 μM), 2) diatom abundance is 80% lower than at adjacent near-island and plateau stations, with pennate HNLC species dominating the diatom community (90% of MICRO), and 3) given the time of year, surface waters are likely stratifying (evident in the CTD density profile over the KG plateau, Figure 3.2C; Trull et al., 2015). Stratification renders CRYPTO assemblages more competitive since they are able to tolerate high surface irradiances (Mendes et al., 2017) while other phytoplankton species such as diatoms and haptophytes become photo-inhibited at high light (Trimborn et al., 2019). Surface stratification driven by warming, with a possible secondary role for island-derived freshwater inputs, is common over the plateau in mid-summer (Trull et al., 2015). While the influence of runoff cannot be evaluated due to a lack of surface salinity data, CRYPTO populations are known to thrive under fresher conditions (Moreau et al., 2015) such that any freshwater inputs will render the near-shore environment even more favourable for them. CRYPTO populations are also able to proliferate at depth under low light due to a combination of light-harvesting pigments, including Chl-*a* & *c*, carotenoid alloxanthin and phycobiliproteins (Gould et al., 2008; Trimborn et al., 2019). This implies that in regions where they are less competitive at the surface, they may nonetheless succeed at depth. In the depth profiles of phytoplankton abundance from the *Island Sector* (Figure 4.8A), the RA of CRYPTO (relative to nano- and picoplankton) increases by >40% with depth, increasing their

relative C biomass contribution to >80% (Figure 4.8B). The versatility of CRYPTO populations highlights their potentially underrated role in C cycling in the Subantarctic, especially under stratified conditions. Cryptophyte-specific studies are generally lacking, with the majority that have been conducted focusing on CRYPTO populations near the Antarctic continent (e.g., Ducklow et al., 2007; Mendes et al., 2017; Trimborn et al., 2019); this has left a gap in our understanding of the CRYPTO role in Subantarctic C and nutrient cycling.

An overall decrease in productivity is observed in the *Open Ocean Sector* compared to the *Island Sector* (e.g., Planquette et al., 2007; Trull et al., 2015; Holmes et al., 2019). This is evident in the significant decrease (p <0.05) in the MICRO cell counts as well as a >60% decrease in CRYPTO and NEUKS counts, particularly in the *OO SAZ Sector*. The decrease in productivity is attributed to sustained Fe-limitation across the *Open Ocean Sectors*, even at the SAF upwelling where low-levels of Fe supply are reported (Janson et al., 2020). The observed shift in RA and RCC to smaller phytoplankton assemblages is therefore a product of Fe limitation (with the higher surface area-to-volume ratio of smaller cells making it easier for them to acquire Fe; Webb et al., 2001) and the progressive Si depletion over the summer season. Although there is an apparent intrusion of high-Si PF waters on the western side of the *OO PFZ* (Figure 4.1B), Si* in the *OO PFZ* is the lowest of anywhere in the Indian Subantarctic (Figure 4.2, Table 5.1). The mean Si* of the *OO PFZ* (-20.4±1.7 μM) is significantly different (p <0.05) from that of the *Island Sector* (-14.5±3.0 μM) and AAIW at the time of formation (where Si* = -10 to -15 μM; Sarmiento et al., 2004), suggesting an increase in the biological uptake of Si relative to NO_3^- in the *OO PFZ* (Si:NO_3^- uptake ~4:1), likely as a result of no IME-driven resupply of Fe. This drives the mean Si concentrations to limiting levels for heavily-silicified MICRO diatoms even as [NO_3^-] remains high. In contrast, Si* in the *OO SAZ* is similar to that of the *Island Sector* and SAMW, with a mean of -13.6±5.4 μM. However, unlike the *Island Sector* that is resupplied with Si by upwelling, Si* in the *OO SAZ* is set by increased NO_3^- uptake by non-siliceous phytoplankton populations under persistent Si-depletion. These observations suggest that there are three different nutrient cycling regimes in the three different sectors of the Indian Subantarctic: 1) Nutrient cycling in the *Island Sector* is driven by diatoms, including the centric populations abundant near the islands and the pennate populations that dominate offshore; 2) nutrient cycling in the *OO PFZ* is driven by diatoms (Trull et al., 2001) until Fe and Si co-limitation sets in, at which point a shift to non-siliceous phytoplankton-driven nutrient cycling occurs; and 3) the *OO SAZ* is characterized by non-siliceous phytoplankton-driven nutrient cycling year-round (de Sales et al., 2011; Rigual-Hernandez et al., 2015), likely due to Fe limitation.

Notwithstanding the significant decrease in MICRO cell counts in the *Open Ocean Sector*, the relatively high abundances (for this sector) of smaller pennate and centric diatoms are associated with the high Si waters near the PF. *Fragilariopsis* spp. dominate the MICRO diatom assemblage with a RA of 40%, while small *Chaetoceros* spp. contribute 20%. These larger size classes are indicative of the assemblages that might have been present in this region during the spring bloom, driving intensive Si drawdown and nutrient cycling. An early-spring study by Lasbleiz et al. (2016) suggests centric assemblage dominance (>50%) in the *OO PFZ* region near the PF and a significant contribution of this group to C biomass. By the time of sampling in mid-summer, however, the RA of the MICRO populations is extremely low (< 0.1%) and they contribute little to the C biomass (Figures 4.7A & B). Instead, the bulk of the C biomass is held by CRYPTO and NEUK populations (>70%). The relatively high CRYPTO RA in the middle of the *OO PFZ* sector can be explained by surface stratification, as some CRYPTOs are able to withstand high surface irradiance (Mendes et al., 2017; Trimborn et al., 2019). The NEUKS, on the other hand, become more dominant at depth (Figures 4.8A & B) as well as during bloom-decline conditions around the PF and SAF. The majority of the NEUKS assemblage is likely composed of large *P. antarctica* (since environmental conditions and biological adaptations are favourable; see below), and when $[Si(OH)_4]$ is >1 µM, a small assemblage of *Pseudo-nitzchia* spp. (Lasbleiz et al., 2016). Since most of the C biomass is held by soft-bodied haptophytes, a lower C export flux compared to the island assemblages is expected due to their smaller size and lack of mineral ballasting.

The significant (p <0.05) decline in NEUK RA and (p <0.05) increase in PEUK RA in the *Open Ocean Sectors* is consistent with a HNLC regime that favors the growth of smaller phytoplankton assemblages. Because of the availability of nutrients – or lack thereof – it is likely that the PEUKS and NEUKS are composed of similar genera, with smaller species being present at higher abundance. Given the environmental conditions (e.g., SST and nutrient availability) in the *Open Ocean Sectors*, different haptophyte populations are hypothesized to inhabit the waters of the *OO PFZ* and *OO SAZ*, with Phaeocystales dominating in the south and Coccolithales dominating to the north. Phaeocystales *P. antarctica* is well-adapted for HNLC conditions given its micronutrient storage and grazer evasion strategies, including 1) the ability to form colonies (which increases their size from PEUKS to NEUKS) to escape microzooplankton grazing (Schoemann et al., 2005), 2) the capacity of colonies to accumulate Fe over time in their mucus (Davidson & Marchant, 1987; Lubbers et al., 1990; Schoemann et al., 2001 & 2005), which allows them to persist in the absence of other Fe sources (Schoemann et al., 2005), and 3) the fact that the PFZ is characterized by optimal temperature conditions for the growth of this species (4-5°C; Matari et al., 1995; Hong et al., 1997; Schoemann et al., 2005). Given the expected success of *P. antarctica* in the PEUKS and NEUKS size classes in the *OO PFZ*, this species may account for >50%

of the total surface phytoplankton RA (assuming *P. antarctica* constitutes ≥80% of the PEUKS and using the RA of *Pseudo-nitzchia* in the NEUKS size class (~10%) reported by Lasbleiz et al., 2016). The growth of *P. antarctica* becomes limited at temperatures >5°C (Schoemann et al., 2005), restricting this species to the waters south of the SAF in the PFZ. A three-fold decrease in the RA of NEUKS is observed in the *OO SAZ*, along with a >50% increase in PEUK RA (Figure 4.7A). This can be attributed to a temperature-driven shift in the PEUKS and NEUKS haptophyte populations from Phaeocystales south of the SAF to Coccolithales north of the SAF. The hypothesized shift to coccolithophore dominance in the *OO SAZ* is consistent with coccolithophore optimum growth temperatures (~8°C; Findlay & Giraudeau, 2000) and the 'Great Calcite Belt', which is an area of the Southern Ocean with increased surface reflectance resulting from calcite-shelled coccolithophores outcompeting diatoms due to Si depletion (Balch et al., 2014; Boyd et al., 2010). Moreover, in the Indian Subantarctic. sediment trap data show a >50% contribution of calcium carbonate to the annual sinking flux (Trull et al., 2001b).

The NEUKS population in the *OO SAZ* is likely composed of larger, less abundant coccolithophore species such as *C. leptoporus* and *S. pulchra* (Rigual-Hernandez et al., 2020), while the PEUKS group probably comprises of *E. huxleyi*, the most common coccolithophore in the Southern Ocean (McIntyre & Be, 1967; Holligan et al., 2010; Poulton et al., 2017; Balch et al., 2019; Rigual-Hernandez et al., 2020). The high PEUK abundances in the SAZ region of the *Island Sector* (SAF crossed at 61°E; Figure 4.7A) are also likely due to a high abundance of *E. huxleyi*. Very high abundances of PEUKS are observed throughout the upper water column in this region; however, due to the small size of these phytoplankton, including *E. huxleyi*, their RCC remains <20%. By contrast, the less abundant but larger NEUKS coccolithophores and CRYPTO populations contribute 25% and ~40% of the surface C biomass, respectively, and 30% and ~60% of the ML C biomass (Figure 4.7B). While the decrease in surface alkalinity that results from calcite platelet production reduces atmospheric CO_2 uptake by the surface ocean (i.e., the carbonate counter pump; Salter et al., 2014; Rigual-Hernandez et al., 2020), the ballasting of organic matter sinking fluxes by calcite shells increases C export to depth (Volk & Hoffert, 1985; Buitenhuis et al, 2001; Boyd & Trull, 2007; Ziveri et al., 2007), leading to strong net CO_2 drawdown (Balch et al., 2016). Additionally, a recent study by Rigual-Hernandez et al. (2020) has shown that while *E. huxleyi* contributes to export, it is the less abundant but larger (NEUKS) coccolithophore species that actually drive the annual export fluxes in the *OO SAZ*.

SYN, the smallest size class (~1.3 μm) sorted in this study, shows a surprising distribution. Due to their small size and related superior nutrient scavenging ability (Partensky et al. 1999a; Goericke & Welschmeyer 1993), the expectation is that their distribution will to be similar to that of PEUKS.

However, this is not the case. SYN shows increased RA proximal to Fe sources, including near the islands and frontal systems, with a significant difference (p <0.05) in their RA in the *Island Sector* versus the *Open Ocean Sector* (15% versus 9%). This distribution can be explained by the unusually high Fe requirements of SYN compared to eukaryotic phytoplankton (discussed further in section 5.5; Raven, 1990; Brand 1991; Wilhelm et al., 1996; Morrissey & Bowler, 2012; Lis et al., 2015). Interestingly, SYN has the highest C density of all the sorted groups (250 fg C μm^3, Table 3.2); however, its small size means that it contributes <1% of the total autotrophic C (Figure 4.7B). The higher RA of SYN near areas of upwelling may also be due to a putative requirement for Si (Baines et al., 2012; Ohnemus et al., 2016 & 2018), although the reason for this remains unclear. While it is unlikely that SYN will have a significant impact on the Subantarctic Si cycle due to their small size and the significantly higher Si requirement of diatoms, Si availability may nonetheless play a role in constraining the distribution of SYN across the Subantarctic.

Throughout this section, the contribution to C biomass has been addressed for all phytoplankton populations encountered during sampling. It is widely accepted that diatoms are the main vectors of C export in the Southern Ocean (Brusseler et al., 2005; Rigual-Hernandez et al., 2015) and that their diversity and abundances increase in Fe-fertilized areas, driving a two- to three-fold enhancement of C export (Blain et al., 2007). However, diatom export efficiencies are influenced by the degree of silicification, community structure, and aggregate formation (Assmy et al., 2013; Queguiner 2013; Sackett et al., 2014). Additionally, non-silicified soft-bodied phytoplankton such as CRYPTO also contribute significantly to C biomass across the Subantarctic. While the export potential of these non-ballasted phytoplankton species may be limited compared to diatoms, there is some evidence that preservation of soft-bodied populations in sediment traps is unreliable (Metfies et al., 2017) such that their contribution to the export flux may be higher than has been estimated to-date. Population-specific contributions to C export potential can also be evaluated using the new production paradigm as a framework (Dugdale & Goering, 1967; Fawcett et al. 2011 & 2014). Below, population-specific reliance on new versus recycled nutrients is examined, with a view to quantifying the potential contribution of the different phytoplankton groups to the Subantarctic Ocean's biological pump.

5.3: Implications of NH_4^+ versus NO_3^- assimilation by phytoplankton

A major goal of this study is to understand phytoplankton population-specific C export potential, in order to answer the question: *who drives C export in the Indian Sector of the Subantarctic?* While it is widely accepted that larger eukaryotic cells are the main drivers of C export in the global oceans (Omand

et al., 2020), including in the Southern Ocean (Salter et al., 2007 & 2012; Assmy et al., 2013), a number of studies have suggested that this might not be the case (in the Subantarctic; Trull et al., 2001b, and in the global ocean; e.g., Barber, 2007; Richardson & Jackson, 2007; Lomas & Moran, 2011). For example, Trull et al. (2001b) pointed out that although the PFZ hosts the highest concentration of large diatom biomass, the greater degree of NO_3^- consumption that occurs in the SAZ (where large diatoms are less abundant) implies a larger export flux in this latter zone, calling into question the dominant role attributed to large diatoms in export production. Numerous studies have shown that specific phytoplankton populations prefer particular N substrates (e.g., Lomas & Glibert, 1999a & b; Glibert & Berg, 2009; Fawcett et al. 2011 & 2014), which, within the framework of the new production paradigm, has implications for their importance for C export. For instance, under N-rich, cold conditions, larger diatoms (generally >20 μm) have been observed to preferentially utilize NO_3^- even when NH_4^+ is available (Probyn & Painting, 1985; Lomas & Glibert, 1999a & b; Glibert & Berg, 2009). Conversely, the smaller size classes, including cyanobacteria, have been observed to preferentially consume NH_4^+ (Probyn & Painting, 1985; Karsh et al., 2003; Fawcett et al., 2011; Glibert et al., 2016), while global studies indicate that dinoflagellates, regardless of size, preferentially assimilate reduced forms of (regenerated) N rather than oxidized species (e.g., Berg et al., 2003; Glibert et al., 2006; Heil et al., 2007; Rothenberger et al., 2009; Glibert et al., 2016). The data presented in this thesis show that the Indian Sector of the Subantarctic is characterized by phytoplankton-N use (and by extension, C export potential) trends (Table 5.2 & 5.3) that do not always conform to existing theories.

Table 5.2: Surface phytoplankton population-specific NO_3^- dependence (0-1), relative carbon (C) contributions (%), and potential contributions to C export (%)

Island Sector

Phytoplankton group	NO_3^- Dependence[1]	Relative POC (%)[2]	*f*-ratio[3]	Potential C export (%)[4]
PON[5]	0.50			
MICRO	0.72	25		22
CRYPTO	0.69	43	**0.80**	38
NEUKS	> 0.95	31		37
PEUKS	0.88	2		2
SYN	0.88	< 1		< 1

PF Sector

Phytoplankton group	NO_3^- Dependence	Relative POC (%)	*f*-ratio	Potential C export (%)
PON	0.02			
MICRO	0.50	28		15
CRYPTO	> 0.95	30	**0.92**	32
NEUKS	> 0.95	48		52
PEUKS	> 0.95	< 1		< 1
SYN	> 0.95	< 1		< 1

Open Ocean PFZ Sector

Phytoplankton group	NO_3^- Dependence	Relative POC (%)	*f*-ratio	Potential C export (%)
PON	0.08			
MICRO	0.60	34		71
CRYPTO	0.07	49	**0.29**	12
NEUKS	0.26	16		14
PEUKS	0.63	2		3
SYN	0.58	< 1		< 1

Open Ocean SAZ Sector

Phytoplankton group	NO_3^- Dependence	Relative POC (%)	*f*-ratio	Potential C export (%)
PON	0.32			
MICRO	0.49	35		28
CRYPTO	0.45	37	**0.61**	28
NEUKS	0.79	26		34
PEUKS	0.60	10		9
SYN	0.60	< 1		< 1

Subantarctic Transect[6]

Phytoplankton group	NO_3^- Dependence	Relative POC	*f*-ratio	Potential C export (%)
PON	0.38			
MICRO	0.66	31		30
CRYPTO	0.55	43	**0.68**	34
NEUKS	0.85	24		30
PEUKS	0.78	4		5
SYN	0.77	< 1		< 1

[1]For phytoplankton population-specific NO_3^- dependence calculations see methods 3.7.3

[2]For phytoplankton population-specific POC content calculations see methods 3.7.4

[3] Phytoplankton-specific *f*-ratio. Calculated from the sum of the population-specific NO_3^- dependence multiplied by the associated RCC (%) (equation 3.15, methods 3.7.6)

[4]Using the calculated phytoplankton-specific *f*-ratio, the relative contribution of each phytoplankton population to C export can be estimated (equation 3.16; methods 3.7.7)

[5]For NO_3^- dependence calculations, bulk PON is assumed to represent the integrated growth product over the season whereas the sorted phytoplankton populations are assumed to better represent instantaneous growth products.

[6]Average calculated from all the Subantarctic sectors including the *Island Sector*, the *PF Sector*, the *Open Ocean PFZ Sector* and the *Open Ocean SAZ Sector*.

Table 5.3: ML phytoplankton population-specific NO_3^- dependence (0-1), relative carbon (C) contribution (%), and potential contributions to C export (%)

Island Sector

	CTD 1				CTD 2				CTD 3			
Phyto. group	NO_3^- Dependence[1]	Relative POC (%)[2]	*f*-ratio[3]	Potential C export (%)[4]	NO_3^- Dependence	Relative POC (%)	*f*-ratio	Potential C export (%)	NO_3^- Dependence	Relative POC (%)	*f*-ratio	Potential C export (%)
PON[5]	0.80				> 0.95				0.70			
CRYPTO	> 0.95	14		14	0.55	13		12	<0.05	78		8
NEUKS	> 0.95	81	**0.98**	83	> 0.95	43	**0.59**	73	> 0.95	21	**0.29**	74
PEUKS	0.66	4		3	-[5]	-		-	0.92	5		17
SYN	0.44	< 1		< 1	> 0.95	9		15	> 0.95	< 1		1

PF Sector

	CTD 4			
Phyto. group	NO_3^- Dependence	Relative POC (%)	*f*-ratio	Potential C export (%)
PON	> 0.95			
CRYPTO	> 0.95	78		83
NEUKS	0.64	18	**0.94**	12
PEUKS	> 0.95	4		5
SYN	> 0.95	< 1		1

OO PFZ Sector

	CTD 5			
Phyto. group	NO_3^- Dependence	Relative POC (%)	*f*-ratio	Potential C export (%)
PON	0.59			
CRYPTO	0.52	79		61
NEUKS	> 0.95	18	**0.67**	27
PEUKS	> 0.95	7		10
SYN	> 0.95	1		1

OO SAZ Sector

	CTD 6				CTD 7			
Phyto. group	NO_3^- Dependence	Relative POC (%)	*f*-ratio	Potential C export (%)	NO_3^- Dependence	Relative POC (%)	*f*-ratio	Potential C export (%)
PON	<0.05				> 0.95			
CRYPTO	> 0.95	82		81	> 0.95	64		68
NEUKS	> 0.95	9	**1.02**[6]	9	0.92	6	**0.94**	6
PEUKS	0.90	11		10	> 0.95	22		23
SYN	0.47	1		< 1	0.53	6		3

[1]For phytoplankton population-specific NO_3^- dependence calculations see methods 3.7.3. Note, these are biomass concentration-weighted values.

[2]For phytoplankton population-specific POC content calculations see methods 3.7.4

[3]Phytoplankton-specific *f*-ratio. Calculated from the sum of the population-specific NO_3^- dependence multiplied by the associated RCC (%) (equation 3.15, methods 3.7.6)

[4]Using the calculated phytoplankton-specific *f*-ratio, the relative contribution of each phytoplankton population to C export can be estimated (equation 3.16; methods 3.7.7)

[5]For NO_3^- dependence calculations, bulk PON is assumed to represent the integrated growth product over the season whereas the sorted phytoplankton populations are assumed to better represent instantaneous growth products

[6]Values >1 indicate limitation of the *f*-ratio model and are likely indicative of the influence of Subantarctic frontal upwelling

Broadly, the phytoplankton population-specific $\delta^{15}N$ data reveal the following trends for the Indian Sector of the Subantarctic in mid-summer:

1) Estimates of the *f*-ratio ratio computed from sorted phytoplankton $\delta^{15}N$ indicate that the contribution of the upper Subantarctic ecosystem to new production and C export potential may be higher than previously reported, at least in mid-summer.
2) All phytoplankton groups, including PEUKS and SYN, preferentially consume NO_3^-, at the surface and deeper in the ML, across the Indian Subantarctic.
3) The three largest size classes, MICRO, CRYPTO and NEUKS are the main contributors to C export potential across the surface Subantarctic (~30% each), as estimated from the extent of their reliance on new NO_3^- (inferred from their biomass $\delta^{15}N$) as well as their relative abundances.
4) Across the Subantarctic, C export potential inferred from NO_3^- dependence is highest in the *Island Sector*, with the lowest C export potential estimated for the *OO PFZ Sector*.
5) On average across all sectors, micro- and nanoplankton diatoms preferentially utilize new NO_3^-; however, they are also observed to rely on regenerated N (either NH_4^+ or NO_3^- as a product of nitrification) to support a significant amount of their growth, even under conditions of elevated Fe supply.
6) The relative abundance and degree of NO_3^- dependence of SYN appears to be positively related to Fe supply.

Each of these trends is explored in detail below.

5.3.1 FACS-based estimates of the f-ratio

The phytoplankton population-specific $\delta^{15}N$ data from mid-summer can be compiled to yield an estimate of the *f*-ratio for each sector ("phytoplankton-specific *f*-ratio"; methods 3.7.6, equation 3.15). These estimates, which consider only the autotrophic contribution to upper ocean biomass, imply N utilization strategies that contradict previous studies not based on FACS-$\delta^{15}N$. Rather than a general decrease to low *f*-ratios in mid-summer as has been suggested based on traditional ^{15}N tracer-based approaches that do not account for the potentially confounding effects of heterotrophic and/or detrital biomass on N uptake estimates (Mosseri et al., 2008; Cavanga et al., 2015; Trull et al., 2015), the phytoplankton-specific *f*-ratio remains relatively high across the region, except for in the *OO PFZ* (Table 5.2). Across the Subantarctic transect, the average phytoplankton-specific *f*-ratio is 0.7, significantly higher than the previously reported value of 0.4 for the same time of year (Mosseri et al., 2008; Trull et al., 2015). The

FACS-$\delta^{15}N$ data thus suggest that Subantarctic C export potential may be significantly higher than previously estimated, at least in mid-summer.

The highest phytoplankton-specific *f*-ratio is observed in the *Island Sector* (0.8) and can be attributed to the partial alleviation of Fe limitation of NO_3^- uptake. The surface *OO PFZ Sector* has the lowest phytoplankton-specific *f*-ratio (0.3), which describes a system largely supported by regenerated N that, in a mass balance sense, contributes less to C export. This is consistent with the PFZ described by Trull et al. (2001b), wherein diatom affinity for NO_3^- utilization is reduced compared to KG populations. However, contrary to the apparently low surface NO_3^- dependence of various phytoplankton populations in the *OO PFZ Sector*, higher NO_3^- dependence is observed at depth, such that the phytoplankton-specific *f*-ratio increases to 0.7 when all the ML data are considered (Table 5.3; CTD 5). A phytoplankton-specific *f*-ratio of 0.6 is estimated for the *OO SAZ Sector*, which describes an increase in surface NO_3^- dependence compared to the *OO PFZ Sector*. Additionally, the average ML phytoplankton-specific *f*-ratio is >0.9, similarly higher than the phytoplankton-specific *f*-ratio implied by the surface data alone. It is important to note that the ML *f*-ratio calculated for CTD 6 in the *OO SAZ Sector* is >1, indicating the limitations associated with the *f*-ratio model (Trull et al., 2015) but also described the influence of the SAF.

At most CTD stations, the phytoplankton-specific *f*-ratios increase when all the ML data are considered relative to the values estimated from the underway surface data alone (Table 5.3). Indeed, most of the CTD casts show near exclusive NO_3^- utilization, with *f*-ratios >0.9. While these estimates should be interpreted with caution since the dataset often includes only two or three ML $\delta^{15}N_{phyto}$ values and the number of CTD casts is far fewer than the number of underway stations, the general increase in population-specific $\delta^{15}N$ with depth implies an increase in new production (and thus C export potential). This may be due to greater potential access to the upwardly-mixed Fe (Tagliabue et al., 2014), therefore supporting Fe enzymic requirements for NO_3^- reduction (Sunda, 1989; Timmermans et al., 1994; Milligan & Harrison, 2000) at depth in the water column. The only ML system apparently supported mainly by regenerated N is that of the KG Plateau (CTD 3) where a phytoplankton-specific *f*-ratio of 0.3 is estimated (Table 5.3). This indicates a localized shift (relative to the other island systems) to regenerated production, potentially fueled by regenerated NO_3^- supplied via ML nitrification or ammonification, which has been observed to be extremely high near KG (Cavagna et al., 2014; Fripiat et al., 2015; Dehairs et al., 2015). The different *f*-ratio estimates implied by the surface versus ML samples underscores a potential limitation of using surface populations as representative of integrated upper water column C export potential (Trull et al., 2015). That said, the high number of surface

measurements included in this study means that the trends among zones and populations are likely robust and representative of the general functioning of the upper ocean ecosystem.

5.3.2 Extent of phytoplankton NO_3^- dependence and contributions to C export potential

Across the Subantarctic transect, the MICRO population apparently consumes a mix of new and regenerated N (Figure 4.9B). It is generally accepted that Southern Ocean diatoms are NO_3^- specialists owing to their large number of high-affinity nitrate transporters (HAT-NRTs) and high cell-specific rates of NO_3^- transport (Lomas & Glibert, 2000; Armbrust et al., 2004; Glibert et al., 2016). The MICRO diatom (>20 μM) populations in this study that appear to consume only new NO_3^- occur at Fe- and Si-fertilized sites associated with islands and frontal crossings. Without this partial alleviation of Fe stress, Subantarctic diatoms utilize a combination of new and regenerated N (e.g., between PEI and CR, the average $\delta^{15}N_{MICRO}$ is 0.7±1.0‰, suggesting combined new and regenerated N utilization). The diatom-dominated MICRO assemblages near KG Island and Plateau grow largely on regenerated N, which is perhaps surprising given that Fe is relatively high in these surface waters. This observation may evince KG diatoms utilizing regenerated NO_3^- (i.e., from surface layer nitrification), which is low in $\delta^{15}N$ as a result of the branching isotope effect associated with coincident NH_4^+ oxidation and uptake (DiFiore et al., 2010). Indeed*, in situ* ammonification and/or nitrification has been estimated to account for ~47% of phytoplankton NO_3^- uptake over the plateau during the summer (Dehairs et al., 2015; Cavagna et al. 2015). This is an interesting theory to consider, that even when diatoms are seemingly utilizing regenerated N substrates, they are still expending the energy associated with NO_3^- uptake.

While large numbers of HAT-NRTs are generally observed in diatoms, differences have been observed in the regulation of HAT-NRTs in centric versus pennate diatoms (Bender et al., 2014), however, the implications for NO_3^- assimilation between the two groups has yet to be quantified. Additionally, different Fe storage mechanisms adopted by pennate and centric diatoms (i.e., *FTN* and intracellular vacuoles, respectively) promote different growth rates, where *FTN* allows for pennate diatoms to rapidly store high quantities of Fe (while avoiding Fe toxicity) to sustain continued slower growth for longer periods compared to intracellular vacuoles (Boyd & Mackie, 2008; Lampe et al., 2018). In this study, most sites of new production are associated with increases in centric chain-forming diatoms, namely *C. radicans* and *C. inerme*, suggesting either 1) *Chaetoceros* (and perhaps other species of centric diatoms) are more efficient HAT-NRTs compared to the other species observed across the transect or 2) the enhanced Fe supply supports the faster growth rates of centric *Chaetoceros* species compared to pennates such as *Pseudo-nitzschia* (Boyd, 2019) and because of the centric vacuolar Fe storage (Strzepek

et al., 2012), they are unlikely to proliferate long term away from the Fe source like pennate diatoms with *FTN* Fe storage (Marchetti et al., 2009; Mock et al., 2012; Lampe et al., 2018). Similar mechanisms likely play a role in the *OO PFZ Sector* where, although the phytoplankton-specific *f*-ratio is low, the potential contribution of MICRO diatoms to C export is 70%, while CRYPTO and NEUKS contribute 12% and 14%, respectively. Higher C export potential thus coincides with sites characterized by increased centric chain-forming diatom abundances.

A recent study by Leblanc et al. (2018) suggests that nanoplanktonic diatoms (2 – 20 μM) are globally overlooked with regards to the large role they play in C export and are thus poorly characterized in ocean models. The NEUKS in the current study, largely comprising the pennate diatom *Pseudo-nitzschia* spp. (in addition to other Prymnesiophycae, coccolithophores species), have the highest affinity for NO_3^- assimilation across the transect (0.85 on average, Table 5.2). This is particularly evident near the islands and frontal upwelling areas where only new N utilization is observed, yielding large potential NEUKS contributions to C export (~40%). High NEUKS NO_3^- dependence is also a feature at depth (Table 5.3), with NEUKS contributing ~77% of the potential C export from the ML in the *Island Sector* (where *Pseudo-nitzschia* spp. are expected to be most abundant), far surpassing the potential C export contribution of the larger CRYPTO group (12%). While there are no $\delta^{15}N$ or NO_3^- dependence data for MICRO populations in the ML, the dominance of NEUKS over the MICRO group at the surface in terms of NO_3^- use and C export potential likely hold with depth, suggesting that the NEUKS population plays a significant role in C export in the *Island Sector*. One implication of these observations – that under the right conditions, NEUKS can be the main driver of C export – has implications for oceanic models that assume the MICRO groups dominate C export (e.g., Legendre and Lefevre (1995) bifurcation model).

The CRYPTO population shows the largest decoupling between surface and ML export potential trends. Across the surface transect, CRYPTO sustains relatively high contributions to C export (34%; Table 5.2), except in the *OO PFZ Sector* where a significant amount of CRYPTO growth is fueled by regenerated N (NO_3^- dependence = 0.07), resulting in a contribution of ~12% to surface C export potential. The ability of these populations to proliferate at depth (Gould et al., 2008; Trimborn et al., 2019) likely explains the increase in NO_3^- dependence (and thus the contribution to C export) with depth in the ML in the *OO PFZ and SAZ Sectors* where CRYPTO populations contribute >60% of the ML C export. This amounts to a five-fold increase from the surface export estimates in the *OO PFZ Sector*. By contrast, in the *Island Sector*, C export potential decreases three-fold from surface-based estimates to whole-ML estimates. This can be explained by a coincident rise in the relative abundance of NEUKS that appear to near-exclusively assimilate new N at depth, thus driving the CRYPTO to fill a different

niche. Additionally, the CRYPTO shift to enhanced growth on regenerated N over the KG Plateau could indicate uptake of newly nitrified (i.e., regenerated) NO_3^- (Cavagna et al., 2014; Fripiat et al., 2015; Dehairs et al., 2015), similar to that of MICRO diatoms, rather than a transition to NH_4^+ dependence.

Although abundant across the transect, dinoflagellates are only numerically dominant over diatoms in the *OO SAZ Sector*. Contrary to previous studies that suggest dinoflagellates prefer regenerated N forms (e.g., Berg et al., 2003; Glibert et al., 2006; Heil et al., 2007), the SAZ populations appear to consume a combination of new and recycled N, in a ~1:1 ratio. This suggests a larger dinoflagellate contribution to C export potential than other workers anticipated, with 28% of *OO SAZ Sector* C export potential attributable to dinoflagellates. Since the *OO Sectors* are overwhelmingly dominated by one group of dinoflagellate, *Creatium spp*. (constituting 84% of all the dinoflagellates observed in this sector), it is possible that the observed N utilization trend reflects their ecology rather than that of Subantarctic dinoflagellates in general. However, at the stations in the *Island Sector* where dinoflagellates dominate the MICRO population (e.g., east of CR), the dinoflagellate community is more diverse, yet combined new and regenerated N utilization is still observed. It therefore appears that combined new and regenerated N utilization is broadly characteristic of Subantarctic dinoflagellates.

5.4. C export dynamics: cell size versus abundance

While picophytoplankton have been suggested to contribute substantially to C export in the global ocean (Barber, 2007; Richardson & Jackson, 2007; Stukel & Landry, 2010), the findings of the present study suggest that this is not the case in the HNLC Indian Sector of the Subantarctic. Across the region, the larger size classes (nano- and micro-) contribute >90% of the C export potential, while picophytoplankton contribute ~5% (Table 5.2). Even when the picophytoplankton populations are numerically dominant (e.g., in the *OO SAZ Sector* where they constitute 88% of phytoplankton cells), they contribute ≤10% of the C export potential. The disconnect between picophytoplankton abundance and C export contribution can be attributed to the following: 1) cellular C content (associated with cell size and volume), 2) sinking velocity, and 3) incorporation into the microbial loop/grazing pressure (Basu & Mackey, 2018).

In terms of cell volume, the MICRO size class is >1000x larger, CRYPTO is ~90x larger, and NEUKS is ~16x larger than the picophytoplankton. Although carbon content is also a function of species, the large differences in cell volume have significant implications for cellular C (Basu & Mackey, 2018). For example, for the NEUKS and PEUKS groups in this study, which comprise similar species (see

Discussion 5.2), C biomass per cell estimates are ~16x higher for NEUKS than PEUKS as a result of the difference in cell volume. In addition to the different C capacities of the various size classes, the C uptake mechanisms also differ. Smaller cells have a larger surface area-to-volume ratio and can therefore accommodate more transporters on the cell surface, supporting a greater diffusive uptake of CO_2 and nutrients. Larger cells overcome their lower surface area-to-volume ratio by relying on CO_2 concentrating mechanisms (CCMs) rather than diffusive uptake (Raven & Beardall, 2003; Armbrust et al., 2004; Granum et al. 2005; Wilhelm et al., 2006; Roberts et al. 2007; Raven et al. 2008; Hopkinson et al. 2011). Eukaryotic CCMs have a greater affinity for CO_2 when phytoplankton assimilate NO_3^- (Guo et al., 2007), increasing the likelihood that larger phytoplankton will consume new N (and thus contribute to C export potential) in HNLC regions such as the Subantarctic.

The lower C capacity of smaller cells along with their slower sinking velocities of <0.5 m/day (compared to 0.4 to 35 m/day for larger phytoplankton groups, particularly ballasted cells; Ragueneau et al., 2006; Richardson & Jackson, 2007; Miklasz & Denny, 2010; Collins & Rynerson, 2014) and high turnover rates due to significant microzooplankton grazing pressure (Jones et al., 1998; Griffiths et al., 1999; Kopczyńska et al., 2001; Safi et al., 2007; Pearce et al., 2011) result in a lower contribution to C export potential of picophytoplankton in the Subantarctic. Richardson and Jackson (2007) propose alternative mechanisms of picophytoplankton C export such as accumulating into secondary export by higher trophic levels; however, the overwhelmingly large and direct contribution to C export by nano- and microphytoplankton in the Indian Subantarctic likely far outweighs any picophytoplankton contribution, which emphasizes the importance of cell size over abundance in the Southern Ocean, at least at the smaller end of the size spectrum.

Cell size appears to become a less accurate predictor of C export potential in the case of the larger phytoplankton. Microphytoplankton are, on average, 65-times bigger (by volume) than nanophytoplankton, yet the two groups each contribute ~30% of C export potential across the Subantarctic transect (Table 5.2). Since diatoms are a large component of both the NEUKS and MICRO populations and use a CCM for CO_2 uptake (Wu et al., 2014 a & b), a balance between abundance and cell size must occur for the NEUKS and MICRO groups to have similar C export potential. The average Subantarctic NEUKS RA is 90-times higher than that of the MICRO population, suggesting that the difference in size between these two groups is offset by NEUKS abundance. This implies that cell size and abundance both play a role in the C export dynamics of the Subantarctic, although a fine balance between cell size, CCMs utilization, and abundance is required for different size classes to exhibit similar export dynamics.

5.5. *Synechococcus*: Unexpected ecological findings

SYN are one of the most ubiquitous photoautotrophs in the global ocean, reaching higher abundances in the nutrient-rich higher latitudes than in the oligotrophic subtropical ocean gyres (Partensky et al., 1999a; Scanlan, 2003; Van Oostende et al., 2017). The N nutrition of SYN has been extensively studied, with most strains showing the ability to assimilate both new and regenerated (i.e., oxidized and reduced) N (Glibert et al., 1986; Paerl, 1991; Lindell et al., 1998; Collier et al., 1999; Moore et al., 2002; Bird & Wyman, 2003; Fuller et al., 2003). However, a preference for reduced N has been reported from culture work (Glibert & Ray, 1990; Lindell & Post, 2001), as well as from FACS-$\delta^{15}N$ measurements in the oligotrophic North Atlantic (Fawcett et al., 2011 & 2014; Treibergs et al., 2014). By contrast, Subantarctic SYN show a clear preference for NO_3^- utilization, with a NO_3^- dependence of 0.77 across the surface Subantarctic transect that is highest in the *Island Sector* (0.88; Table 5.2) where high ambient concentrations of NH_4^+ are available (1.9±1.3 μM; Table 5.1). A number of explanations for these observations, including a high Fe requirement (Raven, 1990; Brand 1991; Wilhelm et al., 1996; Morrissey & Bowler, 2012; Lis et al., 2015), temperature dependence (e.g., Waterbury et al., 1986; Li & Dickie 2001; Hunert-Cevera et al., 2020), and Si dynamics (Brezeinski et al., 2017) are discussed below.

SYN appear to thrive in the well-lit surface of the Subantarctic, decreasing in abundance with depth (Figure 4.8A), as have been observed in the subtropics (DuRand et al., 2001; Lomas et al., 2013; Treibergs et al., 2014). This distribution is attributed to their reduced photosynthetic efficiency under low light conditions relative to eukaryotic assemblages (Glover et al., 1987; Prezelin et al., 1989; Moore et al., 1988), likely a result of the higher ratio of photosystem I to photosystem II observed in SYN (Sunda & Huntsman et al., 2015). Since photosystem I is Fe-rich relative to photosystem II, this yields an unusually high Fe requirement for SYN (Raven, 1990; Brand 1991, Wilhelm et al., 1996; Morrissey and Bowler, 2012; Lis et al., 2015). As a result, SYN have been described as "excluded from low light and low Fe environments" (Sunda & Huntsman et al., 2015). The RA and NO_3^- dependent growth displayed by SYN across the Subantarctic surface and in the upper ML are consistent with this statement, with increases in both observed near natural sources of Fe-fertilization (e.g., fronts and islands). The high surface light conditions that characterize the mid-summer, when combined with elevated Fe availability, appear sufficient to support the reduction of oxidized N, thus explaining the tendency towards new N utilization by Subantarctic SYN.

It has also been hypothesized that the high Fe requirement of SYN may result from a lack of C-rich moieties inside their cells (Twining & Baines, 2013), although recent studies have suggested that SYN may be able to directly assimilate organic C nutrients (Yelton et al., 2016; Fourquez et al., 2020), which could allow them to proliferate under Fe-fertilized bloom conditions in a semi-mixotrophic state. While the ability of SYN to assimilate organic C has yet to be directly shown (Fourquez et al., 2020), this is nonetheless an intriguing idea that is not inconsistent with the observations reported here. All things considered, it appears that these small phytoplankton may play a larger-than-expected role in Fe assimilation and drawdown in naturally Fe-fertilized regions (Fourquez et al., 2020), the implications of which have yet to be explored.

Numerous studies have shown a strong relationship between SYN abundance and temperature (Waterbury et al., 1986; Agawin et al., 1998; Li, 1998; Li & Dickie, 2001; Tsai et al., 2008; Hunert-Cevera et al., 2020), albeit mostly for oligotrophic and coastal regions. Here, the temperature threshold for the spring bloom is 5-6 °C, above which cell division rates and SYN abundances increase (Hunert-Cevera et al., 2020). SYN also seems to have a surprisingly high dissolved intracellular Si concentration (e.g., Baines et al., 2011; Brzezinski et al., 2017; Ohnemus et al., 2018) that, while strain-dependent (Brzezinski et al., 2017), is comparable to diatoms when normalized for size (Baines et al., 2011). In the present study, the highest SYN RAs are associated with upwelling sites where the SST is 4-6 °C and Si is actively being supplied, along with Fe. While the upwelled Fe supply is likely the primary driver of the increased SYN RA, optimum temperatures and increased Si concentrations may also play a role. Due to the potential introduction of ballasting effects, questions have been raised as to whether Si-incorporation by SYN can be linked to increased vertical export of C (Lomas & Moran, 2011; Guidi et al., 2016). The results from the present study show that even when SYN is supported by new N and proliferates, it contributes <1 % of total C export potential such that potential Si ballasting of SYN is unlikely to affect the export dynamics of the Subantarctic.

6. Conclusions and future directions

Measurements of nutrients, SST, phytoplankton RA and RCC, $\delta^{15}N_{NO3}$ and phytoplankton group-specific $\delta^{15}N$ reveal that the IME in the Indian Sector of the Subantarctic plays a large role in shaping its chemical and biological regimes. This leads to elevated C export potential across the region, at least in mid-summer, which may have been previously underestimated. The data show that all phytoplankton groups (including PEUKS and SYN) preferentially consume NO_3^-, at the surface and deeper in the ML, across the Indian Subantarctic. Near the Subantarctic Islands, however, this NO_3^- utilization appears to be enhanced with all phytoplankton populations showing, on average, a >10% increase in NO_3^- dependence compared to the Subantarctic sector average. Additionally, estimates of the *f*-ratio (Subantarctic sector average of 0.7) computed from sorted phytoplankton $\delta^{15}N$ (rather than the traditional PON $\delta^{15}N$ estimates) indicate that the contribution of the Subantarctic surface and ML phytoplankton populations to new production and C export potential are higher than previously reported (~0.4; Mosseri et al., 2008; Trull et al., 2015), at least in mid-summer. Unsurprisingly, this is only enhanced by the IME where a *f*-ratio of 0.8 is calculated.

The three largest phytoplankton size classes, MICRO, CRYPTO, and NEUKS are the main contributors to C export potential across the surface Subantarctic (~30% each), while the numerically dominant picophytoplankton populations contribute ~5%. This disconnect between abundance and potential contribution to C export is largely attributed to cellular C content, with cell size (which is related to cell volume and cellular C density) determining the quantitative contribution to export. Specifically, in terms of cell volume, the MICRO size class are >1000-times larger, the CRYPTO are ~90-time larger, and the NEUKS are ~16-times larger than the picophytoplankton. Furthermore, the faster sinking velocities of larger cells, particularly those that are ballasted, means that they can escape the ML up to seven times faster than smaller cells (Ragueneau et al., 2006; Richardson & Jackson, 2007; Miklasz & Denny, 2010; Collins & Rynerson, 2014), contributing to a larger seasonal (and thus, annual) C export flux while also escaping microzooplankton grazing to which the smaller cells are heavily subjected (e.g., Jones et al., 1998; Griffiths et al., 1999; Kopczyńska et al., 2001).

This study has yielded some unexpected findings. First, although micro- and nanoplankton diatoms preferentially utilize new N, this is not exclusive, and regenerated N utilization is also observed. For example, even under conditions of elevated Fe supply around the KG Plateau, MICRO populations dominated by diatoms exclusively utilize regenerated N. This is likely an effect of *in situ* ammonification and/or nitrification taking place over the plateau during the summer (Dehairs et al., 2015; Cavagna et al.

2015). Given the high rates of nitrification that have been measured in this region in summer (Dehairs et al., 2015; Cavagna et al. 2015), the MICRO diatoms may have been consuming NO_3^-, which is consistent with expectations for diatoms in the Southern Ocean (Maestrini et al., 1982; Probyn & Painting, 1985; Lomas & Glibert, 1999a & b), but rather than constituting a source of new N, a significant fraction of that NO_3^- may have been regenerated in the ML. This would also explain previous, apparently incongruous, observations of low-$\delta^{15}N$ bulk PON measured near KG in summer when Fe and light are not limiting and enhanced NO_3^- uptake is expected (Trull et al., 2015). A second largely unexpected finding of the work described in this thesis is that the RA and degree of NO_3^- dependence by the SYN populations appear to be positively related to Fe supply, with a possible secondary role for temperature and Si. This is likely a result of the higher ratio of Fe-rich photosystem I to photosystem II in SYN compared eukaryotes (Sunda & Huntsman et al., 2015), which drives an unusually high Fe requirement (e.g., Raven, 1990; Morrissey & Bowler, 2012; Lis et al., 2015). Recent studies have also suggested that SYN may have a high intracellular dissolved Si concentration (e.g., Baines et al., 2011; Brzezinski et al., 2017; Ohnemus et al., 2018) that, when normalized for size, is comparable to that of diatoms (Baines et al., 2011). In SYN, however, this putative Si requirement remains poorly understood. Fe and Si supply via upwelling coincide with SSTs of 4-6°C, which fall within the range of temperatures favourable for SYN growth (Hunert-Cevera et al., 2020). While SYN dynamics in the Subantarctic requires further investigation, it is likely that a combination of Fe, Si and temperature play a role in its distribution and the extent of its NO_3^- dependence. Although the overall potential C export contribution of SYN remains low (<1%) due to their size, these ecological findings are nonetheless significant.

In order to refine future estimates of C export in the Subantarctic, a better understanding of the sensitivity of the $^{15}\varepsilon$ for NO_3^- assimilation for all phytoplankton groups to environmental variables such as Fe and light stress is required. The results discussed here have assumed a $^{15}\varepsilon$ of 4.6 – 5.3‰ for eukaryotes (this study; Karsh et al., 2003; Trull et al., 2008; DiFiore et al., 2006, 2009 & 2010; Fripiat et al., 2009) and 3.9‰ for SYN (Granger et al., 2010). However, previous field- and culture work has shown the $^{15}\varepsilon$ to vary from 1 – 30‰ (e.g., Altabet & Francois, 2001; Lourey et al., 2003; Karsh et al., 2003 & 2012; Granger et al., 2004; DiFiore et al., 2009 & 2010; Smart et al., 2015), although a mechanistic understanding of this variability remains elusive. More tightly constrained $^{15}\varepsilon$ estimates for individual phytoplankton groups would yield improved estimates of phytoplankton groups-specific contribution to Subantarctic C export that can be used in future models. Lastly, further research into phytoplankton responses to Fe supply, including how N utilization strategies change, is required. Such data will be extremely valuable for predictions of the functioning of the Southern Ocean in future given that the Fe supply to this region is expected to increase (Andrew et al., 2019).

7. Appendices

A: TS (temperature-salinity) plots from the CTD casts (1 – 7)

A: CTD 1 (PEI, *Island Sector*)

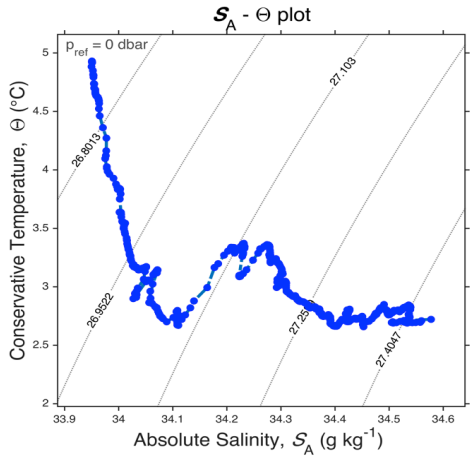

B: CTD 2 (CR, *Island Sector*)

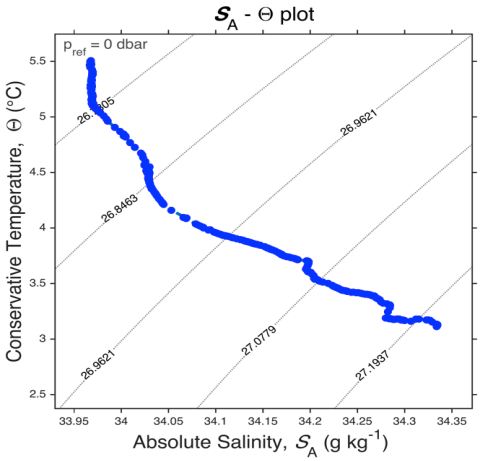

C: CTD 3 (KG, *Island Sector*)

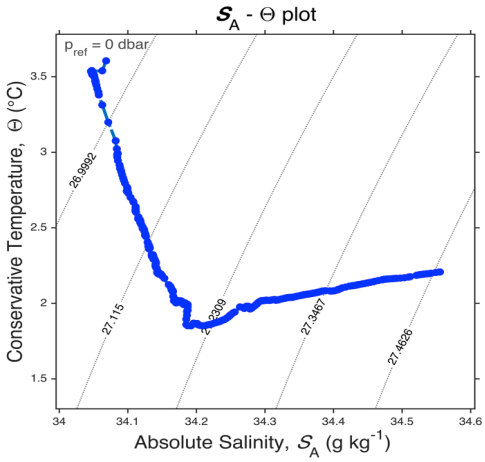

D: CTD 4 (*PF Sector*)

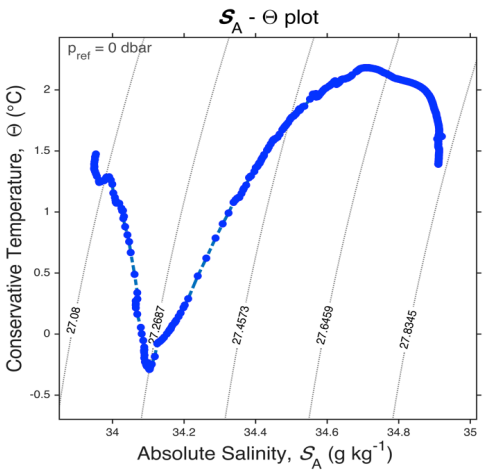

E: CTD 5 (*OO PFZ Sector*)

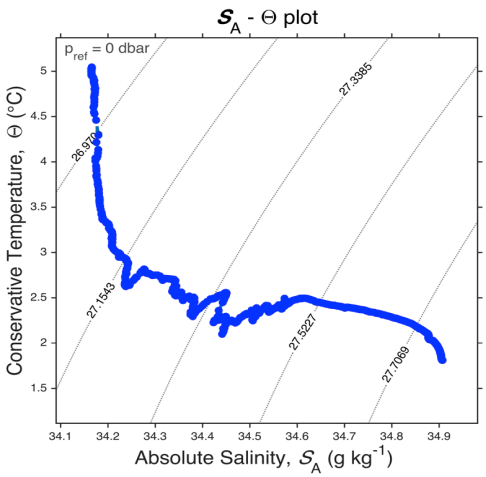

F: CTD 6 (SAF,*OO SAZ Sector*)

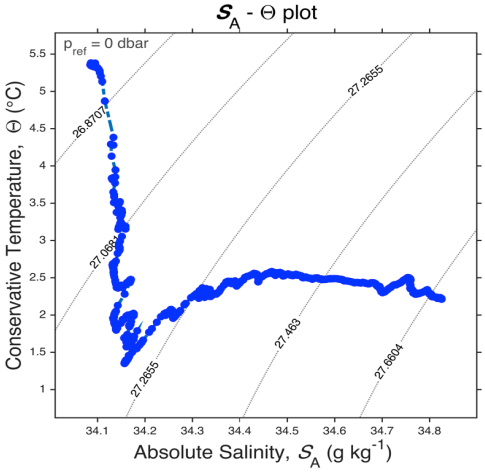

G: CTD 7 (STF, *OO SAZ Sector*)

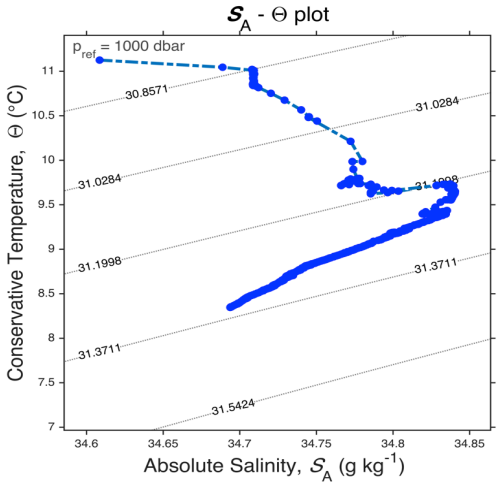

Appendix A: TS (temperature-salinity) plots from the CTD casts (1 – 7) assisting in the identifying of water masses. Conservative temperature (°C) is plotted against absolute salinity (g.kg^{-1}) with density (psu) gradients indicated by the diagonal lines across the plot. These plots were made using the Sea-Water Oceanographic Toolbox Matlab package (v3 06/11) and the gsw_SA_CT_plot function.

B: Oxygen depth profiles from the CTD casts (1 – 7)

A: CTD 1 (PEI, *Island Sector*)

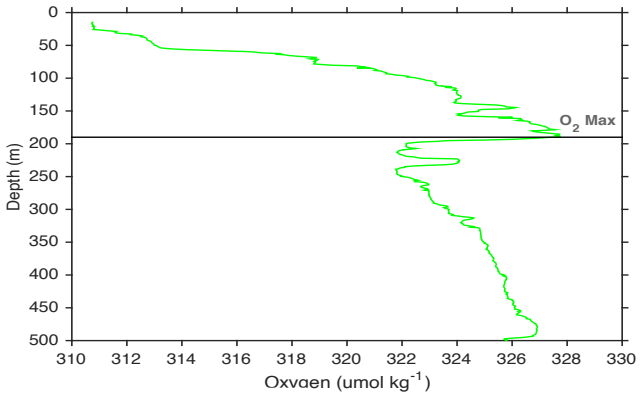

B: CTD 2 (CR, *Island Sector*)

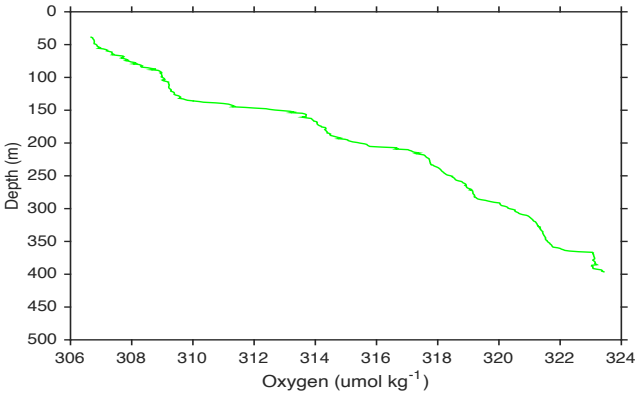

C: CTD 3 (KG, *Island Sector*)

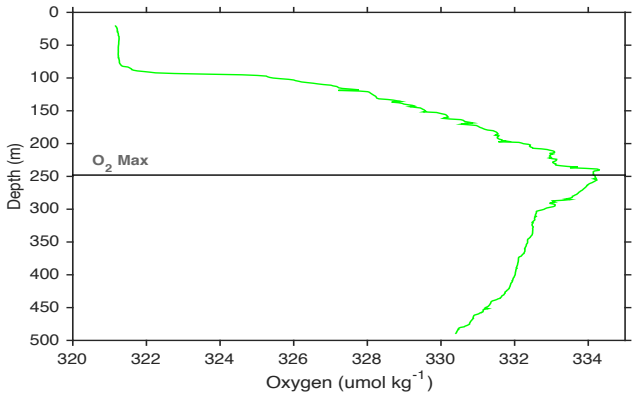

D: CTD 4 (*PF Sector*)

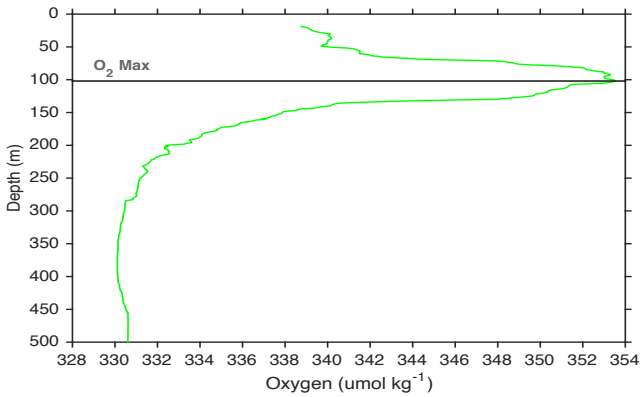

E: CTD 5 (*OO PFZ Sector*)

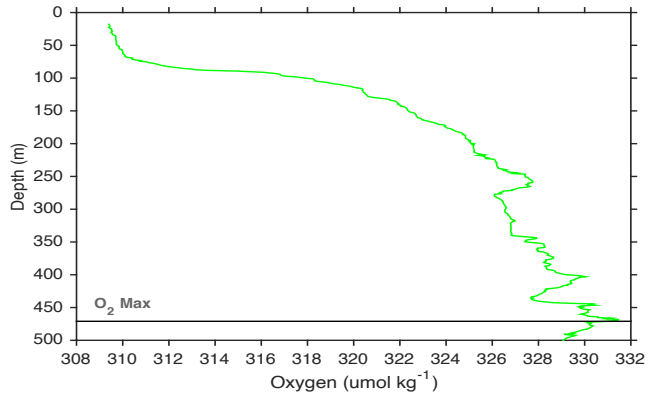

F: CTD 6 (*OO SAZ Sector*)

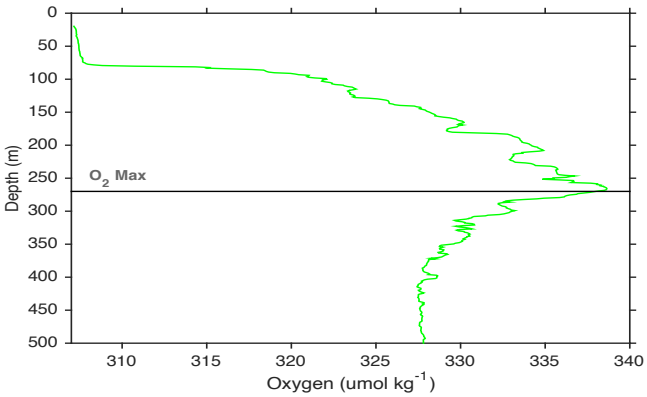

G: CTD 7 (*OO SAZ Sector*)

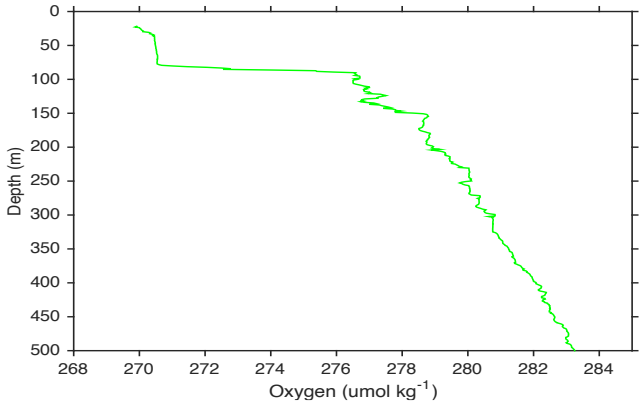

Appendix B: Oxygen (µmol kg^{-1}) depth profiles from the CTD casts (1 – 7) assisting in the identifying of water masses. The O_2 maximum, where detected, is indicated by the grey horizontal line.

C: Calculating the N content and $\delta^{15}N$ of the "missing" N pool

The bulk PON pool (i.e., $[N]_{PON}$ and $\delta^{15}N_{PON}$) is not necessarily well-approximated by the sum of its various autotrophic components because it also includes unmeasured heterotrophic and detrital N that was excluded during cell sorting. The contribution of this "missing" N pool to the bulk PON can be calculated as follows. First, the $[N]_{MICRO}$, $[N]_{CRYPTO}$, $[N]_{NEUKS}$, $[N]_{PEUKS}$ and $[N]_{SYN}$ are added to yield $[N]_{SUM}$, which represents the autotrophic [N] component of the bulk [PON]; only the stations where all of the phytoplankton populations were measured are included in this calculation. The [N] per cell is then calculated from the C content estimates assuming Redfield stoichiometry.

Second, the [N] contribution of the autotrophic component to the bulk [PON] is calculated:

$$\text{Autotrophic contribution (\%)} = ([N]_{SUM} / [N]_{PON}) \times 100 \quad \text{(C.1)}$$

For example, if $[N]_{SUM}$ is 7.0 μM and $[N]_{PON}$ is 13.3 μM, the autotrophic contribution is 53%. This suggests that the remaining 47% of the bulk PON pool comprises heterotrophic and detrital material.

Third, the N-weighted $\delta^{15}N_{SUM}$ (the $\delta^{15}N$ of the autotrophic fraction of PON) is calculated:

$$\delta^{15}N_{SUM} = \Sigma_{\text{phyto. populations}} (\Sigma\, \delta^{15}N \times \Sigma\, [N]) / (\Sigma\, [N]_{\text{phyto. populations}}) \quad \text{(C.2)}$$

Finally, the $\delta^{15}N$ of the "missing" heterotrophic and detrital component ($\delta^{15}N_{unmeasured}$) is calculated:

$$\delta^{15}N_{unmeasured} = ((\delta^{15}N_{PON} \times [N]_{PON}) - (\delta^{15}N_{SUM} \times [N]_{SUM}))/([N]_{PON} - [N]_{SUM}) \quad \text{(C.3)}$$

For example, the $\delta^{15}N_{unmeasured}$ for *Island Sector* surface is calculated as follows: $\delta^{15}N_{unmeasured}$ = ((0.2‰ x 13.3 μM) – (1.0‰ x 7.0 μM))/(13.3 μM - 7.0 μM) = -0.7‰. In general, the autotrophic PON is relatively high in $\delta^{15}N$ compared to the $\delta 15N_{PON}$. This suggests that the "missing" N pools are lower in $\delta^{15}N$ than the autotrophs, as has been observed in subtropical waters (Fawcett et al., 2011).

The "missing" or unmeasured N pool calculations are presented in Table C below.

Table C: The calculated PON concentration and $\delta^{15}N$ for the "missing" or unmeasured N pool that contributes towards the bulk PON that is not accounted for by the autotrophic phytoplankton groups.

Surface[1]	***Island Sector***			***PF Sector***	***OO PFZ Sector***	***OO SAZ Sector***	
Sum autotrophic [N] (µM)[2] | Conc. W. $\delta^{15}N_{phyto.}$ (‰)[3]	7.0 | 0.96			0.4 | 2.3	2.3 | -0.2	2.5 | 0.7	
Sum "missing" [N] (µM)[4] | Conc. W. $\delta^{15}N_{unmeas.}$ (‰)[5]	6.2 | -0.7			1.7 | -1.0	2.4 | -1.7	1.3 | -2.1	
Contribution of "missing" pool to bulk PON pool (%)[6]	47			81	51	35	
Sum bulk [PON] (µM) | Conc. W. $\delta^{15}N_{PON}$ (‰)	13.3 | 0.2			2.2 | -0.4	4.7 | -1.0	3.9 | -0.3	
ML[7] – excl. MICRO[8]	**CTD 1**	**CTD 2**	**CTD 3**	**CTD 4**	**CTD 5**	**CTD 6**	**CTD 7**
Sum autotrophic [N] (µM) | Conc. W. $\delta^{15}N_{phyto.}$ (‰)	1.6 | 1.2	0.8 | 1.1	2.1 | -0.3	0.4 | 1.2	0.6 | 1.5	0.2 | 3.1	0.4 | 3.7
Sum "missing" [N] (µM) | Conc. W. $\delta^{15}N_{unmeas.}$ (‰)	0.4 | 2.2	1.8 | 3.9	2.2 | 2.39	1.8 | 1.4	2.4 | 0.5	1.6 | -1.4	2.8 | 0.8
Contribution of "missing" pool to bulk PON pool (%)	19	69	51	82	81	91	88
Sum bulk [PON] (µM) | Conc. W. $\delta^{15}N_{PON}$ (‰)	2.0 | 1.4	2.5 | 3.0	4.3 | 1.1	2.2 | 1.3	3.0 | 0.7	1.8 | -1.1	3.1 | 1.1

[1] Samples from 5 m depth including underway and CTD samples
[2] Calculated from the C mass per cell using Redfield C:N stoichiometry.
[3] The average concentration-weighted $\delta^{15}N$ of the autotrophic group, $\delta^{15}N_{phyto}$
[4] Calculated using the difference between the surface concentration-weighted bulk PON and autotrophic groups including MICRO, CRYPTO, NEUKS, PEUKS, and SYN
[5] Calculated using equation C.3, appendix C
[6] The % contribution of the "missing" N pool to the bulk PON pool.
[7] The ML average is calculated from the surface to MLD for each of the CTD casts (Figure 4.10)
[8] Calculated using ML concentration-weighted bulk PON and phytoplankton groups including CRYPTO, NEUKS, PEUKS, and SYN. MICRO was not measured at depth and thus was not included in the calculations. In this case, MICRO would fall into the ML $\delta^{15}N_{unmeasured}$ pool.

7. References

Abbott, M. R., Richman, J. G., Letelier, R. M., & Bartlett, J. S. (2000). The spring bloom in the Antarctic Polar Frontal Zone as observed from a mesoscale array of bio-optical sensors. *Deep Sea Research Part II: Topical Studies in Oceanography*, *47*(15-16), 3285-3314.

Abrantes, F., Cermeno, P., Lopes, C., Romero, O., Matos, L., Iperen, J. V., ... & Magalhães, V. (2016). Diatoms Si uptake capacity drives carbon export in coastal upwelling systems. *Biogeosciences*, *13*(14), 4099-4109.

Agawin, N. S., Duarte, C. M., & Agusti, S. (1998). Growth and abundance of Synechococcus sp. in a Mediterranean Bay: seasonality and relationship with temperature. *Marine Ecology Progress Series*, *170*, 45-53.

Alcaraz, M., Saiz, E. Fernandez, J. A., Trepat, I., Figueiras, F., Calbet, A., & Bautista, B. (1998). Antarctic zooplankton metabolism: carbon requirements and ammonium excretion of salps and crustacean zooplankton in the vicinity of the Bransfield Strait during January 1994. *Journal of Marine Systems*, *17*(1-4), 347-359.

Allanson, B. R., Boden, B., Parker, L., & Rae, C. D. (1985). A contribution to the oceanology of the Prince Edward Islands. In *Antarctic nutrient cycles and food webs* (pp. 38-45). Springer, Berlin, Heidelberg.

Allanson, B. R., Hart, R. C., & Lutjeharms, J. R. E. (1971). Observations on the nutrients, chlorophyll and primary production of the Southern Ocean south of Africa. *Vol 4*.

Altabet, M. A. (1988). Variations in nitrogen isotopic composition between sinking and suspended particles: Implications for nitrogen cycling and particle transformation in the open ocean. *Deep Sea Research Part A. Oceanographic Research Papers*, *35*(4), 535-554.

Altabet, M. A., & Small, L. F. (1990). Nitrogen isotopic ratios in fecal pellets produced by marine zooplankton. *Geochimica et Cosmochimica Acta*, *54*(1), 155-163.

Altabet, M. A., & Francois, R. (2001). Nitrogen isotope biogeochemistry of the Antarctic Polar Frontal Zone at 170 W. *Deep Sea Research Part II: Topical Studies in Oceanography* 48.19-20: 4247-4273.

Amante, C. & Eakins B.W. (2009). ETOPO1 1 Arc-Minute Global Relief Model: Procedures, Data Sources and Analysis. NOAA Technical Memorandum NESDIS NGDC-24. National Geophysical Data Center, NOAA. doi:10.7289/V5C8276M [April 2019].

Anderson, J. B., Shipp, S. S., Lowe, A. L., Wellner, J. S., & Mosola, A. B. (2002). The Antarctic Ice Sheet during the Last Glacial Maximum and its subsequent retreat history: a review. *Quaternary Science Reviews*, *21*(1-3), 49-70.

Anderson, L. A., & Sarmiento, J. L. (1994). Redfield ratios of remineralization determined by nutrient data analysis. *Global biogeochemical cycles*, *8*(1), 65-80.

Ansorge, I. J., Durgadoo, J. V., & Pakhomov, E. A. (2009). Dynamics of physical and biological systems of the Prince Edward Islands in a changing climate. In *Papers and Proceedings of the Royal Society of Tasmania* (Vol. 143, No. 1, pp. 15-18).

Ansorge, I. J., Froneman, P. W., Pakhomov, E. A., Lutjeharms, J. R. E., Perissinotto, R., & Van Ballegooyen, R. C. (1999). Physical-biological coupling in the waters surrounding the Prince Edward Islands (Southern Ocean). *Polar Biology*, *21*(3), 135-145.

Ardelan, M. V., Holm-Hansen, O., Hewes, C. D., Reiss, C. S., Silva, N. S., Dulaiova, H., ... & Sakshaug, E. (2010). Natural iron enrichment around the Antarctic Peninsula in the Southern Ocean. *Biogeosciences*, *7*(1).

Ardyna, M., Lacour, L., Sergi, S., d'Ovidio, F., Sallée, J. B., Rembauville, M., ... & Arrigo, K. R. (2019). Hydrothermal vents trigger massive phytoplankton blooms in the Southern Ocean. *Nature communications*, *10*(1), 1-8.

Arístegui, J., Duarte, C. M., Reche, I., & Gómez-Pinchetti, J. L. (2014). Krill excretion boosts microbial activity in the Southern Ocean. *PLoS One*, *9*(2), e89391.

Armand, L. K., Cornet-Barthaux, V., Mosseri, J., & Queguiner, B. (2008). Late summer diatom biomass and community structure on and around the naturally iron-fertilised Kerguelen Plateau in the Southern Ocean. *Deep Sea Research Part II: Topical Studies in Oceanography*, *55*(5-7), 653-676.

Armbrust, E. V. (2009). The life of diatoms in the world's oceans. *Nature*, *459*(7244), 185-192.

Armbrust, E. V., Berges, J. A., Bowler, C., Green, B. R., Martinez, D., Putnam, N. H., ... & Brzezinski, M. A. (2004). The genome of the diatom Thalassiosira pseudonana: ecology, evolution, and metabolism. *Science*, *306*(5693), 79-86.

Armstrong, R. A., Lee, C., Hedges, J. I., Honjo, S., & Wakeham, S. G. (2001). A new, mechanistic model for organic carbon fluxes in the ocean based on the quantitative association of POC with ballast minerals. *Deep Sea Research Part II: Topical Studies in Oceanography*, *49*(1-3), 219-236.

Arrigo, K. R., van Dijken, G. L., & Bushinsky, S. (2008). Primary production in the Southern Ocean, 1997–2006. *Journal of Geophysical Research: Oceans*, *113*(C8).

Assmy, P., Smetacek, V., Montresor, M., Klaas, C., Henjes, J., Strass, V. H., ... & Cisewski, B. (2013). Thick-shelled, grazer-protected diatoms decouple ocean carbon and silicon cycles in the iron-limited Antarctic Circumpolar Current. *Proceedings of the National Academy of Sciences*, *110*(51), 20633-20638

Azam, F., Fenchel, T., Field, J. G., Gray, J. S., Meyer-Reil, L. A., & Thingstad, F. (1983). The ecological role of water-column microbes in the sea. *Marine ecology progress series*, 257-263.

Balarin, MG. (2000). Size fractionated phytoplankton biomass and production in the Southern Ocean. MSc thesis. Rhodes University, Pp 132.

Balch, W. M., Bates, N. R., Lam, P. J., Twining, B. S., Rosengard, S. Z., Bowler, B. C., ... & Rauschenberg, S. (2016). Factors regulating the Great Calcite Belt in the Southern Ocean and its biogeochemical significance. *Global Biogeochemical Cycles*, *30*(8), 1124-1144.

Balch, W. M., Bowler, B. C., Drapeau, D. T., Lubelczyk, L. C., Lyczkowski, E., Mitchell, C., & Wyeth, A. (2019). Coccolithophore distributions of the north and South Atlantic ocean. *Deep Sea Research Part I: Oceanographic Research Papers*, *151*, 103066.

Balch, W. M., Drapeau, D. T., Bowler, B. C., Lyczkowski, E. R., Lubelczyk, L. C., Painter, S. C., & Poulton, A. J. (2014). Surface biological, chemical, and optical properties of the Patagonian Shelf coccolithophore bloom, the brightest waters of the Great Calcite Belt. *Limnology and Oceanography*, *59*(5), 1715-1732.

Banse, K. (1996). Low seasonality of low concentrations of surface chlorophyll in the Subantarctic water ring: Underwater irradiance, iron, or grazing? *Progress in Oceanography, 37*, 241-291.

Barford, C. C., Montoya, J. P., Altabet, M. A., & Mitchell, R. (1999). Steady-state nitrogen isotope effects of N2 and N2O production in Paracoccus denitrificans. *Applied and Environmental Microbiology*, *65*(3), 989-994.

Barnola, J. M., Raynaud, D. Y. S. N., Korotkevich, Y. S., & Lorius, C. (1987). Vostok ice core provides 160,000-year record of atmospheric CO2. *Nature*, *329*(6138), 408-414.

Basu, S., & Mackey, K. R. (2018). Phytoplankton as key mediators of the biological carbon pump: Their responses to a changing climate. *Sustainability*, *10*(3), 869.

Bates, T. S., Charlson, R. J., & Gammon, R. H. (1987). Evidence for the climatic role of marine biogenic sulphur. *Nature*, *329*(6137), 319-321.

Becquevort, S., & Smith Jr, W. O. (2001). Aggregation, sedimentation and biodegradability of phytoplankton-derived material during spring in the Ross Sea, Antarctica. *Deep Sea Research Part II: Topical Studies in Oceanography*, *48*(19-20), 4155-4178.

Becquevort, S., Menon, P., & Lancelot, C. (2000). Differences of the protozoan biomass and grazing during spring and summer in the Indian sector of the Southern Ocean. *Polar biology*, *23*(5), 309-320.

Behrenfeld, M. J., & Falkowski, P. G. (1997). Photosynthetic rates derived from satellite-based chlorophyll concentration. *Limnology and oceanography*, *42*(1), 1-20.

Belkin, I. M., & Gordon, A. L. (1996). Southern Ocean fronts from the Greenwich meridian to Tasmania. *Journal of Geophysical Research: Oceans*, *101*(C2), 3675-3696.

Bender, S. J., Durkin, C. A., Berthiaume, C. T., Morales, R. L., & Armbrust, E. (2014). Transcriptional responses of three model diatoms to nitrate limitation of growth. *Frontiers in Marine Science*, *1*, 3.

Bendschneider, K., & Robinson, R. J. (1952). A new spectrophotometric method for the determination of nitrite in sea water.

Berg, G. M., Balode, M., Purina, I., Bekere, S., Béchemin, C., & Maestrini, S. Y. (2003). Plankton community composition in relation to availability and uptake of oxidized and reduced nitrogen. *Aquatic Microbial Ecology*, *30*(3), 263-274.

Berger, A. (1988). Milankovitch theory and climate. *Reviews of geophysics*, *26*(4), 624-657.

Bergkvist, J., Klawonn, I., Whitehouse, M. J., Lavik, G., Brüchert, V., & Ploug, H. (2018). Turbulence simultaneously stimulates small-and large-scale CO 2 sequestration by chain-forming diatoms in the sea. *Nature communications*, *9*(1), 1-10.

Bergmann, T. I. (2004). *The physiological ecology and natural distribution patterns of cryptomonad algae in coastal aquatic ecosystems* (Doctoral dissertation, Rutgers University).

Bird, C., & Wyman, M. (2003). Nitrate/nitrite assimilation system of the marine picoplanktonic cyanobacterium Synechococcus sp. strain WH 8103: effect of nitrogen source and availability on gene expression. *Applied and environmental microbiology*, *69*(12), 7009-7018.

Bishop, J. K., Rossow, W. B., & Dutton, E. G. (1997). Surface solar irradiance from the international satellite cloud climatology project 1983–1991. *Journal of Geophysical Research: Atmospheres*, *102*(D6), 6883-6910.

Blain, S., Quéguiner, B., Armand, L., Belviso, S., Bombled, B., Bopp, L., ... & Christaki, U. (2007). Effect of natural iron fertilization on carbon sequestration in the Southern Ocean. *Nature*, *446*(7139), 1070-1074.

Blain, S., Sarthou, G., & Laan, P. (2008). Distribution of dissolved iron during the natural iron-fertilization experiment KEOPS (Kerguelen Plateau, Southern Ocean). *Deep Sea Research Part II: Topical Studies in Oceanography*, *55*(5-7), 594-605.

Blain, S., Tréguer, P., Belviso, S., Bucciarelli, E., Denis, M., Desabre, S., ... & Marty, J. C. (2001). A biogeochemical study of the island mass effect in the context of the iron hypothesis: Kerguelen Islands, Southern Ocean. *Deep Sea Research Part I: Oceanographic Research Papers*, *48*(1), 163-187.

Blankenship, R. E., SADEKAR, S., & RAYMOND, J. (2007). The evolutionary transition from anoxygenic to oxygenic photosynthesis. In *Evolution of primary producers in the sea* (pp. 21-35). Academic Press.

Boden, B. P. (1988). Observations of the island mass effect in the Prince Edward Archipelago. *Polar Biology*, *9*(1), 61-68.

Böhlke, J. K., & Coplen, T. B. (1995). *Interlaboratory comparison of reference materials for nitrogen-isotope-ratio measurements* (No. IAEA-TECDOC--825).

Böhlke, J. K., Mroczkowski, S. J., & Coplen, T. B. (2003). Oxygen isotopes in nitrate: New reference materials for 18O: 17O: 16O measurements and observations on nitrate-water equilibration. *Rapid Communications in Mass Spectrometry*, *17*(16), 1835-1846.

Booth, B. C., Lewin, J., & Lorenzen, C. J. (1988). Spring and summer growth rates of subarctic Pacific phytoplankton assemblages determined from carbon uptake and cell volumes estimated using epifluorescence microscopy. *Marine Biology*, *98*(2), 287-298.

Bopp, L., Monfray, P., Aumont, O., Dufresne, J. L., Le Treut, H., Madec, G., ... & Orr, J. C. (2001). Potential impact of climate change on marine export production. *Global Biogeochemical Cycles*, *15*(1), 81-99.

Bouman, H. A., Lepère, C., Scanlan, D. J., & Osvaldo, U. (2012). Phytoplankton community structure in a high-nutrient, low-chlorophyll region of the eastern Pacific Subantarctic region during winter-mixed and summer-stratified conditions. *Deep Sea Research Part I: Oceanographic Research Papers*, *69*, 1-11.

Bowie, A. R., Lannuzel, D., Remenyi, T. A., Wagener, T., Lam, P. J., Boyd, P. W., ... & Trull, T. W. (2009). Biogeochemical iron budgets of the Southern Ocean south of Australia: Decoupling of iron and nutrient cycles in the subantarctic zone by the summertime supply. *Global Biogeochemical Cycles*, *23*(4).

Bowie, A. R., Van Der Merwe, P., Quéroué, F., Trull, T., Fourquez, M., Planchon, F., ... & Sallée, J. B. (2015). Iron budgets for three distinct biogeochemical sites around the Kerguelen Archipelago (Southern Ocean) during the natural fertilisation study, KEOPS-2. *Biogeosciences*, *12*(14), 4421-4445.

Boyce, D. G., Lewis, M. R., & Worm, B. (2010). Global phytoplankton decline over the past century. *Nature*, *466*(7306), 591-596.

Boyd, P. W. (2002). The role of iron in the biogeochemistry of the Southern Ocean and equatorial Pacific: a comparison of in situ iron enrichments. *Deep Sea Research Part II: Topical Studies in Oceanography*, *49*(9-10), 1803-1821.

Boyd, P. W. (2019). Physiology and iron modulate diverse responses of diatoms to a warming Southern Ocean. *Nature Climate Change*, *9*(2), 148-152.

Boyd, P. W., & Brown, C. J. (2015). Modes of interactions between environmental drivers and marine biota. *Frontiers in Marine Science*, *2*, 9.

Boyd, P. W., & Ellwood, M. J. (2010). The biogeochemical cycle of iron in the ocean. *Nature Geoscience*, *3*(10), 675-682.

Boyd, P. W., & Law, C. S. (2001a). The Southern Ocean iron release experiment (SOIREE)—introduction and summary. *Deep Sea Research Part II: Topical Studies in Oceanography*, *48*(11-12), 2425-2438.

Boyd, P. W., & Newton, P. P. (1999). Does planktonic community structure determine downward particulate organic carbon flux in different oceanic provinces?. *Deep Sea Research Part I: Oceanographic Research Papers*, *46*(1), 63-91.

Boyd, P. W., & Trull, T. W. (2007). Understanding the export of biogenic particles in oceanic waters: Is there consensus?. *Progress in Oceanography*, *72*(4), 276-312.

Boyd, P. W., Crossley, A. C., DiTullio, G. R., Griffiths, F. B., Hutchins, D. A., Queguiner, B., ... & Trull, T. W. (2001b). Control of phytoplankton growth by iron supply and irradiance in the subantarctic Southern Ocean: Experimental results from the SAZ Project. *Journal of Geophysical Research: Oceans*, *106*(C12), 31573-31583.

Boyd, P. W., Dillingham, P. W., McGraw, C. M., Armstrong, E. A., Cornwall, C. E., Feng, Y. Y., ... & Nunn, B. L. (2016). Physiological responses of a Southern Ocean diatom to complex future ocean conditions. *Nature Climate Change*, *6*(2), 207-213.

Boyd, P. W., Jickells, T., Law, C. S., Blain, S., Boyle, E. A., Buesseler, K. O., ... & Harvey, M. (2007). Mesoscale iron enrichment experiments 1993-2005: synthesis and future directions. *science*, *315*(5812), 612-617.

Boyd, P. W., Strzepek, R., Fu, F., & Hutchins, D. A. (2010). Environmental control of open-ocean phytoplankton groups: Now and in the future. *Limnology and Oceanography*, *55*(3), 1353-1376.

Boyd, P. W., Watson, A. J., Law, C. S., Abraham, E. R., Trull, T., Murdoch, R., ... & Charette, M. (2000). A mesoscale phytoplankton bloom in the polar Southern Ocean stimulated by iron fertilization. *Nature*, *407*(6805), 695-702.

Boyd, P., LaRoche, J., Gall, M., Frew, R., & McKay, R. M. L. (1999). Role of iron, light, and silicate in controlling algal biomass in subantarctic waters SE of New Zealand. *Journal of Geophysical Research: Oceans*, *104*(C6), 13395-13408.

Boyd, P.W., & Mackie, D. (2008) Comment on "the Southern Ocean biological response to aeolian iron deposition" *Science 319:159.*

Boyle, E. (1998). Pumping iron makes thinner diatoms. *Nature*, *393*(6687), 733-734.

Bracher, A. U., Kroon, B. M. A., & Lucas, M. I. (1999). Primary production, physiological state and composition of phytoplankton in the Atlantic Sector of the Southern Ocean. *Marine Ecology Progress Series*, *190*, 1-16.

Braman, R. S., & Hendrix, S. A. (1989). Nanogram nitrite and nitrate determination in environmental and biological materials by vanadium (III) reduction with chemiluminescence detection. *Analytical chemistry*, *61*(24), 2715-2718.

Brand, L. E. (1991). Minimum iron requirements of marine phytoplankton and the implications for the biogeochemical control of new production. *Limnology and oceanography*, *36*(8), 1756-1771.

Britto, D. T., & Kronzucker, H. J. (2002). NH4+ toxicity in higher plants: a critical review. *Journal of plant physiology*, *159*(6), 567-584.

Broecker W. S. (1982a) Glacial to interglacial changes in ocean chemistry. *Progress Oceanography*, *2*, 151 – 197.

Broecker W. S. (1982b) Ocean chemistry during glacial time. *Geochimica et Cosmochimica Acta*, *46*, 1689 – 1706.

Bronk, D. A., Glibert, P. M., & Ward, B. B. (1994). Nitrogen uptake, dissolved organic nitrogen release, and new production. *Science*, *265*(5180), 1843-1846.

Bruland, K. W., Rue, E. L., & Smith, G. J. (2001). Iron and macronutrients in California coastal upwelling regimes: Implications for diatom blooms. *Limnology and Oceanography*, *46*(7), 1661-1674.

Brzezinski, M. A. (1985), The Si:C:N ratio of marine diatoms: Interspecific variability and the effect of some environmental variables, *Journal of Phycology, 21*, 347–357.

Brzezinski, M. A., Dickson, M. L., Nelson, D. M., & Sambrotto, R. (2003). Ratios of Si, C and N uptake by microplankton in the Southern Ocean. *Deep Sea Research Part II: Topical Studies in Oceanography*, *50*(3-4), 619-633.

Buchwald, C., Santoro, A. E., McIlvin, M. R., & Casciotti, K. L. (2012). Oxygen isotopic composition of nitrate and nitrite produced by nitrifying cocultures and natural marine assemblages. *Limnology and Oceanography*, *57*(5), 1361-1375.

Buck, K. R., Uttal-Cooke, L., Pilskaln, C. H., Roelke, D. L., Villac, M. C., Fryxell, G. A., ... & Chavez, F. P. (1992). Autecology of the diatom Pseudonitzschia australis, a domoic acid producer, from Monterey Bay, California. *Marine Ecology Progress Series*, 293-302.

Buesseler, K. O. (1998). The decoupling of production and particulate export in the surface ocean. *Global Biogeochemical Cycles*, *12*(2), 297-310.

Buitenhuis, E. T., Li, W. K., Vaulot, D., Lomas, M. W., Landry, M. R., Partensky, F., ... & Lantoine, F. (2012). Picophytoplankton biomass distribution in the global ocean. *Earth System Science Data*, *4*(1), 37-46.

Buitenhuis, E. T., Pangerc, T., Franklin, D. J., Le Quéré, C., & Malin, G. (2008). Growth rates of six coccolithophorid strains as a function of temperature. *Limnology and Oceanography*, *53*(3), 1181-1185.

Buitenhuis, E. T., van der Wal, P., & de Baar, H. J. (2001). Blooms of Emiliania huxleyi are sinks of atmospheric carbon dioxide: A field and mesocosm study derived simulation. *Global Biogeochemical Cycles*, *15*(3), 577-587.

Buma, A. G. J., Bano, N., Veldhuis, M. J. W., & Kraay, G. W. (1991). Comparison of the pigmentation of two strains of the prymnesiophyte Phaeocystis sp. *Netherlands Journal of Sea Research*, *27*(2), 173-182.

Burger, J. M., Moloney, C. L., Walker, D. R., Parrott, R. G., & Fawcett, S. E. (2020). Drivers of short-term variability in phytoplankton production in an embayment of the southern Benguela upwelling system. *Journal of Marine Systems*, 103341.

Bush, M. J. (2020). The Carbon Cycle. In *Climate Change and Renewable Energy* (pp. 109-141). Palgrave Macmillan, Cham.

Campbell, L., & Vaulot, D. (1993). Photosynthetic picoplankton community structure in the subtropical North Pacific Ocean near Hawaii (station ALOHA). *Deep Sea Research Part I: Oceanographic Research Papers*, *40*(10), 2043-2060.

Carpenter, J. H. (1965). THE ACCURACY OF THE WINKLER METHOD FOR DISSOLVED OXYGEN ANALYSIS 1. *Limnology and Oceanography*, *10*(1), 135-140.

Carter, G. S., Gregg, M. C., & Merrifield, M. A. (2006). Flow and mixing around a small seamount on Kaena Ridge, Hawaii. *Journal of physical oceanography*, *36*(6), 1036-1052.

Carter, L., McCave, I. N., & Williams, M. J. (2008). Circulation and water masses of the Southern Ocean: a review. *Developments in earth and environmental sciences*, *8*, 85-114.

Casciotti, K. L. (2016). Nitrogen and oxygen isotopic studies of the marine nitrogen cycle. *Annual review of marine science*, *8*, 379-407.

Casciotti, K. L., & Buchwald, C. (2012). Insights on the marine microbial nitrogen cycle from isotopic approaches to nitrification. *Frontiers in microbiology*, *3*, 356.

Casciotti, K. L., Sigman, D. M., Hastings, M. G., Böhlke, J. K., & Hilkert, A. (2002). Measurement of the oxygen isotopic composition of nitrate in seawater and freshwater using the denitrifier method. *Analytical chemistry*, *74*(19), 4905-4912.

Casey, J. R., Lomas, M. W., Michelou, V. K., Dyhrman, S. T., Orchard, E. D., Ammerman, J. W., & Sylvan, J. B. (2009). Phytoplankton taxon-specific orthophosphate (Pi) and ATP utilization in the western subtropical North Atlantic. *Aquatic microbial ecology*, *58*(1), 31-44.

Cassar, N., Bender, M. L., Barnett, B. A., Fan, S., Moxim, W. J., Levy, H., & Tilbrook, B. (2007). The Southern Ocean biological response to aeolian iron deposition. *Science*, *317*(5841), 1067-1070.

Cassar, N., Wright, S. W., Thomson, P. G., Trull, T. W., Westwood, K. J., de Salas, M., ... & Matear, R. J. (2015). The relation of mixed-layer net community production to phytoplankton community composition in the Southern Ocean. *Global Biogeochemical Cycles*, *29*(4), 446-462.

Cavagna, A. J., Fripiat, F., Elskens, M., Mangion, P., Chirurgien, L., Closset, I., ... & Fernandez, C. (2015). Production regime and associated N cycling in the vicinity of Kerguelen Island, Southern Ocean. *Biogeosciences*, *12*(21), 6515-6528.

Cefarelli, A. O., Ferrario, M. E., Almandoz, G. O., Atencio, A. G., Akselman, R., & Vernet, M. (2010). Diversity of the diatom genus Fragilariopsis in the Argentine Sea and Antarctic waters: morphology, distribution and abundance. *Polar biology*, *33*(11), 1463-1484.

Cefarelli, A. O., Vernet, M., & Ferrario, M. E. (2011). Phytoplankton composition and abundance in relation to free-floating Antarctic icebergs. *Deep Sea Research Part II: Topical Studies in Oceanography*, *58*(11-12), 1436-1450.

Cerovečki, I., Talley, L. D., Mazloff, M. R., & Maze, G. (2013). Subantarctic mode water formation, destruction, and export in the eddy-permitting Southern Ocean state estimate. *Journal of physical oceanography*, *43*(7), 1485-1511.

Charalampopoulou, A., Poulton, A. J., Bakker, D. C., Lucas, M. I., Stinchcombe, M. C., & Tyrrell, T. (2016). Environmental drivers of coccolithophore abundance and calcification across Drake Passage (Southern Ocean). *Biogeosciences*, *13*, 5917-5935.

Charlson, R. J., Lovelock, J. E., Andreae, M. O., & Warren, S. G. (1987). Oceanic phytoplankton, atmospheric sulphur, cloud albedo and climate. *Nature*, *326*(6114), 655-661.

Checkley Jr, D. M., & Miller, C. A. (1989). Nitrogen isotope fractionation by oceanic zooplankton. *Deep Sea Research Part A. Oceanographic Research Papers*, *36*(10), 1449-1456.

Chelton, D. B., Schlax, M. G., Witter, D. L., & Richman, J. G. (1990). Geosat altimeter observations of the surface circulation of the Southern Ocean. *Journal of Geophysical Research: Oceans*, *95*(C10), 17877-17903.

Chen, Y. Q., Wang, N., Zhang, P., Zhou, H., & Qu, L. H. (2002). Molecular evidence identifies bloom-forming Phaeocystis (Prymnesiophyta) from coastal waters of southeast China as Phaeocystis globosa. *Biochemical Systematics and Ecology*, *30*(1), 15-22.

Chisholm, S. W. (2000). Stirring times in the Southern Ocean. *Nature*, *407*(6805), 685-686.

Chisholm, S. W., & Morel, F. M. M. (1991). Preface to What controls phytoplankton production in nutrient-rich areas of the open sea. *Limnol. Oceanogr*, *36*.

Christaki, U., Lefèvre, D., Georges, C., Colombet, J., Catala, P., Courties, C., ... & Obernosterer, I. (2014). Microbial food web dynamics during spring phytoplankton blooms in the naturally iron-fertilized Kerguelen area (Southern Ocean). *Biogeosciences*, *11*(23), 6739.

Clay, B. L., & Kugrens, P. (1999). Characterization of Hemiselmis amylosa sp. nov. and phylogenetic placement of the blue-green cryptomonads H. amylosa and Falcomonas daucoides. *Protist*, *150*(3), 297-310.

Cochlan, W. P. (2008). Nitrogen uptake in the Southern Ocean. *Nitrogen in the Marine Environment, edited by: Capone, DG, Bronk, DA, Mulholland, MR, and Carpenter, EJ, 2nd Edition, Academic Press, Elsevier*, 569-596.

Cochlan, W. P., & Bronk, D. A. (2003). Effects of ammonium on nitrate utilization in the Ross Sea, Antarctica: implications for f-ratio estimates. *Biogeochemistry of the Ross Sea*, *78*, 159-178.

Cochlan, W. P., & Kudela, R. M. (2006). The Southern Ocean iron enrichment experiment: the nitrogen uptake response. In *Report of the 2004 Workshop on In Situ Iron Enrichment Experiments in the Eastern and Western Subarctic Pacific, PICES Sci. Rep* (Vol. 31, pp. 26-31).

Cochlan, W. P., Bronk, D. A., & Coale, K. H. (2002). Trace metals and nitrogenous nutrition of Antarctic phytoplankton: experimental observations in the Ross Sea. *Deep Sea Research Part II: Topical Studies in Oceanography*, *49*(16), 3365-3390.

Cochlan, W. P., Harrison, P. J., & Denman, K. L. (1991). Diel periodicity of nitrogen uptake by marine phytoplankton in nitrate-rich environments. *Limnology and Oceanography*, *36*(8), 1689-1700.

Codispoti, L. A. (1989). Phosphorus vs. nitrogen limitation of new and export production. *Proxuctivity of the Ocean: Present and Past*, 377-394.

Coello-Camba, A., Llabrés, M., Duarte, C. M., & Agusti, S. (2017). Zooplankton excretion metabolites stimulate Southern Ocean phytoplankton growth. *Polar Biology*, *40*(10), 2035-2045.

Cohen, N. R., Mann, E., Stemple, B., Moreno, C. M., Rauschenberg, S., Jacquot, J. E., ... & Marchetti, A. (2018). Iron storage capacities and associated ferritin gene expression among marine diatoms. *Limnology and Oceanography*, *63*(4), 1677-1691.

Collier, J. L., Brahamsha, B., & Palenik, B. (1999). The marine cyanobacterium Synechococcus sp. WH7805 requires urease (urea amiohydrolase, EC 3.5. 1.5) to utilize urea as a nitrogen source: molecular-genetic and biochemical analysis of the enzyme. *Microbiology*, *145*(2), 447-459.

Collins, S., Rost, B., & Rynearson, T. A. (2014). Evolutionary potential of marine phytoplankton under ocean acidification. *Evolutionary applications*, *7*(1), 140-155.

Constable, A. J., Melbourne-Thomas, J., Corney, S. P., Arrigo, K. R., Barbraud, C., Barnes, D. K., ... & Davidson, A. T. (2014). Climate change and Southern Ocean ecosystems I: how changes in physical habitats directly affect marine biota. *Global change biology*, *20*(10), 3004-3025.

Conway, H. L., & Harrison, P. J. (1977). Marine diatoms grown in chemostats under silicate or ammonium limitation. IV. Transient response of Chaetoceros debilis, Skeletonema costatum, and Thalassiosira gravida to a single addition of the limiting nutrient. *Marine Biology*, *43*(1), 33-43.

Corner, E. D. S., & Davies, A. G. (1971). Plankton as a factor in the nitrogen and phosphorus cycles in the sea. In *Advances in Marine Biology* (Vol. 9, pp. 101-204). Academic Press.

Cornet-Barthaux, V., Armand, L., & Quéguiner, B. (2007). Biovolume and biomass estimates of key diatoms in the Southern Ocean. *Aquatic Microbial Ecology*, *48*(3), 295-308.

Cox, P. M., Betts, R. A., Jones, C. D., Spall, S. A., & Totterdell, I. J. (2000). Acceleration of global warming due to carbon-cycle feedbacks in a coupled climate model. *Nature*, *408*(6809), 184-187.

Croot, P. L., Baars, O., & Streu, P. (2011). The distribution of dissolved zinc in the Atlantic sector of the Southern Ocean. *Deep Sea Research Part II: Topical Studies in Oceanography*, *58*(25-26), 2707-2719.

Croot, P. L., Frew, R. D., Sander, S., Hunter, K. A., Ellwood, M. J., Pickmere, S. E., ... & Boyd, P. W. (2007). Physical mixing effects on iron biogeochemical cycling: FeCycle experiment. *Journal of Geophysical Research: Oceans*, *112*(C6).

Cubillos, J. C., Wright, S. W., Nash, G., De Salas, M. F., Griffiths, B., Tilbrook, B., ... & Hallegraeff, G. M. (2007). Calcification morphotypes of the coccolithophorid Emiliania huxleyi in the Southern Ocean: changes in 2001 to 2006 compared to historical data. *Marine Ecology Progress Series*, *348*, 47-54.

Cullen, J. J. (1991). Hypotheses to explain high-nutrient conditions in the open sea. *Limnology and Oceanography*, *36*(8), 1578-1599.

Cullen, J. T., Lane, T. W., Morel, F. M., & Sherrell, R. M. (1999). Modulation of cadmium uptake in phytoplankton by seawater CO 2 concentration. *Nature*, *402*(6758), 165-167.

d'Ovidio, F., Della Penna, A., Trull, T. W., Nencioli, F., Pujol, M. I., Rio, M. H., ... & Blain, S. (2015). The biogeochemical structuring role of horizontal stirring: Lagrangian perspectives on iron delivery downstream of the Kerguelen plateau.

Davidson, A. T., & Marchant, H. J. (1987). Binding of manganese by Antarctic Phaeocystis pouchetii and the role of bacteria in its release. *Marine biology*, *95*(3), 481-487.

Davidson, A. T., Scott, F. J., Nash, G. V., Wright, S. W., & Raymond, B. (2010). Physical and biological control of protistan community composition, distribution and abundance in the seasonal ice zone of the Southern Ocean between 30 and 80 E. *Deep Sea Research Part II: Topical Studies in Oceanography*, *57*(9-10), 828-848.

Davis, P. G., & Sieburth, J. M. (1984). Estuarine and oceanic microflagellate predation of actively growing bacteria: estimation by frequency of dividing-divided bacteria. *Marine ecology progress series. Oldendorf*, *19*(3), 237-246.

de Baar, H. J., Boyd, P. W., Coale, K. H., Landry, M. R., Tsuda, A., Assmy, P., ... & Buesseler, K. O. (2005). Synthesis of iron fertilization experiments: from the iron age in the age of enlightenment. *Journal of Geophysical Research: Oceans*, *110*(C9).

de Baar, H. J., de Jong, J. T., Bakker, D. C., Löscher, B. M., Veth, C., Bathmann, U., & Smetacek, V. (1995). Importance of iron for plankton blooms and carbon dioxide drawdown in the Southern Ocean. *Nature*, *373*(6513), 412-415.

de Boyer Montégut, C., Madec, G., Fischer, A. S., Lazar, A., & Iudicone, D. (2004). Mixed layer depth over the global ocean: An examination of profile data and a profile-based climatology. *Journal of Geophysical Research: Oceans*, *109*(C12).

de Broyer, C., & Danis, B. (2011). How many species in the Southern Ocean? Towards a dynamic inventory of the Antarctic marine species. *Deep sea research Part II: Topical studies in oceanography*, *58*(1-2), 5-17.

de Salas, M. F., Eriksen, R., Davidson, A. T., & Wright, S. W. (2011). Protistan communities in the Australian sector of the Sub-Antarctic Zone during SAZ-Sense. *Deep Sea Research Part II: Topical Studies in Oceanography*, *58*(21-22), 2135-2149.

Deacon, G. E. R. (1937). The hydrology of the Southern Ocean. *Discovery Rep.*, *15*, 3-122.

Deacon, G. E. R. (1982). Physical and biological zonation in the Southern Ocean. *Deep Sea Research Part A. Oceanographic Research Papers*, *29*(1), 1-15.

Deacon, G. E. R. (1983). Kerguelen, Antarctic and subantarctic. *Deep Sea Research Part A. Oceanographic Research Papers*, *30*(1), 77-81.
Deacon, G. E. R. (1933). A general account of the hydrology of the South Atlantic ocean. *Discovery Reports*, *7*.
Dehairs, F., Fripiat, F., Cavagna, A. J., Trull, T. W., Fernandez, C., Davies, D., ... & Elskens, M. (2015). Nitrogen cycling in the Southern Ocean Kerguelen Plateau area: evidence for significant surface nitrification from nitrate isotopic compositions. *Biogeosciences*, *12*(5), 1459-1482.
DeNiro, M. J., & Epstein, S. (1981). Influence of diet on the distribution of nitrogen isotopes in animals. *Geochimica et cosmochimica acta*, *45*(3), 341-351.
Denman, K. L. (2008). Climate change, ocean processes and ocean iron fertilization. *Marine Ecology Progress Series*, *364*, 219-225.
Deppeler, S. L., & Davidson, A. T. (2017). Southern Ocean phytoplankton in a changing climate. *Frontiers in Marine Science*, *4*, 40.
DeVries, T., Primeau, F., & Deutsch, C. (2012). The sequestration efficiency of the biological pump. *Geophysical Research Letters*, *39*(13).
Diamond, D. (1994). QuikChem Method 10-114-21-1-B: Silicate by flow injection analysis. *Milwaukee, WI: Lachat Instruments*.
DiFiore, P. J., Sigman, D. M., & Dunbar, R. B. (2009). Upper ocean nitrogen fluxes in the Polar Antarctic Zone: Constraints from the nitrogen and oxygen isotopes of nitrate. *Geochemistry, Geophysics, Geosystems*, *10*(11).
DiFiore, P. J., Sigman, D. M., Karsh, K. L., Trull, T. W., Dunbar, R. B., & Robinson, R. S. (2010). Poleward decrease in the isotope effect of nitrate assimilation across the Southern Ocean. *Geophysical Research Letters*, *37*(17).
DiFiore, P. J., Sigman, D. M., Trull, T. W., Lourey, M. J., Karsh, K., Cane, G., & Ho, R. (2006). Nitrogen isotope constraints on subantarctic biogeochemistry. *Journal of Geophysical Research: Oceans*, *111*(C8).
DiTullio, G. R., & Smith Jr, W. O. (1995). Relationship between dimethylsulfide and phytoplankton pigment concentrations in the Ross Sea, Antarctica. *Deep Sea Research Part I: Oceanographic Research Papers*, *42*(6), 873-892.
DiTullio, G. R., Grebmeier, J. M., Arrigo, K. R., Lizotte, M. P., Robinson, D. H., Leventer, A., ... & Dunbar, R. B. (2000). Rapid and early export of Phaeocystis antarctica blooms in the Ross Sea, Antarctica. *Nature*, *404*(6778), 595-598.
Doblin, M. A., Petrou, K. L., Shelly, K., Westwood, K., Van den Enden, R., Wright, S., ... & Ralph, P. J. (2011). Diel variation of chlorophyll-a fluorescence, phytoplankton pigments and productivity in the Sub-Antarctic and Polar Front Zones south of Tasmania, Australia. *Deep Sea Research Part II: Topical Studies in Oceanography*, *58*(21-22), 2189-2199.
Dolgin, A., & Adolf, J. (2019). Scanning Electron Microscopy of Phytoplankton: Achieving High Quality Images Through the Use of Safer Alternative Chemical Fixatives. *Journal of Young Investigators*, *37*(1).
Dong, S., Sprintall, J., & Gille, S. T. (2006). Location of the Antarctic polar front from AMSR-E satellite sea surface temperature measurements. *Journal of Physical Oceanography*, *36*(11), 2075-2089.
Doolittle, D. F., Li, W. K., & Wood, A. M. (2008). Wintertime abundance of picoplankton in the Atlantic sector of the Southern Ocean. *Nova Hedwigia*, *133*, 147-160.
Dortch, Q. (1990). The interaction between ammonium and nitrate uptake in phytoplankton. *Marine ecology progress series. Oldendorf*, *61*(1), 183-201.
Dortch, Q., & Conway, H. L. (1984). Interactions between nitrate and ammonium uptake: variation with growth rate, nitrogen source and species. *Marine Biology*, *79*(2), 151-164.
Doty, M. S., & Oguri, M. (1956). The island mass effect. *ICES Journal of Marine Science*, *22*(1), 33-37.

Doust, A. B., Wilk, K. E., Curmi, P. M., & Scholes, G. D. (2006). The photophysics of cryptophyte light-harvesting. *Journal of Photochemistry and Photobiology A: Chemistry*, *184*(1-2), 1-17.

Ducklow, H. W., Baker, K., Martinson, D. G., Quetin, L. B., Ross, R. M., Smith, R. C., ... & Fraser, W. (2007). Marine pelagic ecosystems: the west Antarctic Peninsula. *Philosophical Transactions of the Royal Society B: Biological Sciences*, *362*(1477), 67-94.

Ducklow, H. W., Steinberg, D. K., & Buesseler, K. O. (2001). Upper ocean carbon export and the biological pump. *OCEANOGRAPHY-WASHINGTON DC-OCEANOGRAPHY SOCIETY-*, *14*(4), 50-58.

Dugdale, R. C., & Goering, J. J. (1967). Uptake of new and regenerated forms of nitrogen in primary productivity 1. *Limnology and oceanography*, *12*(2), 196-206.

Dugdale, R. C., Morel, A., Bricaud, A., & Wilkerson, F. P. (1989). Modeling new production in upwelling centers: a case study of modeling new production from remotely sensed temperature and color. *Journal of Geophysical Research: Oceans*, *94*(C12), 18119-18132.

Duncombe Rae, C. M. (1989). Physical and chemical marine environment of the Prince Edward Islands (Southern Ocean) during April/May 1987. *South African Journal of Marine Science*, *8*(1), 301-311.

DuRand, M. D., Olson, R. J., & Chisholm, S. W. (2001). Phytoplankton population dynamics at the Bermuda Atlantic Time-series station in the Sargasso Sea. *Deep Sea Research Part II: Topical Studies in Oceanography*, *48*(8-9), 1983-2003.

Dutkiewicz, S., Hickman, A. E., Jahn, O., Henson, S., Beaulieu, C., & Monier, E. (2019). Ocean colour signature of climate change. *Nature communications*, *10*(1), 1-13.

Ellwood, M. J., Boyd, P. W., & Sutton, P. (2008). Winter-time dissolved iron and nutrient distributions in the Subantarctic Zone from 40–52S; 155–160E. *Geophysical Research Letters*, *35*(11).

Ellwood, M. J., Strzepek, R. F., Strutton, P. G., Trull, T. W., Fourquez, M., & Boyd, P. W. (2020). Distinct iron cycling in a Southern Ocean eddy. *Nature communications*, *11*(1), 1-8.

Eppley, R. W., & Peterson, B. J. (1979). Particulate organic matter flux and planktonic new production in the deep ocean. *Nature*, *282*(5740), 677-680.

Eppley, R. W., Rogers, J. N., & McCarthy, J. J. (1969). Half-saturation constants for uptake of nitrate and ammonium by marine phytoplankton 1. *Limnology and oceanography*, *14*(6), 912-920.

Falkowski, P. G., Flagg, C. N., Rowe, G. T., Smith, S. L., Whitledge, T. E., & Wirick, C. D. (1988). The fate of a spring phytoplankton bloom: export or oxidation?. *Continental Shelf Research*, *8*(5-7), 457-484.

Fan, C., Glibert, P. M., Alexander, J., & Lomas, M. W. (2003). Characterization of urease activity in three marine phytoplankton species, Aureococcus anophagefferens, Prorocentrum minimum, and Thalassiosira weissflogii. *Marine Biology*, *142*(5), 949-958.

Farrant, G. K., Doré, H., Cornejo-Castillo, F. M., Partensky, F., Ratin, M., Ostrowski, M., ... & Acinas, S. G. (2016). Delineating ecologically significant taxonomic units from global patterns of marine picocyanobacteria. *Proceedings of the National Academy of Sciences*, *113*(24), E3365-E3374.

Fawcett, S. E., & Ward, B. B. (2011). Phytoplankton succession and nitrogen utilization during the development of an upwelling bloom. *Marine Ecology Progress Series*, *428*, 13-31.

Fawcett, S. E., Lomas, M. W., Casey, J. R., Ward, B. B., & Sigman, D. M. (2011). Assimilation of upwelled nitrate by small eukaryotes in the Sargasso Sea. *Nature Geoscience*, *4*(10), 717-722.

Fawcett, S. E., Lomas, M. W., Ward, B. B., & Sigman, D. M. (2014). The counterintuitive effect of summer-to-fall mixed layer deepening on eukaryotic new production in the Sargasso Sea. *Global biogeochemical cycles*, *28*(2), 86-102.

Fawcett, S. E., Ward, B. B., Lomas, M. W., & Sigman, D. M. (2015). Vertical decoupling of nitrate assimilation and nitrification in the Sargasso Sea. *Deep Sea Research Part I: Oceanographic Research Papers*, *103*, 64-72.

Fennel, K., & Boss, E. (2003). Subsurface maxima of phytoplankton and chlorophyll: Steady-state solutions from a simple model. *Limnology and Oceanography*, *48*(4), 1521-1534.

Fennel, K., Abbott, M. R., Spitz, Y. H., Richman, J. G., & Nelson, D. M. (2014). Modeling controls of phytoplankton production in the southwest Pacific sector of the Southern Ocean. *JOM-Journal of the Minerals, Metals and Materials Society*, *1*, 173.

Field, C. B., Behrenfeld, M. J., Randerson, J. T., & Falkowski, P. (1998). Primary production of the biosphere: integrating terrestrial and oceanic components. *science*, *281*(5374), 237-240.

Fielding, S., Ward, P., Pollard, R. T., Seeyave, S., Read, J. F., Hughes, J. A., ... & Castellani, C. (2007). Community structure and grazing impact of mesozooplankton during late spring/early summer 2004/2005 in the vicinity of the Crozet Islands (Southern Ocean). *Deep Sea Research Part II: Topical Studies in Oceanography*, *54*(18-20), 2106-2125.

Findlay, C. S., & Giraudeau, J. (2000). Extant calcareous nannoplankton in the Australian Sector of the Southern Ocean (austral summers 1994 and 1995). *Marine Micropaleontology*, *40*(4), 417-439.

Flombaum, P., Gallegos, J. L., Gordillo, R. A., Rincón, J., Zabala, L. L., Jiao, N., ... & Vera, C. S. (2013). Present and future global distributions of the marine Cyanobacteria Prochlorococcus and Synechococcus. *Proceedings of the National Academy of Sciences*, *110*(24), 9824-9829.

FlowJo™ Software (for Mac) [software application] Version *10.5.3*. Ashland, OR: Becton, Dickinson and Company; 2019.

Fofono, N. P. (1985). Physical properties of seawater: A new salinity scale and equation of state for seawater. *Journal of Geophysical Research, 90*, 3332- 3342.

Fourquez, M., Bressac, M., Deppeler, S. L., Ellwood, M., Obernosterer, I., Trull, T. W., & Boyd, P. W. (2020). Microbial competition in the subpolar southern ocean: an Fe–C Co-limitation experiment. *Frontiers in Marine Science*, *6*(JAN), 1-15.

Franck, V. M., Brzezinski, M. A., Coale, K. H., & Nelson, D. M. (2000). Iron and silicic acid concentrations regulate Si uptake north and south of the Polar Frontal Zone in the Pacific Sector of the Southern Ocean. *Deep Sea Research Part II: Topical Studies in Oceanography*, *47*(15-16), 3315-3338.

Francois, R. F., Altabet, M. A., Yu, E. F., Sigman, D. M., Bacon, M. P., Frank, M., ... & Labeyrie, L. D. (1997). Water column stratification in the Southern Ocean contributed to the lowering of glacial atmospheric CO2. *Nature*, *389*, 929-935.

Frankignoulle, M. (1994). A complete set of buffer factors for acid/base CO2 system in seawater. *Journal of Marine Systems*, *5*(2), 111-118.

Freeman, N. M., Lovenduski, N. S., Munro, D. R., Krumhardt, K. M., Lindsay, K., Long, M. C., & Maclennan, M. (2018). The variable and changing Southern Ocean silicate front: insights from the CESM Large Ensemble. *Global Biogeochemical Cycles*, *32*(5), 752-768.

Fripiat, F., Cavagna, A. J., Dehairs, F., Speich, S., André, L., & Cardinal, D. (2011). Silicon pool dynamics and biogenic silica export in the Southern Ocean inferred from Si-isotopes.

Fripiat, F., Elskens, M., Trull, T. W., Blain, S., Cavagna, A. J., Fernandez, C., ... & Dehairs, F. (2015). Significant mixed layer nitrification in a natural iron-fertilized bloom of the Southern Ocean. *Global Biogeochemical Cycles*, *29*(11), 1929-1943.

Fripiat, F., Martínez-García, A., Fawcett, S. E., Kemeny, P. C., Studer, A. S., Smart, S. M., ... & Haug, G. H. (2019). The isotope effect of nitrate assimilation in the Antarctic Zone: Improved estimates and paleoceanographic implications. *Geochimica et Cosmochimica Acta*, *247*, 261-279.

Frölicher, T. L., Sarmiento, J. L., Paynter, D. J., Dunne, J. P., Krasting, J. P., & Winton, M. (2015). Dominance of the Southern Ocean in anthropogenic carbon and heat uptake in CMIP5 models. *Journal of Climate*, *28*(2), 862-886.

Funk, C., Alami, M., Tibiletti, T., & Green, B. R. (2011). High light stress and the one-helix LHC-like proteins of the cryptophyte Guillardia theta. *Biochimica et Biophysica Acta (BBA)-Bioenergetics*, *1807*(7), 841-846.

Gall, M. P., Boyd, P. W., Hall, J., Safi, K. A., & Chang, H. (2001). Phytoplankton processes. Part 1: community structure during the Southern Ocean iron release experiment (SOIREE). *Deep Sea Research Part II: Topical Studies in Oceanography*, *48*(11-12), 2551-2570.

Garibotti, I. A., Vernet, M., & Ferrario, M. E. (2005). Annually recurrent phytoplanktonic assemblages during summer in the seasonal ice zone west of the Antarctic Peninsula (Southern Ocean). *Deep Sea Research Part I: Oceanographic Research Papers*, *52*(10), 1823-1841.

Garside, C. (1982). A chemiluminescent technique for the determination of nanomolar concentrations of nitrate and nitrite in seawater. *Marine Chemistry*, *11*(2), 159-167.

Gerringa, L. J., Alderkamp, A. C., Laan, P., Thuroczy, C. E., De Baar, H. J., Mills, M. M., ... & Arrigo, K. R. (2012). Iron from melting glaciers fuels the phytoplankton blooms in Amundsen Sea (Southern Ocean): Iron biogeochemistry. *Deep Sea Research Part II: Topical Studies in Oceanography*, *71*, 16-31.

Gervais, F., Riebesell, U., & Gorbunov, M. Y. (2002). Changes in primary productivity and chlorophyll a in response to iron fertilization in the Southern Polar Frontal Zone. *Limnology and Oceanography*, *47*(5), 1324-1335.

Gille, S. T. (1994). Mean sea surface height of the Antarctic Circumpolar Current from Geosat data: Method and application. *Journal of Geophysical Research: Oceans*, *99*(C9), 18255-18273.

Glibert, P. M., & Ray, R. T. (1990). Different patterns of growth and nitrogen uptake in two clones of marineSynechococcus spp. *Marine Biology*, *107*(2), 273-280.

Glibert, P. M., Harrison, J., Heil, C., & Seitzinger, S. (2006). Escalating worldwide use of urea–a global change contributing to coastal eutrophication. *Biogeochemistry*, *77*(3), 441-463.

Glibert, P. M., Kana, T. M., Olson, R. J., Kirchman, D. L., & Alberte, R. S. (1986). Clonal comparisons of growth and photosynthetic responses to nitrogen availability in marine Synechococcus spp. *Journal of experimental marine biology and ecology*, *101*(1-2), 199-208.

Glibert, P. M., Wilkerson, F. P., Dugdale, R. C., Raven, J. A., Dupont, C. L., Leavitt, P. R., ... & Kana, T. M. (2016). Pluses and minuses of ammonium and nitrate uptake and assimilation by phytoplankton and implications for productivity and community composition, with emphasis on nitrogen-enriched conditions. *Limnology and Oceanography*, *61*(1), 165-197.

Glover, H. E., Prézelin, B. B., Campbell, L., Wyman, M., & Garside, C. (1988). A nitrate-dependent Synechococcus bloom in surface Sargasso Sea water. *Nature*, *331*(6152), 161-163.

Goericke, R., & Welschmeyer, N. A. (1993). The marine prochlorophyte Prochlorococcus contributes significantly to phytoplankton biomass and primary production in the Sargasso Sea. *Deep Sea Research Part I: Oceanographic Research Papers*, *40*(11-12), 2283-2294.

Gonfiantini, R. (1984). Stable isotope reference samples for geochemical and hydrological investigations. *Report of Advisory Group, Vienna*.

González, M. L., Molina, V., Florez-Leiva, L., Oriol, L., Cavagna, A. J., Dehairs, F., ... & Fernandez, C. (2014). Nitrogen fixation in the Southern Ocean: a case of study of the Fe-fertilized Kerguelen region (KEOPS II cruise). *Biogeosciences Discussions*, *11*(12), 17151-17185.

Gordon, A. L. (1975). An Antarctic oceanographic section along 170 E. In *Deep Sea Research and Oceanographic Abstracts* (Vol. 22, No. 6, pp. 357-377). Elsevier.

Gordon, A. L., Molinelli, E., & Baker, T. (1978). Large-scale relative dynamic topography of the Southern Ocean. *Journal of Geophysical Research: Oceans*, *83*(C6), 3023-3032.

Gould, S. B., Waller, R. F., & McFadden, G. I. (2008). Plastid evolution. *Annual review of plant biology*, *59*.

Gove, J. M., McManus, M. A., Neuheimer, A. B., Polovina, J. J., Drazen, J. C., Smith, C. R., ... & Dillon, A. K. (2016). Near-island biological hotspots in barren ocean basins. *Nature communications*, *7*(1), 1-8.

Granger, J., & Sigman, D. M. (2009). Removal of nitrite with sulfamic acid for nitrate N and O isotope analysis with the denitrifier method. *Rapid Communications in Mass Spectrometry: An International Journal Devoted to the Rapid Dissemination of Up-to-the-Minute Research in Mass Spectrometry*, *23*(23), 3753-3762.

Granger, J., Sigman, D. M., Needoba, J. A., & Harrison, P. J. (2004). Coupled nitrogen and oxygen isotope fractionation of nitrate during assimilation by cultures of marine phytoplankton. *Limnology and Oceanography*, *49*(5), 1763-1773.

Granger, J., Sigman, D. M., Rohde, M. M., Maldonado, M. T., & Tortell, P. D. (2010). N and O isotope effects during nitrate assimilation by unicellular prokaryotic and eukaryotic plankton cultures. *Geochimica et Cosmochimica Acta*, *74*(3), 1030-1040.

Granum, E., Raven, J. A., & Leegood, R. C. (2005). How do marine diatoms fix 10 billion tonnes of inorganic carbon per year?. *Canadian journal of botany*, *83*(7), 898-908.

Grasshoff K, Kremling K & Ehrhardt M. (1983). Methods of Seawater Analysis. *Verlag*

Grasshoff, K., Kremling, K., & Ehrhardt, M. (1999). Methods of seawater analysis, *Wiley VCH*.

Gravalosa, J. M., Flores, J. A., Sierro, F. J., & Gersonde, R. (2008). Sea surface distribution of coccolithophores in the eastern Pacific sector of the Southern Ocean (Bellingshausen and Amundsen Seas) during the late austral summer of 2001. *Marine Micropaleontology*, *69*(1), 16-25.

Green, S. E., & Sambrotto, R. N. (2006). Plankton community structure and export of C, N, P and Si in the Antarctic Circumpolar Current. *Deep Sea Research Part II: Topical Studies in Oceanography*, *53*(5-7), 620-643.

Griffiths, F. B., Bates, T. S., Quinn, P. K., Clementson, L. A., & Parslow, J. S. (1999). Oceanographic context of the First Aerosol Characterization Experiment (ACE 1): A physical, chemical, and biological overview. *Journal of Geophysical Research: Atmospheres*, *104*(D17), 21649-21671.

Grindley, J. R., & David, P. (1985). Nutrient upwelling and its effects in the lee of Marion Island. In *Antarctic Nutrient Cycles and Food Webs* (pp. 46-51). Springer, Berlin, Heidelberg.

Gruber, N. (2008). The marine nitrogen cycle: overview and challenges. *Nitrogen in the marine environment*, *2*, 1-50.

Gruber, N., Landschützer, P., & Lovenduski, N. S. (2019). The variable Southern Ocean carbon sink. *Annual review of marine science*, *11*, 159-186.

Guidi, L., Chaffron, S., Bittner, L., Eveillard, D., Larhlimi, A., Roux, S., ... & Coelho, L. P. (2016). Plankton networks driving carbon export in the oligotrophic ocean. *Nature*, *532*(7600), 465-470.

Guiry, M. D., & Guiry, G. M. (2018). AlgaeBase. National University of Ireland, Galway.

Guo, S., Zhou, Y., Shen, Q., & Zhang, F. (2007). Effect of ammonium and nitrate nutrition on some physiological processes in higher plants-growth, photosynthesis, photorespiration, and water relations. *Plant Biology*, *9*(1), 21-29.

Haberman, K. L., Quetin, L. B., & Ross, R. M. (2003a). Diet of the Antarctic krill (Euphausia superba Dana): I. Comparisons of grazing on Phaeocystis antarctica (Karsten) and Thalassiosira antarctica (Comber). *Journal of Experimental Marine Biology and Ecology*, *283*(1-2), 79-95.

Haberman, K. L., Ross, R. M., & Quetin, L. B. (2003b). Diet of the Antarctic krill (Euphausia superba Dana): II. Selective grazing in mixed phytoplankton assemblages. *Journal of Experimental Marine Biology and Ecology*, *283*(1-2), 97-113.

Hamm, C. E., Merkel, R., Springer, O., Jurkojc, P., Maier, C., Prechtel, K., & Smetacek, V. (2003). Architecture and material properties of diatom shells provide effective mechanical protection. *Nature*, *421*(6925), 841-843.

Hannides, C. C., Popp, B. N., Choy, C. A., & Drazen, J. C. (2013). Midwater zooplankton and suspended particle dynamics in the North Pacific Subtropical Gyre: A stable isotope perspective. *Limnology and Oceanography*, *58*(6), 1931-1946.

Hasle, G. R., Syvertsen, E. E., Steidinger, K. A., Tangen, K., & Tomas, C. R. (1996). *Identifying marine diatoms and dinoflagellates*. Elsevier.

Hawkings, J. R., Wadham, J. L., Tranter, M., Raiswell, R., Benning, L. G., Statham, P. J., ... & Telling, J. (2014). Ice sheets as a significant source of highly reactive nanoparticulate iron to the oceans. *Nature communications*, *5*(1), 1-8.

Heil, C. A., Revilla, M., Glibert, P. M., & Murasko, S. (2007). Nutrient quality drives differential phytoplankton community composition on the southwest Florida shelf. *Limnology and oceanography*, *52*(3), 1067-1078.

Heinze, C., Maier-Reimer, E., & Winn, K. (1991). Glacial pCO2 reduction by the world ocean: Experiments with the Hamburg carbon cycle model. *Paleoceanography*, *6*(4), 395-430.

Henley, S. F., Cavan, E. L., Fawcett, S. E., Kerr, R., Monteiro, T., Sherrell, R. M., ... & Marshall, T. (2020). Changing biogeochemistry of the Southern Ocean and its ecosystem implications. *Frontiers in Marine Science*.

Herndon, J., & Cochlan, W. P. (2007). Nitrogen utilization by the raphidophyte Heterosigma akashiwo: growth and uptake kinetics in laboratory cultures. *Harmful Algae*, *6*(2), 260-270.

Herraiz-Borreguero, L., & Rintoul, S. R. (2011). Subantarctic mode water: distribution and circulation. *Ocean Dynamics*, *61*(1), 103-126.

Heywood, K. J., Barton, E. D., & Simpson, J. H. (1990). The effects of flow disturbance by an oceanic island. *Journal of Marine Research*, *48*(1), 55-73.

Higgins, M. B., Robinson, R. S., Casciotti, K. L., McIlvin, M. R., & Pearson, A. (2009). A method for determining the nitrogen isotopic composition of porphyrins. *Analytical Chemistry*, *81*(1), 184-192.

Hildebrand, M. (2008). Diatoms, biomineralization processes, and genomics. *Chemical reviews*, *108*(11), 4855-4874.

Hill, D. R., & Rowan, K. S. (1989). The biliproteins of the Cryptophyceae. *Phycologia*, *28*(4), 455-463.

Hiscock, M. R., Lance, V. P., Apprill, A. M., Bidigare, R. R., Johnson, Z. I., Mitchell, B. G., ... & Barber, R. T. (2008). Photosynthetic maximum quantum yield increases are an essential component of the Southern Ocean phytoplankton response to iron. *Proceedings of the National Academy of Sciences*, *105*(12), 4775-4780.

Hiscock, M. R., Marra, J., Smith Jr, W. O., Goericke, R., Measures, C., Vink, S., ... & Barber, R. T. (2003). Primary productivity and its regulation in the Pacific Sector of the Southern Ocean. *Deep Sea Research Part II: Topical Studies in Oceanography*, *50*(3-4), 533-558.

Hoch, M. P., Fogel, M. L., & Kirchman, D. L. (1992). Isotope fractionation associated with ammonium uptake by a marine bacterium. *Limnology and oceanography*, *37*(7), 1447-1459.

Hoffmann, L. J., Peeken, I., Lochte, K., Assmy, P., & Veldhuis, M. (2006). Different reactions of Southern Ocean phytoplankton size classes to iron fertilization. *Limnology and Oceanography*, *51*(3), 1217-1229.

Holeton, C. L., Nedelec, F., Sanders, R., Brown, L., Moore, C. M., Stevens, D. P., ... & Lucas, C. H. (2005). Physiological state of phytoplankton communities in the Southwest Atlantic sector of the Southern Ocean, as measured by fast repetition rate fluorometry. *Polar Biology*, *29*(1), 44-52.

Holliday, N. P., & Read, J. F. (1998). Surface oceanic fronts between Africa and Antarctica. *Deep Sea Research Part I: Oceanographic Research Papers*, *45*(2-3), 217-238.

Holligan, P. M., Charalampopoulou, A., & Hutson, R. (2010). Seasonal distributions of the coccolithophore, Emiliania huxleyi, and of particulate inorganic carbon in surface waters of the Scotia Sea. *Journal of Marine Systems*, *82*(4), 195-205.

Holmes, R. M., Aminot, A., Kérouel, R., Hooker, B. A., & Peterson, B. J. (1999). A simple and precise method for measuring ammonium in marine and freshwater ecosystems. *Canadian Journal of Fisheries and Aquatic Sciences*, *56*(10), 1801-1808.

Holmes, T. M., Wuttig, K., Chase, Z., van der Merwe, P., Townsend, A. T., Schallenberg, C., ... & Bowie, A. R. (2019). Iron availability influences nutrient drawdown in the Heard and McDonald Islands region, Southern Ocean. *Marine Chemistry*, *211*, 1-14.

Hong, Y., Smith Jr, W. O., & White, A. M. (1997). Studies on transparent exopolymer particles (Tep) produced in the Ross Sea (Antarctica) and by Phaeocystis antarctica (Prymnesiophyceae) 1. *Journal of Phycology*, *33*(3), 368-376.

Honjo, S. (2004). Particle export and the biological pump in the Southern Ocean. *Antarctic Science*, *16*(4), 501.

Hopkinson, B. M., Dupont, C. L., Allen, A. E., & Morel, F. M. (2011). Efficiency of the CO2-concentrating mechanism of diatoms. *Proceedings of the National Academy of Sciences*, *108*(10), 3830-3837.

Hoppe, C. J. M., Klaas, C., Ossebaar, S., Soppa, M. A., Cheah, W., Laglera, L. M., ... & Hoppema, M. (2017). Controls of primary production in two phytoplankton blooms in the Antarctic Circumpolar Current. *Deep Sea Research Part II: Topical Studies in Oceanography*, *138*, 63-73.

Huang, S., Wilhelm, S. W., Harvey, H. R., Taylor, K., Jiao, N., & Chen, F. (2012). Novel lineages of Prochlorococcus and Synechococcus in the global oceans. *The ISME journal*, *6*(2), 285-297.

Hunter-Cevera, K. R., Neubert, M. G., Olson, R. J., Shalapyonok, A., Solow, A. R., & Sosik, H. M. (2020). Seasons of Syn. *Limnology and Oceanography*, *65*(5), 1085-1102.

Hut, G. (1987). Consultants' group meeting on stable isotope reference samples for geochemical and hydrological investigations. Report to the Director General, International Atomic Energy Agency, Vienna, April 1987.

Hutchins, D. A., & Bruland, K. W. (1998). Iron-limited diatom growth and Si: N uptake ratios in a coastal upwelling regime. *Nature*, *393*(6685), 561-564.

Hutchins, D. A., Sedwick, P. N., DiTullio, G. R., Boyd, P. W., Queguiner, B., Griffiths, F. B., & Crossley, C. (2001). Control of phytoplankton growth by iron and silicic acid availability in the subantarctic Southern Ocean: Experimental results from the SAZ Project. *Journal of Geophysical Research: Oceans*, *106*(C12), 31559-31572.

Ilmavirta, V. (1988). Phytoflagellates and their ecology in Finnish brown-water lakes. In *Flagellates in Freshwater Ecosystems* (pp. 255-270). Springer, Dordrecht.

Janssen, D. J., Sieber, M., Ellwood, M. J., Conway, T. M., Barrett, P. M., Chen, X., ... & Jaccard, S. L. (2020). Trace metal and nutrient dynamics across broad biogeochemical gradients in the Indian and Pacific sectors of the Southern Ocean. *Marine chemistry*, 103773.

Jickells, T. D., An, Z. S., Andersen, K. K., Baker, A. R., Bergametti, G., Brooks, N., ... & Kawahata, H. (2005). Global iron connections between desert dust, ocean biogeochemistry, and climate. *science*, *308*(5718), 67-71.

Jickells, T. D., Buitenhuis, E., Altieri, K., Baker, A. R., Capone, D., Duce, R. A., ... & Lee, K. (2017). A reevaluation of the magnitude and impacts of anthropogenic atmospheric nitrogen inputs on the ocean. *Global Biogeochemical Cycles*, *31*(2), 289-305.

Johnson, Z. I., Zinser, E. R., Coe, A., McNulty, N. P., Woodward, E. M. S., & Chisholm, S. W. (2006). Niche partitioning among Prochlorococcus ecotypes along ocean-scale environmental gradients. *Science*, *311*(5768), 1737-1740.

Jones, G. B., Curran, M. A., Swan, H. B., Greene, R. M., Griffiths, F. B., & Clementson, L. A. (1998). Influence of different water masses and biological activity on dimethylsulphide and dimethylsulphoniopropionate in the subantarctic zone of the Southern Ocean during ACE 1. *Journal of Geophysical Research: Atmospheres*, *103*(D13), 16691-16701.

Jones, R. I. (1988). Vertical distribution and diel migration of flagellated phytoplankton in a small humic lake. *Hydrobiologia*, *161*(1), 75-87.

Kalnay, E., Kanamitsu, M., Kistler, R., Collins, W., Deaven, D., Gandin, L., ... & Zhu, Y. (1996). The NCEP/NCAR 40-year reanalysis project. *Bulletin of the American meteorological Society*, *77*(3), 437-472.

Kaňa, R., Kotabová, E., Sobotka, R., & Prášil, O. (2012). Non-photochemical quenching in cryptophyte alga Rhodomonas salina is located in chlorophyll a/c antennae. *PLoS One*, *7*(1), e29700.

Kana, T. M., & Glibert, P. M. (1987). Effect of irradiances up to 2000 μE m− 2 s− 1 on marine Synechococcus WH7803—I. Growth, pigmentation, and cell composition. *Deep Sea Research Part A. Oceanographic Research Papers*, *34*(4), 479-495.

Kana, T. M., Glibert, P. M., Goericke, R., & Welschmeyer, N. A. (1988). Zeaxanthin and ß-carotene in Synechococcus WH7803 respond differently to irradiance. *Limnology and Oceanography*, *33*(6part2), 1623-1626.

Kang, S. H., Kang, J. S., Lee, S., Chung, K. H., Kim, D., & Park, M. G. (2001). Antarctic phytoplankton assemblages in the marginal ice zone of the northwestern Weddell Sea. *Journal of Plankton Research*, *23*(4), 333-352.

Kaprelyants, A. S., & Kell, D. B. (1993). Dormancy in stationary-phase cultures of Micrococcus luteus: flow cytometric analysis of starvation and resuscitation. *Applied and environmental microbiology*, *59*(10), 3187-3196.

Karl DM, Bidigare RR, Letelier RM (2001) Long-term changes in plankton community structure and productivity in the North Pacific Subtropical Gyre: the domain shift hypothesis. Deep-Sea Res II 48: 1449−1470

Karsh, K. L., Trull, T. W., Lourey, M. J., & Sigman, D. M. (2003). Relationship of nitrogen isotope fractionation to phytoplankton size and iron availability during the Southern Ocean Iron RElease Experiment (SOIREE). *Limnology and Oceanography*, *48*(3), 1058-1068.

Kemp, A. E. S., Pearce, R. B., Grigorov, I., Rance, J., Lange, C. B., Quilty, P., & Salter, I. (2006). Production of giant marine diatoms and their export at oceanic frontal zones: Implications for Si and C flux from stratified oceans. *Global Biogeochemical Cycles*, *20*(4).

Khatiwala, S. P., Tanhua, T., Mikaloff Fletcher, S. E., Gerber, M., Doney, S. C., Graven, H. D., ... & Sabine, C. L. (2013). Global ocean storage of anthropogenic carbon. *Biogeosciences*, *10*(4), 2169-2191.

Kirkham, A. R., Lepère, C., Jardillier, L. E., Not, F., Bouman, H., Mead, A., & Scanlan, D. J. (2013). A global perspective on marine photosynthetic picoeukaryote community structure. *The ISME journal*, *7*(5), 922-936.

Knapp, A. N., Casciotti, K. L., & Prokopenko, M. G. (2018). Dissolved Organic Nitrogen Production and Consumption in Eastern Tropical South Pacific Surface Waters. *Global Biogeochemical Cycles*, *32*(5), 769-783.

Knapp, A. N., Casciotti, K. L., Berelson, W. M., Prokopenko, M. G., & Capone, D. G. (2016). Low rates of nitrogen fixation in eastern tropical South Pacific surface waters. *Proceedings of the National Academy of Sciences*, *113*(16), 4398-4403.

Knapp, A. N., Sigman, D. M., & Lipschultz, F. (2005). N isotopic composition of dissolved organic nitrogen and nitrate at the Bermuda Atlantic Time-series Study site. *Global Biogeochemical Cycles*, *19*(1).

Knox, F., & McElroy, M. B. (1984). Changes in atmospheric CO2: Influence of the marine biota at high latitude. *Journal of Geophysical Research: Atmospheres*, *89*(D3), 4629-4637.

Koch, F., & Trimborn, S. (2019). Limitation by Fe, Zn, Co and B12 results in similar physiological responses in two Antarctic phytoplankton species. *Frontiers in Marine Science*, *6*, 514.

Kopczyńska, E. E., Dehairs, F., Elskens, M., & Wright, S. (2001). Phytoplankton and microzooplankton variability between the Subtropical and Polar Fronts south of Australia: Thriving under regenerative and new production in late summer. *Journal of Geophysical Research: Oceans*, *106*(C12), 31597-31609.

Kopczyńska, E. E., Savoye, N., Dehairs, F., Cardinal, D., & Elskens, M. (2007). Spring phytoplankton assemblages in the Southern Ocean between Australia and Antarctica. *Polar Biology*, *31*(1), 77-88.

Koroleff, E (1972), in: *New Baltic Manual, Coop. Res Rep. Ser. A*. (29): Carlberg, S.R. (Ed.).

Kruskal, W. H., & Wallis, W. A. (1952). Use of ranks in one-criterion variance analysis. *Journal of the American statistical Association*, *47*(260), 583-621.

Kudela, R. M., & Dugdale, R. C. (2000). Nutrient regulation of phytoplankton productivity in Monterey Bay, California. *Deep Sea Research Part II: Topical Studies in Oceanography*, *47*(5-6), 1023-1053.

Kustka, A. B., Allen, A. E., & Morel, F. M. (2007). Sequence analysis and transcriptional regulation of iron acquisition genes in two marine diatoms 1. *Journal of Phycology*, *43*(4), 715-729.

Kwon, E. Y., Primeau, F., & Sarmiento, J. L. (2009). The impact of remineralization depth on the air–sea carbon balance. *Nature Geoscience*, *2*(9), 630-635.

l'Helguen, S., Maguer, J. F., & Caradec, J. (2008). Inhibition kinetics of nitrate uptake by ammonium in size-fractionated oceanic phytoplankton communities: implications for new production and f-ratio estimates. *Journal of Plankton Research*, *30*(10), 1179-1188.

Lampe, R. H., Hernandez, G., Lin, Y. Y., & Marchetti, A. (2020). Representative diatom and coccolithophore species exhibit divergent responses throughout simulated upwelling cycles. *bioRxiv*.

Lampe, R. H., Mann, E. L., Cohen, N. R., Till, C. P., Thamatrakoln, K., Brzezinski, M. A., ... & Marchetti, A. (2018). Different iron storage strategies among bloom-forming diatoms. *Proceedings of the National Academy of Sciences*, *115*(52), E12275-E12284.

Lancelot, C., Wassmann, P., & Barth, H. (1994). Ecology of Phaeocystis-dominated ecosystems. *Journal of Marine Systems*, *5*(1), 1-4.

Landry, M. R., Selph, K. E., Brown, S. L., Abbott, M. R., Measures, C. I., Vink, S., ... & Nolla, H. (2002). Seasonal dynamics of phytoplankton in the Antarctic Polar Front region at 170° W. *Deep Sea Research Part II: Topical Studies in Oceanography*, *49*(9-10), 1843-1865.

Landschützer, P., Gruber, N., & Bakker, D. C. (2016). Decadal variations and trends of the global ocean carbon sink. *Global Biogeochemical Cycles*, *30*(10), 1396-1417.

Landschützer, P., Gruber, N., Bakker, D. C., & Schuster, U. (2014). Recent variability of the global ocean carbon sink. *Global Biogeochemical Cycles*, *28*(9), 927-949.

Lannuzel, D., Bowie, A. R., Remenyi, T., Lam, P., Townsend, A., Ibisanmi, E., ... & Schoemann, V. (2011). Distributions of dissolved and particulate iron in the sub-Antarctic and Polar Frontal Southern Ocean (Australian sector). *Deep Sea Research Part II: Topical Studies in Oceanography*, *58*(21-22), 2094-2112.

Lasbleiz, M., Leblanc, K., Armand, L. K., Christaki, U., Georges, C., Obernosterer, I., & Queguiner, B. (2016). Composition of diatom communities and their contribution to plankton biomass in the naturally iron-fertilized region of Kerguelen in the Southern Ocean. *FEMS microbiology ecology*, *92*(11), fiw171.

Laurenceau-Cornec, E. C., Trull, T. W., Davies, D. M., Bray, S. G., Doran, J., Planchon, F., ... & Blain, S. (2015). The relative importance of phytoplankton aggregates and zooplankton fecal pellets to carbon export: insights from free-drifting sediment trap deployments in naturally iron-fertilised waters near the Kerguelen Plateau. *Biogeosciences*, *12*(4), 1007-1027.

Legendre, L., & Le Fèvre, J. (1995). Microbial food webs and the export of biogenic carbon in oceans. *Aquatic Microbial Ecology*, *9*(1), 69-77.

Lehette, P., Tovar-Sánchez, A., Duarte, C. M., & Hernández-León, S. (2012). Krill excretion and its effect on primary production. *Marine Ecology Progress Series*, *459*, 29-38.

Leichter, J. J., Stewart, H. L., & Miller, S. L. (2003). Episodic nutrient transport to Florida coral reefs. *Limnology and Oceanography*, *48*(4), 1394-1407.

Li, H., Ilyina, T., Müller, W. A., & Landschützer, P. (2019). Predicting the variable ocean carbon sink. *Science advances*, *5*(4), eaav6471.

Li, W. K. (1994). Primary production of prochlorophytes, cyanobacteria, and eucaryotic ultraphytoplankton: measurements from flow cytometric sorting. *Limnology and Oceanography*, *39*(1), 169-175.

Li, W. K. W., & Dickie, P. M. (2001). Monitoring phytoplankton, bacterioplankton, and virioplankton in a coastal inlet (Bedford Basin) by flow cytometry. *Cytometry: The Journal of the International Society for Analytical Cytology*, *44*(3), 236-246.

Lin, H., Rauschenberg, S., Hexel, C. R., Shaw, T. J., & Twining, B. S. (2011). Free-drifting icebergs as sources of iron to the Weddell Sea. *Deep Sea Research Part II: Topical Studies in Oceanography*, *58*(11-12), 1392-1406.

Lindell, D., & Post, A. F. (2001). Ecological Aspects of ntcA Gene Expression and Its Use as an Indicator of the Nitrogen Status of MarineSynechococcus spp. *Applied and Environmental Microbiology*, *67*(8), 3340-3349.

Lindell, D., Padan, E., & Post, A. F. (1998). Regulation of ntcA expression and nitrite uptake in the marine Synechococcus sp. strain WH 7803. *Journal of Bacteriology*, *180*(7), 1878-1886.

Lipschultz, F. (2001). A time-series assessment of the nitrogen cycle at BATS. *Deep Sea Research Part II: Topical Studies in Oceanography*, *48*(8-9), 1897-1924.

Lis, H., Shaked, Y., Kranzler, C., Keren, N., & Morel, F. M. (2015). Iron bioavailability to phytoplankton: an empirical approach. *The ISME journal*, *9*(4), 1003-1013.

Liu, K. K., & Kaplan, I. R. (1989). The eastern tropical Pacific as a source of 15N-enriched nitrate in seawater off southern California. *Limnology and Oceanography*, *34*(5), 820-830.

Liu, K. K., Kao, S. J., Chiang, K. P., Gong, G. C., Chang, J., Cheng, J. S., & Lan, C. Y. (2013). Concentration dependent nitrogen isotope fractionation during ammonium uptake by phytoplankton under an algal bloom condition in the Danshuei estuary, northern Taiwan. *Marine Chemistry*, *157*, 242-252.

Liu, Y., Debeljak, P., Rembauville, M., Blain, S., & Obernosterer, I. (2019). Diatoms shape the biogeography of heterotrophic prokaryotes in early spring in the Southern Ocean. *Environmental microbiology*, *21*(4), 1452-1465.

Llort, J., Lévy, M., Sallée, J. B., & Tagliabue, A. (2015). Onset, intensification, and decline of phytoplankton blooms in the Southern Ocean. *ICES Journal of Marine Science*, *72*(6), 1971-1984.

Lochte, K., Bjørnsen, P. K., Giesenhagen, H., & Weber, A. (1997). Bacterial standing stock and production and their relation to phytoplankton in the Southern Ocean. *Deep Sea Research Part II: Topical Studies in Oceanography*, *44*(1-2), 321-340.

Lomas, M. W., & Glibert, P. M. (1999a). Interactions between NH+ 4 and NO− 3 uptake and assimilation: comparison of diatoms and dinoflagellates at several growth temperatures. *Marine Biology*, *133*(3), 541-551.

Lomas, M. W., & Glibert, P. M. (1999b). Temperature regulation of nitrate uptake: A novel hypothesis about nitrate uptake and reduction in cool-water diatoms. *Limnology and Oceanography*, *44*(3), 556-572.

Lomas, M. W., & Moran, S. B. (2011). Evidence for aggregation and export of cyanobacteria and nano-eukaryotes from the Sargasso Sea euphotic zone. *Biogeosciences*, *8*(1).

Lomas, M. W., Bronk, D. A., & van den Engh, G. (2011). Use of flow cytometry to measure biogeochemical rates and processes in the ocean. *Annual review of marine science*, *3*, 537-566.

Lourey, M. J., & Trull, T. W. (2001). Seasonal nutrient depletion and carbon export in the Subantarctic and Polar Frontal Zones of the Southern Ocean south of Australia. *Journal of Geophysical Research: Oceans*, *106*(C12), 31463-31487.

Lourey, M. J., Trull, T. W., & Sigman, D. M. (2003). Sensitivity of δ15N of nitrate, surface suspended and deep sinking particulate nitrogen to seasonal nitrate depletion in the Southern Ocean. *Global Biogeochemical Cycles*, *17*(3).

Lubbers, G. W., Gieskes, W. W. C., Del Castilho, P., Salomons, W., & Bril, J. (1990). Manganese accumulation in the high pH microenvironment of Phaeocystis sp.(Haptophyceae) colonies from the North Sea. *Marine Ecology Progress Series*, 285-293.

Lucas, M., Seeyave, S., Sanders, R., Moore, C. M., Williamson, R., & Stinchcombe, M. (2007). Nitrogen uptake responses to a naturally Fe-fertilised phytoplankton bloom during the 2004/2005 CROZEX study. *Deep Sea Research Part II: Topical Studies in Oceanography*, *54*(18-20), 2138-2173.

Lutjeharms, J. E., & Valentine, H. R. (1984). Southern Ocean thermal fronts south of Africa. *Deep Sea Research Part A. Oceanographic Research Papers*, *31*(12), 1461-1475.

Lutjeharms, J. R. E. (1985). Location of frontal systems between Africa and Antarctica: some preliminary results. *Deep Sea Research Part A. Oceanographic Research Papers*, *32*(12), 1499-1509.

Macko, S. A., Estep, M. L. F., Engel, M. H., & Hare, P. E. (1986). Kinetic fractionation of stable nitrogen isotopes during amino acid transamination. *Geochimica et Cosmochimica Acta*, *50*(10), 2143-2146.

Maestrini, S. Y., SY, M., & JM, R. (1982). Simultaneous uptake of ammonium and nitrate by oyster-pond algae.

Maguer, J. F., l'Helguen, S., Madec, C., Labry, C., & Le Corre, P. (2007). Nitrogen uptake and assimilation kinetics in alexandrium minutum (dynophyceae): effect of n-limited growth rate on nitrate and ammonium interactions 1. *Journal of Phycology*, *43*(2), 295-303.

Mahowald, N., Kohfeld, K., Hansson, M., Balkanski, Y., Harrison, S. P., Prentice, I. C., ... & Rodhe, H. (1999). Dust sources and deposition during the last glacial maximum and current climate: A comparison of model results with paleodata from ice cores and marine sediments. *Journal of Geophysical Research: Atmospheres*, *104*(D13), 15895-15916.

Maldonado, M. T., & Price, N. M. (1999). Utilization of iron bound to strong organic ligands by plankton communities in the subarctic Pacific Ocean. *Deep Sea Research Part II: Topical Studies in Oceanography*, *46*(11-12), 2447-2473.

Malinverno, E., Triantaphyllou, M. V., & Dimiza, M. D. (2015). Coccolithophore assemblage distribution along a temperate to polar gradient in the West Pacific sector of the Southern Ocean (January 2005). *Micropaleontology*, 489-506.

Malviya, S., Scalco, E., Audic, S., Vincent, F., Veluchamy, A., Poulain, J., ... & Zingone, A. (2016). Insights into global diatom distribution and diversity in the world's ocean. *Proceedings of the National Academy of Sciences*, *113*(11), E1516-E1525.

Maraldi, C., Mongin, M., Coleman, R., & Testut, L. (2009). The influence of lateral mixing on a phytoplankton bloom: Distribution in the Kerguelen Plateau region. *Deep Sea Research Part I: Oceanographic Research Papers*, *56*(6), 963-973.

Marañón, E., Behrenfeld, M. J., González, N., Mouriño, B., & Zubkov, M. V. (2003). High variability of primary production in oligotrophic waters of the Atlantic Ocean: uncoupling from phytoplankton biomass and size structure. *Marine Ecology Progress Series*, *257*, 1-11.

Marchant, H. J. (2005). *Antarctic marine protists* (pp. 295-307). F. J. Scott (Ed.). Canberra: Australian Biological Resources Study.

Marchetti, A., Maldonado, M. T., Lane, E. S., & Harrison, P. J. (2006). Iron requirements of the pennate diatom Pseudo-nitzschia: Comparison of oceanic (high-nitrate, low-chlorophyll waters) and coastal species. *Limnology and oceanography*, *51*(5), 2092-2101.

Marchetti, A., Parker, M. S., Moccia, L. P., Lin, E. O., Arrieta, A. L., Ribalet, F., ... & Armbrust, E. V. (2009). Ferritin is used for iron storage in bloom-forming marine pennate diatoms. *Nature*, *457*(7228), 467-470.

Marie, D., Brussaard, C. P., Thyrhaug, R., Bratbak, G., & Vaulot, D. (1999). Enumeration of marine viruses in culture and natural samples by flow cytometry. *Applied and environmental microbiology*, *65*(1), 45-52.

Marie, D., Simon, N., & Vaulot, D. (2005). Phytoplankton cell counting by flow cytometry. *Algal culturing techniques*, *1*, 253-267.

Marinov, I., Gnanadesikan, A., Toggweiler, J. R., & Sarmiento, J. L. (2006). The southern ocean biogeochemical divide. *Nature*, *441*(7096), 964-967.

Mariotti, A., Germon, J. C., Hubert, P., Kaiser, P., Letolle, R., Tardieux, A., & Tardieux, P. (1981). Experimental determination of nitrogen kinetic isotope fractionation: some principles; illustration for the denitrification and nitrification processes. *Plant and soil*, *62*(3), 413-430.

Martin, J. H. (1990). Glacial-interglacial CO2 change: The iron hypothesis. *Paleoceanography*, *5*(1), 1-13.

Martínez-García, A., Sigman, D. M., Ren, H., Anderson, R. F., Straub, M., Hodell, D. A., ... & Haug, G. H. (2014). Iron fertilization of the Subantarctic Ocean during the last ice age. *Science*, *343*(6177), 1347-1350.

Massana, R. (2011). Eukaryotic picoplankton in surface oceans. *Annual review of microbiology*, *65*, 91-110.

MATLAB. (2010). *version 8.5.0 (R2015a)*. Natick, Massachusetts: The MathWorks Inc.

Matrai, P. A., Vernet, M., Hood, R., Jennings, A., Brody, E., & Saemundsdottir, S. (1995). Light-dependence of carbon and sulfur production by polar clones of the genus Phaeocystis. *Marine Biology*, *124*(1), 157-167.

Mayzaud, P., Tirelli, V., Errhif, A., Labat, J.P., Razouls, S., Perissinotto,R., (2002). Carbon intake by zooplankton. Importance and role ofzooplankton grazing in the Indian sector of the Southern Ocean. *Deep-Sea Research Part II, 49*, 3169–3187.

McCarthy, J. J. 1981. The kinetics of nutrient utilization. *Canadian Journal of Fishies and Aquatic Sciences Bulletin*. *210*: 211–213.

McCartney, M. S. (1976). The interaction of zonal currents with topography with applications to the Southern Ocean. In *Deep Sea Research and Oceanographic Abstracts* (Vol. 23, No. 5, pp. 413-427). Elsevier.

McCartney, M. S. (1977), Subantarctic mode water, Deep Sea Res.,24,103–119.

McCartney, M. S., & Donohue, K. A. (2007). A deep cyclonic gyre in the Australian–Antarctic Basin. *Progress in Oceanography*, *75*(4), 675-750.

McDougall, T.J. & Barker, P.M. (2011). Getting started with TEOS-10 and the Gibbs Seawater (GSW) Oceanographic Toolbox, 28pp., SCOR/IAPSO WG127, ISBN 978-0-646-55621-5.

McFadden, G. I. (2001). Transitions from Water to Land and Sky. *Journal of Phycology, 37*(6), 951-959

McIlvin, M. R., & Casciotti, K. L. (2011). Technical updates to the bacterial method for nitrate isotopic analyses. *Analytical Chemistry*, *83*(5), 1850-1856.

McIntyre, A., & Bé, A. W. (1967, October). Modern coccolithophoridae of the Atlantic Ocean—I. Placoliths and cyrtoliths. In *Deep Sea Research and Oceanographic Abstracts* (Vol. 14, No. 5, pp. 561-597). Elsevier.

McNeil, B. I., Tilbrook, B., & Matear, R. J. (2001). Accumulation and uptake of anthropogenic CO2 in the Southern Ocean, south of Australia between 1968 and 1996. *Journal of Geophysical Research: Oceans*, *106*(C12), 31431-31445.

McQuaid, C. (2018). Implications of Long-Term Climate Change for Biogeography and Ecological Processes in the Southern Ocean. *Oceanography and Marine Biology: An Annual Review*. *56*, 1-72. 10.1201/9780429454455-1.

Mdutyana, M., Thomalla, S. J., Philibert, R., Ward, B. B., & Fawcett, S. E. (2020). The seasonal cycle of nitrogen uptake and nitrification in the Atlantic sector of the Southern Ocean. *Global Biogeochemical Cycles*, *34*(7), e2019GB006363.

Medlin, L. K., Fensome, R. A., Lewis, J. M., Marret, F., & Bradley, L. (2013). Dinoflagellate macroevolution: some considerations based on an integration of molecular, morphological and fossil evidence. *Biological and geological perspectives of dinoflagellates*, 255-266.

Menden-Deuer, S., & Lessard, E. J. (2000). Carbon to volume relationships for dinoflagellates, diatoms, and other protist plankton. *Limnology and oceanography*, *45*(3), 569-579.

Mendes, C. R. B., Tavano, V. M., Dotto, T. S., Kerr, R., De Souza, M. S., Garcia, C. A. E., & Secchi, E. R. (2018). New insights on the dominance of cryptophytes in Antarctic coastal waters: a case study in Gerlache Strait. *Deep Sea Research Part II: Topical Studies in Oceanography*, *149*, 161-170.

Mendes, C. R. B., Tavano, V. M., Leal, M. C., de Souza, M. S., Brotas, V., & Garcia, C. A. E. (2013). Shifts in the dominance between diatoms and cryptophytes during three late summers in the Bransfield Strait (Antarctic Peninsula). *Polar biology*, *36*(4), 537-547.

Mengesha, S., Dehairs, F., Fiala, M., Elskens, M., & Goeyens, L. (1998). Seasonal variation of phytoplankton community structure and nitrogen uptake regime in the Indian Sector of the Southern Ocean. *Polar Biology*, *20*(4), 259-272.

Menzel, D. W., & Ryther, J. H. (1960). The annual cycle of primary production in the Sargasso Sea off Bermuda. *Deep-Sea Res*, *6*(35), l-367.

Metfies, K., Bauerfeind, E., Wolf, C., Sprong, P., Frickenhaus, S., Kaleschke, L., ... & Nöthig, E. M. (2017). Protist Communities in Moored Long-Term Sediment Traps (Fram Strait, Arctic)–Preservation with Mercury Chloride Allows for PCR-Based Molecular Genetic Analyses. *Frontiers in Marine Science*, *4*, 301.

Metzl, N., Tilbrook, B., & Poisson, A. (1999). The annual f CO2 cycle and the air'sea CO2 flux in the sub-Antarctic Ocean. *Tellus B: Chemical and Physical Meteorology*, *51*(4), 849-861.

Miklasz, K. A., & Denny, M. W. (2010). Diatom sinkings speeds: Improved predictions and insight from a modified Stokes' law. *Limnology and Oceanography*, *55*(6), 2513-2525.

Milligan, A. J., & Harrison, P. J. (2000). Effects of non-steady-state iron limitation on nitrogen assimilatory enzymes in the marine diatom thalassiosira weissflogii (BACILLARIOPHYCEAE). *Journal of Phycology*, *36*(1), 78-86.

Möbius, J. (2013). Isotope fractionation during nitrogen remineralization (ammonification): Implications for nitrogen isotope biogeochemistry. *Geochimica et Cosmochimica Acta*, *105*, 422-432.

Mock, T., & Medlin, L. K. (2012). Genomics and genetics of diatoms. In *Advances in botanical research* (Vol. 64, pp. 245-284). Academic Press.

Mohan, R., Mergulhao, L. P., Guptha, M. V. S., Rajakumar, A., Thamban, M., AnilKumar, N., ... & Ravindra, R. (2008). Ecology of coccolithophores in the Indian sector of the Southern Ocean. *Marine Micropaleontology*, *67*(1-2), 30-45.

Moline, M. A., & Prezelin, B. B. (1996). Long-term monitoring and analyses of physical factors regulating variability in coastal Antarctic phytoplankton biomass, in situ productivity and taxonomic composition over subseasonal, seasonal and interannual time scales. *Marine Ecology Progress Series*, *145*, 143-160.

Moline, M. A., Claustre, H., Frazer, T. K., Schofield, O., & Vernet, M. (2004). Alteration of the food web along the Antarctic Peninsula in response to a regional warming trend. *Global Change Biology*, *10*(12), 1973-1980.

Molinelli, E. J. (1981). The Antarctic influence on Antarctic Intermediate Water. *Journal of Marine Research, 39*, 267 – 293.

Mongin, M. M., Abraham, E. R., & Trull, T. W. (2009). Winter advection of iron can explain the summer phytoplankton bloom that extends 1000 km downstream of the Kerguelen Plateau in the Southern Ocean. *Journal of Marine Research*, *67*(2), 225-237.

Mongin, M., Molina, E., & Trull, T. W. (2008). Seasonality and scale of the Kerguelen plateau phytoplankton bloom: A remote sensing and modeling analysis of the influence of natural iron fertilization in the Southern Ocean. *Deep Sea Research Part II: Topical Studies in Oceanography*, *55*(5-7), 880-892.

Montes-Hugo, M., Doney, S. C., Ducklow, H. W., Fraser, W., Martinson, D., Stammerjohn, S. E., & Schofield, O. (2009). Recent changes in phytoplankton communities associated with rapid regional climate change along the western Antarctic Peninsula. *Science*, *323*(5920), 1470-1473.

Montoya, J. P., Carpenter, E. J., & Capone, D. G. (2002). Nitrogen fixation and nitrogen isotope abundances in zooplankton of the oligotrophic North Atlantic. *Limnology and Oceanography*, *47*(6), 1617-1628.

Moore, C. M., Hickman, A. E., Poulton, A. J., Seeyave, S., & Lucas, M. I. (2007b). Iron–light interactions during the CROZet natural iron bloom and EXport experiment (CROZEX): II—Taxonomic responses and elemental stoichiometry. *Deep Sea Research Part II: Topical Studies in Oceanography*, *54*(18-20), 2066-2084.

Moore, C. M., Mills, M. M., Arrigo, K. R., Berman-Frank, I., Bopp, L., Boyd, P. W., ... & Jickells, T. D. (2013). Processes and patterns of oceanic nutrient limitation. *Nature geoscience*, *6*(9), 701-710.

Moore, C. M., Seeyave, S., Hickman, A. E., Allen, J. T., Lucas, M. I., Planquette, H., ... & Poulton, A. J. (2007a). Iron–light interactions during the CROZet natural iron bloom and EXport experiment (CROZEX) I: Phytoplankton growth and photophysiology. *Deep Sea Research Part II: Topical Studies in Oceanography*, *54*(18-20), 2045-2065.

Moore, J. K., & Abbott, M. R. (2000). Phytoplankton chlorophyll distributions and primary production in the Southern Ocean. *Journal of Geophysical Research: Oceans*, *105*(C12), 28709-28722.

Moore, J. K., Abbott, M. R., & Richman, J. G. (1999). Location and dynamics of the Antarctic Polar Front from satellite sea surface temperature data. *Journal of Geophysical Research: Oceans*, *104*(C2), 3059-3073.

Moore, J. K., Doney, S. C., & Lindsay, K. (2004). Upper ocean ecosystem dynamics and iron cycling in a global three-dimensional model. *Global Biogeochemical Cycles*, *18*(4).

Moore, L. R., Goericke, R., & Chisholm, S. W. (1995). Comparative physiology of Synechococcus and Prochlorococcus: influence of light and temperature on growth, pigments, fluorescence and absorptive properties. *Marine Ecology Progress Series*, 259-275.

Moore, L. R., Post, A. F., Rocap, G., & Chisholm, S. W. (2002). Utilization of different nitrogen sources by the marine cyanobacteria Prochlorococcus and Synechococcus. *Limnology and oceanography*, *47*(4), 989-996.

Moreau, S., Mostajir, B., Bélanger, S., Schloss, I. R., Vancoppenolle, M., Demers, S., & Ferreyra, G. A. (2015). Climate change enhances primary production in the western Antarctic Peninsula. *Global change biology*, *21*(6), 2191-2205.

Morel, F. M., & Price, N. M. (2003). The biogeochemical cycles of trace metals in the oceans. *Science*, *300*(5621), 944-947.

Morel, F. M., Rueter, J. G., & Price, N. M. (1991). Iron nutrition of phytoplankton and its possible importance in the ecology of ocean regions with high nutrient and low biomass. *Oceanography*, *4*(2), 56-61.

Morin, P. M. V. M., Wafar, M. V. M., & Le Corre, P. (1993). Estimation of nitrate flux in a tidal front from satellite-derived temperature data. *Journal of Geophysical Research: Oceans*, *98*(C3), 4689-4695.

Morris, M., Stanton, B., & Neil, H. (2001). Subantarctic oceanography around New Zealand: preliminary results from an ongoing survey. *New Zealand Journal of Marine and Freshwater Research*, *35*(3), 499-519.

Morrison, J. M., Gaurin, S., Codispoti, L. A., Takahashi, T., Millero, F. J., Gardner, W. D., & Richardson, M. J. (2001). Seasonal evolution of hydrographic properties in the Antarctic circumpolar current at 170 W during 1997–1998. *Deep Sea Research Part II: Topical Studies in Oceanography*, *48*(19-20), 3943-3972.

Morrissey, J., & Bowler, C. (2012). Iron utilization in marine cyanobacteria and eukaryotic algae. *Frontiers in microbiology*, *3*, 43.

Mosseri, J., Queguiner, B., Armand, L., & Cornet-Barthaux, V. (2008). Impact of iron on silicon utilization by diatoms in the Southern Ocean: A case study of Si/N cycle decoupling in a naturally iron-enriched area. *Deep Sea Research Part II: Topical Studies in Oceanography*, *55*(5-7), 801-819.

Muggli, D. L., & Harrison, P. J. (1996). Effects of nitrogen source on the physiology and metal nutrition of Emiliania huxleyi grown under different iron and light conditions. *Marine Ecology Progress Series*, *130*, 255-267.

Muggli, D. L., & Harrison, P. J. (1997). Effects of iron on two oceanic phytoplankters grown in natural NE subarctic Pacific seawater with no artificial chelators present. *Journal of experimental marine Biology and Ecology*, *212*(2), 225-237.

Müller, M. N., Trull, T. W., & Hallegraeff, G. M. (2015). Differing responses of three Southern Ocean Emiliania huxleyi ecotypes to changing seawater carbonate chemistry. *Marine Ecology Progress Series*, *531*, 81-90.

Mullin, M. M., Sloan, P. R., & Eppley, R. W. (1966). Relationship between carbon content, cell volume, and area in phytoplankton. *Limnology and oceanography*, *11*(2), 307-311.

NASA Goddard Space Flight Center, Ocean Ecology Laboratory, Ocean Biology Processing Group. Moderate-resolution Imaging Spectroradiometer (MODIS) Aqua Sea Surface Temperature Data; 2014 Reprocessing. NASA OB.DAAC, Greenbelt, MD, USA.

NASA Goddard Space Flight Center, Ocean Ecology Laboratory, Ocean Biology Processing Group. Moderate-resolution Imaging Spectroradiometer (MODIS) Aqua Chlorophyll Concentration Data; 2014 Reprocessing. NASA OB.DAAC, Greenbelt, MD, USA.

Nayak, A. R., Twardowski, M. S., (2020). Breaking news for the ocean's carbon budget. Science 367 (6479) 738 – 739.

Nelson, D. M., Brzezinski, M. A., Sigmon, D. E., & Franck, V. M. (2001). A seasonal progression of Si limitation in the Pacific sector of the Southern Ocean. *Deep Sea Research Part II: Topical Studies in Oceanography*, *48*(19-20), 3973-3995.

Nelson, D. M., Tréguer, P., Brzezinski, M. A., Leynaert, A., & Quéguiner, B. (1995). Production and dissolution of biogenic silica in the ocean: revised global estimates, comparison with regional data and relationship to biogenic sedimentation. *Global Biogeochemical Cycles*, *9*(3), 359-372.

Nissen, C., Vogt, M., Münnich, M., Gruber, N., & Haumann, F. A. (2018). Factors controlling coccolithophore biogeography in the Southern Ocean. *Biogeosciences*, *15*(22), 6997-7024.

Odate, T., & FuKucHi, M. (1995). Distribution and community structure of picophytoplankton in the Southern Ocean during late austral summer of 1992. In *Proc. NIPR Symp. Polar Biol., Nat. Inst. Polar Res.* (Vol. 8, pp. 86-100).

Ohnemus, D. C., Krause, J. W., Brzezinski, M. A., Collier, J. L., Baines, S. B., & Twining, B. S. (2018). The chemical form of silicon in marine Synechococcus. *Marine Chemistry*, *206*, 44-51.

Ohnemus, D. C., Rauschenberg, S., Krause, J. W., Brzezinski, M. A., Collier, J. L., Geraci-Yee, S., ... & Twining, B. S. (2016). Silicon content of individual cells of Synechococcus from the North Atlantic Ocean. *Marine Chemistry*, *187*, 16-24.

Olguín, H. F., & Alder, V. A. (2011). Species composition and biogeography of diatoms in antarctic and subantarctic (Argentine shelf) waters (37–76 S). *Deep Sea Research Part II: Topical Studies in Oceanography*, *58*(1-2), 139-152.

Olson, R. J., Frankel, S. L., Chisholm, S. W., & Shapiro, H. M. (1983). An inexpensive flow cytometer for the analysis of fluorescence signals in phytoplankton: chlorophyll and DNA distributions. *Journal of Experimental Marine Biology and Ecology*, *68*(2), 129-144.

Omand, M. M., Govindarajan, R., He, J., & Mahadevan, A. (2020). Sinking flux of particulate organic matter in the oceans: Sensitivity to particle characteristics. *Scientific reports*, *10*(1), 1-16.

Ong, L. J., Glazer, A. N., & Waterbury, J. B. (1984). An unusual phycoerythrin from a marine cyanobacterium. *Science*, *224*(4644), 80-83.

Orsi, A. H., Johnson, G. C., & Bullister, J. L. (1999). Circulation, mixing, and production of Antarctic Bottom Water. *Progress in Oceanography*, *43*(1), 55-109.

Orsi, A. H., Whitworth III, T., & Nowlin Jr, W. D. (1995). On the meridional extent and fronts of the Antarctic Circumpolar Current. *Deep Sea Research Part I: Oceanographic Research Papers*, *42*(5), 641-673.

Pakhomov, E. A., & Chown, S. L. (2003). The Prince Edward islands: southern ocean oasis. *Ocean Yearbook Online*, *17*(1), 348-379.

Pakhomov, E. A., & Froneman, P. W. (1999). The Prince Edward Islands pelagic ecosystem, south Indian Ocean: a review of achievements, 1976–1990. *Journal of Marine Systems*, *18*(4), 355-367.

Pakhomov, E. A., Ansorge, I. J., & Froneman, P. W. (2000). Variability in the inter-island environment of the Prince Edward Islands (Southern Ocean). *Polar Biology*, *23*(9), 593-603.

Parekh, P., Follows, M. J., & Boyle, E. A. (2005). Decoupling of iron and phosphate in the global ocean. *Global Biogeochemical Cycles*, *19*(2).

Park, Y. H., Charriaud, E., & Fieux, M. (1998). Thermohaline structure of the Antarctic surface water/winter water in the Indian sector of the Southern Ocean. *Journal of Marine Systems*, *17*(1-4), 5-23.

Park, Y. H., Durand, I., Kestenare, E., Rougier, G., Zhou, M., d'Ovidio, F., ... & Lee, J. H. (2014). Polar Front around the Kerguelen Islands: An up-to-date determination and associated circulation of surface/subsurface waters. *Journal of Geophysical Research: Oceans*, *119*(10), 6575-6592.

Park, Y. H., Fuda, J. L., Durand, I., & Garabato, A. C. N. (2008b). Internal tides and vertical mixing over the Kerguelen Plateau. *Deep Sea Research Part II: Topical Studies in Oceanography*, *55*(5-7), 582-593.

Park, Y. H., Roquet, F., Durand, I., & Fuda, J. L. (2008a). Large-scale circulation over and around the Northern Kerguelen Plateau. *Deep Sea Research Part II: Topical Studies in Oceanography*, *55*(5-7), 566-581.

Partensky, F., Blanchot, J., & Vaulot, D. (1999a). Differential distribution and ecology of Prochlorococcus and Synechococcus in oceanic waters: a review. *Bulletin-Institut Oceanographique Monaco-Numero Special-*, 457-476.

Partensky, F., Hess, W. R., & Vaulot, D. (1999b). Prochlorococcus, a marine photosynthetic prokaryote of global significance. *Microbiology and molecular biology reviews*, *63*(1), 106-127.

Paulsen, M. L., Riisgaard, K., Thingstad, T. F., John, M. S., & Nielsen, T. G. (2015). Winter-spring transition in the subarctic Atlantic: Microbial response to deep mixing and pre-bloom production. *Aquatic Microbial Ecology*, *76*(1), 49-69.

Pawlowicz, R. (2020). M_Map: A mapping package for MATLAB. *version 1.4m*, [Computer software], available online at *www.eoas.ubc.ca/~rich/map.html*.

Pearce, I., Davidson, A. T., Thomson, P. G., Wright, S., & van den Enden, R. (2011). Marine microbial ecology in the Sub-Antarctic Zone: rates of bacterial and phytoplankton growth and grazing by heterotrophic protists. *Deep Sea Research Part II: Topical Studies in Oceanography*, *58*(21-22), 2248-2259.

Peers, G., & Price, N. M. (2006). Copper-containing plastocyanin used for electron transport by an oceanic diatom. *Nature*, *441*(7091), 341-344.

Pennock, J. R., Velinsky, D. J., Ludlam, J. M., Sharp, J. H., & Fogel, M. L. (1996). Isotopic fractionation of ammonium and nitrate during uptake by Skeletonema costatum: Implications for δ15N dynamics under bloom conditions. *Limnology and Oceanography*, *41*(3), 451-459.

Pérez-Tribouillier, H., Noble, T. L., Townsend, A. T., Bowie, A. R., & Chase, Z. (2020). Quantifying lithogenic inputs to the Southern Ocean using long-lived thorium isotopes. *Frontiers in Marine Science*, *7*(APR), 1-16.

Perissinotto, R., & Duncombe Rae, C. (1990). Occurrence of anticyclonic eddies on the Prince Edward Plateau (Southern Ocean): effects on phytoplankton biomass and production. *Deep Sea Research Part A. Oceanographic Research Papers*, *37*(5), 777-793.

Perissinotto, R., Duncombe Rae, C., Boden, B. P., & Allanson, B. R. (1990). Vertical stability as a controlling factor of the marine phytoplankton production at the Prince Edward Archipelago (Southern Ocean). *Marine Ecology Progress Series*, 205-209.

Perissinotto, R., Laubscher, R. K., & McQuaid, C. D. (1992). Marine productivity enhancement around Bouvet and the South Sandwich Islands (Southern Ocean). *Marine Ecology-Progress Series*, *88*, 41-41.

Petit, J. R., Jouzel, J., Raynaud, D., Barkov, N. I., Barnola, J. M., Basile, I., ... & Delmotte, M. (1999). Climate and atmospheric history of the past 420,000 years from the Vostok ice core, Antarctica. *Nature*, *399*(6735), 429.

Pickard, G. L., & Emery, W. J. (1990). Descriptive Physical Oceanography. *Butterworth Heinemann*, 320 pp

Piola, A. R., & Georgi, D. T. (1982). Circumpolar properties of Antarctic intermediate water and Subantarctic Mode Water. *Deep Sea Research Part A. Oceanographic Research Papers*, *29*(6), 687-711.

Planquette, H., Statham, P. J., Fones, G. R., Charette, M. A., Moore, C. M., Salter, I., ... & Mahowald, N. (2007). Dissolved iron in the vicinity of the Crozet Islands, Southern Ocean. *Deep Sea Research Part II: Topical Studies in Oceanography*, *54*(18-20), 1999-2019.

Pollard, R. T., & Read, J. F. (2001). Circulation pathways and transports of the Southern Ocean in the vicinity of the Southwest Indian Ridge. *Journal of Geophysical Research: Oceans*, *106*(C2), 2881-2898.

Pollard, R. T., Lucas, M. I., & Read, J. F. (2002). Physical controls on biogeochemical zonation in the Southern Ocean. *Deep Sea Research Part II: Topical Studies in Oceanography*, *49*(16), 3289-3305.

Pollard, R. T., Salter, I., Sanders, R. J., Lucas, M. I., Moore, C. M., Mills, R. A., ... & Charette, M. A. (2009). Southern Ocean deep-water carbon export enhanced by natural iron fertilization. *Nature*, *457*(7229), 577-580.

Pollard, R. T., Venables, H. J., Read, J. F., & Allen, J. T. (2007b). Large-scale circulation around the Crozet Plateau controls an annual phytoplankton bloom in the Crozet Basin. *Deep Sea Research Part II: Topical Studies in Oceanography*, *54*(18-20), 1915-1929.

Pollard, R., Sanders, R., Lucas, M., & Statham, P. (2007a). The Crozet natural iron bloom and export experiment (CROZEX). *Deep Sea Research Part II: Topical Studies in Oceanography*, *54*(18-20), 1905-1914.

Popp, B. N., Trull, T., Kenig, F., Wakeham, S. G., Rust, T. M.,Tilbrook, B., Griffiths, B., Wright, S. W., Marchant, H. J., Bidi-gare, R. R., and Laws, E. A. (1999). Controls on the carbon iso-topic composition of southern ocean phytoplankton. *Global Biogeochemical Cycles*, *13*, 827–843,

Post, A., Meijers, A., Fraser, A., Meiners, K., Ayers, J., Bindoff, N., ... & Raymond, B. (2014). Chapter 14. *Environmental Setting, in de Broyer, C., Koubbi, P., Griffiths, H., Raymond, B., and d'Udekem d'Acoz, C., eds., Biogeographic Atlas of the Southern Ocean: Scientific Committee on Antarctic Research, Cambridge UK*, 46-64.

Poulton, A. J., Holligan, P. M., Charalampopoulou, A., & Adey, T. R. (2017). Coccolithophore ecology in the tropical and subtropical Atlantic Ocean: New perspectives from the Atlantic meridional transect (AMT) programme. *Progress in Oceanography*, *158*, 150-170.

Poulton, A. J., Moore, C. M., Seeyave, S., Lucas, M. I., Fielding, S., & Ward, P. (2007). Phytoplankton community composition around the Crozet Plateau, with emphasis on diatoms and Phaeocystis. *Deep Sea Research Part II: Topical Studies in Oceanography*, *54*(18-20), 2085-2105.

Price, N. M. (2005). The elemental stoichiometry and composition of an iron-limited diatom. *Limnology and oceanography*, *50*(4), 1159-1171.

Priddle, J., Boyd, I. L., Whitehouse, M. J., Murphy, E. J., & Croxall, J. P. (1998). Estimates of Southern Ocean primary production—constraints from predator carbon demand and nutrient drawdown. *Journal of Marine Systems*, *17*(1-4), 275-288.

Probyn, T. A., & Painting, S. J. (1985). Nitrogen uptake by size-fractionated phytoplankton populations in Antarctic surface waters 1. *Limnology and Oceanography*, *30*(6), 1327-1332.

Qi, H., Coplen, T. B., Geilmann, H., Brand, W. A., & Böhlke, J. K. (2003). Two new organic reference materials for δ13C and δ15N measurements and a new value for the δ13C of NBS 22 oil. *Rapid Communications in Mass Spectrometry*, *17*(22), 2483-2487.

Queguiner, B. (2013). Iron fertilization and the structure of planktonic communities in high nutrient regions of the Southern Ocean. *Deep Sea Research Part II: Topical Studies in Oceanography*, *90*, 43-54.

Quere, C. L., Harrison, S. P., Colin Prentice, I., Buitenhuis, E. T., Aumont, O., Bopp, L., ... & Klaas, C. (2005). Ecosystem dynamics based on plankton functional types for global ocean biogeochemistry models. *Global Change Biology*, *11*(11), 2016-2040.

Quéroué, F., Sarthou, G., Planquette, H., Bucciarelli, E., Chever, F., Van Der Merwe, P., ... & d'Ovidio, F. (2015). High variability in dissolved iron concentrations in the vicinity of the Kerguelen Islands (Southern Ocean). *Biogeosciences*, *12*(12), 3869-3883.

Rafter, P. A., Bagnell, A., Marconi, D., & DeVries, T. (2019). Global trends in marine nitrate N isotopes from observations and a neural network-based climatology. *Biogeosciences*, *16*(13), 2617-2633.

Rafter, P. A., DiFiore, P. J., & Sigman, D. M. (2013). Coupled nitrate nitrogen and oxygen isotopes and organic matter remineralization in the Southern and Pacific Oceans. *Journal of Geophysical Research: Oceans*, *118*(10), 4781-4794.

Rafter, P. A., Sigman, D. M., Charles, C. D., Kaiser, J., & Haug, G. H. (2012). Subsurface tropical Pacific nitrogen isotopic composition of nitrate: Biogeochemical signals and their transport. *Global Biogeochemical Cycles*, *26*(1).

Ragueneau, O., Tréguer, P., Leynaert, A., Anderson, R. F., Brzezinski, M. A., DeMaster, D. J., ... & Heinze, C. (2000). A review of the Si cycle in the modern ocean: recent progress and missing gaps in the application of biogenic opal as a paleoproductivity proxy. *Global and Planetary Change*, *26*(4), 317-365.

Rau, G. H., Teyssie, J.-L., Rassoulzadegan, F., and Fowler, S. W. (1990) 13C/12C and15N/14N variations among size-fractionated marineparticles: implications for their origin and trophic relationships. *Marine Ecolology Progress Series, 59*, 33–38.

Raven, J. A. (1990). Predictions of Mn and Fe use efficiencies of phototrophic growth as a function of light availability for growth and of C assimilation pathway. *New Phytologist*, *116*(1), 1-18.

Raven, J. A., & Beardall, J. (2003). Carbon acquisition mechanisms of algae: carbon dioxide diffusion and carbon dioxide concentrating mechanisms. In *Photosynthesis in algae* (pp. 225-244). Springer, Dordrecht.

Raven, J. A., & Falkowski, P. G. (1999). Oceanic sinks for atmospheric CO2. Pant, Cell and Environment, 22 (6): 741–755.

Raven, J. A., & Johnston, A. M. (1991). Mechanisms of inorganic-carbon acquisition in marine phytoplankton and their implications for the use of other resources. *Limnology and Oceanography*, *36*(8), 1701-1714.

Raven, J. A., & Kübler, J. E. (2002). New light on the scaling of metabolic rate with the size of algae. *Journal of Phycology*, *38*(1), 11-16.

Raven, J. A., & Waite, A. M. (2004). The evolution of silicification in diatoms: inescapable sinking and sinking as escape?. *New phytologist*, *162*(1), 45-61.

Raven, J. A., B. Wollenweber, Handley, L. L. (1992). A comparison of ammonium and nitrate as nitrogen sources for photolithotrophs. *New Phytologist. 121*: 19–32. doi:10.1111/j.1469-8137.1992.tb01088.x

Raven, J. A., Cockell, C. S., & De La Rocha, C. L. (2008). The evolution of inorganic carbon concentrating mechanisms in photosynthesis. *Philosophical Transactions of the Royal Society B: Biological Sciences*, *363*(1504), 2641-2650.

Read, J. F., Pollard, R. T., & Allen, J. T. (2007). Sub-mesoscale structure and the development of an eddy in the Subantarctic Front north of the Crozet Islands. *Deep Sea Research Part II: Topical Studies in Oceanography*, *54*(18-20), 1930-1948.

Read, J.F., R.T. Pollard, A.I. Morrison, and C. Symon, (1995). On the southerly extent of the Antarctic Circumpolar Current in the southeast Pacific. *Deep-Sea Research Part II, 42*, 933–954.

Redfield, A. C. (1934). On the proportions of organic derivatives in sea water and their relation to the composition of plankton. *James Johnstone memorial volume*, 176-192.

Redfield, A. C. (1958). The biological control of chemical factors in the environment. *American scientist*, *46*(3), 230A-221.

Rembauville, M., Blain, S., Armand, L., Queguiner, B., & Salter, I. (2015b). Export fluxes in a naturally iron-fertilized area of the Southern Ocean-Part 2: Importance of diatom resting spores and faecal pellets for export. *Biogeosciences*, *12*(11), 3171-3195.

Rembauville, M., Manno, C., Tarling, G. A., Blain, S., & Salter, I. (2016b). Strong contribution of diatom resting spores to deep-sea carbon transfer in naturally iron-fertilized waters downstream of South Georgia. *Deep Sea Research Part I: Oceanographic Research Papers*, *115*, 22-35.

Rembauville, M., Meilland, J., Ziveri, P., Schiebel, R., Blain, S., & Salter, I. (2016a). Planktic foraminifer and coccolith contribution to carbonate export fluxes over the central Kerguelen Plateau.

Rembauville, M., Salter, I., Leblond, N., Gueneugues, A., & Blain, S. (2015a). Export fluxes in a naturally iron-fertilized area of the Southern Ocean-Part 1: Seasonal dynamics of particulate organic carbon export from a moored sediment trap. *Biogeosciences*, *12*(11), 3153-3170.

Richardson, T. L., & Jackson, G. A. (2007). Small phytoplankton and carbon export from the surface ocean. *Science*, *315*(5813), 838-840.

Ridgwell, A. J. (2002). Dust in the Earth system: the biogeochemical linking of land, air and sea. *Philosophical Transactions of the Royal Society of London. Series A: Mathematical, Physical and Engineering Sciences*, *360*(1801), 2905-2924.

Rigual Hernández, A. S., Trull, T. W., Nodder, S. D., Flores Villarejo, J. A., Bostock, H., Abrantes, F., ... & Fuertes Prieto, M. Á. (2020). Coccolithophore biodiversity controls carbonate export in the Southern Ocean. *Biogeosciences*, *17*(1), 245-263.

Rigual-Hernández, A. S., Trull, T. W., Bray, S. G., Closset, I., & Armand, L. K. (2015). Seasonal dynamics in diatom and particulate export fluxes to the deep sea in the Australian sector of the southern Antarctic Zone. *Journal of Marine Systems*, *142*, 62-74.

Rijkenberg, M. J., Middag, R., Laan, P., Gerringa, L. J., van Aken, H. M., Schoemann, V., ... & De Baar, H. J. (2014). The distribution of dissolved iron in the West Atlantic Ocean. *PloS one*, *9*(6), e101323.

Rintoul, S. R., & Trull, T. W. (2001). Seasonal evolution of the mixed layer in the Subantarctic Zone south of Australia. *Journal of Geophysical Research: Oceans*, *106*(C12), 31447-31462.

Roberts, K., Granum, E., Leegood, R. C., & Raven, J. A. (2007). C3 and C4 pathways of photosynthetic carbon assimilation in marine diatoms are under genetic, not environmental, control. *Plant physiology*, *145*(1), 230-235.

Roberts, K., Granum, E., Leegood, R. C., & Raven, J. A. (2007). Carbon metabolism in diatoms. *Photosynth. Res*, *93*, 79-88.

Rothenberger, M. B., Burkholder, J. M., & Wentworth, T. R. (2009). Use of long-term data and multivariate ordination techniques to identify environmental factors governing estuarine phytoplankton species dynamics. *Limnology and Oceanography*, *54*(6), 2107-2127.

Saavedra-Pellitero, M., Baumann, K. H., Flores, J. A., & Gersonde, R. (2014). Biogeographic distribution of living coccolithophores in the Pacific sector of the Southern Ocean. *Marine Micropaleontology*, *109*, 1-20.

Sackett, O., Armand, L., Beardall, J., Hill, R., Doblin, M., Connelly, C., ... & Heraud, P. (2014). Taxon-specific responses of Southern Ocean diatoms to Fe enrichment revealed by synchrotron radiation FTIR microspectroscopy. *Biogeosciences*, *11*(20), 5795-5808.

Safi, K. A., Griffiths, F. B., & Hall, J. A. (2007). Microzooplankton composition, biomass and grazing rates along the WOCE SR3 line between Tasmania and Antarctica. *Deep Sea Research Part I: Oceanographic Research Papers*, *54*(7), 1025-1041.

Saito, M. A., Sigman, D. M., & Morel, F. M. (2003). The bioinorganic chemistry of the ancient ocean: the co-evolution of cyanobacterial metal requirements and biogeochemical cycles at the Archean–Proterozoic boundary?. *Inorganica Chimica Acta*, *356*, 308-318.

Sallée, J. B., Wienders, N., Speer, K., & Morrow, R. (2006). Formation of subantarctic mode water in the southeastern Indian Ocean. *Ocean Dynamics*, *56*(5-6), 525-542.

Salter, I., Kemp, A. E., Moore, C. M., Lampitt, R. S., Wolff, G. A., & Holtvoeth, J. (2012). Diatom resting spore ecology drives enhanced carbon export from a naturally iron-fertilized bloom in the Southern Ocean. *Global Biogeochemical Cycles*, *26*(1).

Salter, I., Lampitt, R. S., Sanders, R., Poulton, A., Kemp, A. E., Boorman, B., ... & Pearce, R. (2007). Estimating carbon, silica and diatom export from a naturally fertilised phytoplankton bloom in the Southern Ocean using PELAGRA: A novel drifting sediment trap. *Deep Sea Research Part II: Topical Studies in Oceanography*, *54*(18-20), 2233-2259.

Salter, I., Schiebel, R., Ziveri, P., Movellan, A., Lampitt, R., & Wolff, G. A. (2014). Carbonate counter pump stimulated by natural iron fertilization in the Polar Frontal Zone. *Nature Geoscience*, *7*(12), 885-889.

Sambrotto, R. N., & Mace, B. J. (2000). Coupling of biological and physical regimes across the Antarctic Polar Front as reflected by nitrogen production and recycling. *Deep Sea Research Part II: Topical Studies in Oceanography*, *47*(15-16), 3339-3367.

Sánchez-Baracaldo, P., Ridgwell, A., & Raven, J. A. (2014). A neoproterozoic transition in the marine nitrogen cycle. *Current Biology*, *24*(6), 652-657.

Santoso, A., & England, M. H. (2004). Antarctic Intermediate Water circulation and variability in a coupled climate model. *Journal of Physical Oceanography*, *34*(10), 2160-2179.

Sarmiento, J. L., & Toggweiler, J. R. (1984). A new model for the role of the oceans in determining atmospheric pCO2. *Nature*, *308*(5960), 621-624.

Sarmiento, J. L., Gruber, N., Brzezinski, M. A., & Dunne, J. P. (2004). High-latitude controls of thermocline nutrients and low latitude biological productivity. *Nature*, *427*(6969), 56-60.

Sarmiento, J. L., Simeon, J., Gnanadesikan, A., Gruber, N., Key, R. M., & Schlitzer, R. (2007). Deep ocean biogeochemistry of silicic acid and nitrate. *Global Biogeochemical Cycles*, *21*(1).

Sarthou, G., Timmermans, K. R., Blain, S., & Tréguer, P. (2005). Growth physiology and fate of diatoms in the ocean: a review. *Journal of sea research*, *53*(1-2), 25-42.

Savoye, N., Trull, T. W., Jacquet, S. H. M., Navez, J., & Dehairs, F. (2008). 234Th-based export fluxes during a natural iron fertilization experiment in the Southern Ocean (KEOPS). *Deep Sea Research Part II: Topical Studies in Oceanography*, *55*(5-7), 841-855.

Saxberg, B. E., & Kowalski, B. R. (1979). Generalized standard addition method. *Analytical Chemistry*, *51*(7), 1031-1038.

Scanlan, D. J. (2003). Physiological diversity and niche adaptation in marine Synechococcus.

Schallenberg, C., Bestley, S., Klocker, A., Trull, T. W., Davies, D. M., Gault-Ringold, M., ... & Townsend, A. T. (2018). Sustained upwelling of subsurface iron supplies seasonally persistent phytoplankton blooms around the southern Kerguelen plateau, Southern Ocean. *Journal of Geophysical Research: Oceans*, *123*(8), 5986-6003.

Schmidt, M. A., & Hutchins, D. A. (1999). Size-fractionated biological iron and carbon uptake along a coastal to offshore transect in the NE Pacific. *Deep Sea Research Part II: Topical Studies in Oceanography*, *46*(11-12), 2487-2503.

Schoemann, V., Becquevort, S., Stefels, J., Rousseau, V., & Lancelot, C. (2005). Phaeocystis blooms in the global ocean and their controlling mechanisms: a review. *Journal of Sea Research*, *53*(1-2), 43-66.

Schoemann, V., Wollast, R., Chou, L., & Lancelot, C. (2001). Effects of photosynthesis on the accumulation of Mn and Fe by Phaeocystis colonies. *Limnology and Oceanography*, *46*(5), 1065-1076.

Schultes, S., Verity, P. G., & Bathmann, U. (2006). Copepod grazing during an iron-induced diatom bloom in the Antarctic Circumpolar Current (EisenEx): I. Feeding patterns and grazing impact on prey populations. *Journal of Experimental Marine Biology and Ecology*, *338*(1), 16-34.

Sedwick, P. N., Blain, S., Quéguiner, B., Griffiths, F. B., Fiala, M., Bucciarelli, E., & Denis, M. (2002). Resource limitation of phytoplankton growth in the Crozet Basin, Subantarctic Southern Ocean. *Deep Sea Research Part II: Topical Studies in Oceanography*, *49*(16), 3327-3349.

Seeyave, S., Lucas, M. I., Moore, C. M., & Poulton, A. J. (2007). Phytoplankton productivity and community structure in the vicinity of the Crozet Plateau during austral summer 2004/2005. *Deep Sea Research Part II: Topical Studies in Oceanography*, *54*(18-20), 2020-2044.

Selph, K. E., Landry, M. R., Allen, C. B., Calbet, A., Christensen, S., & Bidigare, R. R. (2001). Microbial community composition and growth dynamics in the Antarctic Polar Front and seasonal ice zone during late spring 1997. *Deep Sea Research Part II: Topical Studies in Oceanography*, *48*(19-20), 4059-4080.

Semeneh, M., Dehairs, F., Elskens, M., Baumann, M. E. M., Kopczynska, E. E., Lancelot, C., & Goeyens, L. (1998). Nitrogen uptake regime and phytoplankton community structure in the Atlantic and Indian sectors of the Southern Ocean. *Journal of marine systems*, *17*(1-4), 159-177.

Shapiro, L. P., & Haugen, E. M. (1988). Seasonal distribution and temperature tolerance of Synechococcus in Boothbay Harbor, Maine. *Estuarine, Coastal and Shelf Science*, *26*(5), 517-525.

Shaw, T. J., Raiswell, R., Hexel, C. R., Vu, H. P., Moore, W. S., Dudgeon, R., & Smith Jr, K. L. (2011). Input, composition, and potential impact of terrigenous material from free-drifting icebergs in the Weddell Sea. *Deep Sea Research Part II: Topical Studies in Oceanography*, *58*(11-12), 1376-1383.

Siegel, D. A., Buesseler, K. O., Doney, S. C., Sailley, S. F., Behrenfeld, M. J., & Boyd, P. W. (2014). Global assessment of ocean carbon export by combining satellite observations and food-web models. *Global Biogeochemical Cycles*, *28*(3), 181-196.

Siegenthaler, U., & Wenk, T. (1984). Rapid atmospheric CO 2 variations and ocean circulation. *Nature*, *308*(5960), 624-626.

Sievers, H. A., & Emery, W. J. (1978). Variability of the Antarctic Polar frontal Zone in the Drake Passage—summer 1976–1977. *Journal of Geophysical Research: Oceans*, *83*(C6), 3010-3022.

Sigman, D. M., & Boyle, E. A. (2000). Glacial/interglacial variations in atmospheric carbon dioxide. *Nature*, *407*(6806), 859-869.

Sigman, D. M., & Fripiat, F. (2019). Nitrogen isotopes in the ocean. *Encyclopedia of Ocean Sciences*, *1*, 263-278.

Sigman, D. M., & Hain, M. P. (2012). The biological productivity of the ocean. *Nature Education Knowledge*, *3*(6), 1-16.

Sigman, D. M., Altabet, M. A., McCorkle, D. C., Francois, R., & Fischer, G. (2000). The δ15N of nitrate in the Southern Ocean: Nitrogen cycling and circulation in the ocean interior. *Journal of Geophysical Research: Oceans*, *105*(C8), 19599-19614.

Sigman, D. M., Altabet, M. A., McCorkle, D. C., Francois, R., & Fischer, G. (1999). The δ15N of nitrate in the Southern Ocean: Consumption of nitrate in surface waters. *Global Biogeochemical Cycles*, *13*(4), 1149-1166.

Sigman, D. M., Casciotti, K. L., Andreani, M., Barford, C., Galanter, M. B. J. K., & Böhlke, J. K. (2001). A bacterial method for the nitrogen isotopic analysis of nitrate in seawater and freshwater. *Analytical chemistry*, *73*(17), 4145-4153.

Sigman, D. M., Hain, M. P., & Haug, G. H. (2010). The polar ocean and glacial cycles in atmospheric CO 2 concentration. *Nature*, *466*(7302), 47-55.

Sigman, D. M., Karsh, K. L., & Casciotti, K. L. (2009). Ocean process tracers: nitrogen isotopes in the ocean.

Sigman, D. M., Lehman, S. J., & Oppo, D. W. (2003). Evaluating mechanisms of nutrient depletion and 13C enrichment in the intermediate-depth Atlantic during the last ice age. *Paleoceanography*, *18*(3).

Silfer, J. A., Engel, M. H., & Macko, S. A. (1992). Kinetic fractionation of stable carbon and nitrogen isotopes during peptide bond hydrolysis: experimental evidence and geochemical implications. *Chemical Geology: Isotope Geoscience section*, *101*(3-4), 211-221.

Sloyan, B. M., & Rintoul, S. R. (2001). Circulation, renewal, and modification of Antarctic Mode and Intermediate Water. *Journal of physical oceanography*, *31*(4), 1005-1030.

Smart, S. M., Fawcett, S. E., Ren, H., Schiebel, R., Tompkins, E. M., Martínez-García, A., ... & Sigman, D. M. (2020). The Nitrogen Isotopic Composition of Tissue and Shell-Bound Organic Matter of Planktic Foraminifera in Southern Ocean Surface Waters. *Geochemistry, Geophysics, Geosystems*, *21*(2), e2019GC008440.

Smart, S. M., Fawcett, S. E., Thomalla, S. J., Weigand, M. A., Reason, C. J., & Sigman, D. M. (2015). Isotopic evidence for nitrification in the Antarctic winter mixed layer. *Global Biogeochemical Cycles*, *29*(4), 427-445.

Smetacek, V., Assmy, P., & Henjes, J. (2004). The role of grazing in structuring Southern Ocean pelagic ecosystems and biogeochemical cycles. *Antarctic Science*, *16*(4), 541.

Smith Jr, K. L., Sherman, A. D., Shaw, T. J., Murray, A. E., Vernet, M., & Cefarelli, A. O. (2011). Carbon export associated with free-drifting icebergs in the Southern Ocean. *Deep Sea Research Part II: Topical Studies in Oceanography*, *58*(11-12), 1485-1496.

Sohm, J. A., Ahlgren, N. A., Thomson, Z. J., Williams, C., Moffett, J. W., Saito, M. A., ... & Rocap, G. (2016). Co-occurring Synechococcus ecotypes occupy four major oceanic regimes defined by temperature, macronutrients and iron. *The ISME journal*, *10*(2), 333-345.

Sokolov, S., & Rintoul, S. R. (2009). Circumpolar structure and distribution of the Antarctic Circumpolar Current fronts: 1. Mean circumpolar paths. *Journal of Geophysical Research: Oceans*, *114*(C11).

Solomon, C. M., Collier, J. L., Berg, G. M., & Glibert, P. M. (2010). Role of urea in microbial metabolism in aquatic systems: a biochemical and molecular review. *Aquatic Microbial Ecology*, *59*(1), 67-88.

Sosik, H. M., Chisholm, S. W., & Olson, R. J. (1989). Chlorophyll fluorescence from single cells: interpretation of flow cytometric signals. *Limnology and Oceanography*, *34*(8), 1749-1761.

Sparrow, M. D., Heywood, K. J., Brown, J., & Stevens, D. P. (1996). Current structure of the south Indian Ocean. *Journal of Geophysical Research: Oceans*, *101*(C3), 6377-6391.

Stammer, D. (1997). Global characteristics of ocean variability estimated from regional TOPEX/POSEIDON altimeter measurements. *Journal of Physical Oceanography*, *27*(8), 1743-1769.

Stefels, J., Dijkhuizen, L., & Gieskes, W. W. C. (1995). DMSP-lyase activity in a spring phytoplankton bloom off the Dutch coast, related to Phaeocystis sp. abundance. *Marine Ecology Progress Series*, *123*, 235-243.

Stephens, B. B., & Keeling, R. F. (2000). The influence of Antarctic sea ice on glacial–interglacial CO 2 variations. *Nature*, *404*(6774), 171-174.

Stockner, J. G. (1988). Phototrophic picoplankton: an overview from marine and freshwater ecosystems. *Limnology and Oceanography*, *33*(4part2), 765-775.

Stockner, J. G., & Antia, N. J. (1986). Algal picoplankton from marine and freshwater ecosystems: a multidisciplinary perspective. *Canadian journal of fisheries and aquatic sciences*, *43*(12), 2472-2503.

Strickland, J. D. H., (1967.), The Ecology of the Plankton off La Jolla, California, in the Period April Through September, 1967, *University of California Press,* Berkeley, Calif.

Strickland, J.D.H., & Parsons, T.R. (1972). A Practical Handbook of Seawater Analysis. *Bulletin of the Fisheries Research Board of Canada* 2nd edition. Vol. 167.

Strzepek, R. F., & Harrison, P. J. (2004). Photosynthetic architecture differs in coastal and oceanic diatoms. *Nature*, *431*(7009), 689-692.

Strzepek, R. F., Boyd, P. W., & Sunda, W. G. (2019). Photosynthetic adaptation to low iron, light, and temperature in Southern Ocean phytoplankton. *Proceedings of the National Academy of Sciences*, *116*(10), 4388-4393.

Strzepek, R. F., Hunter, K. A., Frew, R. D., Harrison, P. J., & Boyd, P. W. (2012). Iron-light interactions differ in Southern Ocean phytoplankton. *Limnology and Oceanography*, *57*(4), 1182-1200.

Strzepek, R. F., Maldonado, M. T., Hunter, K. A., Frew, R. D., & Boyd, P. W. (2011). Adaptive strategies by Southern Ocean phytoplankton to lessen iron limitation: Uptake of organically complexed iron and reduced cellular iron requirements. *Limnology and Oceanography*, *56*(6), 1983-2002.

Stukel, M. R., & Landry, M. R. (2010). Contribution of picophytoplankton to carbon export in the equatorial Pacific: A reassessment of food web flux inferences from inverse models. *Limnology and Oceanography*, *55*(6), 2669-2685.

Sunda, W. G. (1989). Trace metal interactions with marine phytoplankton. *Biological Oceanography*, *6*(5-6), 411-442.

Sunda, W. G. (2012). Feedback interactions between trace metal nutrients and phytoplankton in the ocean, Front. Microbiol., 3, 204.

Sunda, W. G., & Huntsman, S. A. (1995). Iron uptake and growth limitation in oceanic and coastal phytoplankton. *Marine chemistry*, *50*(1-4), 189-206.

Sunda, W. G., & Huntsman, S. A. (1997). Interrelated influence of iron, light and cell size on marine phytoplankton growth. *Nature*, *390*(6658), 389-392.

Sunda, W. G., & Huntsman, S. A. (2015). High iron requirement for growth, photosynthesis, and low-light acclimation in the coastal cyanobacterium Synechococcus bacillaris. *Frontiers in Microbiology*, *6*, 561.

Sunda, W. K. D. J., Kieber, D. J., Kiene, R. P., & Huntsman, S. (2002). An antioxidant function for DMSP and DMS in marine algae. *Nature*, *418*(6895), 317-320.

Switzer, A. C., Kamykowski, D., & Zentara, S. J. (2003). Mapping nitrate in the global ocean using remotely sensed sea surface temperature. *Journal of Geophysical Research: Oceans*, *108*(C8).

Syrett, P. J., & Morris, I. (1963). The inhibition of nitrate assimilation by ammonium in Chlorella. *Biochimica et Biophysica Acta (BBA)-Specialized Section on Enzymological Subjects*, *67*, 566-575.

Tabita, F. R., Hanson, T. E., Li, H., Satagopan, S., Singh, J., & Chan, S. (2007). Function, structure, and evolution of the RubisCO-like proteins and their RubisCO homologs. *Microbiology and Molecular Biology Reviews*, *71*(4), 576-599.

Tagliabue, A., Bopp, L., Dutay, J. C., Bowie, A. R., Chever, F., Jean-Baptiste, P., ... & Aumont, O. (2010). Hydrothermal contribution to the oceanic dissolved iron inventory. *Nature Geoscience*, *3*(4), 252-256.

Tagliabue, A., Sallée, J. B., Bowie, A. R., Lévy, M., Swart, S., & Boyd, P. W. (2014). Surface-water iron supplies in the Southern Ocean sustained by deep winter mixing. *Nature Geoscience*, *7*(4), 314-320.

Takahashi, T., Sutherland, S. C., Sweeney, C., Poisson, A., Metzl, N., Tilbrook, B., ... & Olafsson, J. (2002). Global sea–air CO2 flux based on climatological surface ocean pCO2, and seasonal biological and temperature effects. *Deep Sea Research Part II: Topical Studies in Oceanography*, *49*(9-10), 1601-1622.

Takahashi, T., Sutherland, S. C., Wanninkhof, R., Sweeney, C., Feely, R. A., Chipman, D. W., ... & Watson, A. (2009). Climatological mean and decadal change in surface ocean pCO2, and net

sea–air CO2 flux over the global oceans. *Deep Sea Research Part II: Topical Studies in Oceanography*, *56*(8-10), 554-577.
Takeda, S. (1998). Influence of iron availability on nutrient consumption ratio of diatoms in oceanic waters. *Nature*, *393*(6687), 774-777.
Talley, L. D. (1996). Antarctic intermediate water in the South Atlantic. In *The South Atlantic* (pp. 219-238). Springer, Berlin, Heidelberg.
Talley, L. D. (2011). *Descriptive physical oceanography: an introduction*. Academic press.
Tarran, G. A., & Bruun, J. T. (2015). Nanoplankton and picoplankton in the Western English Channel: abundance and seasonality from 2007–2013. *Progress in Oceanography*, *137*, 446-455.
Tarran, G. A., Heywood, J. L., & Zubkov, M. V. (2006). Latitudinal changes in the standing stocks of nano-and picoeukaryotic phytoplankton in the Atlantic Ocean. *Deep Sea Research Part II: Topical Studies in Oceanography*, *53*(14-16), 1516-1529.
Tatur, A., & Myrcha, A. (1983). Changes in chemical composition of waters running off from the penguin rookeries in the Admiralty Bay region (King George Island, South Shetland Islands, Antarctica). *Polish Polar Research*, 113-125.
Thingstad, T. F., Øvreås, L., Egge, J. K., Løvdal, T., & Heldal, M. (2005). Use of non-limiting substrates to increase size; a generic strategy to simultaneously optimize uptake and minimize predation in pelagic osmotrophs?. *Ecology Letters*, *8*(7), 675-682.
Timmermans, K. R., Stolte, W., & De Baar, H. J. W. (1994). Iron-mediated effects on nitrate reductase in marine phytoplankton. *Marine Biology*, *121*(2), 389-396.
Timmermans, K. R., Van Der Wagt, B., & De Baar, H. J. (2004). Growth rates, half-saturation constants, and silicate, nitrate, and phosphate depletion in relation to iron availability of four large, open-ocean diatoms from the Southern Ocean. *Limnology and Oceanography*, *49*(6), 2141-2151.
Timmermans, K. R., Van Leeuwe, M. A., De Jong, J. T. M., McKay, R. M. L., Nolting, R. F., Witte, H. J., ... & De Baar, H. J. (1998). Iron stress in the Pacific region of the Southern Ocean: evidence from enrichment bioassays. *Marine Ecology Progress Series*, *166*, 27-41.
Toggweiler, J. R. (1999). Variation of atmospheric CO2 by ventilation of the ocean's deepest water. *Paleoceanography*, *14*(5), 571-588.
Tomas, C. R., & Haste, G. R. (1997). Identifying Marine Phytoplankton Academic Press. *New York*.
Tomczak, M., & Liefrink, S. (2005). Interannual variations of water mass volumes in the Southern Ocean. *Journal of Atmospheric & Ocean Science*, *10*(1), 31-42.
Tortell, P. D., Maldonado, M. T., Granger, J., & Price, N. M. (1999). Marine bacteria and biogeochemical cycling of iron in the oceans. *FEMS Microbiology Ecology*, *29*(1), 1-11.
Traganza, E. D., Nestor, D. A., & McDonald, A. K. (1980). Satellite observations of a nutrient upwelling off the coast of California. *Journal of Geophysical Research: Oceans*, *85*(C7), 4101-4106.
Treasure, A. M., Ruzicka, J. J., Moloney, C. L., Gurney, L. J., & Ansorge, I. J. (2015). Land–sea interactions and consequences for sub-Antarctic marine food webs. *Ecosystems*, *18*(5), 752-768.
Treasure, A. M., Ruzicka, J. J., Pakhomov, E. A., & Ansorge, I. J. (2019). Physical transport mechanisms driving sub-Antarctic Island marine ecosystems. *Ecosystems*, *22*(5), 1069-1087.
Tréguer, P. J. (2014). The Southern Ocean silica cycle. *Comptes Rendus Geoscience*, *346*(11-12), 279-286.
Tréguer, P., & Jacques, G. (1992). Review Dynamics of nutrients and phytoplankton, and fluxes of carbon, nitrogen and silicon in the Antarctic Ocean. In *Weddell Sea Ecology* (pp. 149-162). Springer, Berlin, Heidelberg.
Tréguer, P., & Van Bennekom, A. J. (1991). The annual production of biogenic silica in the Antarctic Ocean. *Marine Chemistry*, *35*(1-4), 477-487.
Tréguer, P., Bowler, C., Moriceau, B., Dutkiewicz, S., Gehlen, M., Aumont, O., ... & Jahn, O. (2018). Influence of diatom diversity on the ocean biological carbon pump. *Nature Geoscience*, *11*(1), 27-37.

Tréguer, P., Nelson, D. M., Van Bennekom, A. J., DeMaster, D. J., Leynaert, A., & Queguiner, B. (1995). The silica balance in the world ocean: a reestimate. *Science*, *268*(5209), 375-379.

Treibergs, L. A., Fawcett, S. E., Lomas, M. W., & Sigman, D. M. (2014). Nitrogen isotopic response of prokaryotic and eukaryotic phytoplankton to nitrate availability in Sargasso Sea surface waters. *Limnology and oceanography*, *59*(3), 972-985.

Tremblay, J. E., Lucas, M. I., Kattner, G., Pollard, R., Strass, V. H., Bathmann, U., & Bracher, A. (2002). Significance of the Polar Frontal Zone for large-sized diatoms and new production during summer in the Atlantic sector of the Southern Ocean. *Deep Sea Research Part II: Topical Studies in Oceanography*, *49*(18), 3793-3811.

Trimborn, S., Hoppe, C. J., Taylor, B. B., Bracher, A., & Hassler, C. (2015). Physiological characteristics of open ocean and coastal phytoplankton communities of Western Antarctic Peninsula and Drake Passage waters. *Deep Sea Research Part I: Oceanographic Research Papers*, *98*, 115-124.

Trimborn, S., Thoms, S., Karitter, P., & Bischof, K. (2019). Ocean acidification and high irradiance stimulate the photo-physiological fitness, growth and carbon production of the Antarctic cryptophyte Geminigera cryophila. *Biogeosciences*, *16*(15), 2997-3008.

Trull, T. W., Bray, S. G., Manganini, S. J., Honjo, S., & Francois, R. (2001b). Moored sediment trap measurements of carbon export in the Subantarctic and Polar Frontal Zones of the Southern Ocean, south of Australia. *Journal of Geophysical Research: Oceans*, *106*(C12), 31489-31509.

Trull, T. W., Davies, D. M., Dehairs, F., Cavagna, A. J., Lasbleiz, M., Laurenceau-Cornec, E. C., ... & Blain, S. (2015). Chemometric perspectives on plankton community responses to natural iron fertilisation over and downstream of the Kerguelen Plateau in the Southern Ocean. *Biogeosciences*, *12*(4), 1029-1056.

Trull, T. W., Davies, D., & Casciotti, K. (2008). Insights into nutrient assimilation and export in naturally iron-fertilized waters of the Southern Ocean from nitrogen, carbon and oxygen isotopes. *Deep Sea Research Part II: Topical Studies in Oceanography*, *55*(5-7), 820-840.

Trull, T. W., Passmore, A., Davies, D. M., Smit, T., Berry, K., & Tilbrook, B. (2018). Distribution of planktonic biogenic carbonate organisms in the Southern Ocean south of Australia: a baseline for ocean acidification impact assessment. *Biogeosciences*, *15*, 31-49.

Trull, T., Rintoul, S. R., Hadfield, M., & Abraham, E. R. (2001a). Circulation and seasonal evolution of polar waters south of Australia: Implications for iron fertilization of the Southern Ocean. *Deep Sea Research Part II: Topical Studies in Oceanography*, *48*(11-12), 2439-2466.

Tsai, A. Y., Chiang, K. P., Chang, J., & Gong, G. C. (2008). Seasonal variations in trophic dynamics of nanoflagellates and picoplankton in coastal waters of the western subtropical Pacific Ocean. *Aquatic microbial ecology*, *51*(3), 263-274.

Turner, J. T. (2015). Zooplankton fecal pellets, marine snow, phytodetritus and the ocean's biological pump. *Progress in Oceanography*, *130*, 205-248.

Twining, B. S., & Baines, S. B. (2013). The trace metal composition of marine phytoplankton. *Annual review of marine science*, *5*, 191-215.

Twining, B. S., Baines, S. B., & Fisher, N. S. (2004). Element stoichiometries of individual plankton cells collected during the Southern Ocean Iron Experiment (SOFeX). *Limnology and oceanography*, *49*(6), 2115-2128.

Tyrrell, T., Merico, A., Waniek, J. J., Wong, C. S., Metzl, N., & Whitney, F. (2005). Effect of seafloor depth on phytoplankton blooms in high-nitrate, low-chlorophyll (HNLC) regions. *Journal of Geophysical Research: Biogeosciences*, *110*(G2).

Van Der Merwe, P., Bowie, A. R., Quéroué, F., Armand, L., Blain, S., Chever, F., ... & Townsend, A. T. (2015). Sourcing the iron in the naturally fertilised bloom around the Kerguelen Plateau: particulate trace metal dynamics. *Biogeosciences*, *12*(3), 739-755.

Van Leeuwe, M. A., Visser, R. J., & Stefels, J. (2014). The pigment composition of P haeocystis antarctica (H aptophyceae) under various conditions of light, temperature, salinity, and iron. *Journal of phycology*, *50*(6), 1070-1080.

Van Oostende, N., Fawcett, S. E., Marconi, D., Lueders-Dumont, J., Sabadel, A. J. M., Woodward, E. M. S., ... & Ward, B. B. (2017). Variation of summer phytoplankton community composition and its relationship to nitrate and regenerated nitrogen assimilation across the North Atlantic Ocean. *Deep Sea Research Part I: Oceanographic Research Papers*, *121*, 79-94.

Varela, D. E., & Harrison, P. J. (1999). Effect of ammonium on nitrate utilization by Emiliania huxleyi, a coccolithophore from the oceanic northeastern Pacific. *Marine Ecology Progress Series*, *186*, 67-74.

Vaulot, D., Eikrem, W., Viprey, M., & Moreau, H. (2008). The diversity of small eukaryotic phytoplankton (≤ 3 μm) in marine ecosystems. *FEMS microbiology reviews*, *32*(5), 795-820.

Veldhuis, M. J., & Kraay, G. W. (1993). Cell abundance and fluorescence of picoplankton in relation to growth irradiance and nitrogen availability in the Red Sea. *Netherlands Journal of Sea Research*, *31*(2), 135-145.

Veldhuis, M. J., Timmermans, K. R., Croot, P., & van der Wagt, B. (2005). Picophytoplankton; a comparative study of their biochemical composition and photosynthetic properties. *Journal of Sea Research*, *53*(1-2), 7-24.

Venables, H. J., Pollard, R. T., & Popova, E. E. (2007). Physical conditions controlling the development of a regular phytoplankton bloom north of the Crozet Plateau, Southern Ocean. *Deep Sea Research Part II: Topical Studies in Oceanography*, *54*(18-20), 1949-1965.

Venables, H., & Moore, C. M. (2010). Phytoplankton and light limitation in the Southern Ocean: Learning from high-nutrient, high-chlorophyll areas. *Journal of Geophysical Research: Oceans*, *115*(C2).

Vernet, M., Sines, K., Chakos, D., Cefarelli, A. O., & Ekern, L. (2011). Impacts on phytoplankton dynamics by free-drifting icebergs in the NW Weddell Sea. *Deep Sea Research Part II: Topical Studies in Oceanography*, *58*(11-12), 1422-1435.

Vernet, M., Smith Jr, K. L., Cefarelli, A. O., Helly, J. J., Kaufmann, R. S., Lin, H., ... & Shaw, T. J. (2012). Islands of ice: Influence of free-drifting Antarctic icebergs on pelagic marine ecosystems. *Oceanography*, *25*.

Villareal, T. A., Altabet, M. A., & Culver-Rymsza, K. (1993). Nitrogen transport by vertically migrating diatom mats in the North Pacific Ocean. *Nature*, *363*(6431), 709-712.

Volk, T., & Hoffert, M. I. (1985). Ocean carbon pumps: Analysis of relative strengths and efficiencies in ocean-driven atmospheric CO2 changes. *The carbon cycle and atmospheric CO2: natural variations Archean to present*, *32*, 99-110.

Wada, E., & Hattori, A. (1978). Nitrogen isotope effects in the assimilation of inorganic nitrogenous compounds by marine diatoms. *Geomicrobiology Journal*, *1*(1), 85-101.

Ward, P., Whitehouse, M., Shreeve, R., Thorpe, S., Atkinson, A., Korb, R., ... & Young, E. (2007). Plankton community structure south and west of South Georgia (Southern Ocean): Links with production and physical forcing. *Deep Sea Research Part I: Oceanographic Research Papers*, *54*(11), 1871-1889.

Waser, N. A., Yin, K., Yu, Z., Tada, K., Harrison, P. J., Turpin, D. H., & Calvert, S. E. (1998). Nitrogen isotope fractionation during nitrate, ammonium and urea uptake by marine diatoms and coccolithophores under various conditions of N availability. *Marine Ecology Progress Series*, *169*, 29-41.

Wassmann, P. (1994). Significance of sedimentation for the termination of Phaeocystis blooms. *Journal of Marine Systems*, *5*(1), 81-100.

Waterbury, J. B. (1986). Biological and ecological characterization of the marine unicellular cyanobacterium Synechococcus. *Photosynthetic picoplankton*, 71-120.

Waters, R. L., Van den Enden, R., & Marchant, H. J. (2000). Summer microbial ecology off East Antarctica (80–150 E): protistan community structure and bacterial abundance. *Deep Sea Research Part II: Topical Studies in Oceanography*, *47*(12-13), 2401-2435.

Webb, E. A., Moffett, J. W., & Waterbury, J. B. (2001). Iron stress in open-ocean cyanobacteria (synechococcus, trichodesmium, andcrocosphaera spp.): Identification of the idia protein. *Applied and Environmental Microbiology*, *67*(12), 5444-5452.

Weber, L. H., & El-Sayed, S. Z. (1987). Contributions of the net, nano-and picoplankton to the phytoplankton standing crop and primary productivity in the Southern Ocean. *Journal of Plankton Research*, *9*(5), 973-994.

Weber, T. S., & Deutsch, C. (2010). Ocean nutrient ratios governed by plankton biogeography. *Nature*, *467*(7315), 550-554.

Weisse, T., Tande, K., Verity, P., Hansen, F., & Gieskes, W. (1994). The trophic significance of Phaeocystis blooms. *Journal of Marine Systems*, *5*(1), 67-79.

Weissman, G. S. (1964). Effect of ammonium and nitrate nutrition on protein level and exudate composition. *Plant Physiology*, *39*(6), 947.

Welschmeyer, N. A. (1994). Fluorometric analysis of chlorophyll a in the presence of chlorophyll b and pheopigments. *Limnology and Oceanography*, *39*(8), 1985-1992.

Wendt, K., (2000). Quickchem Method 10-107-04-1-A: Determination of nitrate/nitrite in surface and wastewaters by flow injection analysis. *Milwaukee, WI: Lachat Instruments*

Wetz, M. S., & Wheeler, P. A. (2003). Production and partitioning of organic matter during simulated phytoplankton blooms. *Limnology and Oceanography*, *48*(5), 1808-1817.

Wheeler, P. A., & Kokkinakis, S. A. (1990). Ammonium recycling limits nitrate use in the oceanic subarctic Pacific. *Limnology and Oceanography*, *35*(6), 1267-1278.

Whitworth III, T., Orsi, A. H., Kim, S. J., Nowlin Jr, W. D., & Locarnini, R. A. (1985). Water masses and mixing near the Antarctic Slope Front. *Ocean, ice, and atmosphere: interactions at the Antarctic continental margin*, *75*, 1-27.

Wilhelm, C., Büchel, C., Fisahn, J., Goss, R., Jakob, T., LaRoche, J., ... & Valentin, K. (2006). The regulation of carbon and nutrient assimilation in diatoms is significantly different from green algae.

Wilhelm, S. W., Maxwell, D. P., & Trick, C. G. (1996). Growth, iron requirements, and siderophore production in iron-limited Synechococcus PCC 72. *Limnology and oceanography*, *41*(1), 89-97.

Wong, A. P. (2005). Subantarctic mode water and Antarctic intermediate water in the south Indian Ocean based on profiling float data 2000–2004. *Journal of Marine Research*, *63*(4), 789-812.

Wood, A. M., Horan, P. K., Muirhead, K., Phinney, D. A., Yentsch, C. M., & Waterbury, J. B. (1985). Discrimination between types of pigments in marine Synechococcus spp. by scanning spectroscopy, epifluorescence microscopy, and flow cytometry 1. *Limnology and Oceanography*, *30*(6), 1303-1315.

Wood, A. M., Lipsen, M., & Coble, P. (1998). Fluorescence-based characterization of Synechococcus community structure in the Arabian Sea during the Northeast and Southwest Monsoons (1994—95). *Deep-Sea Research II*.

Wood, A. M., Phinney, D. A., & Yentsch, C. S. (1998). Water column transparency and the distribution of spectrally distinct forms of phycoerythrin-containing organisms. *Marine Ecology Progress Series*, *162*, 25-31.

Wright, S. W., & Jeffrey, S. W. (1987). Fucoxanthin pigment markers of marine phytoplankton analysed by HPLC and HPTLC. *Marine Ecology Progress Series*, 259-266.

Wright, S. W., Thomas, D. P., Marchant, H. J., Higgins, H. W., Mackey, M. D., & Mackey, D. J. (1996). Analysis of phytoplankton of the Australian sector of the Southern Ocean: comparisons of microscopy and size frequency data with interpretations of pigment HPLC data using the\'CHEMTAX\'matrix factorisation program. *Marine Ecology Progress Series*, *144*, 285-298.

Wu, J., Calvert, S. E., & Wong, C. S. (1997). Nitrogen isotope variations in the subarctic northeast Pacific: relationships to nitrate utilization and trophic structure. *Deep Sea Research Part I: Oceanographic Research Papers*, *44*(2), 287-314.

Wu, Y., Campbell, D. A., Irwin, A. J., Suggett, D. J., & Finkel, Z. V. (2014a). Ocean acidification enhances the growth rate of larger diatoms. *Limnology and Oceanography*, *59*(3), 1027-1034.

Wu, Y., Jeans, J., Suggett, D. J., Finkel, Z. V., & Campbell, D. A. (2014b). Large centric diatoms allocate more cellular nitrogen to photosynthesis to counter slower RUBISCO turnover rates. *Frontiers in Marine Science*, *1*, 68.

Yelton, A. P., Acinas, S. G., Sunagawa, S., Bork, P., Pedrós-Alió, C., & Chisholm, S. W. (2016). Global genetic capacity for mixotrophy in marine picocyanobacteria. *The ISME journal*, *10*(12), 2946-2957.

Yentsch, C. M., Horan, P. K., Muirhead, K., Dortch, Q., Haugen, E., Legendre, L., ... & Spinrad, R. W. (1983). Flow cytometry and cell sorting: A technique for analysis and sorting of aquatic particles 1. *Limnology and Oceanography*, *28*(6), 1275-1280.

Yih, W., Kim, H. S., Jeong, H. J., Myung, G., & Kim, Y. G. (2004). Ingestion of cryptophyte cells by the marine photosynthetic ciliate Mesodinium rubrum. *Aquatic Microbial Ecology*, *36*(2), 165-170.

Yool, A., Martin, A. P., Fernández, C., & Clark, D. R. (2007). The significance of nitrification for oceanic new production. *Nature*, *447*(7147), 999-1002.

Young, J. N., Rickaby, R. E. M., Kapralov, M. V., & Filatov, D. A. (2012). Adaptive signals in algal Rubisco reveal a history of ancient atmospheric carbon dioxide. *Philosophical Transactions of the Royal Society B: Biological Sciences*, *367*(1588), 483-492.

Zehr, J. P., & Ward, B. B. (2002). Nitrogen cycling in the ocean: new perspectives on processes and paradigms. *Applied and environmental microbiology*, *68*(3), 1015-1024.

Ziveri, P., de Bernardi, B., Baumann, K. H., Stoll, H. M., & Mortyn, P. G. (2007). Sinking of coccolith carbonate and potential contribution to organic carbon ballasting in the deep ocean. *Deep Sea Research Part II: Topical Studies in Oceanography*, *54*(5-7), 659-675.

Zubkov, M. V., Sleigh, M. A., Burkill, P. H., & Leakey, R. J. (2000). Picoplankton community structure on the Atlantic Meridional Transect: a comparison between seasons. *Progress in oceanography*, *45*(3-4), 369-386.

Zwirglmaier, K., Jardillier, L., Ostrowski, M., Mazard, S., Garczarek, L., Vaulot, D., ... & Scanlan, D. J. (2008). Global phylogeography of marine Synechococcus and Prochlorococcus reveals a distinct partitioning of lineages among oceanic biomes. *Environmental microbiology*, *10*(1), 147-161.